



HAL
open science

Nanostructured carbon materials derived from tannin as electrodes for supercapacitors

Jimena Castro-Gutiérrez

► To cite this version:

Jimena Castro-Gutiérrez. Nanostructured carbon materials derived from tannin as electrodes for supercapacitors. Chemical Sciences. Université de Lorraine, 2020. English. NNT : 2020LORR0126 . tel-03070352

HAL Id: tel-03070352

<https://hal.univ-lorraine.fr/tel-03070352v1>

Submitted on 21 Nov 2022

HAL is a multi-disciplinary open access archive for the deposit and dissemination of scientific research documents, whether they are published or not. The documents may come from teaching and research institutions in France or abroad, or from public or private research centers.

L'archive ouverte pluridisciplinaire **HAL**, est destinée au dépôt et à la diffusion de documents scientifiques de niveau recherche, publiés ou non, émanant des établissements d'enseignement et de recherche français ou étrangers, des laboratoires publics ou privés.



AVERTISSEMENT

Ce document est le fruit d'un long travail approuvé par le jury de soutenance et mis à disposition de l'ensemble de la communauté universitaire élargie.

Il est soumis à la propriété intellectuelle de l'auteur. Ceci implique une obligation de citation et de référencement lors de l'utilisation de ce document.

D'autre part, toute contrefaçon, plagiat, reproduction illicite encourt une poursuite pénale.

Contact : ddoc-theses-contact@univ-lorraine.fr

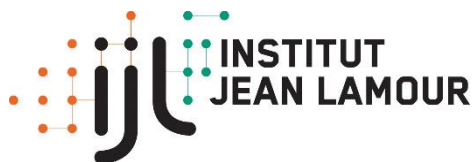
LIENS

Code de la Propriété Intellectuelle. articles L 122. 4

Code de la Propriété Intellectuelle. articles L 335.2- L 335.10

http://www.cfcopies.com/V2/leg/leg_droi.php

<http://www.culture.gouv.fr/culture/infos-pratiques/droits/protection.htm>



THÈSE

Pour l'obtention du titre de:

DOCTEUR de L'UNIVERSITÉ DE LORRAINE

Spécialité: Chimie

Présentée par:

JIMENA CASTRO GUTIÉRREZ

Matériaux carbonés nanostructurés dérivés de tanin pour électrodes de supercondensateurs

Thèse soutenue publiquement le 12 Novembre 2020 à Epinal devant le jury composé de:

Mme Elena SAVINOVA	Professeure, ICPEES UMR 7515 Université de Strasbourg-CNRS	Rapporteur
M. Philippe POULIN	Directeur de Recherches au CNRS, CRPP UMR 5031 Université de Bordeaux-CNRS	Rapporteur
Mme Conchi ANIA	Directrice de Recherches au CNRS, CEMHTI UPR 3079 Université d'Orléans-CNRS	Examineur
M. David FARRUSSENG	Directeur de Recherches au CNRS, IRCELYON UMR 5256 Université Claude Bernard Lyon 1-CNRS	Examineur
Mme Vanessa FIERRO	Directrice de Recherches au CNRS, IJL UMR 7198 Université de Lorraine-CNRS	Directrice de thèse
M. Alain CELZARD	Professeur, IJL UMR 7198 Université de Lorraine-CNRS	Co-directeur de thèse

Institut Jean Lamour – UMR 7198 – Département N2EV – Equipe 402

ENSTIB – BP 21042 – 88051 Épinal Cedex 9

Université de Lorraine – Pôle M4 – Collegium Sciences et Technologie

Remerciements

Je tiens tout d'abord à remercier les membres du jury de ma soutenance de thèse. Les rapporteurs Mme. Elena Savinova, Professeure au ICPEES et à l'Université de Strasbourg, et M. Philippe Poulin, Directeur de Recherches au CRPPet à l'Université de Bordeaux, ainsi que aux examinateurs Mme. Conchi Ania, Directrice de Recherches au CEMHTI et à l'Université d'Orléans, et au M. David Farrusseng, Directeur de Recherches au IRCELYION et à l'Université Claude Bernard Lyon 1. Merci d'avoir donné votre temps pour lire cette mémoire et contribuer à l'enrichir avec vos commentaires.

Je remercie tout particulièrement ma directrice de thèse Dr. Vanessa Fierro, qui m'a donné l'opportunité de travailler sur ce projet au sein de son équipe, merci beaucoup pour les discussions académiques encourageant un échange d'idées très enrichissant. Je tiens également à remercier Prof. Alain Celzard, mon co-directeur de thèse, pour partager ses connaissances scientifiques et toujours poser des questions que m'ont fait réfléchir et améliorer la discussion et compréhension de mes résultats.

J'exprime aussi tous mes remerciements à toutes les personnes des instituts avec lesquels j'avais le plaisir de collaborer et qui m'ont aidé à mener à bien mon travail. Tout particulièrement, je remercie Dr. Jaafar Ghanbaja, à l'IJL à Nancy, pour son aide avec les images MET; Dr. María Teresa Izquierdo, à Zaragoza, Espagne, pour ses apportations dans les études de chimie de surface et XRD; Dr. Marta Sevilla, à l'INCAR à Oviedo, Espagne, pour partager ses expertises dans le domaine de l'électrochimie; et Prof. Matthias Thommes, au TVT-FAU à Erlangen-Nürnberg, Allemagne, pour ses précieux apportations à la discussion sur la caractérisation texturale. Aussi, je remercie Dr. Jan Macutkevic pour m'avoir accueilli pour une semaine dans son laboratoire à l'Université de Vilnius et Prof. Francisco Carrasco et son équipe pour me recevoir à bras ouverts dans son laboratoire pendant trois mois à l'Universidad de Granada, Espagne. Agradezco también el apoyo mostrado por mi país, México, a través del CONACYT por otorgarme la beca (CONACYT-SENER Sustentabilidad Energética 2016, Tercer periodo, 601021/438978) que me permitió realizar mis estudios de doctorado.

Je remercie spécialement Philippe Gadonneix pour son immense patience pour me montrer comme utiliser les équipements, pour sa gentillesse, pour prendre soin de moi et de mes expériences. Mi Ángela querida, muchas gracias por transmitirme tu conocimiento sobre los supercaps, por las largas discusiones para entender y aprender juntas al respecto, pero sobre todo por tus consejos, tu alegría y tu amistad. ¡Claraaaaaaa!, a ti mil gracias por brindarme tu confianza, apoyo y amistad desde el día uno y que no deja de crecer cada día, te quiero a montones. Je remercie très spécialement à mes

trois piliers au labo, qui m'ont accompagné depuis le début de ce voyage: Zélie, la meilleure professeure de Français et ma partenaire de *CASMAR productions*, merci pour être toujours là pour m'aider avec les plusieurs soucis qu'on a rencontrés, pour partager les *fun facts* et devenir copains comme cochons; Blagoj, my favorite maximalist that show me that even if Macedonia and México are so far apart we are more alike than different, thank you for always be there to set an example of courage and resilience; Giuseppe, carissimo, thank you for receiving me with open arms from the first day and for the long, heated, discussions about science and food. Gracias también a mi Pame bonita que me ha apoyado incondicionalmente desde que llegó y a Sara y Dani que llegaron para darme ánimos con el último jalón de la tesis, los quiero mis amigos. I also want to thank the amazing people that I had encounter along this years that made this experience way much better: mis chihuahuenses favoritos Judith y Víctor, lo más bonito de España Fran, mi guapito Oussama, Balázs, Elena, the coffee man Rafa, Séb, Taher, Asma, Amalia, Alex, Sukanya, Karthik, Eduardo, Lara, Caroline, Radouan, Eli, los mejores anfitriones en Granada mi Jesica querida y Alejandro, mis chicas de Granada Diana, Nerea y Safa, and so many others with whom I shared precious moments. A todos ustedes, mi familia internacional, gracias por hacerme sentir como en casa.

Quiero agradecer también a mis grandes amigos en México, Ivonne, Hibra, Lalo, Carlitos, Pillo, Gabriel, Ana y Rubén, que me han demostrado que el tiempo y la distancia son insignificantes cuando se quiere de verdad. Gracias también, especialmente, por un lado, a mi cuñado, Arnulfo que siempre está ahí, con su curiosidad infinita, preguntándome sobre lo que hago y apoyándome siempre; por otro lado, a la familia Martínez Villegas, Miya, Sra. Adelina y Sr. Ángel, que nunca dejaron de estar al pendiente y me han mostrado su apoyo y cariño constantemente desde que los conocí.

Mil gracias a mi familia, a mis maniuninis Nere y Aris y a mis papás Ángeles y Eusebio, que me llenan de amor y orgullo y siempre me han alentado a seguir adelante, a tener confianza para perseguir mis sueños y proyectos, aunque éstos me lleven lejos (físicamente) de ustedes. Los amo y los llevo constantemente en el pensamiento y en el corazón.

Sobre todo, gracias a ti César, no me alcanzan las palabras para agradecerte el gran sacrificio que hiciste por nosotros durante todo este tiempo para poder seguir avanzando juntos, a pesar de las muchas dificultades. Gracias por emprender conmigo esta gran aventura que nos trajo ya del otro lado del mundo, por ser fuerza y corazón, impulso e inspiración. No puedo imaginar mejor compañero que tú, te amo mucho.

“No estudio por saber más, sino por ignorar menos”

“I don't study to know more, but to ignore less”

“Je n'étudie pas pour en savoir plus, mais pour ignorer moins”

– Sor Juana Inés de la Cruz

A César

Table of contents

List of abbreviations	5
Résumé de la thèse	7
Chapter 1. Introduction	23
1.1 Global context	25
1.2 Supercapacitors	26
1.2.1 Basic principles	26
1.2.2 Applications	28
1.2.3 Electrochemical testing techniques.....	29
1.3 Electrolytes used in supercapacitors	33
1.4 Carbon materials as electrodes for supercapacitors	35
1.4.1 Activated carbons.....	35
1.4.2 Carbide-derived carbons and zeolite-templated carbons.....	37
1.4.3 Carbon gels	37
1.4.4 Nanostructured carbons	38
1.4.5 Ordered mesoporous carbons.....	39
1.4.6 Doped materials	41
1.5 Transition to biosourced precursors of porous carbon materials.....	43
1.6 Tannins as carbon precursor	44
1.6.1 Condensed tannins	44
1.6.2 Synthesis of porous carbons.....	46
1.7 Summary and objective of the thesis	57
1.8 References	59
Chapter 2. Characterization techniques	67
2.1 Transmission electron microscopy.....	69
2.2 Physisorption of gas	70
2.3 Immersion calorimetry	74
2.4 Raman spectroscopy.....	75
2.5 X-ray diffraction.....	76
2.6 Thermogravimetric analysis.....	77
2.7 Elemental analysis.....	78
2.8 X-ray photoelectron spectroscopy	79
2.9 Fourier-transform infrared spectroscopy	79

2.10 Electrochemical performance	81
2.11 Contact angle.....	82
2.12 References	84
Chapter 3. Mechano-synthesis.....	87
3.1 Introduction	89
3.2 Effect of components	91
3.3 Effect of milling time	93
3.4 Effect of pH.....	95
3.5 Effect of P:W weight ratio	97
3.6 Effect of carbonization temperature.....	100
3.7 Applications	101
3.7.1 Oil spill remediation	102
3.7.2 CO ₂ adsorption from humid gases	102
3.8 Conclusion.....	103
3.9 References	104
Chapter 4. Detailed study of the mesoporous structure	109
4.1 Introduction	111
4.2 Morphology of the mesoporous carbons.....	113
4.3 Adsorption of Ar, N ₂ and CO ₂	114
4.4 Immersion calorimetry	119
4.5 Vapor adsorption of hexane isomers.....	120
4.6 Applications	123
4.6.1 Supercapacitors	123
4.6.2 Molecular sieves	123
4.7 Conclusion.....	124
4.8 References	125
Chapter 5. CO₂ activation of tannin-derived OMCs.....	129
5.1 Introduction	131
5.2 Textural properties	132
5.3 Surface and bulk composition.....	135
5.4 Electrochemical characterization	136
5.5 Conclusion.....	145
5.6 References	146

Chapter 6. Effect of mesopore order on SC performance.....	149
6.1 Introduction	151
6.2 CO ₂ activation process	152
6.3 Textural properties	153
6.4 Surface and bulk composition.....	159
6.5 Electrochemical characterization	160
6.6 Conclusion.....	166
6.7 References	168
Chapter 7. KOH activation of tannin-derived OMCs	171
7.1 Introduction	173
7.2 Morphology and textural properties.....	174
7.3 Surface and bulk composition.....	177
7.4 Electrochemical characterization	178
7.4.1 Effect of activation method.....	178
7.4.2 Comparison with CO ₂ activated materials.....	182
7.5 Conclusion.....	185
7.6 References	187
Conclusions et perspectives	189
Annex 1. Complementary data for Chapter 3	195
Annex 2. Complementary data for Chapter 5	201
Annex 3. Complementary data for Chapter 6.....	207
Annex 4. Complementary data for Chapter 7	215
Annex 5. List of Figures and Tables.....	221
Annex 6. List of scientific works derived from this thesis study	231

List of abbreviations

22DMB	2,2-dimethylbutane
2D-NLDFT HS	2D non-local density functional theory for heterogeneous surface
2MP	2-methylpentane
AC	Activated carbon
ADMC	Activated disordered mesoporous carbon
AMC	Activated mesoporous carbon
AOMC	Activated ordered mesoporous carbon
AT	Aminated tannin
BET	Brunauer-Emmett-Teller
BJH	Barrett-Joyner-Halenda
BO	Burn-off
CDC	Carbide-derived carbon
CG	Carbon gel
CL	Carbon load
CNF	Carbon nanofibers
CNS	Carbon nanospheres
CNT	Carbon nanotubes
CO₂-AOMC	CO ₂ activated ordered mesoporous carbon
CV	Cyclic voltammetry
DFT	Density functional theory
DMC	Disordered mesoporous carbon
EA	Elemental analysis
EAT	Evaporated aminated tannin
EDL	Electrostatic double-layer
EDR	Equivalent distributed series
EIS	Electrochemical impedance spectroscopy
EISA	Evaporation-induced self-assembly
ESR	Equivalent series resistance
FTIR	Fourier-transform infrared
FWHM	Full width at half maximum
GCD	Galvanostatic charge-discharge
HF	High frequency
HTC	Hydrothermal carbonization
IMP	impregnation
KHO-AOMC	KOH activated ordered mesoporous carbon
KJS	Kruk-Jaroniec-Sayari
LF	Low frequency
MC	Mesoporous carbon
MOF	Metal organic framework
NHEX	n-hexane
NLDFT	Non-local density functional theory
OMC	Ordered mesoporous carbon

P:W	Pluronic to water weight ratio
PM	physical mixing
PNDC	P- and N- doped carbon
PSC	Pseudocapacitor
PSD	Pore size distribution
QSDFT	Quenched solid density functional theory
SC	Supercapacitor
SWAMM	Surfactant-water-assisted mechanochemical mesostructuration
TA	Tannic acid
TEM	Transmission electron microscopy
TF	Tannin formaldehyde
TGA	Thermogravimetric analysis
WCA	Water contact angle
XPS	X-ray spectroscopy
XRD	X-ray diffraction
ZTC	Zeolite templated carbon

A_{BET}	BET area
C_{cell}	Specific cell capacitance
C_e	Specific electrode capacitance
$C_{e,S}$	Interfacial electrode capacitance
C_r	Real part of the complex capacitance
$C_{0.01}$	Real part of the complex capacitance at 0.01 Hz
C_{ret}	Capacitance retention
E	Specific energy
f_{knee}	Knee frequency
I	Specific current
O/S_{NLDFT}	Oxygen surface concentration
P	Specific power
p/p_0	Relative pressure
p_{des}	Starting relative pressure of the scanned desorption branches
S_{NLDFT}	2D-NLDFT HS surface area
V_{2-5nm}	Mesopore volume from pores with width in the 2 to 5 nm range
$V_{>5nm}$	Mesopore volume from pores with width > 5 nm
V_{meso}	Mesopore volume
$V_{S\mu}$	Supermicropore volume
$V_{u\mu}$	Ultramicropore volume
V_{μ}	Micropore volume
w_{av}	Average pore width
$w_{av.meso}$	Average mesopore width
$w_{av.2-5nm}$	Average mesopore width in the 2 to 5 nm range
$w_{av.>5nm}$	Average mesopore width for pores with width > 5 nm
w_c	Critical pore width
Z_i	Imaginary part of the complex impedance
Z_r	Real part of the complex impedance
Z_{CPE}	Impedance of a constant phase element

Résumé de la thèse

La production d'électricité à niveau mondiale a encore une grosse dépendance des combustibles fossiles, de sorte que leur épuisement et le réchauffement de la planète liée aux activités humaines rendent nécessaire une transition vers les technologies plus «vertes». Mais, en raison de l'intermittence des sources d'énergie renouvelables, des dispositifs de stockage d'énergie sont indispensables. C'est sur les applications à moyen et petite échelle qu'on trouve des dispositifs tels que des piles à combustible, des batteries, des supercondensateurs (SC) et des condensateurs. Parmi ces derniers, les SC sont de spécial intérêt, car ils peuvent stocker des quantités d'énergie plus élevées que les condensateurs et avoir une puissance de sortie supérieure à celle des batteries. Ces caractéristiques les rendent adaptés aux applications dans les véhicules électriques, comme dispositif d'appoint ou dans les systèmes hybrides avec batteries.

Les objectifs principaux de la thèse étaient donc de produire des matériaux biosourcés pour des électrodes de SC et en parallèle de réduire l'impact environnemental lié à sa synthèse. En effet, les électrodes dérivés de résines phénoliques utilisent généralement des substances dangereuses tels que le formaldéhyde. Dans ce travail, la caractérisation des matériaux occupe une place centrale car les propriétés physicochimiques affectent directement leurs performances électrochimiques en tant qu'électrodes pour des SC.

Ce travail a été réalisé au sein de l'équipe 402 "Matériaux Biosourcés" de l'Institut Jean Lamour (IJL – UMR CNRS 7198), hébergée par l'Ecole Nationale des Techniques et Industries du Bois (ENSTIB), à l'Université de Lorraine. Les fonds correspondants pour le financement ont été acquis au travers du projet PIA "Lorraine Université d'Excellence" (Référence ANR-15-IDEX-04-LUE), du projet TALiSMAN (FEDER, 2019-000214) et de la bourse mexicaine CONACYT-SENER *Sustentabilidad Energética 2016 Tercer periodo* (Référence 601021/438978). Plusieurs partenaires ont été impliqués dans ce projet, tels que: l'*Instituto Nacional del Carbón* (INCAR – CSIC) à Oviedo, Espagne; le Centre de Compétences en Microscopies, Microsondes et Métallographie (CC3M – IJL – CampusARTEM) à Nancy; l'*Instituto de Carboquímica* (ICB – CSIC) à Zaragoza, Espagne; le *Laboratorio de Materiales Avanzados – Departamento de Química Inorgánica – IUMA – Universidad de Alicante* à Alicante, Espagne; et l'*Institute of Separation Science and Technology – Friedrich-Alexander-Universität* à Erlangen-Nürnberg, Allemagne.

Les chapitres de thèse sont décrit ci-dessous.

Chapitre 1. Introduction

Le premier chapitre décrit les principes du mécanisme de stockage d'énergie dans les SC, c'est-à-dire, la formation d'une double couche électrostatique (DCE) dérivée de l'accumulation de charges à la surface des électrodes (Figure 1a). La formation de la DCE est rapide et réversible, c'est grâce à ces propriétés que les SC peuvent délivrer l'énergie stockée à des puissances plus élevées que celles des batteries (Figure 1b). Ces caractéristiques, combinées à une cyclabilité élevée et à une stabilité à long terme, font des SC des dispositifs attrayants pour le stockage d'énergie. Les principes de fonctionnement des SC sont donc présentés comme un guide pour la recherche des matériaux les plus adéquats pour la fabrication des électrodes. Les carbones poreux sont actuellement utilisés dans les électrodes des SC commerciaux en raison de leur surface spécifique élevée qui permet l'accumulation des charges, et de leur bonne conductivité électrique. Cependant, des nouveaux matériaux poreux sont continuellement développés. Un aperçu des différents carbones poreux utilisés dans des SC et leurs méthodes de synthèse est également présenté.

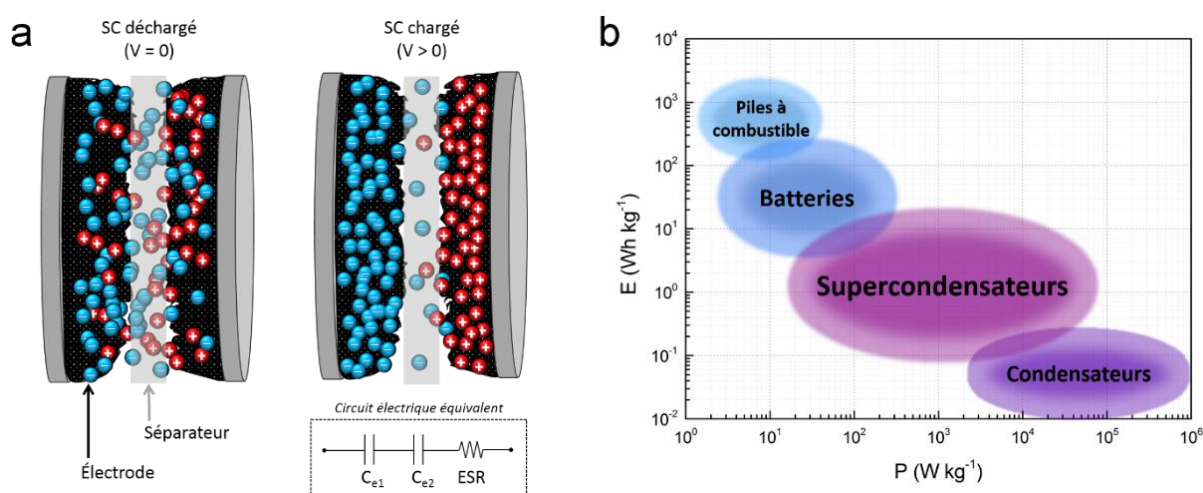


Figure 1. (a) Mécanisme de formation de la double couche électrostatique (DCE) dans un SC. Dans le circuit électrique équivalent, les condensateurs C_{e1} et C_{e2} représentent la contribution à la capacité totale de l'DCE formée à la surface de chaque électrode. La résistance série équivalente (RSE) est également indiquée. (b) Graphique Ragone montrant les valeurs typiques d'énergie et de puissance de différents dispositifs de stockage d'énergie.

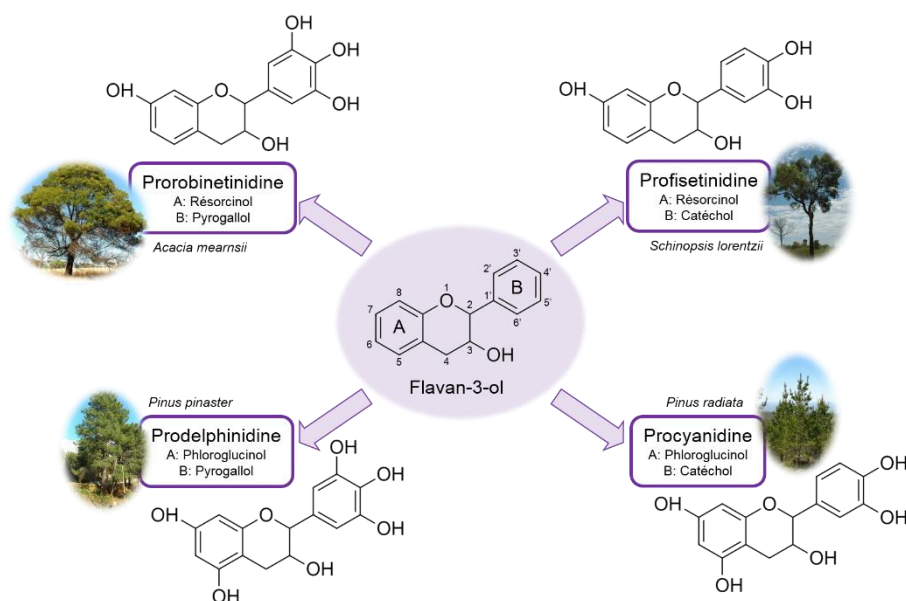


Figure 2. Principales unités flavonoïdes des tanins condensés, ainsi que la plante couramment utilisée pour leur extraction.

Dans le contexte d'un besoin urgent d'évoluer vers le développement de technologies et de méthodes respectueuses de l'environnement, la dernière partie de ce chapitre se concentre sur les études utilisant des précurseurs de carbone biosourcés, tels que les tanins condensés, qui sont des molécules polyphénoliques naturelles (Figure 2). Notamment, les matériaux carbonés dérivés du tanin de mimosa à micro et mésoporosité contrôlées peuvent être produits par des méthodes ayant un impact environnemental et des risques pour la santé et la sécurité réduits.

Chapitre 2. Techniques de caractérisation

Ce chapitre décrit les techniques de caractérisation utilisées pour étudier les propriétés des matériaux. Une caractérisation adéquate des matériaux synthétisés est essentielle pour comprendre leur comportement en tant qu'électrodes pour les SC, car les performances électrochimiques sont profondément liées aux propriétés physico-chimiques.

Des images de microscopie électronique de transmission (MET) permettent la visualisation de l'ordonnement des mesopores dans le carbone; ces-ci sont complétées par des mesures de diffraction des rayons X (DRX) aux petits angles, qui permettent aussi de déterminer l'existence d'une structure mésoporeuse ordonnée. La surface spécifique des matériaux ainsi que le volume et la distribution de taille des pores sont obtenus à partir des isothermes d'adsorption des gaz tels que l'azote, le dioxyde de carbone et l'argon. En plus, la surface accessible à des liquides dont les molécules ont des diamètres cinétiques différents sont étudiés

par calorimétrie d'immersion. La spectroscopie Raman des matériaux carbonés est utilisée pour évaluer le degré de cristallinité à l'échelle nanométrique.

L'analyse élémentaire (AE) est utilisée pour déterminer la composition chimique des matériaux; la présence d'hétéroatomes dans la surface du carbone est révélée par la spectroscopie photoélectronique par rayons X (SPX). La spectroscopie infrarouge à transformée de Fourier (IRTF) fait possible d'observer la création de nouvelles liaisons chimiques lors de la mécanosynthèse par comparaison avec la substance d'origine comme référence. D'un autre côté, la technique d'analyse thermogravimétrique (ATG) permet de suivre l'évolution de la masse d'un matériau à mesure que la température augmente.

La description de la procédure suivie pour la préparation des électrodes des SC est décrite. Finalement, des mesures de l'angle de contact avec de l'eau sont utilisées pour évaluer la mouillabilité des matériaux, ce qui est important lorsque des électrolytes aqueux sont utilisés.

Chapitre 3. Mécanosynthèse

Compte tenu des objectifs du travail de thèse, une première approche a donc consisté à utiliser un précurseur de carbone biosourcé tel que le tanin de mimosa. Ceci est actuellement extrait à grande échelle à partir de l'écorce des arbres et valorisé, entre autres, par l'industrie du cuir et des adhésifs pour le bois. La deuxième stratégie a visé à mettre au point une méthode originale de synthèse évitant l'utilisation de substances toxiques et/ou dangereuses. De ce fait, une méthode de mécanosynthèse simple, «verte» et en une seule étape, pour préparer des carbones mésoporeux ordonnés (CMO) est présentée dans ce chapitre. Le tanin de mimosa (T) et le Pluronic® F127 (P) sont respectivement utilisés comme précurseur de carbone et comme tensioactif. De l'eau (W) est essentiel pour favoriser la formation de micelles mais aussi l'interaction entre T et P; aucun réticulant n'est utilisé et des étapes de séchage ou de durcissement avant la carbonisation ne sont pas nécessaires non plus (Figure 3).

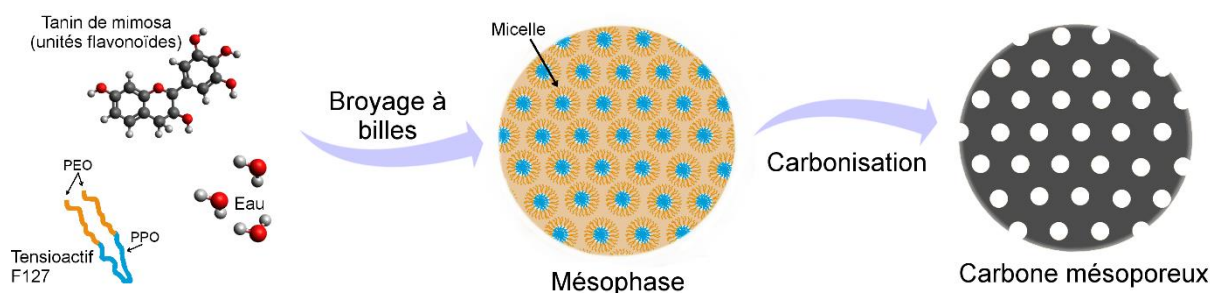


Figure 3. Schéma de la méthode de mécanosynthèse.

Les conditions expérimentales, telles que le temps de broyage, le pH de l'eau ajoutée et le rapport P:W sont optimisés pour obtenir des CMO avec une géométrie hexagonal 2D, avec des aires BET pouvant atteindre presque $600 \text{ m}^2 \text{ g}^{-1}$ après carbonisation à $900 \text{ }^\circ\text{C}$. En modifiant le rapport P:W, il est possible d'obtenir des carbones mésoporeux désordonnés (CMD) ou des CMO, qui sont associés aux des DTP à l'échelle des mésopores bimodales (avec 2 pics) ou unimodales (avec 1 pic), respectivement; plus encore, pour certains matériaux produits avec de faibles quantités de P ($\leq 0.5 \text{ g}$) on ne trouve pas des mésopores, de sorte que les matériaux sont purement microporeux (Figure 4).

Des températures de carbonisation jusqu'à $1500 \text{ }^\circ\text{C}$ ou des procédures d'activation permettent d'augmenter la surface, jusqu'à $\sim 1900 \text{ m}^2 \text{ g}^{-1}$, tout en conservant la structure mésoporeuse ordonnée. Ces matériaux devraient être convenir aux applications de SC, mais aussi à d'autres applications telles que l'assainissement des déversements de pétrole ou à l'adsorption sélective du CO_2 à partir de gaz humides.

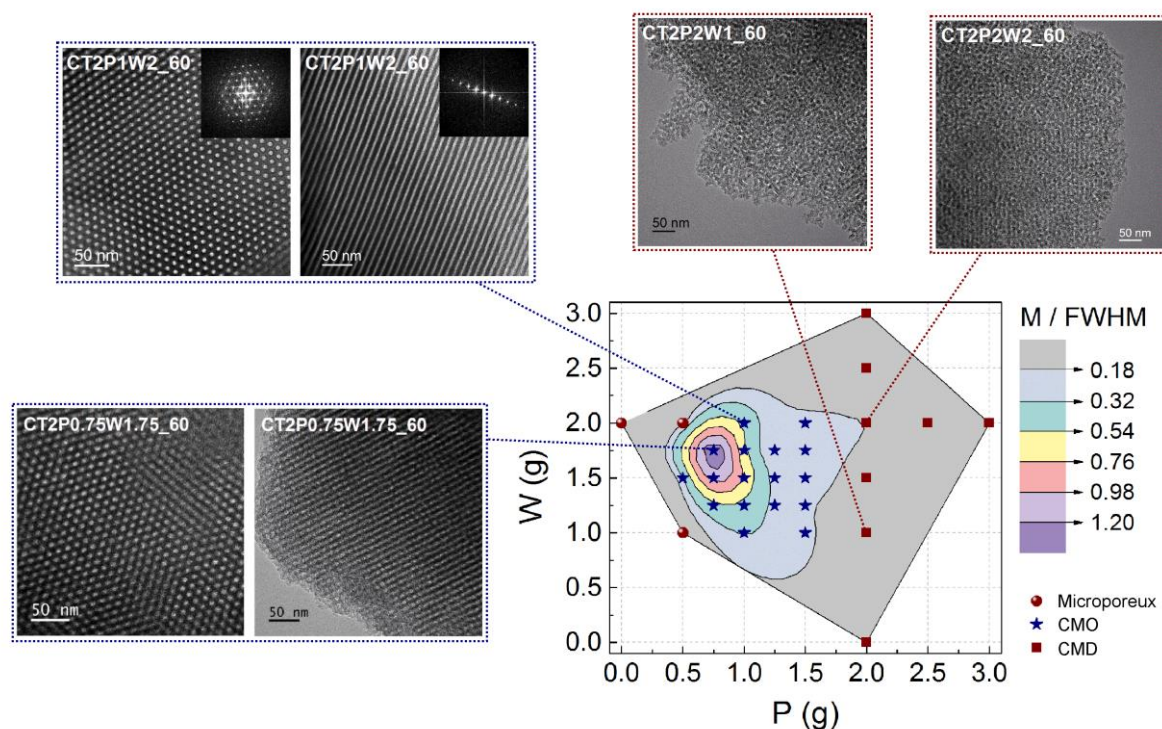


Figure 4. Graphique de contour corrélant le rapport P: W avec les caractéristiques du DTP des matériaux synthétisés et leur structure mésoporeuse.

Chapitre 4. Étude détaillé de la structure mésoporeuse

Deux types de carbones mésoporeux (CM), un CMD et un CMO, sont caractérisés en détail afin de mieux connaître la connectivité de la structure mésoporeuse de ces matériaux et leurs effets possibles sur leurs performances en tant qu'électrodes de SC et dans d'autres possibles applications non liées au stockage d'énergie.

La caractérisation texturale a été réalisé par trois techniques: l'adsorption d'azote et d'argon; la calorimétrie d'immersion dans *n*-hexane (nHEX), 2-methylpentane (2MP) et 2,2-dimethylbutane (22DMB) en phase liquide; et l'adsorption de ces trois alcanes C₆ en phase vapeur. Les résultats ont révélé un réseau de pores bien interconnecté au sein du CMD, tandis que des mésopores ordonnés accessibles uniquement par des micropores étroits se trouvent dans le CMO. Ces pores étroits dans le CMO affectent profondément leur performance d'adsorption, la structure poreuse permettre l'adsorption du nHEX et du 2MP mais pas du 22DMB (Figure 5).

Plus tard, ces différences de connectivité de la structure poreuse dans le CMO et le CMD seront révélées comme une propriété qui a un effet important sur les procédures d'activation et, par conséquent, sur les performances électrochimiques des SC assemblés.

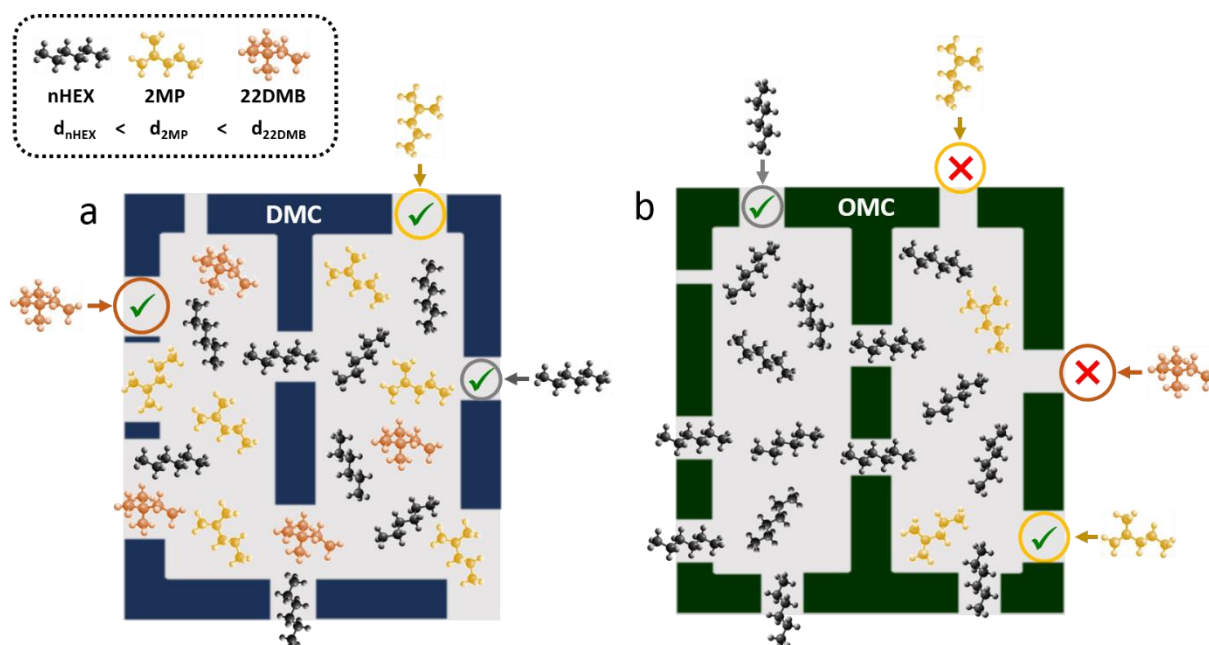


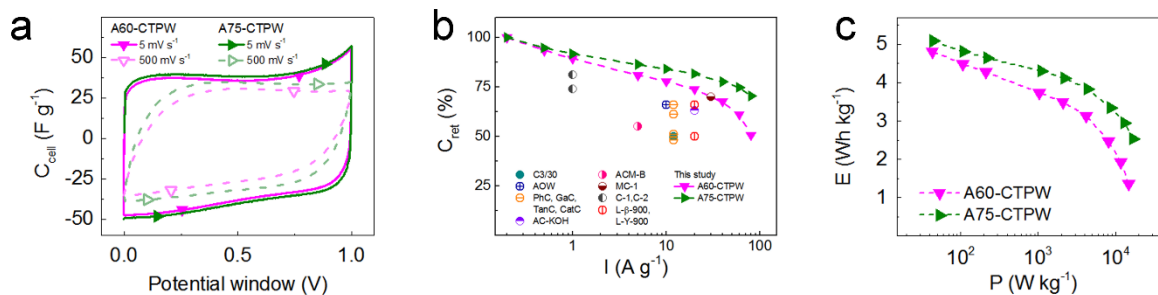
Figure 5. Schéma de la connectivité de la structure poreuse des matériaux (a) DMC et (b) OMC. Les différents diamètres cinétiques des isomères C₆ ($d_{\text{nHEX}} < d_{\text{2MP}} < d_{\text{22DMB}}$) se traduisent par une accessibilité différente de chaque molécule dans la structure poreuse en raison de la présence de pores de tailles similaires ou plus grandes.

Chapitre 5. Activation par CO₂ des CMO dérivées du tanin

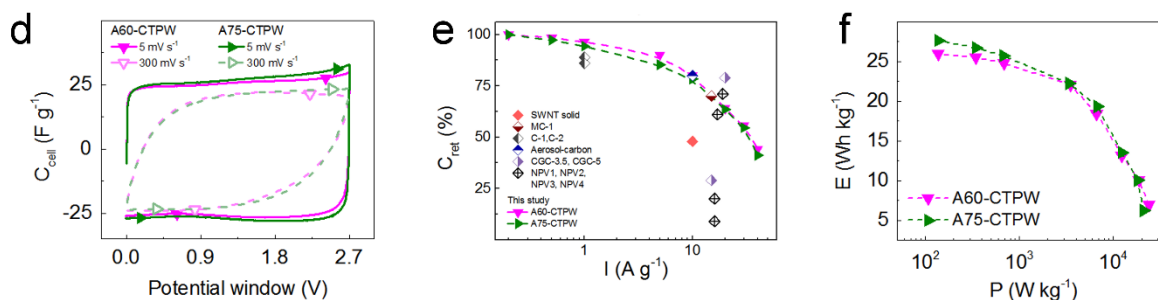
La mésoporosité des matériaux carbonés peut améliorer la diffusion des ions vers les micropores, par conséquent, les CMO ont été considérés comme matériaux pour des électrodes de SC. Cependant, les CMO produits par mécanosynthèse ont généralement des surfaces spécifiques modérées, et une étape d'activation supplémentaire est nécessaire pour améliorer leurs caractéristiques texturales et, par conséquent, leurs performances électrochimiques.

Des CMO ont été physiquement activés avec du CO₂ pour augmenter leur surface de ~500 m² g⁻¹ à ~2000 m² g⁻¹ tout en maintenant la mésoporosité assez inchangée. En effet, la structure mésoporeuse ordonnée était maintenue jusqu'à un taux d'usure de 78%. La performance électrochimique des SC assemblés avec des matériaux sélectionnés a été testée dans des électrolytes aqueux (1 M H₂SO₄ et 1 M Na₂SO₄) et dans une électrolyte organique (1 M TEABF₄/ACN). Les CMO activés exhibaient un comportement supercapacitif, avec des courbes de voltampérométrie cyclique (VC) rectangulaires dans les trois électrolytes testés (Figure 6a, 6d et 6g). La rétention de capacité (C_{ret} , Figure 6b, 6e et 6h) maximale a été obtenue dans le milieu acide (H₂SO₄), diminuée pour le milieu neutre (Na₂SO₄) et atteinte un minimum dans le milieu organique (TEABF₄/ACN). Cela est attribué à la plus grande taille et à la mobilité réduite des ions dans l'électrolyte neutre et l'électrolyte organique par rapport à celle des ions dans l'électrolyte acide. En outre, comme prévu, l'énergie stockée (E , Figure 6c, 6f et 6i) a augmenté dans l'ordre contraire, *i.e.*, $E_{acide} < E_{neutre} < E_{organique}$, en raison de l'augmentation de la fenêtre de potentiel. Les matériaux présentent une bonne stabilité à long terme dans le temps et après des cycles continus à 5 A g⁻¹. Plus précisément, en milieu acide, C_{ret} est restée à ~98% après 10 000 cycles et ~94% après 50 h de maintien potentiostatique à 1 V, tandis que dans l'électrolyte organique, C_{ret} était supérieure à 90% après 8 000 cycles et a atteint 86% après 72 h de maintien le voltage à 2,7 V.

Milieu acide



Milieu organique



Milieu neutre

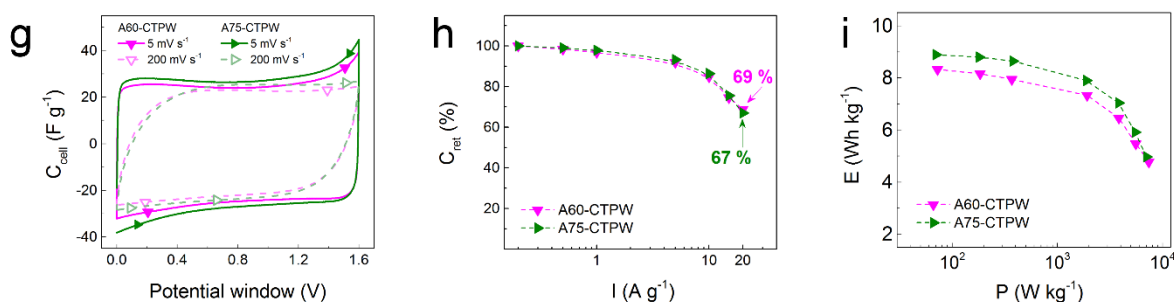


Figure 6. Performances électrochimiques des CMO activés dérivés du tannin: (a, d, g) courbes VC; (b, e, h) rétention de la capacité (C_{ret}) en fonction du courant appliqué pendant des tests de charge-décharge galvanostatique (CDG) et (c, f, i) énergie spécifique en fonction de la puissance spécifique (graphiques de type Ragone) calculés à partir des courbes CDG. Les essais ont été effectués dans (a-c) l'électrolyte aqueux acide, (d-f) l'électrolyte organique et (g-i) l'électrolyte aqueux neutre.

Chapitre 6. Effet de l'ordre des mésopores sur la performance des SC

Dans la plupart des études sur les performances électrochimiques, l'analyse se concentre sur des matériaux avec des différentes surfaces spécifiques et des différentes propriétés de porosité (volumes, taille moyenne et distribution de taille des pores) et ayant soit une structure désordonnée, comme celui des carbones activés (CA), soit une structure ordonnée tel que cela des CMO, mais l'effet du l'ordre des mésopores est généralement ignoré. En outre, la

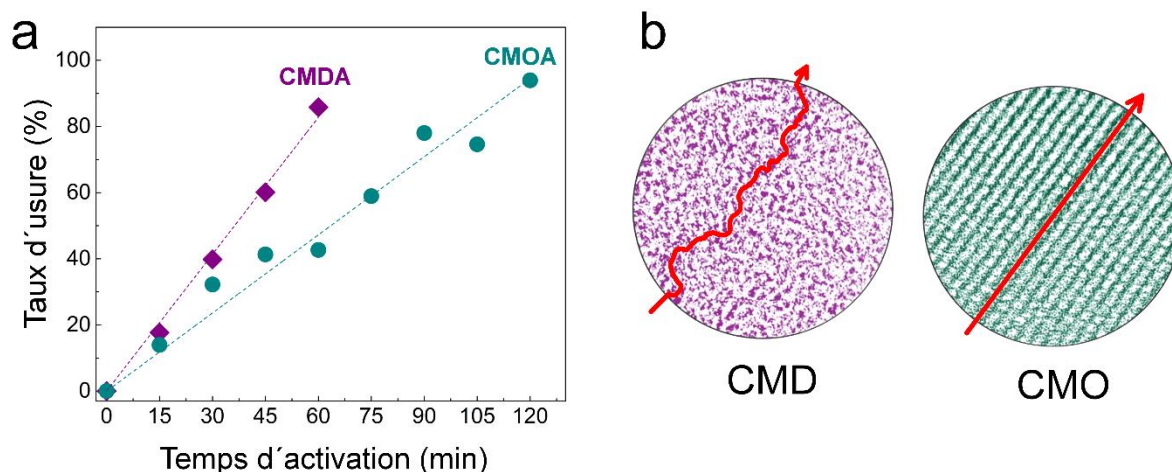


Figure 7. (a) Taux d'usure en fonction du temps d'activation des carbonés mésoporeux ordonnés et désordonnés activés (CMOA et CMDA, respectivement). (b) Schéma des différents chemins de diffusion dans les mésopores au sein d'une particule du CMD et du CMO.

comparaison directe entre les études publiées pour obtenir plus d'informations sur l'effet de l'ordre reste difficile, car l'effet de l'ordre ne peut pas être facilement isolé des autres facteurs qu'influencent également les performances des SC, tels que la surface spécifique, le volume et la taille des pores, la chimie de surface ou même les conditions expérimentales.

Ce chapitre vise ainsi à approfondir la compréhension de l'effet de l'ordre sur les performances électrochimiques des CM activés (CMA). Après l'activation par CO_2 , les propriétés physico-chimiques des CMD activés (CMDA) ont été comparées à celles des CMO activés (CMOA) présentés dans le chapitre précédent. La procédure d'activation s'est révélée sensible à l'ordre de la structure mésoporeuse; en effet, un développement plus rapide des propriétés texturales est observé pour les CMD, du fait d'un temps de résidence plus long du gaz dans les particules (Figure 7).

D'un autre côté, les analyses de balayage des boucles d'hystérèse des isothermes d'adsorption d'azote ont permis d'établir que les mésopores dans les CMDA constituent un réseau ouvert et bien connecté, alors que l'accès aux mésopores dans les CMOA reste plutôt limité car ils sont connectés par des pores très étroits (Figure 8a). Les résultats du balayage des boucles d'hystérèse ont aussi été utilisés pour corrélérer la connectivité et l'ordre de la structure mésoporeuse avec la performance électrochimique des matériaux lorsqu'ils sont utilisés comme électrodes pour des SC. De ce fait, des SC ont été assemblés en utilisant deux matériaux modèles, toutes autres caractéristiques étant égales sauf leur structure mésoporeuse, et ils ont

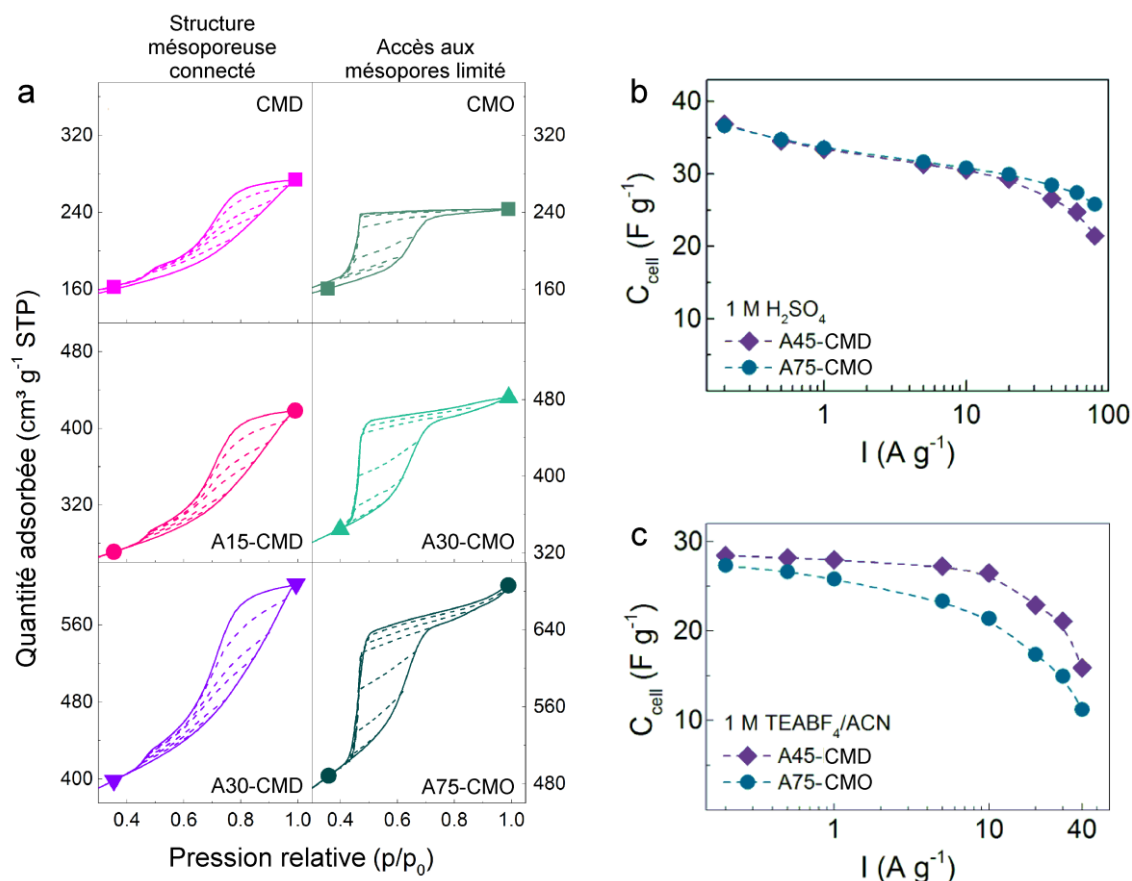


Figure 8. (a) Balayage des boucles d'hystérèse des CMD (colonne à gauche) et des CMO (colonne à droite) avant et après l'activation. Capacité spécifique des SC (C_{cell}) assemblés et testés dans l'électrolyte (b) aqueuse (1 M H₂SO₄) et (c) organique (1 M TEABF₄/ACN).

été testés dans des électrolytes aqueuses et organiques (1 M H₂SO₄ et 1 M TEABF₄/ACN, respectivement). Les mésopores ordonnés dans le CMOA améliorent la diffusion des ions de petite taille de l'électrolyte aqueuse et favorisent donc une meilleure performance à débits élevés, résultant en une C_{ret} 12% plus élevée à 80 A g⁻¹ par rapport à celle obtenue avec le CMDA aux mêmes conditions expérimentales (Figure 8b). D'autre part, la porosité plus interconnectée du CMDA permet une meilleure diffusion des ions de grande taille, améliorant ainsi de 15 % la performance électrochimique dans l'électrolyte organique à 40 A g⁻¹ par rapport à celle obtenu avec le CMOA (Figure 8c).

Chapitre 7. Activation par KOH des CMO dérivées du tanin

L'activation chimique avec du KOH a également été explorée, car elle est connue pour produire des matériaux avec des surfaces spécifiques plus élevées que celles obtenues par activation physique et donc avoir des SC avec des performances supérieures.

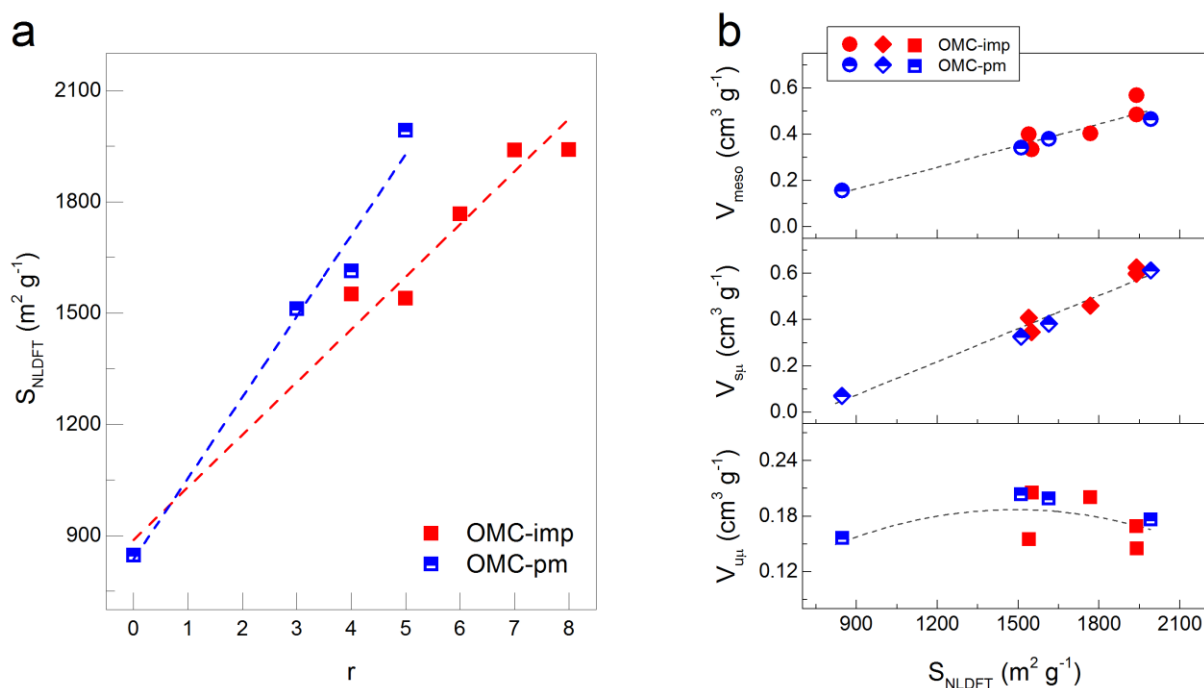


Figure 9. (a) Surface spécifique (S_{NLDFT}) en fonction du rapport massique KOH/Carbone (r). (b) Volume des pores en fonction de S_{NLDFT} à des échelles des mésopores (V_{meso}), supermicropores ($V_{s\mu}$) et ultramicropores ($V_{u\mu}$).

Dans ce chapitre, deux méthodes d'incorporation du KOH aux CMO ont été mises en place: l'imprégnation (*imp*) et le mélange physique (*mp*); comme prévu, la surface spécifique a augmenté à mesure que la quantité d'agent d'activation augmente. Toutefois, la voie d'activation *mp* semble être plus efficace, étant donné que des quantités plus faibles de KOH (r = rapport massique KOH/Carbone) sont requis pour atteindre des valeurs similaires de surface et volume des pores qu'avec la voie *imp* (Figure 9a). Néanmoins, les résultats montrent que le développement des propriétés texturales est similaire pour les deux voies d'activation, *i.e.*, *imp* et *pm* (Figure 9b).

Des tests électrochimiques ont été effectués dans l'électrolyte aqueuse (1 M H_2SO_4), des courbes VC rectangulaires indiquent un comportement de SC (Figure 10a et 10b). Pour des bas taux de charge, les valeurs de capacité augmentent avec la surface; néanmoins à mesure que le taux de charge augmente, soit pendant des VC tests soit pendant CDG tests, la capacité des SC diminue pour tous les matériaux (Figure 10c et 10e), pour des CDG tests C_{ret} à 20 Ag^{-1} arrive jusqu'à $\sim 50\%$ de ses valeurs initiales. Toutefois, l'énergie spécifique atteindre les $\sim 7 \text{ Wh kg}^{-1}$ avec une puissance de sortie de 133 W kg^{-1} , ces valeurs sont supérieures à celles obtenus avec des CMO activés par CO_2 dans les mêmes conditions expérimentales (Figure 10f et Figure 6c). Cela est principalement dû à la haute surface des matériaux activés par KOH; néanmoins,

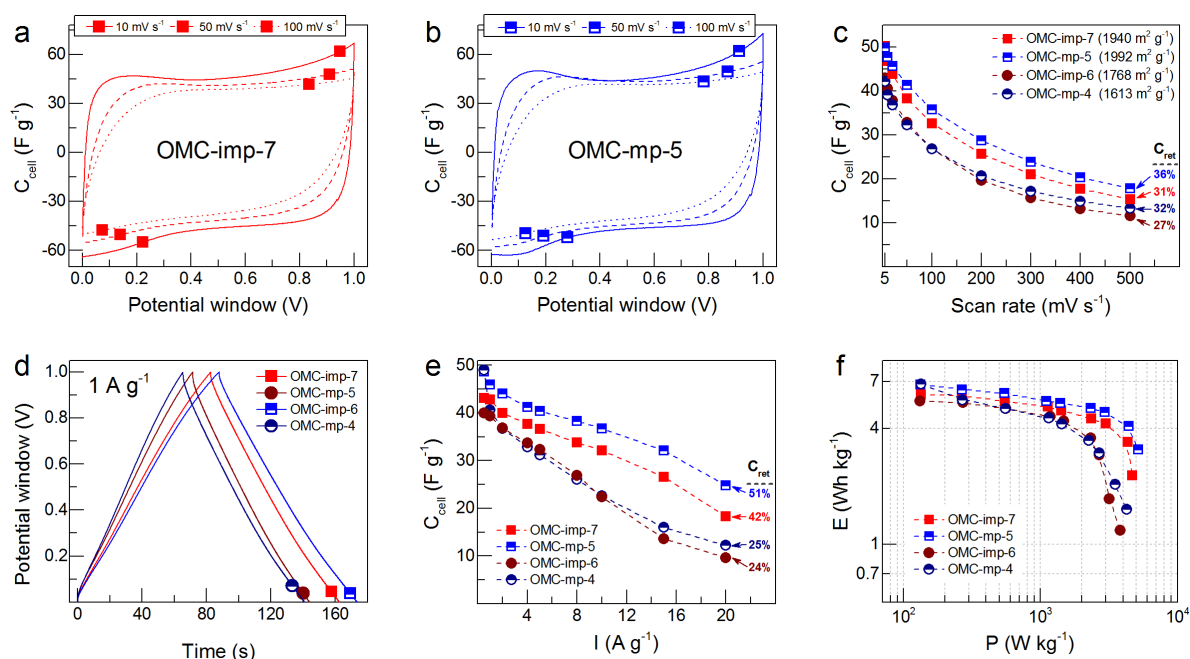


Figure 10. (a, b) Courbes de VC à des différents taux de charge (10, 50 et 100 mV s^{-1}). (c) Capacité spécifique des SC (C_{cell}) en fonction de la taux de charges pendant des VC tests. (d) Curves de charge-décharge à 1 A g^{-1} . (e) C_{cell} en fonction de la courant appliqué pendant CDG tests. (f) Énergie spécifique en fonction de la puissance spécifique (graphiques de type Ragone) calculés à partir des courbes CDG.

les CMO activés par CO_2 présentent des C_{ret} considérablement supérieurs indiquant une meilleure diffusion des ions à l'intérieur du matériau et une surface accessible aux ions plus élevée qui facilite la formation de la DCE.

Il est également important de noter que les matériaux ayant des valeurs de surface similaires mais activés par différentes méthodes présentent différentes valeurs de capacité; c'est le cas, des CMO activés par KOH par la méthode *imp* ou *mp*, ou des CMO activés par KOH par la méthode *mp* ou par CO_2 . Encore, la chimie de surface de ces matériaux est aussi similaire. De ce fait, il est possible de supposer qu'il y a des caractéristiques des matériaux qui ont un effet sur la performance électrochimique, lesquels ne sont pas détectables avec les techniques utilisées. Par exemple, la surface accessible peut ne pas être correctement évaluée; en fait, la microporosité est étudiée grâce à des isothermes d'adsorption de CO_2 , mais les ions H^+ dans le milieu aqueux ont une taille inférieure. Ainsi, une caractérisation approfondie des propriétés texturales et sa connectivité pourrait être effectuée en acquérant des isothermes d'adsorption d'hydrogène et/ou en réalisant des expériences de calorimétrie d'immersion avec des liquides dont les molécules ont des diamètres cinétiques mineurs que ceux déjà utilisés dans

ce travail de thèse. Les informations acquises pourraient aider à mieux comprendre le comportement des matériaux synthétisés en tant qu'électrodes pour les SC.

Pour clore cette mémoire, les conclusions et perspectives sont présentées. Nous pensons que les travaux menés dans cette thèse apporteront des avancées dans la recherche sur la synthèse facile et «verte» des carbones poreux pour des applications de stockage d'énergie dans les SC. Leurs performances comme des électrodes des SC de ces matériaux dérivés du tannin sont très prometteuses et les études de caractérisation présentées montrent que ces molécules extraites du bois sont d'excellents précurseurs pour préparer des matériaux modèles pour approfondir en la compréhension des phénomènes de diffusion dans les électrodes. En plus, l'utilisation de ces carbones poreux dans des applications non liées au stockage d'énergie permettrait d'apporter une valeur ajoutée supplémentaire aux matériaux obtenus par mécanosynthèse.

Une liste des travaux scientifiques auxquels ce travail a donné lieu peut être trouvée à la fin du manuscrit.

Chapter 1

Introduction

1.1 Global context

World's electricity consumption has increased significantly in recent decades, from ~11 000 TWh in 1990 to ~23 000 TWh in 2016, according to the International Energy Agency (IEA), and there is still a strong dependence on fossil fuels such as coal, oil and gas as energy sources.¹ Furthermore, it is generally agreed that the increasing concentration of greenhouse gases in the atmosphere from the 1950s is partly attributable to the burning of fossil fuels, which is causing global climate change.² The limits of fossil fuel reserves and the increasing global warming have amplified awareness on the need to phase out the fossil fuel industry. The transition to energy production from renewable sources and environmentally friendly technologies is a public demand. Currently, electricity production is highly centralized in power plants where it is produced and supplied according to the demands of end consumers and using historical consumption data to predict and regulate the grid load.³ The former poses a challenge for the production of electricity based on fluctuating energy sources such as solar or wind, among others. Thus, research aiming to improve the performance of energy storage devices is of great relevance nowadays.

The role of energy storage devices in the electrical system is to collect the excess of energy during high production peaks and act as a reservoir, releasing energy when required. Figure 1.1 lists some of the different storage technologies used at different steps of the electrical system.^{3,4} Pumped-storage hydropower and compressed air energy storage are widely used in electric power plants for large-scale production. On the other hand, batteries store high amounts of energy and their extensive variety makes them suitable for a wider range of mid- and short-term storage applications such as distribution to remote sites, electric vehicles, small-scale production and off-grid storage for houses or buildings, and portable electronic devices also rely on battery use. On the contrary, supercapacitors (SCs) are high-power devices, meaning that they can supply stored energy at fast rates, and they are mostly used in short-term applications where bursts of electricity are needed.

SCs are presently used in a variety of applications, which could be further developed as stand-alone energy suppliers if their energy densities were increased.^{3,5-7} Accordingly, the international community has established the pursuit of improving SCs performances as one of the short-term actions in the context of research and development on energy storage.⁴

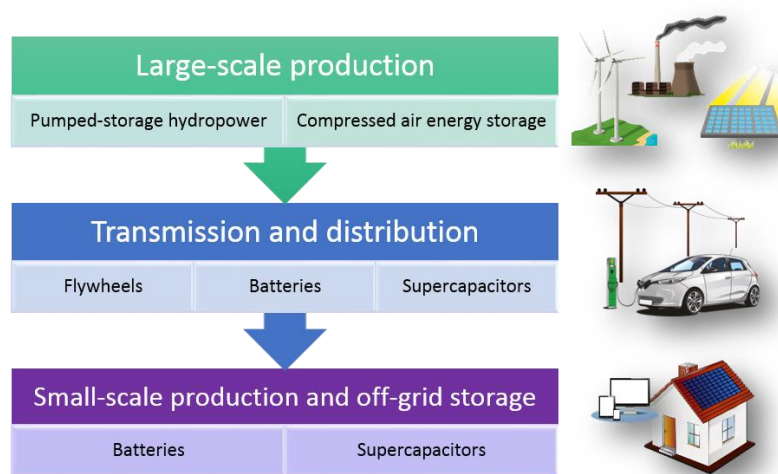


Figure 1.1. Energy storage technologies used at different scales in the power system. [Reproduced from Castro-Gutiérrez et al. (2020)⁸]

This first chapter aims to present a global vision of the principles underlying the energy storage mechanism in SCs and to explain how these principles have guided the research of materials in this field, in particular for the production of carbon electrodes. Given the environmental issues mentioned above, particular interest is given to the studies using non-toxic and environmentally friendly carbon precursors, such as tannin extracts, to produce carbon electrodes for SCs. Finally, a summary, the objectives of this thesis project and a brief description of the chapters are presented.

1.2 Supercapacitors

1.2.1 Basic principles

A SC consists of two parallel electrodes separated by a non-conductive material impregnated with an electrolyte, as illustrated in Figure 1.2a. By applying a potential between the electrodes, the ions in the electrolyte are attracted to the electrode of opposite charge. Derived from charge accumulation and the interaction with the electrode surface, an electrostatic double-layer (EDL) is created on each electrode.⁶ Hence, there are two contributions to the total capacitance of the device, represented by the two capacitors in series shown in the simplified electric circuit of Figure 1.2a. An equivalent series resistance (ESR) is added to the circuit to account for the resistance of all the components of the device.⁹ The

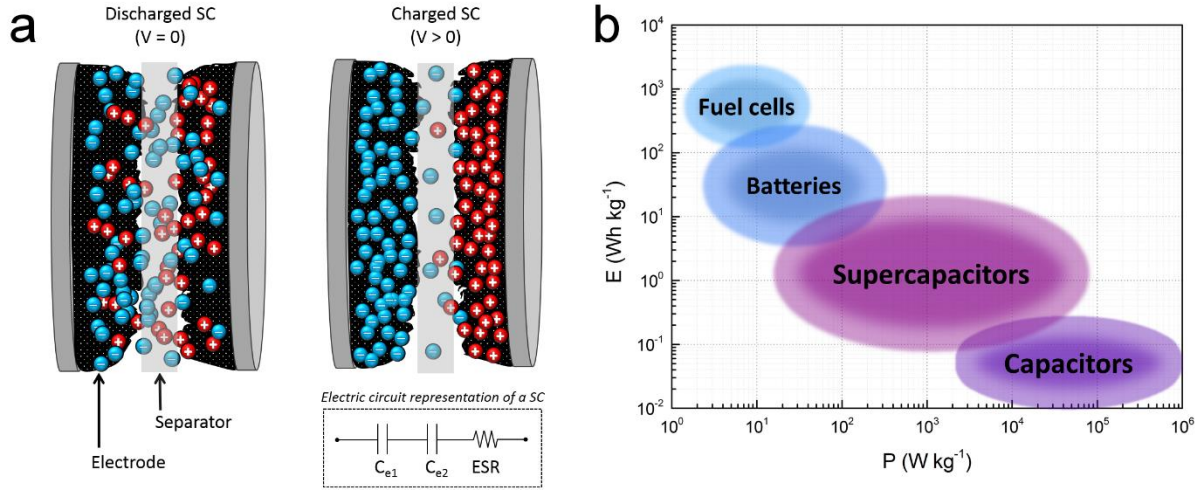


Figure 1.2. (a) Mechanism of formation of the electrostatic double-layer (EDL) in a SC and its associated simplified electric circuit. (b) Ragone plot showing the typical values of energy and power of different energy storage devices. [Adapted from Castro-Gutiérrez et al. (2020)⁸]

EDL generation is an electrostatic process and it is ideally reversible, resulting in fast responses for charge and discharge, which result in high power in SCs. In addition, high cyclability, *i.e.*, retention of capacitance after repetitive cycles of charge and discharge, and long lifetimes are achieved due to the low degradation of components derived from the reversibility of the EDL formation process.

From a macroscopic point of view, the capacitance C of a SC can be calculated as in a regular capacitor of parallel plates:

$$C = \frac{\varepsilon_0 \varepsilon A}{d} \quad (1.1)$$

where ε_0 is the permittivity of vacuum, ε is the permittivity of the electrolyte, A is the area of the electrode, and d is the effective thickness of the EDL. The energy, E , of a capacitor is calculated as follows:

$$E = \int CV dV \quad (1.2)$$

where V is the applied voltage to the device, also called potential window. For an ideal EDL SC, C is not a function of V and Equation (1.2) becomes:

$$E = \frac{1}{2} CV^2 \quad (1.3)$$

The power, P , is then calculated through:

$$P = \frac{E}{t_{dis}} \quad (1.4)$$

where t_{dis} is the discharge time. Figure 1.2b shows a Ragone plot of typical values of energy and power of SCs compared to those of other energy storage devices such as batteries, fuel cells and capacitors.

1.2.2 Applications

The characteristic E and P values of SCs bridge the gap between conventional capacitors and batteries, as shown in Figure 1.2b. Hence, SCs find their applications either as autonomous energy sources or in combination with other devices,^{3,6,7,10–16} as detailed below:

- *Memory back-ups.* Fast-response SCs are a short-term solution to a brief interruption of power supply to the memory without the need for constant replacement due to their long lifetimes.
- *Portable tools.* SCs are used as an energy source in camera flashes or portable screwdrivers since only bursts of energy are required along with rapid and constant recharging.
- *Distribution and storage of electrical energy.* SCs can compensate for short-duration voltage fluctuations in the distribution line and match the variations between production and consumption. Besides, SCs are used to restart collapsed power systems or to supply energy until the primary source is restored. Also, SCs are used as storage devices in renewable energy production plants, especially in wind power applications as they require little maintenance and their performance is not highly affected by cold temperatures.
- *Decoupling of power and energy needs.* SCs are used to meet the power needs while the principal source of energy is provided by a different system. This type of decoupling is found in hybrid and electric vehicles, thanks to which it is possible to reduce the size of the engine or the battery bank.
- *Regeneration devices.* The energy released by machines with repetitive and constant movements can be recovered by SCs, allowing reducing the size of the primary source of energy. Thus, SCs are found, for example, in cranes and elevators or the braking systems of hybrid or electric vehicles like buses, delivery or garbage trucks and trains.

One of the main disadvantages of SCs compared to batteries is that they store less energy, which limits their use as autonomous devices. It is clear from Equation (1.3) that there are two ways to overcome this drawback: widening the potential window or increasing the capacitance. The former is strongly associated with the choice of electrolyte and the latter with the properties of the electrode. Nevertheless, they are intimately related to each other, because there must be

a synergy between all the components of the SC. A clear example of this synergy is the pseudocapacitive behavior that some materials present when used as electrodes, where rapid Faradaic (redox) reactions occur on or near the surface of the electrode. The presence of redox reactions depends on the properties of the electrode material and the affinity of the electrolyte towards it. SC devices with electrodes made of materials in which both EDL and pseudocapacitance storage mechanisms are present are also referred to as pseudocapacitors (PSCs) and could reach even higher values of capacitance. However, the increased capacitance in PSCs may be accompanied by a loss of power and long-term stability compared to that of SCs, since Faradaic reactions are slower compared to EDL formation times, and the surface groups that create pseudocapacitance are prone to degrade over time.⁶

New materials are constantly being developed and their performance as electrodes for SCs must be evaluated. In the following section, the electrochemical testing techniques commonly used on a laboratory scale are briefly described to illustrate the expected behavior of a SC. Next, the types and general characteristics of commonly used electrolytes and the advances in the research for porous materials as electrodes for SCs are discussed.

1.2.3 Electrochemical testing techniques

1.2.3.1 Cell configuration

Figure 1.3 shows schemes of cell configurations normally used for SC testing. The three-electrode cells (Figure 1.3a) are useful for estimating the contributions of pseudocapacitance or for better understanding the more fundamental behavior of materials, while the two-electrode cells (Figure 1.3b) are used to evaluate the performance of materials in operating conditions closer to those of real SC devices.⁹ T-type cells are a combination of two- and three-electrode cell configurations (Figure 1.3c), which allow studying the performance of each electrode in a SC along with the performance of the whole system operating at the equilibrium potential of both electrodes.¹⁷ Thus, a three-electrode configuration measures the performance of a single electrode (the working electrode in Figure 1.3a), whereas a two-electrode configuration evaluates the performance of two electrodes as a system (the cell).

As shown in Figure 1.2, in a symmetric SC, the two electrodes are made of the same material and, based on the associated simplified circuit, its capacitance, C , can be calculated

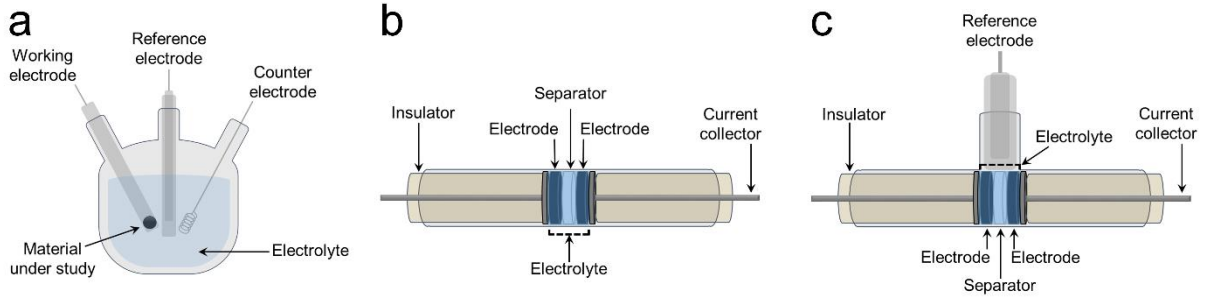


Figure 1.3. Different configurations for the electrochemical characterization of SCs: (a) three-electrode cell, (b) two-electrode cell, and (c) T-type cell. [Reproduced from Castro-Gutiérrez et al. (2020)⁸]

assuming that the contribution of each electrode is identical, *i.e.*, $C_{e1} = C_{e2} = C_e$. Therefore:

$$\frac{1}{C} = \frac{1}{C_e} + \frac{1}{C_e} \quad (1.5)$$

$$C = \frac{C_e}{2} \quad (1.6)$$

Reporting normalized values of capacitance allow for the comparison of results from different studies. Thus, from Equation (1.6) and considering that the normalization factor of the cell is twice the normalization factor of an electrode, *i.e.*, $N = 2N_e$:¹⁸

$$C_N = \frac{C}{N} = \frac{C_e}{2N} = \frac{C_e}{4N_e} = \frac{C_{e,N_e}}{4} \quad (1.7)$$

N is generally chosen to be either the mass or the volume of the electrodes. For simplicity, from now on, C and C_e will refer to the capacitances normalized by the mass of the electrode(s), called specific cell capacitance and specific electrode capacitance, respectively.

Many of the materials that can be used as electrodes for SCs are in powder form, so it is necessary to use a binder to agglomerate the powder particles and create a paste, or slurry, from which the electrodes are obtained. Some additives can also be mixed with the active material to improve their electrical conductivity. Most studies on materials for SCs only take into account the amount of active material in the electrode, by subtracting the quantities of binder and conductive additive for the calculations of normalized capacitance and, consequently, of energy and power. However, a correct assessment of the performance of the materials requires giving these calculations of normalized capacitance as a function of the total mass or the total volume of the electrode, *i.e.*, including the mass of the binder and/or the additives.

1.2.3.2 Cyclic voltammetry (CV)

During cyclic voltammetry (CV) tests, a potential (V) is applied and increased at a constant rate over time (scan rate) while the current response, I , is measured. An ideal SC would exhibit a rectangular curve when I is plotted as a function of V , see Figure 1.4a. During charging, the sharp increase in I at the beginning of the cycle is due to the rapid formation of the EDL and it remains constant when V increases because no Faradaic reaction occurs. Given the reversible nature of the EDL formation mechanism, the CV curve during discharge obtained when V decreases is the exact inverse of the charging curve. Evidently, the CV curves of the real SCs deviate from the ideal one, and those of PSCs also display I peaks due to the generation of charge by redox reactions, as shown in Figure 1.4a. In addition, widening the potential window in CV measurements allows identifying the point at which decomposition of the electrolyte occurs, manifesting by an I peak at each edge of the CV curve. Then, this information can be used to set the operating voltage of a SC cell. From CV data, C is calculated by:

$$C = \frac{\oint IdV}{2sVm} \quad (1.8)$$

where the numerator is the area delimited by the CV curve, s is the scan rate, V is the potential window and m is the sum of the masses of the two electrodes in the cell. If a three-electrode configuration is used, C_e can be calculated by substituting m in Equation (1.7) for the mass of the working electrode, m_e .

1.2.3.3 Galvanostatic charge-discharge (GCD)

In the galvanostatic charge-discharge (GCD) technique, a constant I is applied to the system while the response V is recorded as a function of time. The method is normally carried out with a two-electrode configuration. In an ideal SC, charge and discharge have a linear mirror behavior, resulting in triangular curves. In real SCs and PSCs, the curves deviate from the linear behavior, see Figure 1.4b. Any device will exhibit a sudden drop in potential during the transition from charge to discharge. This is called IR drop and it is directly associated with the ESR of the device. From GCD data, C is calculated by:

$$C = \frac{I}{(\Delta V/\Delta t) m} \quad (1.9)$$

where I is the constant current applied, $\Delta V/\Delta t$ is the slope of the discharge curve and m is the sum of the masses of the two electrodes in the SC. C_e can then be approximated using Equation (1.7). Using this value of C , those of E and P of the SC can be calculated directly from Equations

(1.3) and (1.4), respectively, keeping in mind that V in Equation (1.3) is the actual operating potential, therefore the IR drop must be subtracted from the maximum potential reached by the cell, *i.e.*, $V = V_{max} - IR_{drop}$.

GCD tests performed at increasing values of I provide insight into the kinetic behavior of the materials at faster charging rates. Although this can also be evaluated by increasing the scan rate in CV tests, GCD tests are preferred for kinetic analysis because the operating conditions are closer to those of real devices.^{9,19}

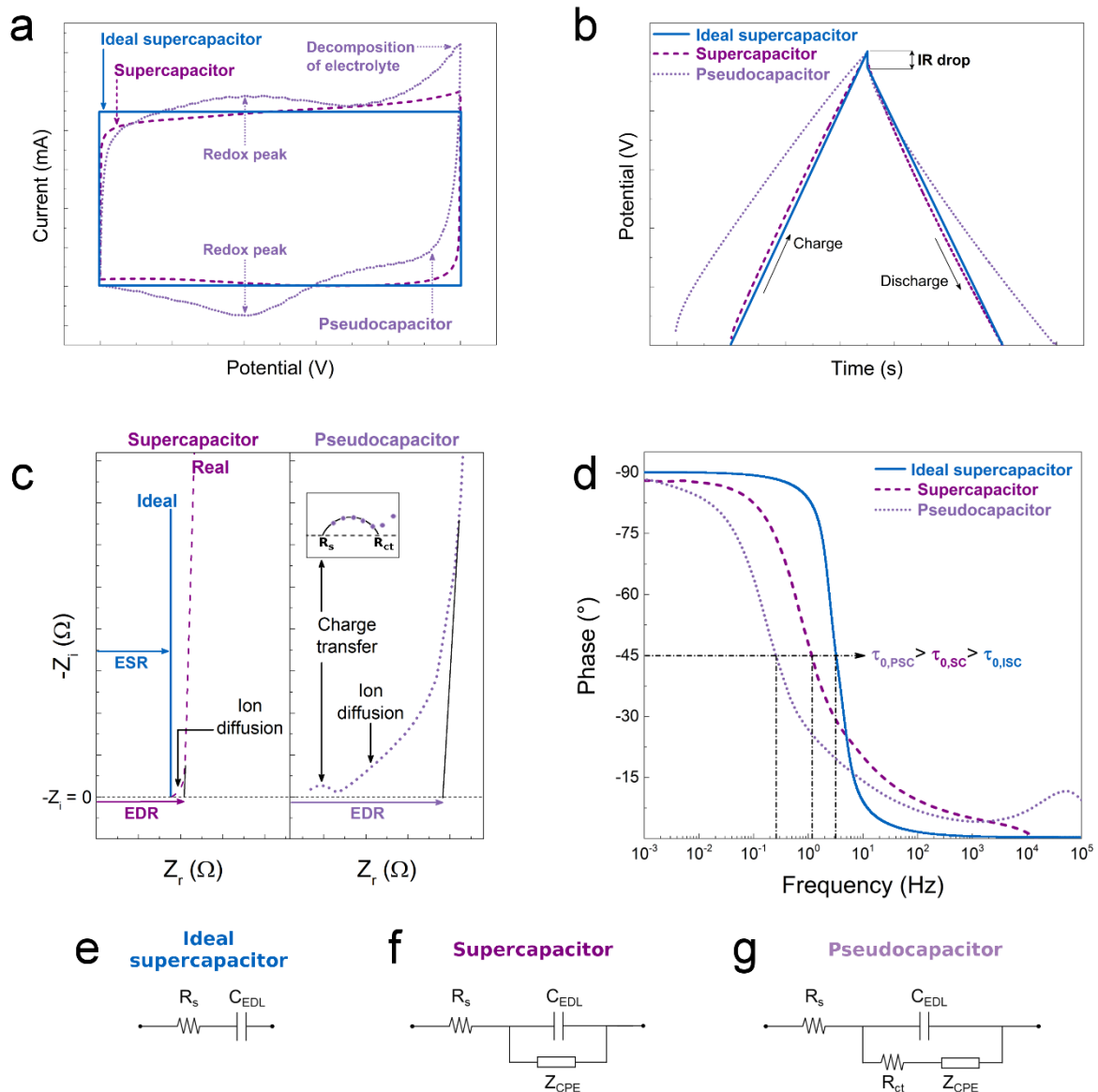


Figure 1.4. Expected behavior of a supercapacitor (SC) and a pseudocapacitor (PSC) compared to that of an ideal SC during different electrochemical tests: (a) cyclic voltammetry, (b) galvanostatic charge-discharge and (c, d) electrochemical impedance spectroscopy. Simplified equivalent circuits for: (e) ideal SC, (f) SC and (g) PSC. [Reproduced from Castro-Gutiérrez et al. (2020)⁸]

1.2.3.4 Electrochemical impedance spectroscopy (EIS)

Electrochemical impedance spectroscopy (EIS) is used to analyze the response of a material to a low-amplitude oscillating potential signal. A Nyquist plot represents the real and imaginary parts of the complex impedance, Z_r and Z_i , respectively. Examples of curves obtained for an ideal SC, a real SC and a PSC are shown in Figure 1.4c. Analysis of Nyquist plots allows associating an equivalent circuit for each type of device, see Figure 1.4e-g, which provides information on the electrochemical system.^{9,19,20} For instance, a straight vertical line appears for a material with an ideal SC behavior. Its point of intersection with the Z_r axis represents the value of the ESR of the device, R_s . The pseudocapacitive behavior adds a second charge transfer resistance to the system, R_{ct} , and a semicircle is observed in the Nyquist plot at high frequencies (HF, $> \sim 10^3$ Hz). In porous materials, the limited ion diffusion within the pores is modeled in the equivalent circuit as a constant phase element, Z_{CPE} , and it manifests itself in the Nyquist plot as a straight line in the HF for a SC and after the semicircle for the PSC.¹⁹ The longer the line, the more difficult it is for the electrolyte to access the whole surface of the material. Once the surface is completely impregnated, the capacitance no longer depends on the frequency, hence the vertical line appearing at low frequencies (LF, $\sim 10^{-3}$ Hz). In all cases, the intersection with the Z_r axis of the vertical line at LF is defined as the equivalent distributed resistance (EDR) that takes into account the ESR and the charge transfer and ion diffusion resistance of the material.

Data obtained from EIS measurements can also be represented in a Bode diagram, see Figure 1.4d, where the phase and/or modulus of the complex impedance are/is plotted as a function of frequency. Bode diagrams are useful tools for easily identifying the relaxation time constant, τ_0 , of the device, which is the inverse of the frequency at which the phase angle is 45° . This parameter is related to the power output of the SC. A low τ_0 leads to a rapid charge-discharge resulting in a high power capability.^{21,22}

1.3 Electrolytes used in supercapacitors

The energy stored in a SC can be considerably increased by widening the operating potential window, see again Equation (1.2), which is essentially limited by the stability of the electrolyte. Increasing the potential beyond this limit causes the decomposition of the electrolyte, resulting in unwanted reactions that sharply increase the current, reduce the performance and can degrade the materials in the SC.²³ Even though the selection of the

electrolyte is mainly defined by its stability, other properties such as conductivity, ion size and mobility, ion-electrode interaction or thermal stability must also be considered. Electrolytes can be classified into different types according to their liquid or solid/quasi-solid state. Within the first group, there are aqueous, organic and ionic liquids whereas the second group can comprise dry polymers or polymer gels.²³ Currently, aqueous and organic electrolytes are the most widely used, Table 1.1 shows their general properties.

Aqueous electrolytes are perhaps the most used in academic research because they have a low cost, they are easy to handle, and they present high ionic conductivity and mobility leading to a low ESR,⁶ among them, acidic, alkaline or neutral solutions can be used.^{5,23} Unlike neutral solutions, acidic and alkaline electrolytes are likely to provide pseudocapacitance contributions by reacting with oxygen or nitrogen surface functional groups present in carbon electrodes.^{24,25} The potential window of aqueous electrolytes is limited to ~1.2 V, beyond which water begins to decompose. Given the freezing and boiling points of water, they are not suitable for applications where the temperature is much lower than 0 °C or much higher than 100 °C.²³ Organic electrolytes predominate on the market because they offer the possibility of using larger potential windows. They consist of salts dissolved in organic solvents that can reach potential windows up to 3.5 V and operate at temperatures as low as -40 °C.²³ However, the larger ion size of typical organic electrolytes limits their mobility, so they have lower conductivities than those of aqueous electrolytes.⁵ In addition, organic electrolytes still face the problems related to their high toxicity, flammability and high costs due to the necessary purification processes and the controlled environment for the assembly of the SCs.²³

Table 1.1. Properties of aqueous and organic electrolytes often used in SCs.^{12,23,26,27} [Adapted from Castro-Gutiérrez et al. (2020)⁸]

Type	Electrolyte	Potential window (V)	Solvated ion size (nm)		Conductivity (S cm ⁻¹) [concentration]	Freezing and boiling point (°C)
			Cation	Anion		
Aqueous	H ₂ SO ₄	0.7 – 1.0	0.28	0.38	0.8 [1 M]	
	KOH	0.9 – 1.0	0.33	0.30	0.6 [6 M]	
	Na ₂ SO ₄	1 – 1.8	0.36	0.38	0.01 [0.1 M]	
Organic	TEABF ₄ /ACN	2.5 – 2.8	1.3	1.16	0.05 [0.65 M]	-49 – +82 °C
	TEABF ₄ /PC	2.5 – 3.5	1.35	1.4	0.01 [0.65 M]	-49 – +242 °C

1.4 Carbon materials as electrodes for supercapacitors

The use of porous carbon materials as electrodes for SCs has increased over the years. Such materials indeed have high chemical and thermal stability, good conductivity, possibility of adjusting their textural properties, and industrial processes for electrode synthesis and production already established.^{5,10,28} From Equation (1.1), it can be seen that a material with a high surface area should result in a high-capacitance SC as long as this surface is accessible to electrolyte ions. The latter highlighted the importance of matching the size of the pores to the size of the electrolyte ions. Some studies had also reported that a hierarchical porous structure connecting micro-, meso- and macropores (pore width $w < 2$ nm, $2 < w < 50$ nm, and $w > 50$ nm, respectively) helps improve SC performances by providing interconnected channels that facilitate ion diffusion in the material.^{29,30} Porous carbon materials are also of particular interest because the addition of specific functional groups to their surface results in higher capacitances due to improved conductivity and/or higher pseudocapacitance contributions.³¹

Efforts to increase the energy density in carbon-based SCs focus on these three aspects: development of porous materials with high surface area, tailoring of pore size, and modification of surface chemistry. The following sections deal with the description of the synthesis processes and the resultant properties of different porous carbon materials for their application as electrodes for SCs.

1.4.1 Activated carbons

Most electrodes in SCs are based on powders of activated carbon (AC) with high surface area (above $1\,000\text{ m}^2\text{ g}^{-1}$). There is a predominant use of biomass as raw material for commercial and laboratory production of ACs, given that agricultural, forestry, municipal and animal byproducts are abundant and inexpensive. Coal or coke can also be used to produce ACs.^{32–34} Figure 1.5 shows schematically the production process by physical or chemical activation methods.

Physical activation is based on the partial and controlled gasification of the carbonaceous material in an atmosphere containing an oxidizing gas, such as steam, CO_2 , air or their mixes, at temperatures ranging from 350 to $1\,000\text{ }^\circ\text{C}$. Before physical activation, pyrolysis at temperatures between 400 and $900\text{ }^\circ\text{C}$ or hydrothermal carbonization (HTC) at lower

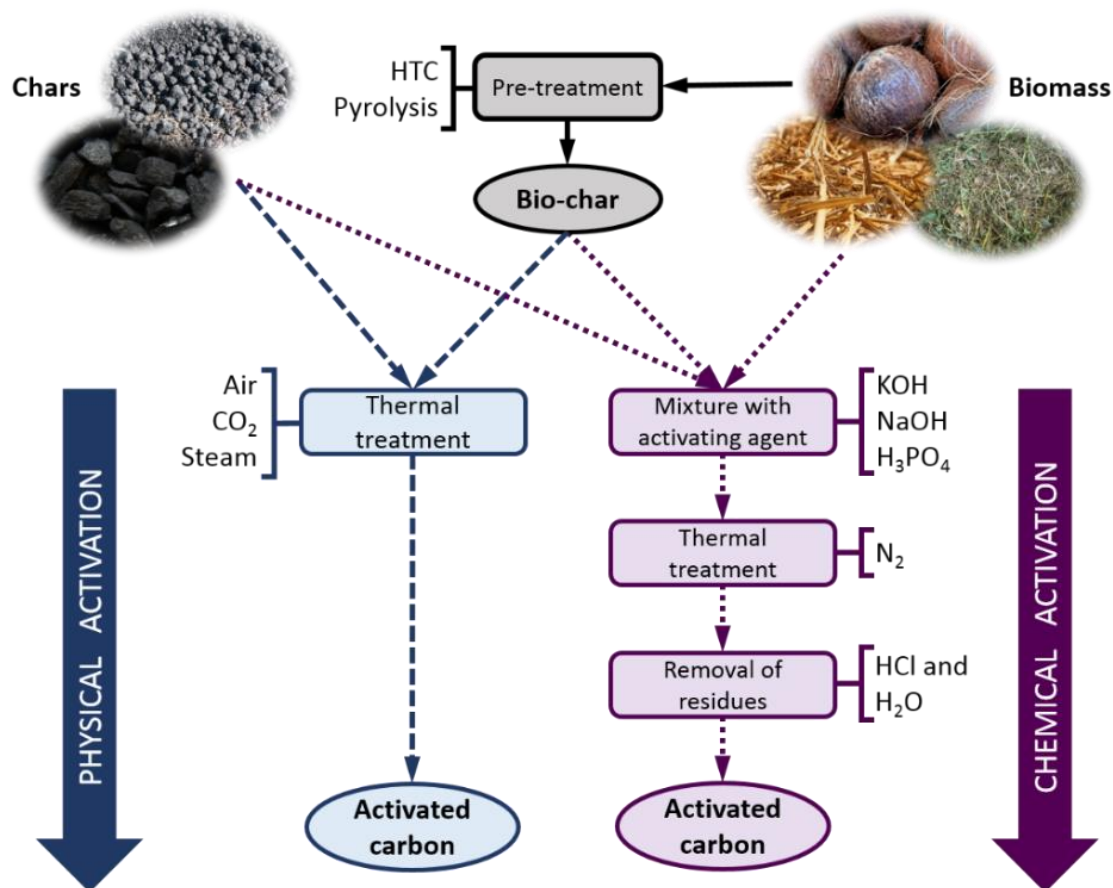


Figure 1.5. Schematic of the production process of activated carbons, from biomass and char, by physical or chemical activation. [Reproduced from Castro-Gutiérrez et al. (2020)⁸]

temperatures (130 to 250 °C) is generally required.^{35–37} The final textural and chemical properties of the ACs depend largely on the activation time and temperature. When the same activating agent is used, a higher degree of activation leads to a higher development of porosity and a broadening of the pore size distribution (PSD). Physical activation normally produces materials with surface areas up to $\sim 1\,800\text{ m}^2\text{ g}^{-1}$ and maximum pore volumes of $\sim 0.9\text{ cm}^3\text{ g}^{-1}$.^{28,34}

Chemical activation is carried out using compounds such as KOH, NaOH, H₃PO₄ or ZnCl₂, among others. The precursor is mixed with the activating agent and then subjected to pyrolysis at temperatures between 400 and 900 °C. Finally, the AC needs to be washed to remove the residues generated during the activation process. Direct chemical activation of biomass is preferred when using ZnCl₂ or H₃PO₄ because they dehydrate biomass, which reduces the quantity of volatile matter released during pyrolysis, thus increasing the carbon yield.^{38,39} KOH or NaOH can be used to activate either untreated biomass or char.^{40–42} Higher amounts of activating agent result in more developed porosity. H₃PO₄ and ZnCl₂ generate

micropores and small mesopores and lead to ACs with surface areas lower than 2 000 m² g⁻¹. On the other hand, KOH can produce higher surface areas, wider PSD and pore volumes of 2.7 cm³ g⁻¹ or more. Such further development of porosity is probably due to the generation of CO₂ as a by-product of the reaction between the carbon and KOH.²⁸ The use of less corrosive or harmless salts for the activation of biomass and biomass-derived precursors, such as potassium carbonate, potassium bicarbonate, potassium oxalate or sodium thiosulfate, has been explored.^{43,44} Materials with high surface areas and pore volumes, up to 2 750 m² g⁻¹ and 2.4 cm³ g⁻¹, respectively, have been reported.

The advanced materials described in the following sections can also be activated to improve their textural properties. However, here they differ from ACs materials since their physicochemical properties are mainly related to synthesis rather than the activation process.

1.4.2 Carbide-derived carbons and zeolite-templated carbons

In order to have higher control of the microporosity, different methods for the synthesis of carbon materials from carbides or zeolites have been developed.^{30,45} High-temperature chlorination (400 – 1 200 °C) of silicon or titanium carbide is used to remove metal atoms and obtain microporous materials. Such carbide-derived carbons (CDCs) exhibit surface areas between 1 000 and 2 000 m² g⁻¹ and a uniform and disordered pore structure. The pore size can be adjusted from 0.6 to 1.1 nm by changing the carbide precursor, the chlorination or the heat-treatment temperature.²⁴ On the other hand, zeolite-templated carbons (ZTCs) are produced by incorporating a carbon precursor, *e.g.* furfuryl alcohol or phenol, inside the zeolite structure and carbonizing it. After template removal, a structure with the same periodicity as the original zeolite is obtained. ZTCs reach surface areas higher than 2 000 m² g⁻¹ and present pore volumes of 1 cm³ g⁻¹ or more.^{45,46} For both CDCs and ZTCs, the pore structure consists only of micropores with a minor presence of mesopores due to the partial collapse of the carbon structure. Activation of these materials introduces mesoporosity and broadens the micropores, which can improve ion diffusion in the porous materials when used as electrodes for SCs.⁴⁶

1.4.3 Carbon gels

Pyrolysis of organic gels prepared from resorcinol-formaldehyde resins has been used to produce carbon gels (CGs) with surface areas between ~500 and ~1 000 m² g⁻¹ and presenting

a high fraction of mesopores. In general, the production of CGs involves five steps: polymerization of the precursor to form an organic gel, aging, solvent exchange, drying and carbonization.^{47,48} CGs are classified, according to the drying technique that has been used, as aerogels, xerogels or cryogels whether supercritical, subcritical or freeze-drying, respectively.⁴⁹ Each step of the synthesis process has an impact on the porous texture of the resultant CGs. On the one hand, the precursor to catalyst ratio and the pH of the solution modify the polymerization process and lead to materials of different textures.^{50,51} On the other hand, controlling the drying process is of paramount importance to avoid the formation of cracks or the shrinkage of the material.⁵² For SC applications, it has been found that the mainly mesoporous structure of CGs limits the effectiveness of the EDL mechanism and that activation generally allows developing a narrow porosity not accessible to ions, leading to a moderate improvement in electrochemical performance compared to the increase in surface area.^{53,54}

1.4.4 Nanostructured carbons

Carbon nanotubes, nanofibers and nanospheres (CNTs, CNFs and CNSs, respectively) have also been used as electrodes of SCs. Although the surface area of CNFs and CNTs is moderate, $\sim 400 \text{ m}^2 \text{ g}^{-1}$, they have been considered for SCs electrodes given that their entanglement results in multiple charge storage sites.¹³ CNFs and CNTs obtained by electrospinning techniques or by direct growth on conductive substrates allow flexible mats to be produced, which can be directly used as electrodes in SCs, as seen in Figure 1.6a.^{13,55,56} Likewise, aligned CNFs and CNTs can be grown directly on current collectors, see Figure 1.6b, and thus have more control on the distance between fibers or tubes.^{57–59} SCs with electrodes based on aligned CNFs or CNTs could exhibit improved performance at high charging rates due to a shortening of the conductive path for the charges as schematized in Figure 1.6c.³⁰ However, the performance of CNTs as electrodes in SCs is strongly affected by the presence of impurities, therefore requiring a purification process so their performance is not compromised.⁶⁰ In addition, activation is generally needed to create micropores on the surface of CNFs and increase the number of charge storage sites.^{13,30} On the other hand, it is nowadays possible to synthesize a wide variety of CNSs, whether solid, hollow, or onion-like, among others, and with micro-, meso- and/or macropores, see examples in Figure 1.6d-h. The surface areas vary from low, $< 100 \text{ m}^2 \text{ g}^{-1}$, to high, $\sim 2\,000 \text{ m}^2 \text{ g}^{-1}$, and the sphere sizes range from tens of nm to hundreds of μm , depending on the synthesis method.⁶¹ The strategies for synthesizing

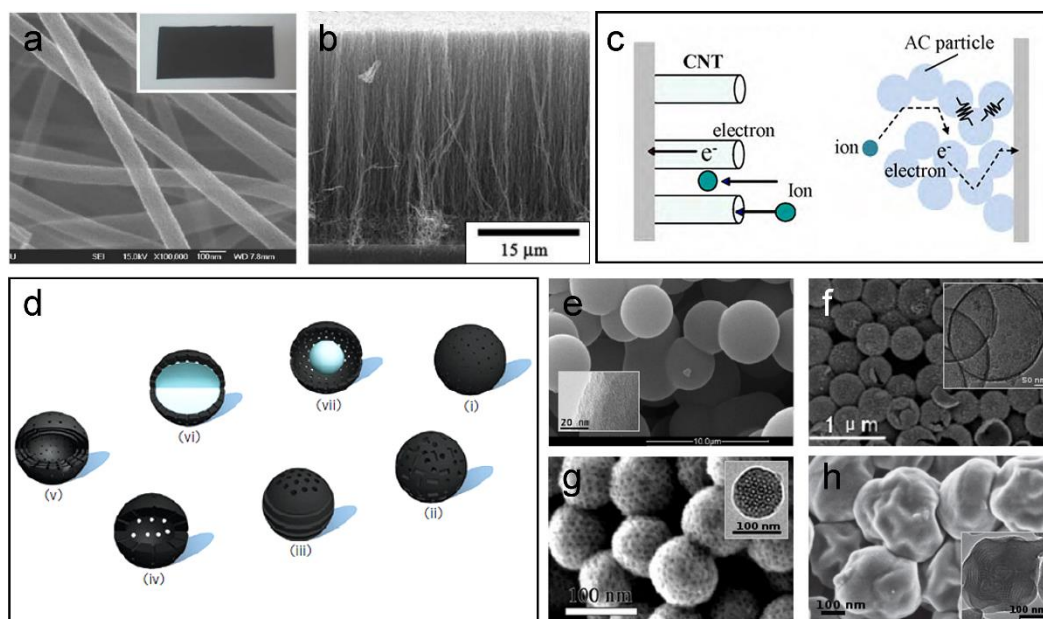


Figure 1.6. (a) Activated CNFs from polyacrylonitrile and derived paper in the inset. (b) Aligned CNTs grew in ammonia atmosphere using acetylene as carbon precursor. (c) Schematic of the conductive paths of electrons and ions in a SC electrode based on aligned CNTs and AC particles. (d) Different types of CNSs structures: solid with disordered (i) micropores and (ii) mesopores; (iii) ordered mesoporous; (iv) hollow; (v) multishelled hollow; (vi) core-shell; (vii) yolk-shell. Images of different types of CNSs (SEM and TEM in the insets): (e) solid derived from tannin; (f) hollow derived from ionic liquid 1-alkyl-3-methylimidazolium bromide; (g) ordered mesoporous derived from phenol; and (h) multishelled hollow derived from resorcinol. [Adapted from Ra et al. (2009)⁵⁵, Kim et al. (2003)⁵⁷, Inagaki et al. (2010)³⁰, Liu et al. (2015)⁶¹, Braghiroli et al. (2012)⁶², Chen et al. (2013)⁶³, Fang et al. (2010)⁶⁴, and Liu et al. (2013)⁶⁵].

CNSs include different types of hard- and soft-template techniques, emulsion polymerization, self-assembly or the Stöber method.^{61,66} Typically, petrochemical precursors are used to produce CNSs, but HTC processes have successfully used glucose, sucrose, cellulose or tannin to obtain CNSs.^{61,66,67} Uniform CNSs can be packed in high-density electrodes, maintaining the electrolyte accessibility thanks to voids between the particles. Therefore, this type of electrode allows a large amount of energy to be stored in small-volume devices.⁶⁸ Despite the advantages of CNSs, the multi-step synthesis process, the use of hazardous substances to etch the hard templates and the low yields associated with soft-template methods limit their extensive use for widespread production.^{61,66}

1.4.5 Ordered mesoporous carbons

To develop materials with a hierarchical pore structure, many studies have been devoted to the design and engineering of ordered mesoporous carbons (OMCs) using different synthesis

methods, by which it is possible to tune the morphology and porosity. If necessary, an activation process is carried out to increase the surface area. In this way, OMCs have the advantage of having a hierarchical pore structure to provide interconnected channels for the diffusion of electroactive species, thus making them suitable for application in SCs.^{5,6,69} OMCs can be synthesized by hard- or soft-template methods. Both are shown in Figure 1.7a, and further details are given below.

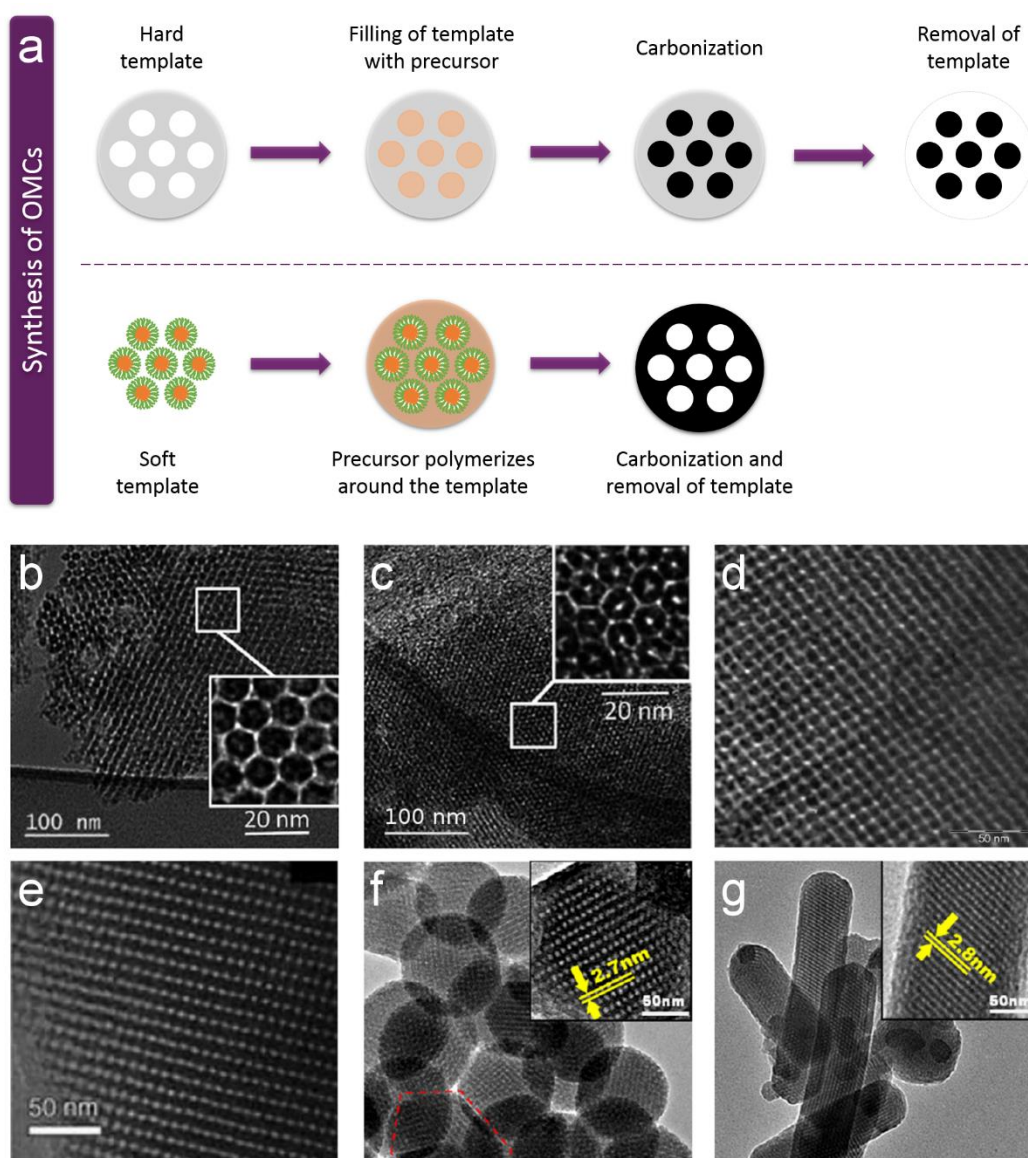


Figure 1.7. (a) Schematic synthesis of OMCs by hard and soft template methods. (b, c) Hard-templated OMCs using SBA-15 as template and aminobenzoic acid as precursor and (d) KIT-6 template and sucrose as precursor. (e-g) Soft-templated OMCs using Pluronic® F127 as surfactant and phenol as precursor. [Adapted from Castro-Gutiérrez et al. (2020)⁸, Sánchez-Sánchez et al. (2016)⁷⁰, Lang et al. (2011)⁷¹, Meng et al. (2005)⁷², and Li and Xue (2012)⁷³]

The hard-template method uses an inorganic material that is filled with the carbon precursor. After polymerization, the composite is subjected to carbonization, and the template is then removed using HF or NaOH. As a result, the OMC obtained is an inverse replica of the template.⁴⁵ Mesoporous silicas are the most used in this kind of technique, but having to synthesize such templates before sacrificing them makes the procedure expensive, polluting and time-consuming. Thus, efforts to synthesize OMCs from biosourced templates have been made to take advantage of naturally ordered and hierarchical structures found in diatomaceous earth, pollen grains or leaves, among others.⁷⁴⁻⁷⁶ However, the procedure still involves the use of hazardous substances to crosslink the precursor and/or to etch the template.

In the soft-template method, an amphiphilic surfactant is used in solution to form micelles. The hydrophilic part of the micelle interacts with the carbon precursor that polymerizes around the surfactant. Then, the carbonization process eliminates the surfactant, revealing the mesoporosity at the same time.⁷⁷ Different combinations of commercially available block copolymers such as Pluronic® (F127, P123, among others) or Vorasurf® as surfactants and phenol, phloroglucinol, resorcinol or tannin as carbon precursors have been used to successfully synthesize OMCs by soft-template methods.⁷⁷⁻⁸⁰

In both hard- and soft-templating, the mesopore order is determined by the characteristics of the template. Given the diversity of templates and precursors available, OMCs have surface areas from ~500 to more than 2 000 m² g⁻¹, and various PSDs in the micro – mesopore range. Thus, the versatility of OMCs turns them into an interesting choice of materials to be used as SC electrodes, because they can be synthesized with a wide range of morphologies and PSDs. Figure 1.7b-g shows examples of OMCs with different pore structures.

1.4.6 Doped materials

A potential route to increase the energy stored in SCs is the heteroatom doping of carbon materials, which promotes fast Faradaic reactions and enhances their performances *via* pseudocapacitance contributions. All the materials described in the previous sections (Sections 1.4.1 to 1.4.5) are subject to surface modification. Although doping with boron, sulfur or phosphorus has been investigated,^{31,81-83} the introduction of heteroatoms such as oxygen (O) or nitrogen (N) is recurrent because it is relatively easy to perform. In consequence, O- and N-

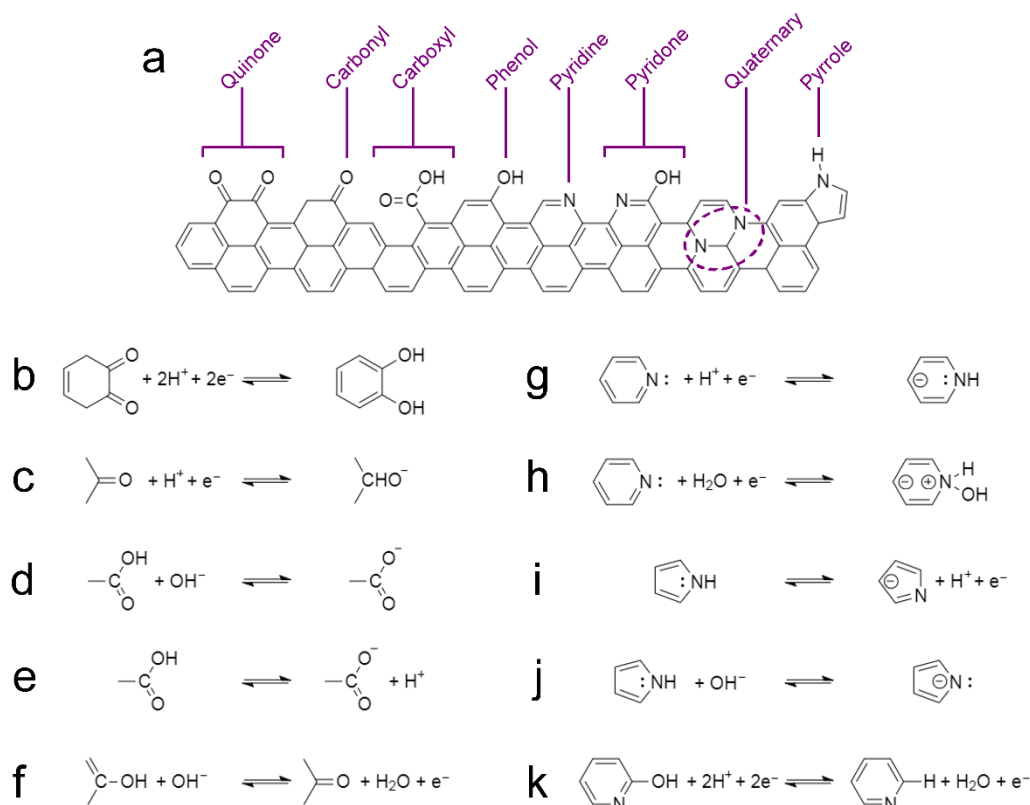


Figure 1.8. (a) Oxygen and nitrogen surface functional groups commonly associated with the enhanced performance of carbon-based SCs. Proposed reactions of such (b – f) oxygen and (g – k) nitrogen surface functionalities.^{70,84,85} [Reproduced from Castro-Gutiérrez et al. (2020)⁸]

doping have been studied in-depth, specifically in aqueous electrolytes where the species are electrochemically active.⁵ Figure 1.8a displays the most common O- and N- surface functional groups associated with improving the performance of carbon-based SCs.

Oxygen functionalities are normally found in porous carbon materials. To dope the materials further with oxygen, activation and/or oxidation treatments in HNO_3 , H_2SO_4 or using O_2 can be carried out.^{28,30} The final amount and the type of functionality on the carbon surface depend on the precursor and the synthesis method. Some of the proposed redox reactions involving oxygen surface groups are shown in Figure 1.8b-f.^{70,84} In acidic electrolytes, it has been reported that quinone functionalities have the largest contribution to capacitance by redox reactions, Figure 1.8b.⁸⁶ Even though the carboxylic groups could increase the capacitance through the generation of charges, see Figure 1.8e, their high polarity could also produce resistance to ion diffusion, reducing the performance, especially at high charging rates.²⁸ Nevertheless, carboxylic and phenolic groups are also likely to react in alkaline solutions, see Figure 1.8d and 1.9f, with a positive impact on the SC performance.⁸⁷

N-doping by post-treatment is carried out by HTC and/or annealing of a mixture of the carbon material with a nitrogen precursor, *e.g.* ammonia, melamine or urea.⁸⁸ N-doping can also be performed *in situ* by direct pyrolysis of a nitrogen-rich carbon precursor⁸⁹ or by multi-step methods to produce CNSs,^{67,68,90} CNTs,⁹¹ or OMCs.^{70,92} Isolating the contribution of N-functionalities to the SCs performance is a difficult task since nitrogen is always present with oxygen and can lead to modifications of textural properties. However, a correlation between SCs performance and the amount and type of nitrogen functionalities has been reported.^{86,93,94} N-doped materials can reach high values of capacitance even if their surface areas are relatively low. This has been attributed to pseudocapacitance contributions but also to improved wettability and conductivity of the materials.³⁰ Most studies agree that the major contribution to pseudocapacitance comes from the pyridinic, pyrrolic and pyridine groups, see Figure 1.8g-k.⁸⁵ However, some studies have suggested that quaternary groups interact with protons or anions in H₂SO₄ or KOH electrolytes, respectively, and could promote electron transfer through the carbon structure.⁸⁵

1.5 Transition to biosourced precursors of porous carbon materials

Apart from ACs, which are often produced on an industrial scale from biomass materials, most of the synthesis methods described in Section 1.4 use precursors of petrochemical origin. For example, phenolic resins derived from the crosslinking of resorcinol or phenol with formaldehyde are widely used to synthesize different types of OMCs.^{26,95,96} In an effort to research more environmentally friendly technologies and methods, biosourced substitutes for ordinary carbon precursors have been explored. A salt template-assisted, chemical activation process was applied by subjecting gelatin, sucrose, glucose or tannic acid (TA) mixed with KCl and Na₂S₂O₃ to carbonization.^{17,43} The resultant micro-mesoporous carbon materials had high surface areas and pore volumes in the range of 1 900 – 2 720 m² g⁻¹ and 0.96 – 2.4 cm³ g⁻¹, respectively. TA has also been used to produce micro-mesoporous CNSs with a disordered structure by direct heat-treatment of the precursor mixed with urea and a eutectic salt (NaCl/ZnCl₂)⁹⁷ and to synthesize CNFs by carbonization of a glass fabric previously impregnated with TA.⁹⁸ Micro – macroporous ordered carbons have been produced using diatomite templates in combination with furfuryl alcohol.⁷⁴ Hard-templating of sucrose with cubic and 2D hexagonal silica templates produced highly porous materials with surface areas as high as 2 000 m² g⁻¹.⁹⁹ Also based on the use of silica templates, OMCs with surface areas

higher than $900 \text{ m}^2 \text{ g}^{-1}$ were synthesized from different types of biomass-derived phenols such as phloroglucinol, gallic acid, catechin and mimosa tannin.¹⁰⁰ By soft-template routes, it has been reported that 2D hexagonal OMCs with surface areas $\sim 700 \text{ m}^2 \text{ g}^{-1}$ were obtained by hydrothermal treatment of β -cyclodextrin, extracted from starch, mixed with Pluronic® F127 and P123¹⁰¹ or by evaporation-induced self-assembly (EISA) using a mixture of lignin, phloroglucinol, glyoxal and Pluronic® F127.¹⁰² Besides, a phase-separation method was able to produce N-doped 2D hexagonal OMC with a moderate area of $523 \text{ m}^2 \text{ g}^{-1}$ from phloroglucinol, glyoxylic acid and guanine.⁹²

1.6 Tannins as carbon precursor

Tannins are polyphenolic substances present in many plants and trees. They have been used in the leather manufacturing process since the Middle Ages.^{103,104} Their industrial production increased in the 1970s thanks to the development of tannin adhesives for wood.¹⁰⁵ Nowadays, tannins are used not only for tanning leather (hence their name) but also as an additive in wine, food supplements and cosmetic ingredients.¹⁰⁶ Although there are several methods for extracting tannins, the solid-liquid method is the one traditionally used on an industrial scale due to its simplicity, efficiency and low cost.¹⁰⁷ The solid-liquid extraction method involves the dissolution of tannins in water at moderate temperatures ($60 - 70 \text{ }^\circ\text{C}$), after which the solution is concentrated and spray-dried to obtain a red-brown powder.^{107,108} The chemical composition of the final powder strongly depends on the plant species and the part of the plant from which the tannin has been extracted. However, the similarities in their compositions allow them to be classified into two broad categories, namely hydrolyzable or condensed.^{107,109} In particular, condensed tannins are of primary interest in the synthesis of carbon materials as they contain more than 70 – 80 % of polyflavonoids. Their aromatic rings with hydroxyl groups give polyflavonoids a reactivity similar to that of phenolic molecules of petrochemical origin such as phenol or resorcinol,^{105,110} as well as a high carbon yield upon pyrolysis, $\sim 50 \%$. More details on the properties of condensed tannins are given next.

1.6.1 Condensed tannins

The polyflavonoids of condensed tannins are composed of flavan-3-ol moieties made up of two phenolic rings (A and B) linked by a heterocyclic ring. Figure 1.9 shows the main four

types of flavonoid molecules of condensed tannins, which differ in the number and position of the –OH groups in rings A and B, as well as with the type of trees in which they are found. Thus, mimosa (*Acacia mearnsii*), quebracho (*Schinopsis balansae* and *Schinopsis lorentzii*) and maritime pine (*Pinus pinaster*) are the most used species for the extraction of condensed tannins, representing 90 % of the world’s production.^{105,111} The reactivity of the flavonoid units depends on the position of the –OH groups and the available reaction sites. In this sense, it has been shown that the A-ring is more reactive than the B-ring.¹¹⁰ Indeed, tannins can naturally auto-condense by linking the units at positions 4,6 for profisetinidin and prorobinetinidin or 4,8 for procyanidin and prodelphinidin (see again Figure 1.9), producing oligomers of up to 10 or 11 units.¹¹² The ability of condensed tannins to auto-condense and react with aldehydes to form phenolic resins makes them an attractive alternative to produce high added-value materials.

In addition to their good chemical reactivity, tannins have the advantage of being non-toxic in the event of exposure to low amounts, and high doses can only cause irritation or have anti-nutritional effects.¹¹³ Compared to the toxicity and hazards of substances like resorcinol, phenol or formaldehyde, as shown in Table 1.2, tannins should be considered as excellent ecological and non-toxic alternative precursors to produce porous carbons.

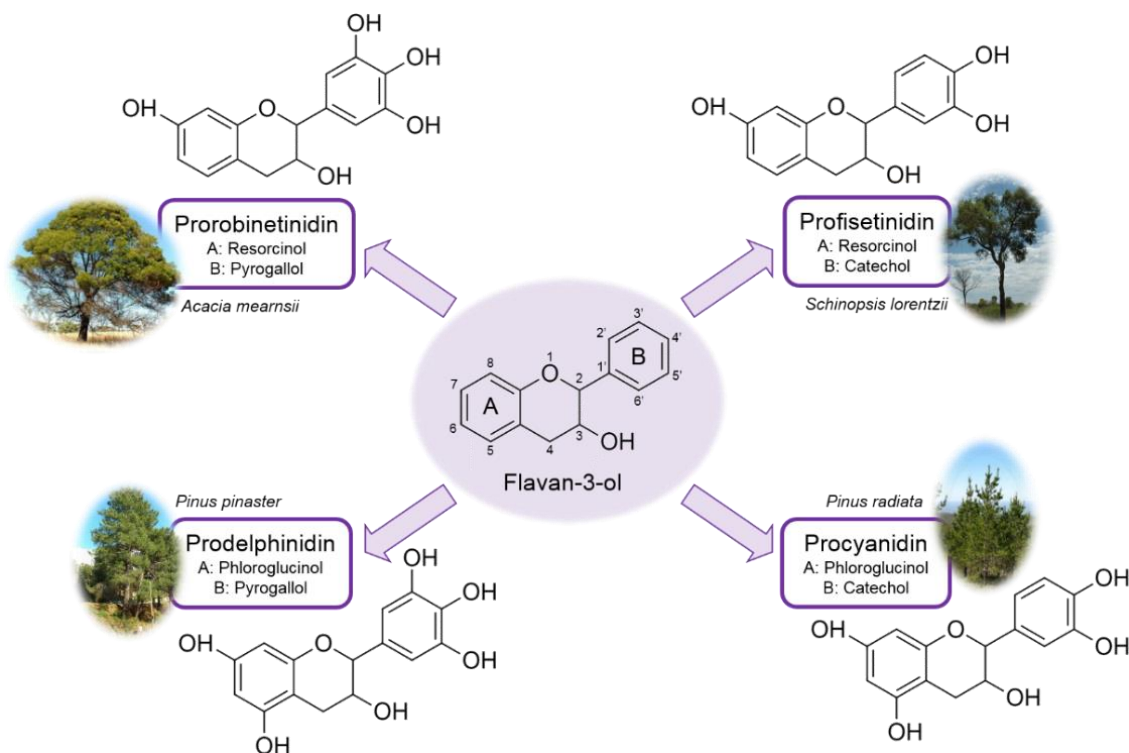


Figure 1.9. Main flavonoid units of condensed tannins, along with the plant commonly used for their extraction. [Reproduced from Castro-Gutiérrez et al. (2020)⁸]

Table 1.2. Hazard statements for phenol, resorcinol, formaldehyde and tannin with data from the National Center for Biotechnology Information ¹¹⁴ and the National Institute for Occupational Safety and Health. ¹¹⁵ [Adapted from Castro-Gutiérrez et al. (2020)⁸]

	Phenol	Resorcinol	Formaldehyde	Tannin
PEL	TWA 5 ppm (skin)	Not reported	TWA 0.75 ppm STEL 2 ppm	No adverse human health effects*
REL	TWA 5 ppm (skin) STEL 15.6 ppm (skin)	TWA 10 ppm STEL 20 ppm	TWA 0.016 ppm STEL 0.1 ppm	Does not have skin or eye irritation effects*
GHS hazards				Not reported for profisetinidin, prorobinetinidin, prodelphinidin and procyanidin
NFPA hazards				Not reported for profisetinidin, prorobinetinidin, prodelphinidin and procyanidin

PEL: permissible exposure limit; REL: recommended exposure limit; TWA: time-weighted average over 8 h; STEL: short-term exposure limits over 15 min; GHS: globally harmonized system; NFPA: National fire protection association. *According to SilvaChimica (St Michelle Mondovi, Italy), provider of mimosa, quebracho and tara tannins.

1.6.2 Synthesis of porous carbons

Given the versatility and reactivity of condensed tannins, they have been used to produce a wide variety of high added-value materials. The tannin-derived products obtained by different methods can be converted into carbon by high-temperature treatment. The resulting materials are glass-like due to the non-graphitizing nature of the precursor, and present isotropic properties and good electrical conductivity. Additional physical or chemical activation open blocked pores and develop their porosity. As for petrochemical precursors, the synthesis of porous materials from tannin usually requires the preparation of a resin by crosslinking with formaldehyde, hexamine or glutaraldehyde, among other possible aldehydes. Thus, different materials have been synthesized such as foams,^{116–120} gels,^{49–51,121} microspheres⁴⁷ or polyHIPEs.¹²² Furthermore, tannin autocondensation reactions enable its polymerization without having to use crosslinkers, opening the way for the production of OMCs by self-assembly techniques.^{78,113} The next subsections are devoted to describe some of the methods used to obtain micro-mesoporous carbon materials from tannin, as well as their performance when used as electrodes for SCs, which are summarized in Table 1.3 at the end of this section.

1.6.2.1 Sol-gel

CGs were produced from mimosa tannin and formaldehyde (TF) organic cryogels.¹²³ The pH of mimosa tannin solutions was adjusted with either acetic acid or NaOH diluted in water to obtain a pH ranging from 3.3 to 7.3. Such solutions were placed in an oven at 85 °C for 5 days, in which gelation and aging took place. After exchanging water for *tert*-butanol, the gels were freeze-dried to obtain TF cryogels. Finally, CGs were produced by carbonization of TF cryogels at 900 °C. Surface areas from 399 to 1 420 m² g⁻¹ were obtained, with minimum values found for pH 4.3 and 5.3 and attributed to pore collapse during carbonization. The highest surface areas were found for pH > 6. This unusual development of the surface area was ascribed to the presence of NaOH, which could act as an activating agent during the carbonization process. The textural characterization revealed that the CGs were mainly micro- and macroporous materials, with an unusually low amount of mesopores.

In order to test their electrochemical performance, the CGs were ground to prepare pellets by mixing the corresponding sample, carbon black and PVDF (75:5:20 wt. %), and then symmetrical SCs were assembled and tested in a T-type cell. CV tests were carried out from 2 to 50 mV s⁻¹ using 4 M H₂SO₄ as the electrolyte in a potential window of 1 V. The values of C_e of the CGs at 2 mV s⁻¹ ranged from 30 to 109 F g⁻¹, similar to the values found for more expensive carbon aerogels. As expected, the best performance was observed for the materials with the highest surface area. However, as the scan rate increased, the CV curves became narrower and lost their quasi-rectangular shapes, indicating a loss of SC behavior and resulting in a decrease of C_e . It was concluded that, although these CGs were highly porous, the values of capacitance were generally lower than expected due to the large amount of macropores that do not account for the capacitance. Besides, the sharp drop in C_e with increasing scan rate was related to the absence of mesopores to facilitate the diffusion of electrolyte ions in the micropores.

1.6.2.2 Hydrothermal carbonization

Hydrothermal treatments of aqueous solutions of tannins take advantage of their autocondensation at very acidic or basic pH. By varying pH, tannin concentration and temperature, it is possible to obtain gels or spheres. Besides, it is possible to perform N-doping *in situ* by using ammonia solutions instead of water during the HTC process. Several examples

of the electrochemical performances of carbonized, tannin-derived, HTC materials are described below.

N-doped materials were produced by HTC of mimosa tannin.^{67,124} Two functionalization routes were followed: (i) dissolution of tannin in an aqueous ammonia solution, evaporation at room temperature, then the dissolution of the solid residue in water solution followed by HTC; and (ii) dissolution of tannin in an aqueous ammonia solution followed by HTC. The former resultant material was called EAT (for “evaporated aminated tannin”), and the latter was called AT (for “aminated tannin”). A reference material, prepared by direct HTC of tannin in water, called T, was also synthesized. HTC was carried out at temperatures ranging from 180 to 220 °C for 24 h, and the recovered materials were carbonized at 900 °C. The morphology radically changed from CNSs for the reference materials to CG structure for the EAT-materials, while the carbon obtained by the AT-route presented a mixed morphology, see Figure 1.10a-c. The carbon materials exhibited surface areas between 113 and 684 m² g⁻¹. AT- and T-materials had a high proportion of ultramicropores (pores of width < 0.7 nm), higher than 79 %, while

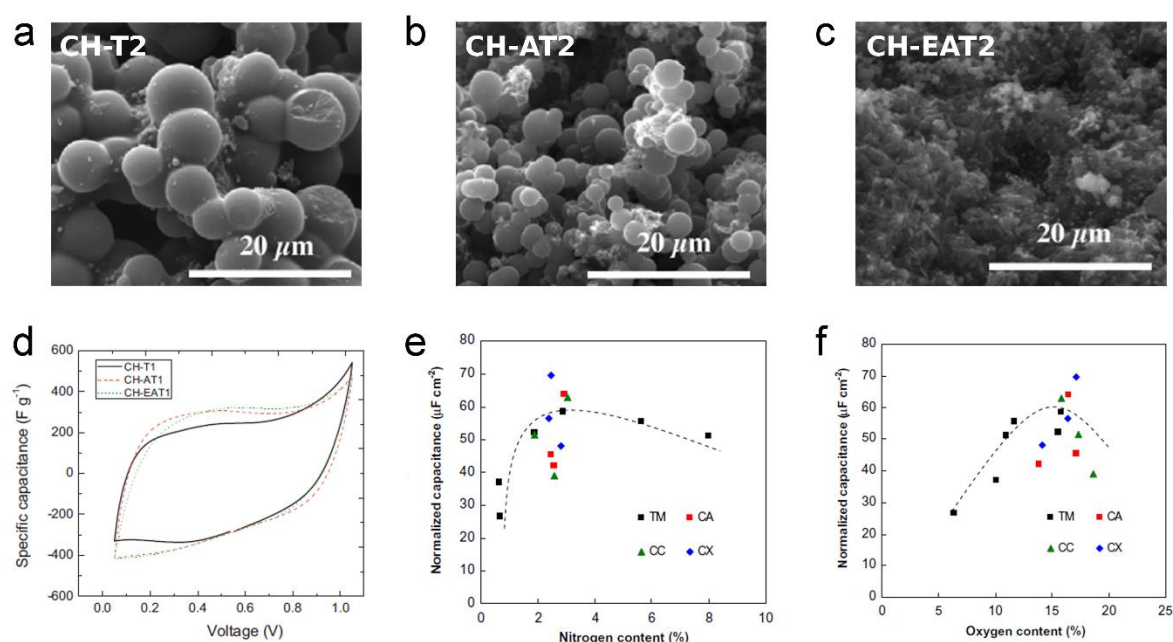


Figure 1.10. SEM images of materials obtained after HTC at 210 °C and subsequent pyrolysis at 900 °C of tannin in (a) water, or (b) ammonia solution, and (c) evaporated aminated tannin in water. (d) Examples of cyclic voltammety curves obtained at 2 mV s⁻¹ from carbonized (900 °C) HTC materials produced at 180 °C. Normalized capacitance as a function of (e) nitrogen and (f) oxygen content of carbonized HTC materials produced at 180 and 210 °C, referred to as TM, and of EAT-derived CGs, referred to as CA, CC and CX for carbon aerogels, cryogels and xerogels, respectively. The sample labels correspond to those used in their respective source references. [Adapted from Braghiroli et al (2015)⁶⁷ and Braghiroli et al (2015)⁹⁴]

EAT-materials presented a majority of mesopores. The micropore volume remained around $\sim 0.21 \text{ cm}^3 \text{ g}^{-1}$ in almost all cases. Regarding the presence of heteroatoms, the AT-route introduced the highest amount of nitrogen into the material with a maximum of 8.1 wt. % for HTC carried out at 220 °C. The oxygen content decreased with the temperature, regardless of the functionalization route, remaining between 5.6 and 15.9 wt. %.

The electrochemical performances of carbon materials derived from HTC at 180 and 210 °C were evaluated.⁶⁷ Electrodes for symmetrical SCs were prepared by mixing the powdered carbon material with carbon black and PVDF (75:5:20 wt. %), and assembled in a T-type cell, using 4 M H₂SO₄ as the electrolyte. CV tests were carried out using a potential window of 1 V. The obtained curves were asymmetric, indicating the existence of considerable resistance; examples are shown in Figure 1.10d. CV curves also showed humps characteristic of redox reactions occurring due to the high content of heteroatoms (N and O). Thanks to the pseudocapacitance contributions of these reactions, C_e reached values as high as 322 F g⁻¹ at 2 mV s⁻¹. However, as the scan rate increased, C_e dropped considerably. This behavior was attributed to the large size of the mesopores, 27 – 34 nm, which do not significantly account for the capacitance and do not successfully shorten the ion diffusion pathways as the narrower mesopores would. To study the effect of doping, the interfacial capacitance was calculated by normalizing C_e by the surface area and was plotted against the O and N contents (wt. %), see Figure 1.10e and 1.11f. It was found that the interfacial capacitance increased with the O content, but showed a maximum value for an N content between 3 and 6 wt. %. A large amount of heteroatoms is believed to block the pores, resulting in reduced electrochemical performance.

A follow-up study evaluated the electrochemical performances of N-doped CGs produced by HTC of EAT.⁹⁴ In this case, aqueous solutions of different concentrations of EAT were submitted to HTC at 180 °C for 24 h. The recovered products were then dried to produce organic aerogels, cryogels or xerogels, and the latter materials were further carbonized at 900 °C to obtain N-doped CGs. The materials exhibited both micro- and mesoporosity in a proportion of $\sim 40/60$ and the highest surface areas were obtained for the highest concentration of EAT, reaching a maximum of 860 m² g⁻¹. For all the CGs, the N content remained around 2.5 wt. %, and an O content higher than 13.9 wt. % was observed. Electrodes for symmetrical SCs were prepared and assembled as described above for AT- and EAT-materials. Again, the CV curves were asymmetrical with the characteristic humps due to redox reactions, similar to those displayed in Figure 1.10d. At a scan rate of 2 mV s⁻¹, the ultramicropore volume was found to have more impact on the C_e values than the surface area. The capacitance increased significantly

up to an ultramicropore volume of $0.2 \text{ cm}^3 \text{ g}^{-1}$, for which it reached a maximum value of $\sim 400 \text{ F g}^{-1}$. A further increase in the volume did not affect the capacitance values. Contrary to what was expected, the values were more scattered than in the trends previously observed when comparing the effect of O and N doping on the interfacial capacitance with the results of Braghiroli et al.⁶⁷ (see again Figure 1.10e and 1.11f). Recalling that all CGs have a similar N content, this scattering might be due to their larger differences of pore texture. The enhancement in the capacitance due to N-doping could be positively or negatively influenced by, for example, a larger or lower surface area, explaining the scattering of the values in Figure 1.10e. Analogous reasoning would also explain the behavior observed for the effect of the O content in Figure 1.10f.

Another study proved that N-doped carbon materials can also be obtained by HTC treatment of aminated pine tannin.¹²⁵ The synthesis reported by Braghiroli et al.⁶⁷ was used by replacing mimosa tannin with pine tannin and carrying out the HTC process at $190 \text{ }^\circ\text{C}$. The tannin extraction from *Pinus pinaster* was carried out by two methods. In method (i), a mix of pine bark and water in a weight ratio of 1:6 was heated up to $90 \text{ }^\circ\text{C}$ for 90 min. In method (ii), the same mix used in (i) but in a 1:5 weight ratio was heated up to $75 \text{ }^\circ\text{C}$; then, an aqueous solution containing 2 and 0.5 % of Na_2SO_3 and Na_2CO_3 , respectively, was added to the mixture while maintaining the temperature for an additional 60 min. The suspensions from methods (i) and (ii) were filtered, washed with water and spray-dried, leading to tannin powders referred as TW or TNa, respectively. The morphology of the carbon materials was similar to that obtained from the same treatment of mimosa tannin, *i.e.*, showing a transition from spherical particles to a gel-like structure. Most of the materials presented a high microporosity that led to surface areas between ~ 300 and $\sim 700 \text{ m}^2 \text{ g}^{-1}$. However, samples obtained from the direct HTC of TNa and the EAT-route did not develop any porous texture, which is the reason why they were excluded from the electrochemical tests.

A three-electrode configuration was used to evaluate the electrochemical performance of the pine tannin-derived materials in a potential window of 0.9 V in $1 \text{ M H}_2\text{SO}_4$. Electrodes were prepared by mixing the porous carbon, carbon black and PTFE (85:5:10 wt. %). Faradaic peaks were observed on the CV curves at low scan rates (0.5 mV s^{-1}). Remarkably, the TW-materials retained a quasi-rectangular CV curve for a high scan rate of 1 V s^{-1} , but the deviations from the ideal rectangular shape suggest that the diffusion of ions in the narrow micropores was hindered. At low scan rate, C_e of TW-materials was above 200 F g^{-1} due to pseudocapacitance contributions. However, for a scan rate of 20 mV s^{-1} , C_e has already decreased to $\sim 40 \%$ of its

original values because redox reactions do not occur at faster scan rates. Capacitance then continued to decrease but at a considerably slower rate, almost reaching a plateau at 1 V s^{-1} . In addition, a linear increase in interfacial capacitance with the surface concentration of heteroatoms (N and O) was observed for the TW-materials. As the scan rate increased, the slope of the fitted line decreased, becoming almost a horizontal line at 1 V s^{-1} . This implies that, for fast scan rates, the heteroatom content does not contribute to the capacitance, in agreement with the previous statements. TNa-A sample, obtained from aminated TNa, exhibited the lowest performance, whatever the scan rate and despite a surface area and density of surface functionalities similar to those of other materials from the TW-series. Furthermore, TNa-A exhibited the lowest value of interfacial capacitance, indicating that a large part of the surface of the material was not accessible to the electrolyte ions. The high amount of surface functionalities was not able to compensate for the lack of charge storage sites resulting in the poor performance observed. Besides, GCD and EIS measurements were carried out using a two-electrode cell. The calculation of C_e from the GCD curves gave values similar to those obtained from the CV curves, and a drastic drop in capacitance was observed as the applied current increased. Again, TNa-A had the lowest performance. In general, the doped materials from the TW-series had the highest values of capacitance, confirming the beneficial role of surface modification. However, there are still some drawbacks to the doping procedure followed, as the EIS and GCD tests also revealed that the doped materials had larger EDR values and lower stability after continuous cycling than their non-doped counterparts.

1.6.2.3 Microwave-assisted synthesis

P- and N-doped carbons (PNDCs) have been successfully produced by a microwave technique using quebracho tannin as carbon precursor.¹²⁶ Melamine and hexamine were used as N source and polyphosphoric acid as P source. The synthesis was carried out by dissolving melamine and tannin in water, then a solution of hexamine was added and the whole mixture was heated to its boiling point. Finally, the resultant material was mixed with polyphosphoric acid and subjected to microwaves for 30 min. The temperature reached was estimated to be between $1\ 200$ and $1\ 400$ °C during the process carried out in a $1.25 \text{ kW} - 2.4 \text{ GHz}$ microwave oven. The physicochemical properties and performances of the PNDCs obtained from three different Tannin:Melamine:Hexamine molar ratios as electrodes for SCs were further studied by the same research group.¹²⁷ The samples were referred to as PNDC- x , where $x = 1, 2$ or 3 : the higher the value of x , the lower the amount of melamine and hexamine used for synthesis.

A large amount of heteroatoms was successfully introduced on the surface of the carbon. However, this was achieved by sacrificing considerably the available surface. The sample PNDC-1, having the highest content of surface functionalities (N 9.7 at. %, P 9.0 at. % and O 14.9 at. %), thus had the lowest BET area, $113 \text{ m}^2 \text{ g}^{-1}$ due to an accumulation of heteroatoms that could hinder access to the pores. Moreover, the higher contents of N and P are the consequence of the use of large quantities of hexamine and polyphosphoric acid, both substances reducing the amount of gases released during pyrolysis, increasing the carbon yield, but also reducing the development of the porous texture. Decreasing the level of doping increased the surface area and increased the volumes of micro- and mesopores. The sample PNDC-3 thus had the lowest content of heteroatoms and exhibited a surface area of $855 \text{ m}^2 \text{ g}^{-1}$ with a total pore volume of $0.65 \text{ cm}^3 \text{ g}^{-1}$. Intermediate values of heteroatom content and textural properties were found for PNDC-2. PNDCs are mesoporous materials, and most of their pore volume is due to narrow mesopores (of width $\sim 3 - 4 \text{ nm}$) at the levels of 99, 78 and 89 % for PNDC-1, PNDC-2 and PNDC-3, respectively.

The electrochemical performance of electrodes composed of the PNDC, carbon black and PTFE (90:5:5 wt. %) was evaluated in a three-electrode cell using either 1 M H_2SO_4 or 6 M KOH as electrolytes. The CV curves of all materials in the acidic medium revealed the typical peaks associated with redox reactions. At 5 mV s^{-1} , the calculated C_e for PNDC-2 and PNDC-3 was 272 and 246 F g^{-1} and, despite its low surface area, PNDC-1 exhibited a capacitance of 172 F g^{-1} mainly due to pseudocapacitance contributions. As expected, C_e decreased for higher scan rates. A faster drop in capacitance was observed for PNDC-2 than for PNDC-3. At 100 mV s^{-1} , PNDC-2 lost 30 % of its capacitance, while PNDC-3 lost only 12 %. The higher content of heteroatoms of PNDC-2, compared to PNDC-3, implies that at low scan rates, the contributions of pseudocapacitance are larger. However, at faster rates, redox reactions no longer occur, which reduces the performance of the material. On the other hand, the more stable performance of PNDC-3 is explained by the strong presence of mesopores and low content of heteroatoms. Thus, for this material, the charge is mainly stored by an EDL mechanism that is not affected by an increase in the scan rate because the mesopores facilitate the diffusion of ions. In the alkaline medium, PNDC-3 exhibited behavior similar to that in acidic medium. However, lower values of C_e were reached. Since pseudocapacitance has a minor contribution to charge storage in PNDC-3, the decrease in capacitance might be caused by the larger size and lower mobility of ions in KOH, compared to those in H_2SO_4 (see Table 1.1). PNDC-2 exhibited the best performance of the series across the range of scan rates, attributed to a

combination of sufficiently high surface area, pore volume and pseudocapacitance contribution of the surface functionalities that are reactive in alkaline media. Subsequent studies have extended this synthesis method to produce PNDCs from aminated quebracho tannin⁸¹ and Si- and P-doped carbons from quebracho tannin.¹²⁸ In both studies, behaviors and values of capacitance similar to those detailed above were found.

1.6.2.4 Hard-templating

OMCs have been produced by hard-templating using mimosa tannin and other tannin-related molecules such as phloroglucinol, gallic acid and catechin.¹⁰⁰ SBA-15 silica template was synthesized using a mixture of tetraethyl orthosilicate (TEOS), Pluronic® P123, HCl and water (molar ratio 1:0.017:6.04:145.8) that was stirred at 40 °C for 4 h and aged at 125 °C for 72 h. The product, recovered by filtration, was heat-treated in air at 550 °C for 6 h. An ethanol solution of the corresponding precursor (0.01 mol/40 mL) was added to the SBA-15, previously degassed under vacuum (150 °C, 2 h). Ethanol was evaporated under vacuum and, if necessary, the obtained solid was washed with deionized water to eliminate the excess of precursor deposited on the silica particles. These composites were carbonized under nitrogen flow according to a two-step temperature program: heating from room temperature to 100 °C (1 °C min⁻¹) and holding the temperature for 2 h to remove moisture and polymerize the precursors, then heating up to 900 °C (2 °C min⁻¹) and holding the temperature for 1 h. The template was removed from the carbonized composites with HF, washed with deionized water and finally dried at 80 °C for 12 h. The OMCs were labeled according to their precursors as TanC, PhC, GaC and CatC for tannin, phloroglucinol, gallic acid and catechin, respectively.

Figure 1.11a shows the schematic synthesis process and TEM images of the produced OMCs. TEM images revealed some discontinuities in the structure for CatC and TanC, indicating that catechin and mimosa tannin permeated the template heterogeneously. The large size of these molecules could block some of the pores, preventing the complete filling of the template and resulting in the gaps observed. Small-angle XRD measurements revealed that all materials exhibited a structure in the *p6mm* space group (2D hexagonal) and that the long-range order decreased as the size of the precursor molecule increased, in agreement with TEM results. Nevertheless, TanC had the advantage of achieving the highest carbon yield (80 %) among the carbon precursors used for this study. The textural characterization showed that all the OMCs exhibited BET surface areas of ~1 000 m² g⁻¹ and total pore volumes higher than 0.87 cm³ g⁻¹,

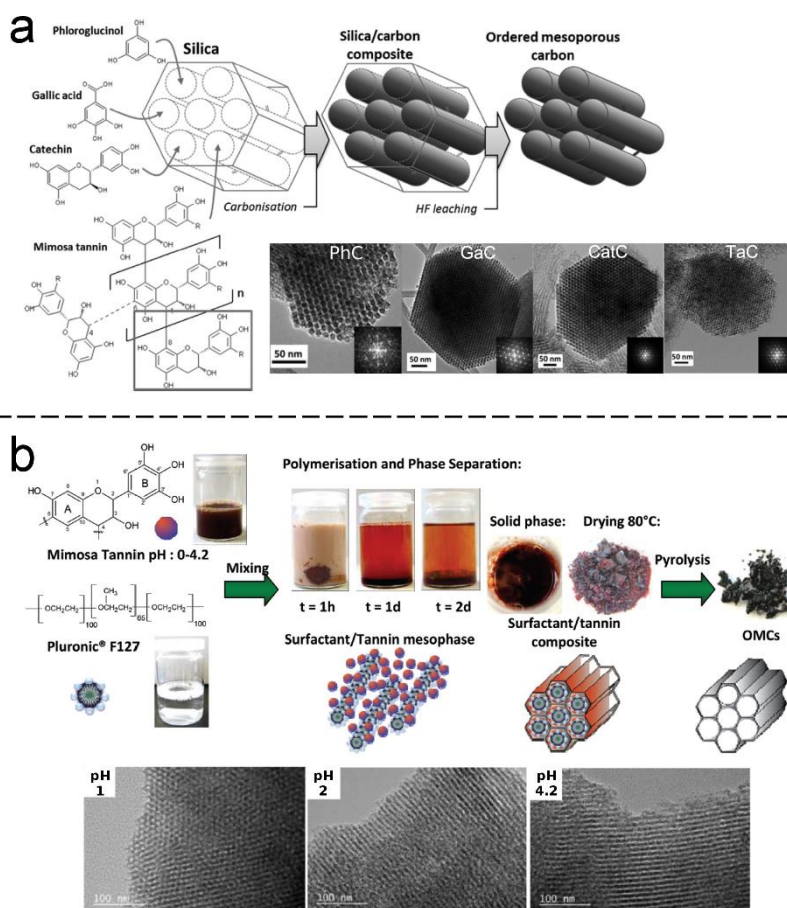


Figure 1.11. Synthesis of OMCs from mimosa tannin by (a) hard-templating, also carried out using other biomass-derived phenolic molecules; and soft-templating through (b) phase separation [Adapted from Sánchez-Sánchez et al. (2017)¹⁰⁰ and Braghiroli et al. (2016)⁷⁸].

of which 75 – 87 % came from mesopores. Chemical characterization by elemental analysis and XPS revealed oxygen as the main heteroatom in the material, which was expected given its abundance in the precursor molecules.

The electrochemical performance was evaluated in 1 M H₂SO₄. CV tests were carried out in a three-electrode cell while GCD and EIS measurements were done in a two-electrode cell. The electrodes, prepared by mixing the OMC, carbon black and PTFE (85:5:10 wt. %), were spread onto graphite foil and pressed at 5 MPa. Rectangular CV curves were observed up to a scan rate of 100 mV s⁻¹. At 0.5 mV s⁻¹ indicating SC behavior, C_e reached values higher than 200 F g⁻¹, which are in the same range of other carbons with similar textural properties but that required additional oxidation post-treatments.^{129,130} GCD tests led to quasi-triangular curves whose slight curvature suggests the occurrence of redox reactions due to the presence of oxygen on the surface. For both CV and GCD tests, as the charging rate increased (scan rate or applied

current), C_e decreased. In particular, TanC presented a capacitance retention of 42 % at 100 mV s^{-1} and 51 % at 12 A g^{-1} , higher than the ~30 % retention reported for the pine tannin-derived HTC carbons described above and tested under similar conditions.¹²⁵ The enhanced performance of OMCs as electrodes for SCs confirms the beneficial role of a hierarchical porous structure as a means of improving ion diffusion in the carbon material.

1.6.2.5 Soft-templating

Mimosa tannin was successfully used as precursor to produce OMCs by an easy and simple phase-separation method.⁷⁸ The synthesis only required the mixing, at room temperature, of two solutions: one of mimosa tannin, the other of Pluronic® F127. Immediately after mixing, a phase-separation occurred and after two days, complete sedimentation of the resultant mesophase was observed. The recovered mesophase was dried at 80 °C and carbonized at temperatures ranging from 400 to 900 °C. The pH of the tannin solution was varied from 0 to 4.2 but no significant changes in the carbon yield or the porosity were observed by modifying this parameter. The synthesis process is shown in Figure 1.11b, and TEM images of OMCs obtained for different pH values are presented. Thermogravimetric analysis showed that the Pluronic® F127 degrades at 400 °C, so carbonization at higher temperatures is required to remove it completely from the material. Higher temperature treatments resulted in more developed microporosity and consequently higher surface areas: a maximum of ~700 $m^2 g^{-1}$ BET area was reached. These values of surface area are ~200 $m^2 g^{-1}$ higher than those obtained from an EISA method also using mimosa tannin as precursor and carbonizing the mesophase at a maximum temperature of 850 °C.¹¹³

Some modifications to the phase-separation method were made in a following study that also investigated the effect of the assembly temperature.¹³¹ The pH was varied from 1 to 4.5 and the assembly temperature ranged from 10 to 30 °C. The mixed tannin/F127 solutions were kept at a constant assembly temperature for 72 h, and then they remained at room temperature for 5 days until complete phase-separation. The retrieved resins were dried at 60 °C and carbonized in two consecutive steps: increasing the temperature up to 400 °C, holding it for 4 h, and then heating until 900 °C and holding for 1 h. In agreement with the previous work of Braghiroli et al.,⁷⁸ it was found that for a fixed temperature, the pH did not change considerably the porous texture. On the contrary, for a given pH, an effect of the assembly temperature was observed, where the greatest change occurred at pH 3 after increasing the temperature from 20

to 30 °C. The solution of pH 3 assembled at 30 °C gave the carbon material, called F3/30, having the highest values of surface area and micro- and mesopore volumes, 750 m² g⁻¹, 0.24 and 0.49 cm³ g⁻¹, respectively. Therefore, F3/30 was selected for CO₂ activation to improve its porous texture further.

As expected, for the resultant activated carbon, labeled C3/30, an increased surface area (~1 100 m² g⁻¹) and a widening of pores were observed. Three- and two-electrode cells were used for its electrochemical characterization, using 2 M H₂SO₄ as electrolyte and electrodes composed of a mixture of the studied carbon, carbon black and PTFE (85:5:10 wt. %). It was found that the main mechanism of storage of energy was the EDL since the contribution of pseudocapacitance from heteroatoms was negligible. In addition, CV and GCD tests showed that the activation process increased the capacitance of the material by 1.5 times, probably due to the widening and opening of previously blocked pores, which resulted in improved connectivity of the pore network and surface accessibility to electrolyte ions. Even more, the electrochemical tests showed that the rate capabilities of C3/30 were comparable to those measured for the hard-templated TanC obtained from the same precursor, mimosa tannin, but through a less eco-friendly synthesis method,¹⁰⁰ thus showing the advantage of the soft-template method.

Table 1.3. Summary of synthesis methods, properties and electrochemical performance of tannin-derived carbon materials.

Tannin precursor / Synthesis method	Carbon material	Activation / Doping	BET area (m ² g ⁻¹)	Cell type	Electrolyte	Potential window (V)	C _e (F g ⁻¹)	Ref.
Mimosa / Sol-gel	Cryo-CGs	--- / ---	399 – 1 420	T	4 M H ₂ SO ₄	1.0	30 – 109, at 2 mV s ⁻¹	123
Mimosa / HTC	CMSs and CG-like	--- / N, O	442 – 684	T	4 M H ₂ SO ₄	1.0	181 – 322, at 2 mV s ⁻¹	67
Mimosa / HTC	Aero-, cryo- and xero-CGs	--- / N, O	496 – 864	T	4 M H ₂ SO ₄	1.0	231 – 388, at 2 mV s ⁻¹	94
Pine / HTC	CMSs and CG-like	--- / N, O	80 – 652	3-e 2-e	1 M H ₂ SO ₄	0.9	114 – 321, at 0.5 mV s ⁻¹ 112 – 258, at 0.1 A g ⁻¹	125
Quebracho / Microwave-assisted	MCs	--- / P, N	113 – 855	3-e	1 M H ₂ SO ₄ 6 M KOH	0.8	172 – 272, at 5 mVs ⁻¹ 176 – 236, at 5 mVs ⁻¹	127
Mimosa / Hard-templating	OMCs	---/ ---	1006	3-e 2-e	1 M H ₂ SO ₄	0.8	~250, at 0.5 mVs ⁻¹ ~196, at 0.1 A g ⁻¹	100
Mimosa / Phase separation	OMCs	CO ₂ / ---	563 – 1137	3-e 2-e	2 M H ₂ SO ₄	0.8	158 – 286, at 0.5 mV s ⁻¹ Up to 244, at 0.1 A g ⁻¹	131

C_e: specific electrode capacitance; HTC: hydrothermal carbonization; CGs: carbon gels; CMSs: carbon microspheres; MCs: mesoporous carbons; OMCs: ordered mesoporous carbons; T: T-type cell; 3-e: three-electrode cell; 2-e: two-electrode cell.

1.7 Summary and objective of the thesis

SCs are devices with high power outputs, rate capability, cyclability and long lifetimes. However, the amount of stored energy in SCs is lower than that found in batteries. In this sense, research in recent decades has focused on the development of new materials that can improve SC performance, not only by increasing the storage capacity but also by increasing the rate capability and the long-term stability.

Porous carbons have proven to be adequate materials for SC electrodes and, indeed, ACs are already widely used in commercial devices. Multiple synthesis methods have been developed to control the textural and chemical properties of porous carbons; in particular, templated carbons, such as OMCs, are promising electrode materials because they can be produced with different morphologies, high surface area and adjusted hierarchical porosity. The possibility of tuning the pore size is of significant importance as it allows full accessibility of the electrolyte into the material, while the hierarchical structure provides channels facilitating the diffusion of ions towards the smallest accessible pores. The modification of the surface chemistry of porous carbons presents another route to increase SC performance, and doping with oxygen, nitrogen or other heteroatoms can induce redox reactions that increase the energy stored in the device. Even if all the surface functionalities do not always induce redox reactions, doping can also improve other characteristics of the material such as electrical conductivity, wettability or stability.

Besides, the quest for environmentally friendly technologies has pushed research to find substitutes for synthetic and hazardous molecules commonly used as carbon precursors or crosslinkers. Among the various biosourced precursors, tannins are excellent alternatives to petrochemical carbon sources because of their phenolic nature. Condensed tannins have a reactivity similar to that of phenol or resorcinol, so tannins can replace them in already established synthesis methods. The autocondensation property of condensed tannins also offers the opportunity of avoiding the use of crosslinkers, which makes them suitable precursors for self-assembly methods. As described in Section 1.6.2, several studies have demonstrated the versatility of tannins to produce porous carbon materials through “green” processes reducing or even eliminating the use of toxic or hazardous substances and thus decreasing their negative environmental impact. In addition, tannins are extracted industrially and marketed on a large scale, because they are essential for the leather, wine and food industry. Therefore, they are

readily available at a low cost. Thus, the production of porous carbons from tannin will provide and add value to this precursor derived from biomass.

In general, the main disadvantages of producing advanced porous carbon materials are their complex multi-step procedures and their tedious synthesis. Therefore, the main objective of this thesis is to focus on the development and optimization of an easy and environmentally friendly procedure to produce templated mesoporous carbons from tannin. Simplifying and reducing the number of steps would reduce costs and increase scalability, resulting in the use of biosourced carbons that is more widespread in commercial SC devices.

This thesis is divided into two interconnected parts: (i) the development of the materials using mimosa tannin as carbon precursor and (ii) their characterization as electrodes for SCs. Thus, the next chapters of the thesis are organized in the following manner:

- Chapter 2 describes the different characterization techniques that were used throughout this study to obtain the physicochemical properties of the materials.
- Chapter 3 describes the development and optimization of an easy, green and one-pot mechanosynthesis method for the production of both ordered and disordered mesoporous carbons by water-assisted ball milling of the precursor and a surfactant.
- A deeper characterization of the porosity properties of an OMC and a disordered mesoporous carbon (DMC), is detailed in Chapter 4, in order to gain more insights into the connectivity of the mesopore structure of such materials.
- CO₂ activation of tannin-derived OMCs and its performance as electrodes for SCs are described in Chapter 5.
- Chapter 6 presents a comparative study of the effect of the order on the CO₂ activation process and the electrochemical performance of such activated mesoporous carbons when used as electrodes for SCs.
- The electrochemical performance of KOH-activated tannin-derived OMCs is studied in Chapter 7. Results from two routes of KOH integration, impregnation and physical mixing, are compared. The performance as electrodes for SC is also compared to that of the CO₂-activated counterparts.
- Finally, the conclusions and perspectives of this study are presented.

1.8 References

1. IEA. Data and statistics. IEA <https://www.iea.org/data-and-statistics> (2019).
2. Climate change 2014: synthesis report. (Intergovernmental Panel on Climate Change, 2015).
3. Aneke, M. & Wang, M. Energy storage technologies and real life applications – A state of the art review. *Applied Energy* 179, 350–377 (2016).
4. IEA. Technology Roadmap Energy storage. 64 (2014).
5. Wang, Y., Song, Y. & Xia, Y. Electrochemical capacitors: mechanism, materials, systems, characterization and applications. *Chemical Society Reviews* 45, 5925–5950 (2016).
6. González, A., Goikolea, E., Barrena, J. A. & Mysyk, R. Review on supercapacitors: Technologies and materials. *Renewable and Sustainable Energy Reviews* 58, 1189–1206 (2016).
7. Sharma, P. & Bhatti, T. S. A review on electrochemical double-layer capacitors. *Energy Conversion and Management* 51, 2901–2912 (2010).
8. Castro-Gutiérrez, J., Fierro, V. & Celzard, A. Energy storage in supercapacitors: focus on tannin-derived carbon electrodes. *Frontiers in Materials* 7, (2020).
9. Xie, J. et al. Puzzles and confusions in supercapacitor and battery: Theory and solutions. *Journal of Power Sources* 401, 213–223 (2018).
10. Kötz, R. & Carlen, M. Principles and applications of electrochemical capacitors. *Electrochimica Acta* 45, 2483–2498 (2000).
11. Miller, J. R. & Burke, A. F. Electrochemical Capacitors: Challenges and Opportunities for Real-World Applications. *The Electrochemical Society Interface* 5 (2008).
12. Conte, M. Supercapacitors Technical Requirements for New Applications. *Fuel Cells* 10, 806–818 (2010).
13. Gu, W. & Yushin, G. Review of nanostructured carbon materials for electrochemical capacitor applications: advantages and limitations of activated carbon, carbide-derived carbon, zeolite-templated carbon, carbon aerogels, carbon nanotubes, onion-like carbon, and graphene: Nanostructured carbon materials for electrochemical capacitor applications. *Wiley Interdisciplinary Reviews: Energy and Environment* 3, 424–473 (2014).
14. Gautham Prasad, G., Shetty, N., Thakur, S., Rakshitha & Bomme Gowda, K. B. Supercapacitor technology and its applications: a review. *IOP Conf. Ser.: Mater. Sci. Eng.* 561, 012105 (2019).
15. IOXUS Inc. Applications. IOXUS <https://ioxus.com/english/applications/> (2020).
16. Maxwell Technologies Inc. Cells - Overview. Maxwell Technologies <https://www.maxwell.com/products/ultracapacitors/cells/> (2020).
17. Sevilla, M., Diez, N., Ferrero, G. A. & Fuertes, A. B. Sustainable supercapacitor electrodes produced by the activation of biomass with sodium thiosulfate. *Energy Storage Materials* 18, 356–365 (2019).
18. Zuliani, J. E., Caguiat, J. N., Kirk, D. W. & Jia, C. Q. Considerations for consistent characterization of electrochemical double-layer capacitor performance. *Journal of Power Sources* 290, 136–143 (2015).
19. Supercapacitors: Materials, Systems, and Applications. (John Wiley & Sons, Ltd, 2013).

20. Bard, A. J. & Faulkner, L. R. *Electrochemical methods: fundamentals and applications*. (Wiley, 2001).
21. Orazem, M. E. & Tribollet, B. *Electrochemical impedance spectroscopy*. (Wiley, 2008).
22. Inamuddin, Ahmer, M. F., Asiri, A. M. & Zaidi, S. *Electrochemical Capacitors: Theory, Materials and Applications*. (Materials Research Forum LLC, 2018).
23. Zhong, C. et al. A review of electrolyte materials and compositions for electrochemical supercapacitors. *Chemical Society Reviews* 44, 7484–7539 (2015).
24. Zhai, Y. et al. Carbon Materials for Chemical Capacitive Energy Storage. *Advanced Materials* 23, 4828–4850 (2011).
25. Salinas-Torres, D., Ruiz-Rosas, R., Morallón, E. & Cazorla-Amorós, D. Strategies to Enhance the Performance of Electrochemical Capacitors Based on Carbon Materials. *Front. Mater.* 6, 115 (2019).
26. Lu, S. et al. Effect of aqueous electrolytes on the electrochemical behaviors of ordered mesoporous carbon composites after KOH activation as supercapacitors electrodes. *Journal of Electroanalytical Chemistry* 818, 58–67 (2018).
27. *CRC Handbook of Chemistry and Physics*. (CRC Press, 2004).
28. Sevilla, M. & Mokaya, R. Energy storage applications of activated carbons: supercapacitors and hydrogen storage. *Energy Environ. Sci.* 7, 1250–1280 (2014).
29. Frackowiak, E. Carbon materials for supercapacitor application. *Physical Chemistry Chemical Physics* 9, 1774 (2007).
30. Inagaki, M., Konno, H. & Tanaike, O. Carbon materials for electrochemical capacitors. *Journal of Power Sources* 195, 7880–7903 (2010).
31. Paraknowitsch, J. P. & Thomas, A. Doping carbons beyond nitrogen: an overview of advanced heteroatom doped carbons with boron, sulphur and phosphorus for energy applications. *Energy & Environmental Science* 6, 2839 (2013).
32. Zhao, W., Fierro, V., Fernández-Huerta, N., Izquierdo, M. T. & Celzard, A. Impact of synthesis conditions of KOH activated carbons on their hydrogen storage capacities. *International Journal of Hydrogen Energy* 37, 14278–14284 (2012).
33. Tellez-Juárez, M. C. et al. Hydrogen storage in activated carbons produced from coals of different ranks: Effect of oxygen content. *International Journal of Hydrogen Energy* 39, 4996–5002 (2014).
34. González-García, P. Activated carbon from lignocellulosics precursors: A review of the synthesis methods, characterization techniques and applications. *Renewable and Sustainable Energy Reviews* 82, 1393–1414 (2018).
35. Cha, J. S. et al. Production and utilization of biochar: A review. *Journal of Industrial and Engineering Chemistry* 40, 1–15 (2016).
36. Selmi, T. et al. Tetracycline removal with activated carbons produced by hydrothermal carbonisation of *Agave americana* fibres and mimosa tannin. *Industrial Crops and Products* 115, 146–157 (2018).
37. Mbarki, F. et al. Hydrothermal pre-treatment, an efficient tool to improve activated carbon performances. *Industrial Crops and Products* 140, 111717 (2019).
38. Fierro, V., Torné-Fernández, V., Montané, D. & Celzard, A. Study of the decomposition of kraft lignin impregnated with orthophosphoric acid. *Thermochimica Acta* 433, 142–148 (2005).

39. Fierro, V., Muñiz, G., Basta, A. H., El-Saied, H. & Celzard, A. Rice straw as precursor of activated carbons: Activation with ortho-phosphoric acid. *Journal of Hazardous Materials* 181, 27–34 (2010).
40. Fierro, V., Torné-Fernández, V. & Celzard, A. Methodical study of the chemical activation of Kraft lignin with KOH and NaOH. *Microporous and Mesoporous Materials* 101, 419–431 (2007).
41. Basta, A. H., Fierro, V., El-Saied, H. & Celzard, A. 2-Steps KOH activation of rice straw: An efficient method for preparing high-performance activated carbons. *Bioresource Technology* 100, 3941–3947 (2009).
42. Acosta, R. et al. Adsorption of Bisphenol A on KOH-activated tyre pyrolysis char. *Journal of Environmental Chemical Engineering* 6, 823–833 (2018).
43. Fuertes, A. B., Ferrero, G. A., Díez, N. & Sevilla, M. A Green Route to High-Surface Area Carbons by Chemical Activation of Biomass-Based Products with Sodium Thiosulfate. *ACS Sustainable Chem. Eng.* 6, 16323–16331 (2018).
44. Díez, N., Ferrero, G. A., Sevilla, M. & Fuertes, A. B. A sustainable approach to hierarchically porous carbons from tannic acid and their utilization in supercapacitive energy storage systems. *J. Mater. Chem. A* 7, 14280–14290 (2019).
45. Lee, J., Kim, J. & Hyeon, T. Recent Progress in the Synthesis of Porous Carbon Materials. *Advanced Materials* 18, 2073–2094 (2006).
46. Mostazo-López, M. J. et al. Ultraporous nitrogen-doped zeolite-templated carbon for high power density aqueous-based supercapacitors. *Carbon* 129, 510–519 (2018).
47. Grishchko, L. I. et al. Biosourced, highly porous, carbon xerogel microspheres. *RSC Advances* 6, 65698–65708 (2016).
48. Ciszewski, M., Koszorek, A., Radko, T., Szatkowski, P. & Janas, D. Review of the Selected Carbon-Based Materials for Symmetric Supercapacitor Application. *Journal of Elec Materi* 48, 717–744 (2019).
49. Braghiroli, Amaral-Labat, Boss, Lacoste & Pizzi. Tannin Gels and Their Carbon Derivatives: A Review. *Biomolecules* 9, 587 (2019).
50. Szczurek, A. et al. The use of tannin to prepare carbon gels. Part I: Carbon aerogels. *Carbon* 49, 2773–2784 (2011).
51. Szczurek, A., Amaral-Labat, G., Fierro, V., Pizzi, A. & Celzard, A. The use of tannin to prepare carbon gels. Part II. Carbon cryogels. *Carbon* 49, 2785–2794 (2011).
52. Feinle, A., Elsaesser, M. S. & Hüsing, N. Sol–gel synthesis of monolithic materials with hierarchical porosity. *Chem. Soc. Rev.* 45, 3377–3399 (2016).
53. Pandolfo, A. G. & Hollenkamp, A. F. Carbon properties and their role in supercapacitors. *Journal of Power Sources* 157, 11–27 (2006).
54. Zhang, L. L. & Zhao, X. S. Carbon-based materials as supercapacitor electrodes. *Chemical Society Reviews* 38, 2520 (2009).
55. Ra, E. J., Raymundo-Piñero, E., Lee, Y. H. & Béguin, F. High power supercapacitors using polyacrylonitrile-based carbon nanofiber paper. *Carbon* 47, 2984–2992 (2009).
56. Kim, Y.-S., Kumar, K., Fisher, F. T. & Yang, E.-H. Out-of-plane growth of CNTs on graphene for supercapacitor applications. *Nanotechnology* 23, 015301 (2012).
57. Kim, T.-Y., Lee, K.-R., Eun, K. Y. & Oh, K.-H. Carbon nanotube growth enhanced by nitrogen incorporation. *Chemical Physics Letters* 372, 603–607 (2003).

58. Gao, L. et al. Growth of aligned carbon nanotube arrays on metallic substrate and its application to supercapacitors. *Solid State Communications* 146, 380–383 (2008).
59. Zheng, W. et al. Nanocellulose-mediated hybrid polyaniline electrodes for high performance flexible supercapacitors. *J. Mater. Chem. A* 5, 12969–12976 (2017).
60. Frackowiak, E. & Beguin, F. Carbon materials for the electrochemical storage of energy in capacitors. *Carbon* 39, 937–950 (2001).
61. Liu, J., Wickramaratne, N. P., Qiao, S. Z. & Jaroniec, M. Molecular-based design and emerging applications of nanoporous carbon spheres. *Nature Materials* 14, 763–774 (2015).
62. Braghiroli, F. L. et al. Nitrogen-doped carbon materials produced from hydrothermally treated tannin. *Carbon* 50, 5411–5420 (2012).
63. Chen, A. et al. Thin-walled, mesoporous and nitrogen-doped hollow carbon spheres using ionic liquids as precursors. *J. Mater. Chem. A* 1, 1045–1047 (2013).
64. Fang, Y. et al. A Low-Concentration Hydrothermal Synthesis of Biocompatible Ordered Mesoporous Carbon Nanospheres with Tunable and Uniform Size. *Angewandte Chemie International Edition* 49, 7987–7991 (2010).
65. Liu, J. et al. A facile soft-template synthesis of mesoporous polymeric and carbonaceous nanospheres. *Nature Communications* 4, (2013).
66. Li, S., Pasc, A., Fierro, V. & Celzard, A. Hollow carbon spheres, synthesis and applications – a review. *Journal of Materials Chemistry A* 4, 12686–12713 (2016).
67. Braghiroli, F. L. et al. Electrochemical performances of hydrothermal tannin-based carbons doped with nitrogen. *Industrial Crops and Products* 70, 332–340 (2015).
68. Ferrero, G. A., Fuertes, A. B. & Sevilla, M. N-doped microporous carbon microspheres for high volumetric performance supercapacitors. *Electrochimica Acta* 168, 320–329 (2015).
69. Lim, E., Jo, C. & Lee, J. A mini review of designed mesoporous materials for energy-storage applications: from electric double-layer capacitors to hybrid supercapacitors. *Nanoscale* 8, 7827–7833 (2016).
70. Sánchez-Sánchez, A., Fierro, V., Izquierdo, M. T. & Celzard, A. Functionalized, hierarchical and ordered mesoporous carbons for high-performance supercapacitors. *J. Mater. Chem. A* 4, 6140–6148 (2016).
71. Lang, J.-W., Yan, X.-B., Yuan, X.-Y., Yang, J. & Xue, Q.-J. Study on the electrochemical properties of cubic ordered mesoporous carbon for supercapacitors. *Journal of Power Sources* 196, 10472–10478 (2011).
72. Meng, Y. et al. Ordered Mesoporous Polymers and Homologous Carbon Frameworks: Amphiphilic Surfactant Templating and Direct Transformation. *Angew. Chem. Int. Ed.* 44, 7053–7059 (2005).
73. Li, M. & Xue, J. Ordered mesoporous carbon nanoparticles with well-controlled morphologies from sphere to rod via a soft-template route. *Journal of Colloid and Interface Science* 377, 169–175 (2012).
74. Liu, D. et al. Facile preparation of hierarchically porous carbon using diatomite as both template and catalyst and methylene blue adsorption of carbon products. *Journal of Colloid and Interface Science* 388, 176–184 (2012).

75. Xia, Y. et al. Biotemplated fabrication of hierarchically porous NiO/C composite from lotus pollen grains for lithium-ion batteries. *Journal of Materials Chemistry* 22, 9209–9215 (2012).
76. Gao, Z., Zhang, Y., Song, N. & Li, X. Biomass-derived renewable carbon materials for electrochemical energy storage. *Materials Research Letters* 5, 69–88 (2017).
77. Libbrecht, W., Verberckmoes, A., Thybaut, J. W., Van Der Voort, P. & De Clercq, J. Soft templated mesoporous carbons: Tuning the porosity for the adsorption of large organic pollutants. *Carbon* 116, 528–546 (2017).
78. Braghiroli, F. L., Fierro, V., Parmentier, J., Pasc, A. & Celzard, A. Easy and eco-friendly synthesis of ordered mesoporous carbons by self-assembly of tannin with a block copolymer. *Green Chem.* 18, 3265–3271 (2016).
79. Wickramaratne, N. P. & Jaroniec, M. Phenolic resin-based carbons with ultra-large mesopores prepared in the presence of poly(ethylene oxide)–poly(butylene oxide)–poly(ethylene oxide) triblock copolymer and trimethyl benzene. *Carbon* 51, 45–51 (2013).
80. Meng, Y. et al. A Family of Highly Ordered Mesoporous Polymer Resin and Carbon Structures from Organic–Organic Self-Assembly. *Chemistry of Materials* 18, 4447–4464 (2006).
81. Bairi, V. G., Nasini, U. B., Kumar Ramasahayam, S., Bourdo, S. E. & Viswanathan, T. Electrocatalytic and supercapacitor performance of Phosphorous and Nitrogen co-doped Porous Carbons synthesized from Aminated Tannins. *Electrochimica Acta* 182, 987–994 (2015).
82. Chen, H. et al. Functional Biomass Carbons with Hierarchical Porous Structure for Supercapacitor Electrode Materials. *Electrochimica Acta* 180, 241–251 (2015).
83. Elmouwahidi, A. et al. Activated carbons from agricultural waste solvothermally doped with sulphur as electrodes for supercapacitors. *Chemical Engineering Journal* 334, 1835–1841 (2018).
84. Chen, C.-M. et al. Hierarchically aminated graphene honeycombs for electrochemical capacitive energy storage. *J. Mater. Chem.* 22, 14076 (2012).
85. Deng, Y., Xie, Y., Zou, K. & Ji, X. Review on recent advances in nitrogen-doped carbons: preparations and applications in supercapacitors. *Journal of Materials Chemistry A* 4, 1144–1173 (2016).
86. Hulicova-Jurcakova, D., Seredych, M., Lu, G. Q. & Bandosz, T. J. Combined Effect of Nitrogen- and Oxygen-Containing Functional Groups of Microporous Activated Carbon on its Electrochemical Performance in Supercapacitors. *Advanced Functional Materials* 19, 438–447 (2009).
87. Zuliani, J. E., Tong, S., Jia, C. Q. & Kirk, D. W. Contribution of surface oxygen groups to the measured capacitance of porous carbon supercapacitors. *Journal of Power Sources* 395, 271–279 (2018).
88. Inagaki, M., Toyoda, M., Soneda, Y. & Morishita, T. Nitrogen-doped carbon materials. *Carbon* 132, 104–140 (2018).
89. Raymundo-Piñero, E., Cadek, M. & Béguin, F. Tuning Carbon Materials for Supercapacitors by Direct Pyrolysis of Seaweeds. *Advanced Functional Materials* 19, 1032–1039 (2009).

90. Wang, J.-G. et al. One-pot synthesis of nitrogen-doped ordered mesoporous carbon spheres for high-rate and long-cycle life supercapacitors. *Carbon* 127, 85–92 (2018).
91. Ayala, P., Arenal, R., Rummeli, M., Rubio, A. & Pichler, T. The doping of carbon nanotubes with nitrogen and their potential applications. *Carbon* 48, 575–586 (2010).
92. Moussa, G., Hajjar-Garreau, S., Taberna, P.-L., Simon, P. & Matei Ghimbeu, C. Eco-Friendly Synthesis of Nitrogen-Doped Mesoporous Carbon for Supercapacitor Application. *C* 4, 20 (2018).
93. Frackowiak, E., Lota, G., Machnikowski, J., Vix-Guterl, C. & Béguin, F. Optimisation of supercapacitors using carbons with controlled nanotexture and nitrogen content. *Electrochimica Acta* 51, 2209–2214 (2006).
94. Braghiroli, F. L. et al. Hydrothermally treated aminated tannin as precursor of N-doped carbon gels for supercapacitors. *Carbon* 90, 63–74 (2015).
95. Zhu, J. et al. Nitrogen-enriched, ordered mesoporous carbons for potential electrochemical energy storage. *Journal of Materials Chemistry A* 4, 2286–2292 (2016).
96. Li, J.-G., Ho, Y.-F., Ahmed, M. M. M., Liang, H.-C. & Kuo, S.-W. Mesoporous Carbons Templated by PEO-PCL Block Copolymers as Electrode Materials for Supercapacitors. *Chemistry - A European Journal* 25, 10456–10463 (2019).
97. Tiruye, G. A. et al. Functional porous carbon nanospheres from sustainable precursors for high performance supercapacitors. *J. Mater. Chem. A* 5, 16263–16272 (2017).
98. Hu, L. et al. A scalable strategy for carbon derived from complex six-membered ring-like tannin on glass fiber for 1D/2D flexible all solid state supercapacitors. *Journal of Electroanalytical Chemistry* 856, 113693 (2020).
99. Vix-Guterl, C. et al. Electrochemical energy storage in ordered porous carbon materials. *Carbon* 43, 1293–1302 (2005).
100. Sanchez-Sanchez, A. et al. Excellent electrochemical performances of nanocast ordered mesoporous carbons based on tannin-related polyphenols as supercapacitor electrodes. *Journal of Power Sources* 344, 15–24 (2017).
101. Feng, S. et al. Hydrothermal synthesis of ordered mesoporous carbons from a biomass-derived precursor for electrochemical capacitors. *Nanoscale* 6, 14657–14661 (2014).
102. Herou, S. et al. Ordered mesoporous carbons from lignin: a new class of biobased electrodes for supercapacitors. *Green Chem.* 21, 550–559 (2019).
103. SilvaTeam. All about tannins. <https://www.silvateam.com/en/who-we-are/extracts-nature/all-about-tannins.html> (2018).
104. CAPPEQ. Tannin, a history close to your own. Tannins <https://www.tannins.org/history-of-tannin/> (2019).
105. Fierro, V., Sánchez-Sánchez, A. & Celzard, A. Tannins as Precursors of Supercapacitor Electrodes. in *Sustainable Energy Technologies* (eds. Rincón-Mejía, E. & de las Heras, A.) 201–228 (CRC Press, 2018).
106. CAPPEQ. Tannin: One substance, different applications. Tannins <https://www.tannins.org/applications/> (2019).
107. de Hoyos-Martínez, P. L., Merle, J., Labidi, J. & Charrier – El Bouhtoury, F. Tannins extraction: A key point for their valorization and cleaner production. *Journal of Cleaner Production* 206, 1138–1155 (2019).

108. CAPPEQ. How to extract tannin? Tannins <https://www.tannins.org/how-to-extract-tannin/> (2019).
109. Tondi, G. & Petutschnigg, A. Middle infrared (ATR FT-MIR) characterization of industrial tannin extracts. *Industrial Crops and Products* 65, 422–428 (2015).
110. Pizzi, A. Condensed tannins for adhesives. *Industrial & Engineering Chemistry Product Research and Development* 21, 359–369 (1982).
111. Shirmohammadli, Y., Efhamisisi, D. & Pizzi, A. Tannins as a sustainable raw material for green chemistry: A review. *Industrial Crops and Products* 126, 316–332 (2018).
112. Haslam, E. Vegetable tannins – Lessons of a phytochemical lifetime. *Phytochemistry* 68, 2713–2721 (2007).
113. Schlienger, S., Graff, A.-L., Celzard, A. & Parmentier, J. Direct synthesis of ordered mesoporous polymer and carbon materials by a biosourced precursor. *Green Chem.* 14, 313–316 (2012).
114. Kim, S. et al. PubChem 2019 update: improved access to chemical data. *Nucleic Acids Research* 47, (2018).
115. National Institute for Occupational Safety and Health. NIOSH Pocket Guide to Chemical Hazards. <https://www.cdc.gov/niosh/npg/npgsyn-a.html#> (2018).
116. Tondi, G., Fierro, V., Pizzi, A. & Celzard, A. Tannin-based carbon foams. *Carbon* 47, 1480–1492 (2009).
117. Jana, P., Fierro, V., Pizzi, A. & Celzard, A. Biomass-derived, thermally conducting, carbon foams for seasonal thermal storage. *Biomass and Bioenergy* 67, 312–318 (2014).
118. Szczurek, A., Fierro, V., Pizzi, A. & Celzard, A. Emulsion-templated porous carbon monoliths derived from tannins. *Carbon* 74, 352–362 (2014).
119. Lacoste, C. et al. Bioresourced pine tannin/furanic foams with glyoxal and glutaraldehyde. *Industrial Crops and Products* 45, 401–405 (2013).
120. Delgado-Sánchez, C., Santiago-Medina, F., Fierro, V., Pizzi, A. & Celzard, A. Optimisation of “green” tannin-furanic foams for thermal insulation by experimental design. *Materials & Design* 139, 7–15 (2018).
121. Amaral-Labat, G. et al. Tannin-based xerogels with distinctive porous structures. *Biomass and Bioenergy* 56, 437–445 (2013).
122. Szczurek, A., Fierro, V., Pizzi, A. & Celzard, A. Mayonnaise, whipped cream and meringue, a new carbon cuisine. *Carbon* 58, 245–248 (2013).
123. Amaral-Labat, G. et al. Pore structure and electrochemical performances of tannin-based carbon cryogels. *Biomass and Bioenergy* 39, 274–282 (2012).
124. Braghiroli, F. L. et al. High surface – Highly N-doped carbons from hydrothermally treated tannin. *Industrial Crops and Products* 66, 282–290 (2015).
125. Sanchez-Sanchez, A. et al. Outstanding electrochemical performance of highly N- and O-doped carbons derived from pine tannin. *Green Chemistry* 19, 2653–2665 (2017).
126. Gopal Bairi, V. et al. Microwave-Assisted Synthesis of Nitrogen and Phosphorus Co-Doped Mesoporous Carbon and Their Potential Application in Alkaline Fuel Cells. *sci adv mat* 5, 1275–1281 (2013).
127. Nasini, U. B. et al. Phosphorous and nitrogen dual heteroatom doped mesoporous carbon synthesized via microwave method for supercapacitor application. *Journal of Power Sources* 250, 257–265 (2014).

128. Ramasahayam, S. K., Nasini, U. B., Shaikh, A. U. & Viswanathan, T. Novel tannin-based Si, P co-doped carbon for supercapacitor applications. *Journal of Power Sources* 275, 835–844 (2015).
129. Jurewicz, K. et al. Capacitance properties of ordered porous carbon materials prepared by a templating procedure. *Journal of Physics and Chemistry of Solids* 65, 287–293 (2004).
130. Tanaka, S. et al. Surface modification of soft-templated ordered mesoporous carbon for electrochemical supercapacitors. *Microporous and Mesoporous Materials* 217, 141–149 (2015).
131. Sanchez-Sanchez, A. et al. Ordered mesoporous carbons obtained by soft-templating of tannin in mild conditions. *Microporous and Mesoporous Materials* 270, 127–139 (2018).

Chapter 2

Characterization techniques

Adequate characterization of the synthesized materials is of the utmost importance in order to understand their behavior as electrodes for SCs. As detailed in Chapter 1, electrochemical performance is deeply related to the physicochemical properties of materials, such as the surface area, the morphology and the pore volume, size, and distribution, as well as chemical properties such as the presence of heteroatoms in the carbon structure. The following sections describe the characterization techniques used to study the physicochemical properties of the materials.

2.1 Transmission electron microscopy

The mesoporous structure of carbon materials can be studied by transmission electron microscopy (TEM) images, allowing to observe whether it is of disordered or ordered in nature. The operating principle of a transmission electron microscope is illustrated in Figure 2.1, it is based on the interaction of a thin layer of the material under study and an electron beam, where the changes of phase or the scattering of the electron wave are used to obtain the images.¹ The image is reconstructed employing electromagnetic lenses that focus the transmitted beam onto a screen; the diffraction mode is used to obtain information about the crystalline structure and orientation in the selected region.

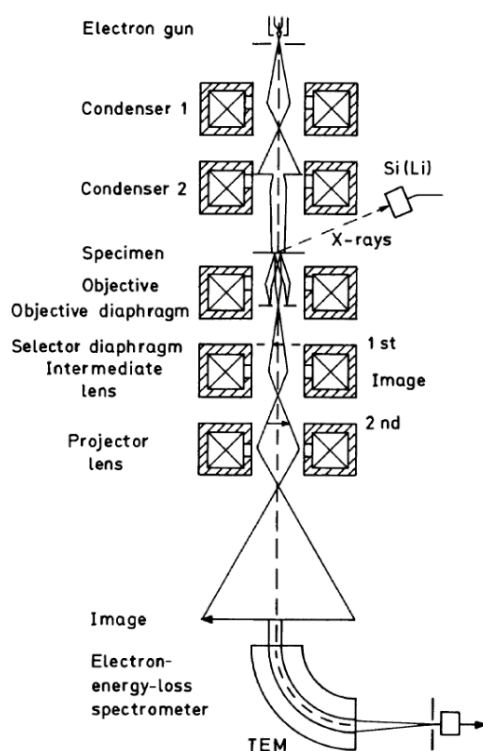


Figure 2.1. Schematic of a transmission electron microscope. [Adapted from Reimer and Kohl (2008)¹]

TEM images were acquired with a JEM-ARM 200F Cold FEG TEM/STEM from JEOL, operated at 200 kV and using a spherical aberration (Cs) probe and image correctors. For TEM observation, samples were prepared by dispersing carbon powder in ethanol using a low-power sonication bath, after which a single drop of the suspension was deposited onto a carbon-coated copper grid (200 mesh) and left to dry in air before observation.

2.2 Physisorption of gas

The physisorption of gas is an analytical technique that has been used for a long time to characterize the pore texture of materials; it is based on the adsorption and desorption of a probe gas on the surface of the solid material. Analysis of the measured amount of adsorbed gas as a function of the relative pressure (p/p_0) at a constant temperature, *i.e.*, the adsorption-desorption isotherms, allows assessing the porosity properties of the material.² The shape of these isotherms donates the first insights into the nature of the material's pore texture. Figure 2.2a displays the IUPAC classification for the different types of isotherms and their associated pore textures are listed in Table 2.1. The appearance of hysteresis loops, shown in Figure 2.2b, is related to the presence of meso- and/or macropores; the particular properties of the pores that give rise to the different hysteresis loops are also listed in Table 2.1.

For the carbon materials synthesized herein, N₂ at -196 °C, Ar at -186 °C and CO₂ at 0 °C isotherms were obtained with the automatic adsorption devices 3Flex, ASAP 2020 and ASAP 2420 from Micromeritics, shown in Figure 2.3a-c, or an Autosorb iQ from Quantachrome, see Figure 2.3d. The samples were degassed under vacuum before adsorption analysis for at least 48 h at 110 °C. Besides, the scanning of the hysteresis loops of N₂ isotherms was carried out using the following process:

- (i). Adsorption is recorded until the relative pressure (p/p_0) reached a value of 1, then desorption is carried out until $p/p_0 = 0.2$.
- (ii). Adsorption is again recorded up to a relative pressure lower than 1.
- (iii). Desorption is recorded down to $p/p_0 \approx 0.3 - 0.4$.
- (iv). Steps (ii) and (iii) are repeated while gradually lowering the maximum value of p/p_0 reached during adsorption in step (ii).

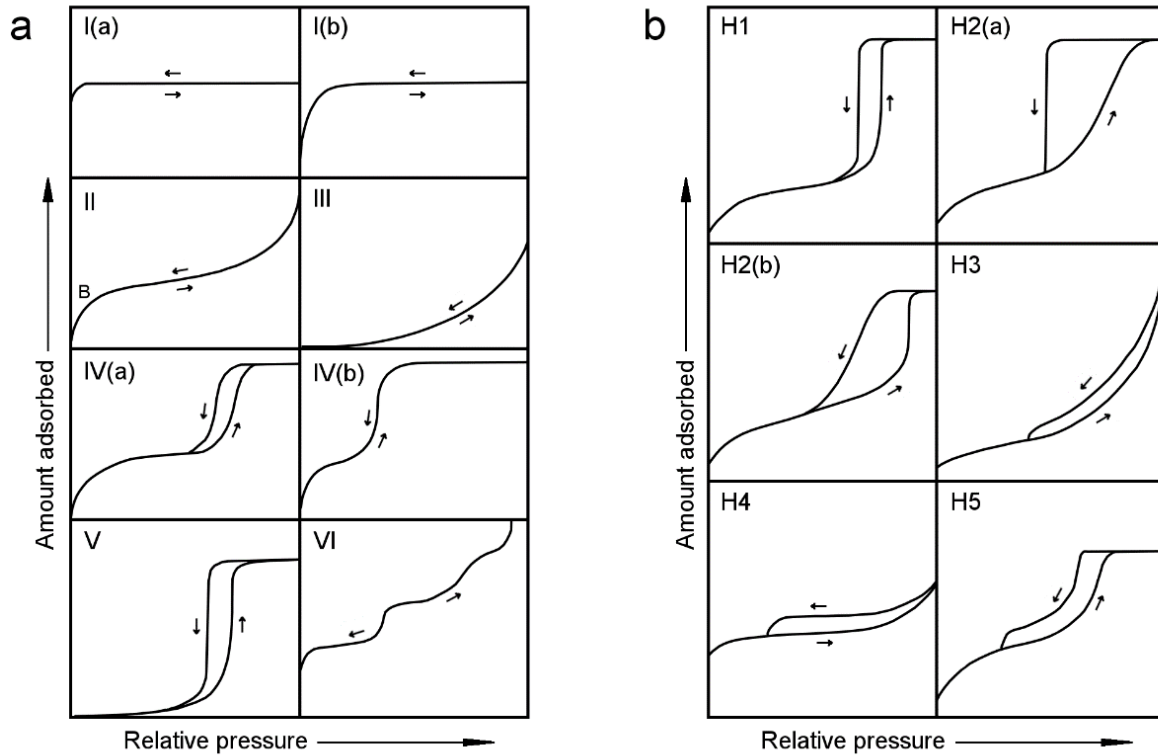


Figure 2.2. IUPAC classification of (a) isotherms and (b) hysteresis loops found in physisorption analysis. [Adapted from Thommes et al. (2015)²]

Table 2.1. Materials associated with the different types of adsorption-desorption isotherms and hysteresis loops, according to the IUPAC classification.²

Adsorption-desorption isotherms		Hysteresis loops	
Type I	(a) Microporous materials with pore size < ~1 nm (b) Materials with wider micropores and narrow mesopores, size < ~2.5 nm	H1	Narrow range of uniform mesopores or inkbottle pores with necks and cavities of similar size
Type II	Non-porous or macroporous materials. The amount of adsorbed gas seems to increase limitlessly at $p/p_0 = 1$	H2	(a) Pore blocking or cavitation induced evaporation in a network with narrow pore necks (b) Pore blocking in networks with wider pore necks
Type III	Non-porous or macroporous materials. The amount of adsorbed gas is finite at $p/p_0 = 1$.	H3	Not completely filled macropores or non-rigid aggregates of plate-like particles
Type IV	(a) Mesoporous materials. (b) Mesoporous materials with pores sizes < ~4nm	H4	Similar to H3, but with an adsorption branch being a combination of Type I and II; found in micro-mesoporous materials.
Type V	Water adsorption on hydrophobic micro- or mesoporous materials.	H5	Network with open and partially blocked mesopores
Type VI	Highly uniform non-porous materials like graphitized carbon blacks.		

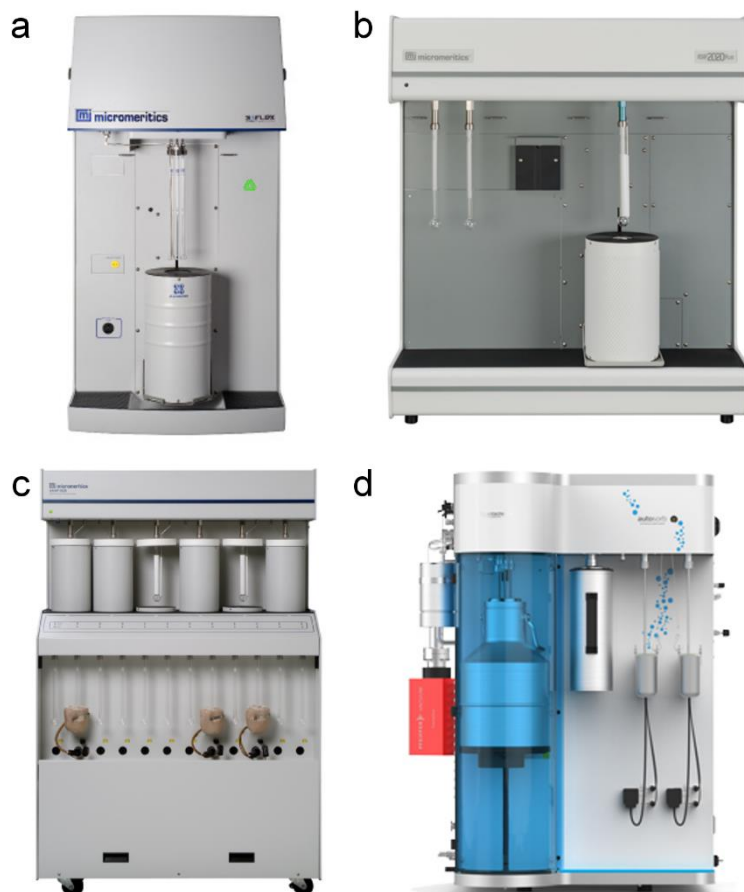


Figure 2.3. Automatic adsorption devices: (a) 3Flex, (b) ASAP 2020, and (c) ASAP 2420 from Micromeritics; and (d) Autosorb iQ from Quantachrome.

From the N_2 isotherms, it is possible to derive directly the total pore volume as the amount of adsorbed gas at $p/p_0 = 0.97$ (V_{tot,N_2}) and to estimate the area by applying the Brunauer-Emmet-Teller (BET) method (A_{BET}). This method consists of determining the monolayer capacity of the material and then, knowing the cross-sectional area of the N_2 molecule, A_{BET} can be calculated. The BET method can be applied to Type II and Type IV isotherms provided that the B point (see Figure 2.2a) is readily identified, as it is approximately equal to the monolayer capacity.^{3,4} The values of A_{BET} for all the materials synthesized in this study were calculated using the Microactive® software, provided by Micromeritics, and following the recommendations of the IUPAC² for the selection of the valid range of p/p_0 for the application of the BET method on the adsorption branch of the N_2 isotherm. However, a high presence of micropores difficult the separation of the monolayer adsorption from the multilayer adsorption and the pore filling, thus the uncertainty of A_{BET} grows.²

Different density functional theories (DFT) have been developed to circumvent the limitations of the BET. DFT models, as their name indicate, calculate the density of the adsorbed fluid in the pores based on the behavior at molecular level.^{5,6} The fluid densities in the pores constitute a theoretical set of isotherms that is expressed as a function of pressure and pore width. These isotherms are called the kernel function, which represents the system and depends on the applied adsorption model, by fitting the experimental data using the calculated kernel it is possible to determine the pore size distribution (PSD).^{6,7} The first developed DFT models relied on a local approach for the calculations and on the assumption of slit-shaped pores with ideal graphitic walls. However, newer implementations improve the DFT model by considering the non-local behavior, the heterogeneity of the carbon surface, and different pore geometries.⁵⁻⁷ Herein, PSDs were obtained by applying the 2D non-local DFT for heterogeneous surface (2D-NLDFT HS) and the quenched solid DFT (QSDFT) that are able to eliminate the known artifacts at 1 and 2 nm found in the PSD obtained using the standard NLDFT.^{5,7} 2D-NLDFT HS was used to calculate the PSD of the materials by analyzing simultaneously the N₂ and CO₂ isotherms using the SAIEUS® software provided by Micromeritics.⁷ The quenched solid DFT (QSDFT) was applied using the ASiQwin® software from Quantachrome to calculate the PSDs assuming a slit/cylindrical hybrid pore model, *i.e.*, a slit pore model in the micropore range applied to the CO₂ isotherms, and a cylindrical pore model for those pores larger than 2 nm applied to Ar or N₂ isotherms.

From the DFT-derived PSDs, it is possible to calculate the surface area of the materials, the total pore volume, and the pore volume in different pore size ranges: ultramicro-, supermicro- and mesopore volumes; also, the average pore volume in all or specific ranges of pore sizes was calculated through:

$$w_{av} = \frac{\sum_i \left(\frac{dV}{dw}\right)_i w_i}{\sum_i \left(\frac{dV}{dw}\right)_i} \quad (2.1)$$

Another method was used to obtain the PSD, particularly in the mesopore range, namely the Barrett–Joyner–Halenda (BJH) method with the Kruk–Jaroniec–Sayari (KJS) correction,⁸ which was applied to the desorption branch of the N₂ isotherms using the Microactive® software.

In addition, adsorption-desorption isotherms of n-hexane (nHEX), 2-methylpentane (2MP) and 2,2-dimethylbutane (22DMB) were performed in a manometric system designed

and manufactured by the LMA group at the University of Alicante and currently commercialized by Quantachrome Instruments under the name Vstar. Before the adsorption measurements, the samples were outgassed at 200 °C for 24h. The adsorption isotherms were performed at either 25 °C or 45 °C up to a relative pressure (p/p_0) of 1 for the three adsorbates evaluated. It is important to highlight that the adsorption measurements were performed according to very strict equilibrium criteria (10 equilibrium points; interval time 15s; sorption rate limit 0.6666 Pa min⁻¹).

2.3 Immersion calorimetry

The PSD in the micropore range can also be obtained by immersion calorimetry into different liquids, whose molecules have different kinetic diameters. This method is based on the assumption that the heat evolved due to the formation of an adsorbed layer of the liquid on the solid's surface, *i.e.*, the heat of immersion ($-\Delta H_{imm}$), is proportional to the available surface to the liquid, S , where the proportionality constant is the areal enthalpy of immersion ($-\Delta h_{imm}$).¹⁵ The calculation of S requires the use of a reference non-porous material, $-\Delta h_{imm}$ being characteristic for a specific solid-liquid system. Consequently, the surface area accessible for a given liquid in a target solid can be estimated provided that the sample and the reference share similar physicochemical characteristics.¹⁵⁻¹⁷

Immersion calorimetry experiments were performed in a Setaram C80 calorimeter, see Figure 2.4a, working at 30 °C using nHEX, 2MP and 22DMB as probe molecules. Before the calorimetric experiment, the material was outgassed at 200 °C for 24h in a specially designed glass reactor under ultra-high vacuum conditions. After the thermal treatment, the glass sample cell was sealed with a flame to maintain the sample under ultra-high vacuum conditions and introduced into the calorimetric chamber with the selected liquid. After stabilization of the thermal signal, the glass tip at the bottom of the sample cell was broken, and the heat released due to the wetting of the sample by the probe molecule was recorded as a function of time. The experimental set-up is shown schematically in Figure 2.4b.¹⁵ The enthalpy of immersion was then calculated from the area (integration) of the obtained peak. Carbon black V3G (now VULCAN® 3) from CABOT was used as a reference, having a surface area of 62 m² g⁻¹ and $-\Delta h_{imm}$ values of 7.89 J g⁻¹, 7.42 J g⁻¹ and 6.73 J g⁻¹ in nHEX, 2MP and 22DMB, respectively.

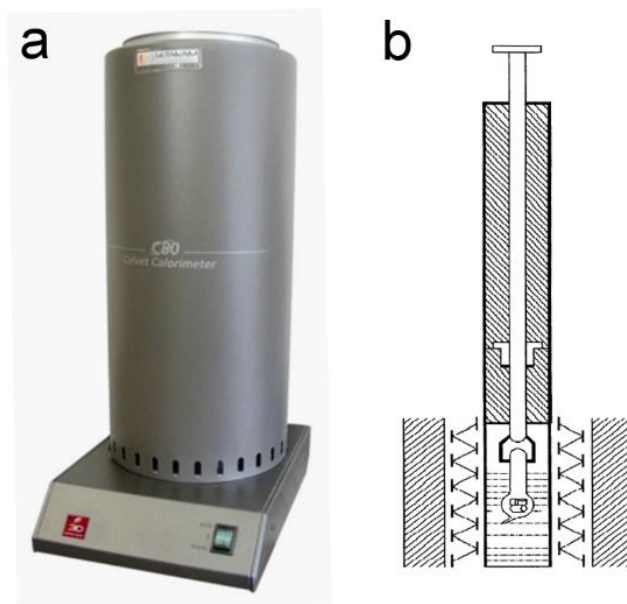


Figure 2.4. (a) Setaram C80 calorimeter. (b) Experimental set-up used for immersion calorimetry tests [Reprinted from Silvestre-Albero et al. (2001)¹⁵].

2.4 Raman spectroscopy

The Raman spectra of carbon materials are used to evaluate the degree of crystallinity in the nanoscale. To perform Raman spectroscopy tests the sample is irradiated with monochromatic light from a laser source and two types of scattering are observed, as seen in Figure 2.5a. The Rayleigh scattering has the same frequency than the source after interacting with the sample, ν_0 , and the Raman scattering, which occurs in a smaller proportion, is light that shifts from its original frequency after the interaction, $\nu_0 \pm \nu_m$. ν_m corresponds to the vibrational frequency of the molecule interacting with the laser beam, the negative, $-\nu_m$, and positive, $+\nu_m$, shifts are called the Stokes and anti-Stokes lines, respectively.¹⁸ The magnitude of the Raman shift provides information about the vibration modes of the molecule structure, thus giving insights on the type of bonds present in it and about its crystallinity.

The spectra were obtained with a Horiba Scientific XploRa Raman spectrometer (Figure 2.5b), based on samples without preparation and investigated with a 50 \times objective. The Raman-scattered light was dispersed by a holographic grating with 1200 lines per mm and detected by a CCD camera. A laser of wavelength 532 nm, circularly polarized and filtered at 10% of its nominal power, was used; such attenuation led to an incident power (~ 1.8 mW) that is too low to heat or damage the samples. Each spectrum was obtained by an accumulation of 2 spectra recorded from 800 to 2200 cm^{-1} over 180 s. Deconvolution of bands was carried out with the Labspec6 software from Horiba.

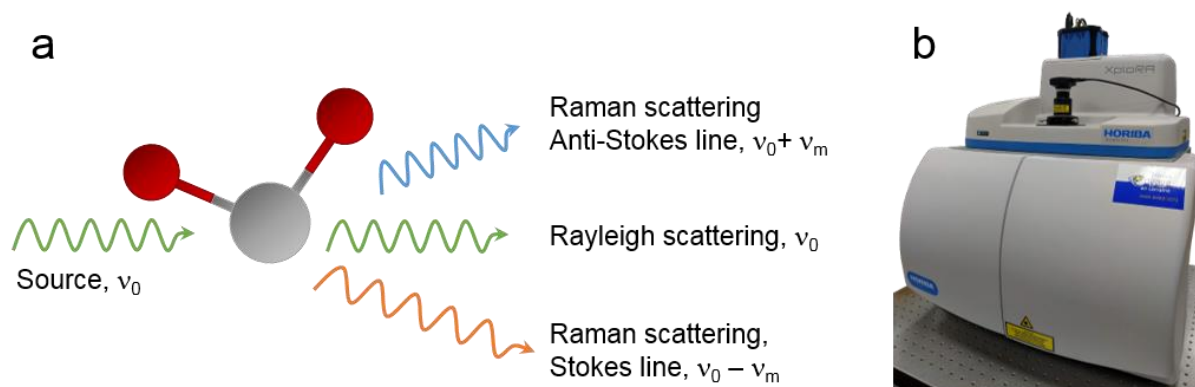


Figure 2.5. (a) Raman and Rayleigh scattering produced after the interaction of a material with a monochromatic source of light. (b) Horiba Scientific XploRa Raman spectrometer used to analyze the carbon materials of this study.

2.5 X-ray diffraction

The X-ray diffraction (XRD) technique is based on the interaction of X-ray waves with the atomic structure. If the material has a periodic array, *i.e.*, a crystalline structure, diffraction of light produces an interference pattern as the wavelength of X-ray radiation, λ , and the distance between the lattice planes, d , is in the same order of magnitude (\AA), see Figure 2.6a.^{19–21} When d , is an integer multiple of the wavelength constructive interference occurs, following Bragg's law:¹⁹

$$n\lambda = 2d \sin(\theta) \quad (2.2)$$

By varying the incidence angle, different peaks of intensity (constructive interference) can be observed allowing to reproduce the 3D crystalline structure by identifying the different lattice planes and the distance between them, see Figure 2.6b and 2.6c; in particular, small-angle XRD, generally $2\theta < 5^\circ$, can be used to study ordered mesoporous structures as exemplified in Figure 2.6d.

Herein, small-angle XRD measurements were carried out in a Bruker D8 Advance X-ray powder diffractometer (Figure 2.6e) equipped with an X-ray source with a Cu anode working at 40 kV and 40 mA, a graphite monochromator and a scintillation detector. Silver behenate was used as low-angle diffraction standard calibration for height correction, and data given for $d(100)$ planes were collected.

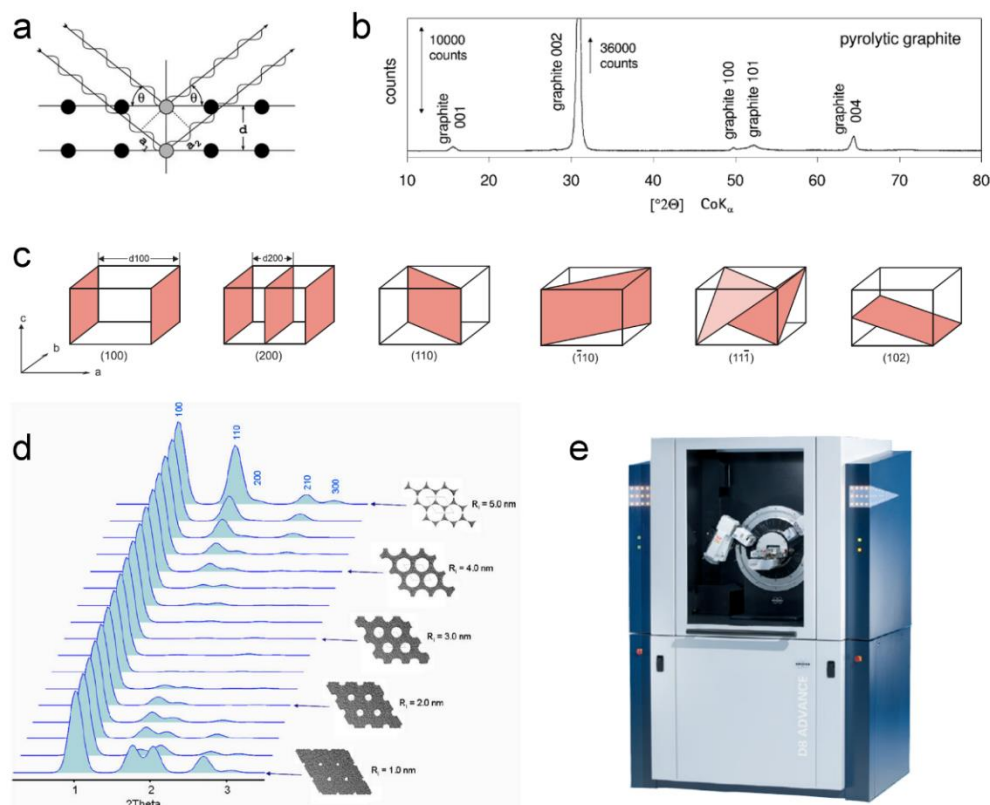


Figure 2.6. (a) Geometric derivation of Bragg's law. (b) XRD pattern of pyrolytic graphite. (c) Examples of lattice planes in a crystal structure. (d) Simulated XRD patterns for OMCs with a 2D hexagonal geometrical structure. (e) Bruker D8 Advance X-ray powder diffractometer. [Adapted from Stanjek and Häusler (2004)¹⁹, Ermrich and Oppen (2013)²¹ and Schmidt (2009)²²]

2.6 Thermogravimetric analysis

The thermogravimetric analysis (TGA) technique is used to monitor changes in the mass of a material in a controlled atmosphere as the temperature increases, *i. e.*, the mass loss as a function of temperature. In this way, it is possible to evaluate the thermal stability of the materials. The derivative of the mass vs temperature curve reveals the peaks of mass change, which provide information on, for example, the amount of humidity present in the analyzed samples or the degradation temperatures of different components within it, as exemplified in Figure 2.7. TGA was carried out in an STA 449F3 Jupiter microbalance from Netzsch, shown in the inset of Figure 2.7. The measurements were performed under inert atmosphere (argon) where ~ 15 mg of material was heated at $10 \text{ }^\circ\text{C min}^{-1}$ up to $900 \text{ }^\circ\text{C}$. Derivative curves were obtained using the Proteus® software, provided by Netzsch.

2.7 Elemental analysis

The bulk chemical composition of the materials was studied using a Vario EL Cube analyzer from Elementar. Before the measurement, the sample is dried to remove humidity and a small quantity of material (~2 mg) is placed in the carousel, which can hold up to 80 different samples. Afterwards, the sample is burned in a furnace from which the gas is separated using trap columns. A thermal conductivity detector (TCD) carries out the identification of carbon, hydrogen, nitrogen and sulfur content. The oxygen content can be calculated by difference or measured by itself by changing the combustion column. The detection method is schematized in Figure 2.8.

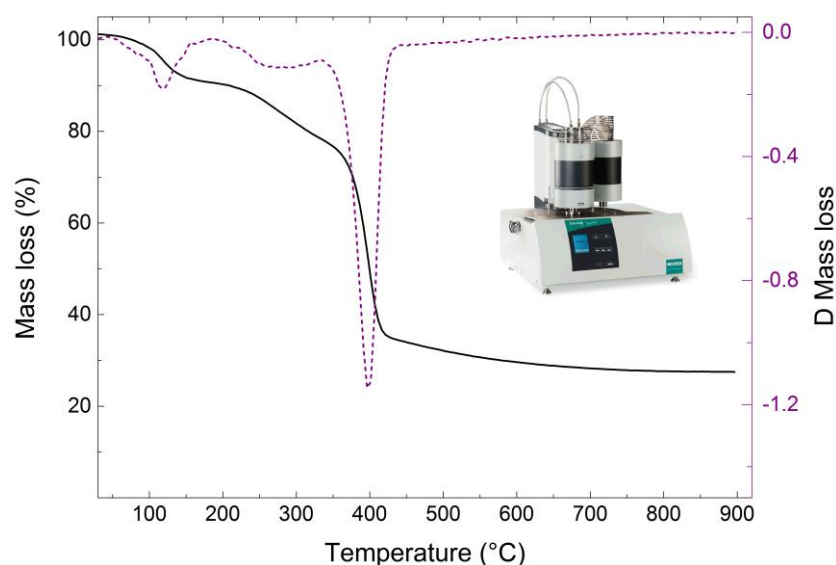


Figure 2.7. Typical curves obtained from the thermogravimetric analysis of samples carried out in the STA 449F3 Jupiter microbalance from Netzsch (inset).

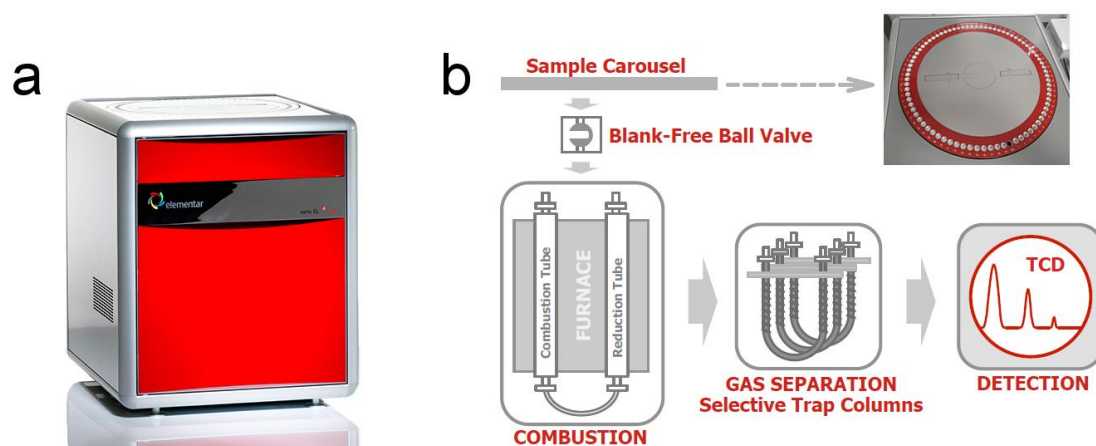


Figure 2.8. (a) Vario EL Cube and (b) working principle of the device. [Adapted from Elementar²³]

2.8 X-ray photoelectron spectroscopy

The heteroatom content on the surface of the materials was studied through X-ray photoelectron spectroscopy (XPS). This characterization technique allows not only to identify the composition of the surface of the material (1 to 20 nm) but also provides information about the types of chemical bonds that they form. An XPS analysis is carried out by irradiating the sample with high-energy photons, such as the ones associated to X-rays, to give enough energy to the electrons in the atoms to escape; the kinetic energy of the released electron is equal to the difference between the energy of the incident photon and the binding energy of the electron. The XPS devices measure the kinetic energy of the electron to calculate the binding energy and thus identify the atoms on the surface, see Figure 2.9a.²⁴ The analysis of the high-resolution spectra allows separating the contributions to each peak and relating them to the different chemical bonds, examples are shown in Figure 2.9b.

The XPS analysis was performed on an ESCAPlus OMICROM system equipped with a hemispherical electron energy analyzer and an area of analysis of 1.75 x 2.75 mm. The device was equipped with an Mg X-Ray source (1253.6 eV) and was operated at 15 kV and 15 mA. Pass energies of 50 eV and 20 eV were used for survey and high-resolution scans, respectively. The peaks were treated with the CASA software, and the atomic content of each element was calculated from the atomic sensitivity factors, the contribution from each type of functional group was obtained from the deconvolution of the peaks.

2.9 Fourier-transform infrared spectroscopy

The infrared spectrum of a molecule is a unique property that can be used, for example, to identify unknown substances by comparison with reference molecules or to observe the introduction of a new component using the original substance as reference. This is possible as the vibrational response to each frequency can be associated to specific functional groups or structural components.²⁶ It is important to note that as the molecule complexity increases a quantitative interpretation of the infrared spectra becomes more difficult; nonetheless, this technique is widely used due to its easy and fast acquisition of data.^{26,27} The Fourier-transform infrared (FTIR) spectroscopy refers to the used instrumentation method in which the sample is irradiated with a beam that contains all the frequencies in the range of interest and collects the response as a function of time. Then the Fourier transform is applied to obtain the spectra as a

function of frequency and finally as a function of the wavenumber, hence the name of the technique.²⁸

FTIR spectra were acquired using a Frontier 400 spectrometer from PerkinElmer in transmission mode, using a range of wavenumbers from 650 to 4000 cm^{-1} , the device automatically reduces the environmental noise by filtering H_2O and CO_2 adsorptions. The device and an example of an obtained spectra are shown in Figure 2.10.

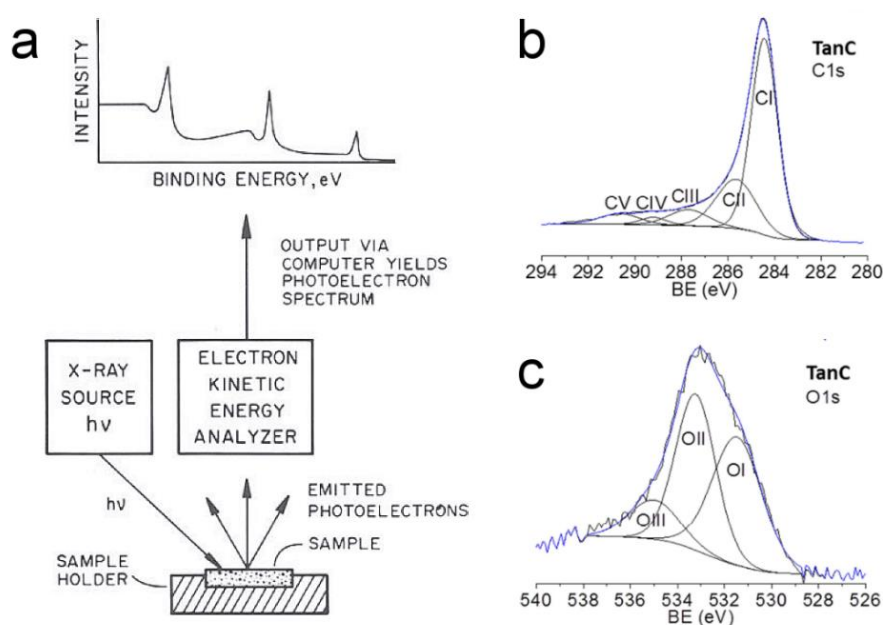


Figure 2.9. (a) Schematized operating principle of the XPS characterization technique. Examples of (a) carbon and (b) oxygen high-resolution XPS spectra of tannin-derived carbon materials. [Adapted from Andrade (1985)²⁴ and Sánchez-Sánchez et al. (2017)²⁵]

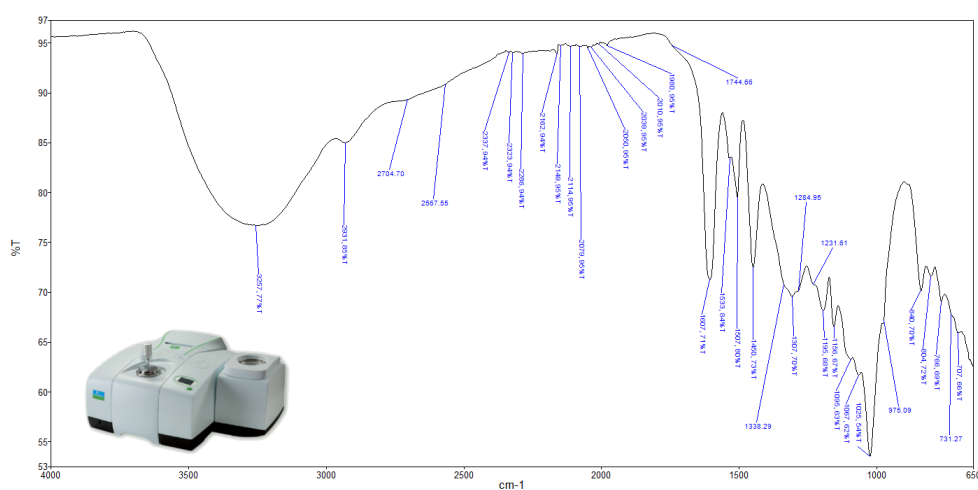


Figure 2.10. Typical FTIR spectra of mimosa tannin; the inset shows the Frontier 400 spectrometer from PerkinElmer used for the acquisition.

2.10 Electrochemical performance

The process of preparation of the carbon electrodes was carried out as follows: first, the carbon materials were ground to reduce and homogenize the particle size. This was carried out in a MM 400 vibrational milling machine from Retsch, see Figure 2.11a, equipped with stainless steel bowl (1.5 ml) and balls (5 mm diameter). Afterwards, a paste was prepared by mixing the material under study with carbon black (from Sigma-Aldrich, CAS:7440-44-0) and PTFE (60 % aqueous solution, from Sigma-Aldrich) in an 85:5:10 weight ratio, the mix was homogenized in an agate mortar by adding small quantities of ethanol and then left to dry overnight at 105 °C. Finally, disc-shaped electrodes with carbon loads (CLs) between 5 and 10 mg cm^{-2} were cut from the paste and impregnated with the corresponding electrolyte before testing.

Cyclic voltammetry (CV), galvanostatic charge-discharge (GCD) and electrochemical impedance spectroscopy (EIS) tests were carried out using a VSP300 electrochemical workstation from Bio-Logic, shown in Figure 2.11b, for which two-electrode cells (Swagelok) were used to test the electrochemical performances (see Figure 2.11c). Two electrodes of comparable mass, separated by a porous glass fiber mat, were placed between two current collectors of either gold (for electrodes impregnated in the aqueous electrolyte) or stainless steel (when impregnated in the organic electrolyte).

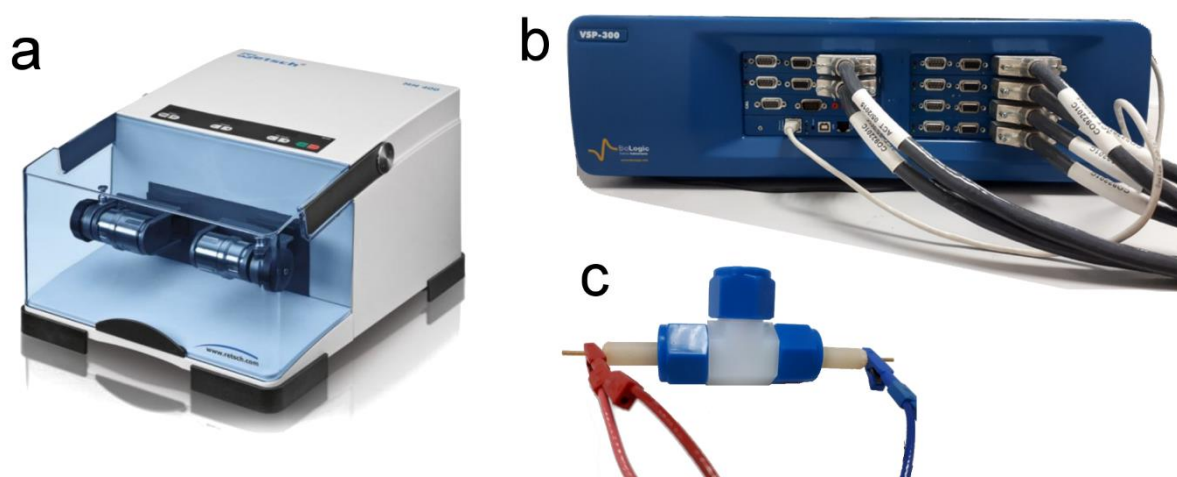


Figure 2.11. (a) MM 400 vibrational milling machine from Retsch. (b) VSP300 electrochemical working station from Bio-Logic and (c) Swagelok electrode cells used for the electrochemical characterization.

2.11 Contact angle

The wettability of the porous carbon materials is of most importance when aqueous electrolytes are used, to evaluate this property the sessile drop method was used. The powdered materials were mixed with PTFE (5 – 10 wt. %) to create a paste similar to the one used to prepare electrodes for electrochemical tests (as described in Section 2.10). Measurements were performed using a DSA100 liquid-solid contact angle analyzer from Krüss, drops of 4 μL of water were deposited on the surface, and images transversal to the surface were captured with the integrated digital camera. Analysis of the images was carried out using the ADVANCE software provided by Krüss, using the Young Laplace fitting method and adjusting the baseline manually. The equipment and an example of the measurement are displayed in Figure 2.12.

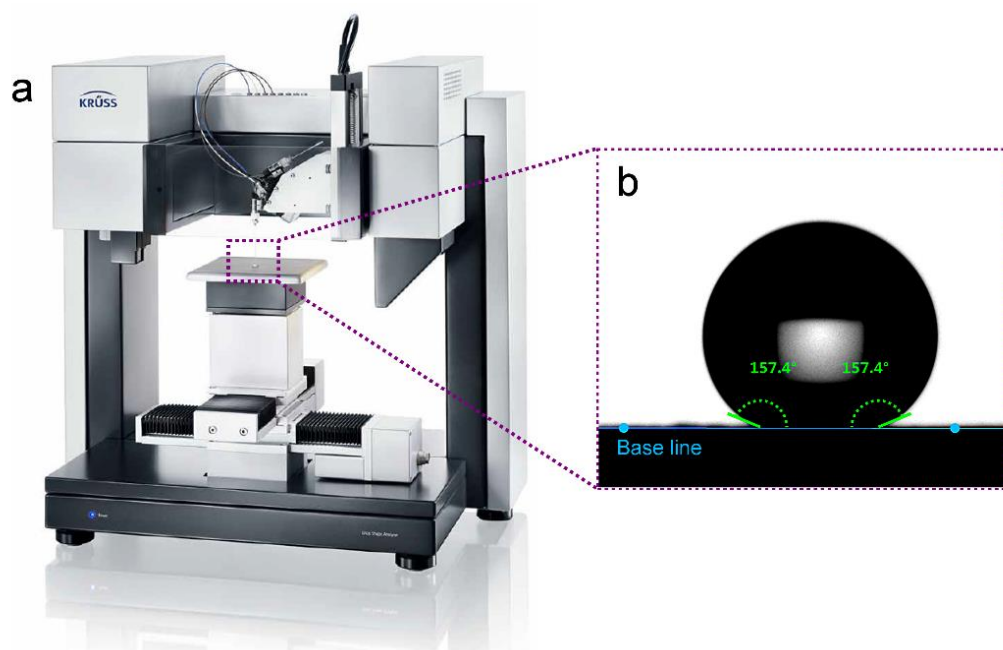


Figure 2.12. (a) DSA100 liquid-solid contact angle analyzer from Krüss and (b) example of measurement taken from the image capture by the device.

Most of these devices are part of the MATERLOR platform of material synthesis and characterization of the *Institut Jean Lamour* located at Epinal, France (Figure 2.13). This platform has been possible thanks to different financial supports over a decade. For example, the financial support of CPER 2007-2013 *Structuration du Pôle de Compétitivité fibres Grand Est* (Competitiveness Fibre Cluster), local support from the *Conseil Général des Vosges*, regional from the Lorraine Region, and national from DRRT and FNADT funds. European (FEDER) funds through CHEERS, TALiSMAN and TALiSMAN2 projects also made possible to complete this platform.



Figure 2.13. Photos of MATERLOR platform of Biosourced Materials Research team at *Institut Jean Lamour* at Epinal, France.

2.12 References

1. Reimer, L. & Kohl, H. Transmission electron microscopy: physics of image formation. (Springer, 2008).
2. Thommes, M. et al. Physisorption of gases, with special reference to the evaluation of surface area and pore size distribution (IUPAC Technical Report). *Pure and Applied Chemistry* 87, (2015).
3. Brunauer, S., Emmett, P. H. & Teller, E. Adsorption of Gases in Multimolecular Layers. *Journal of the American Chemical Society* 60, 309–319 (1938).
4. Fagerlund, G. Determination of specific surface by the BET method. *Matériaux et Constructions* 6, 239–245 (1973).
5. Neimark, A. V., Lin, Y., Ravikovitch, P. I. & Thommes, M. Quenched solid density functional theory and pore size analysis of micro-mesoporous carbons. *Carbon* 47, 1617–1628 (2009).
6. Jagiello, J. & Olivier, J. P. Carbon slit pore model incorporating surface energetical heterogeneity and geometrical corrugation. *Adsorption* 19, 777–783 (2013).
7. Jagiello, J. & Olivier, J. P. 2D-NLDFT adsorption models for carbon slit-shaped pores with surface energetical heterogeneity and geometrical corrugation. *Carbon* 55, 70–80 (2013).
8. Kruk, M., Jaroniec, M. & Sayari, A. Application of Large Pore MCM-41 Molecular Sieves To Improve Pore Size Analysis Using Nitrogen Adsorption Measurements. *Langmuir* 13, 6267–6273 (1997).
9. Thommes, M. & Cychosz, K. A. Physical adsorption characterization of nanoporous materials: progress and challenges. *Adsorption* 20, 233–250 (2014).
10. Cychosz, K. A., Guillet-Nicolas, R., García-Martínez, J. & Thommes, M. Recent advances in the textural characterization of hierarchically structured nanoporous materials. *Chemical Society Reviews* 46, 389–414 (2017).
11. Thommes, M., Smarsly, B., Groenewolt, M., Ravikovitch, P. I. & Neimark, A. V. Adsorption Hysteresis of Nitrogen and Argon in Pore Networks and Characterization of Novel Micro- and Mesoporous Silicas. *Langmuir* 22, 756–764 (2006).
12. Cychosz, K. A., Guillet-Nicolas, R., García-Martínez, J. & Thommes, M. Recent advances in the textural characterization of hierarchically structured nanoporous materials. *Chemical Society Reviews* 46, 389–414 (2017).
13. Cimino, R., Cychosz, K. A., Thommes, M. & Neimark, A. V. Experimental and theoretical studies of scanning adsorption–desorption isotherms. *Colloids and Surfaces A: Physicochemical and Engineering Aspects* 437, 76–89 (2013).
14. Thommes, M. Physical Adsorption Characterization of Nanoporous Materials. *Chemie Ingenieur Technik* 82, 1059–1073 (2010).
15. Silvestre-Albero, J. Characterization of microporous solids by immersion calorimetry. *Colloids and Surfaces A: Physicochemical and Engineering Aspects* 187–188, 151–165 (2001).
16. Gonzalez, M. T., Sepulveda-Escribano, A., Molina-Sabio, M. & Rodriguez-Reinoso, F. Correlation between Surface Areas and Micropore Volumes of Activated Carbons Obtained from Physical Adsorption and Immersion Calorimetry. *Langmuir* 11, 2151–2155 (1995).

17. Denoyel, R., Fernandez-Colinas, J., Grillet, Y. & Rouquerol, J. Assessment of the surface area and microporosity of activated charcoals from immersion calorimetry and nitrogen adsorption data. *Langmuir* 9, 515–518 (1993).
18. Ferraro, J. R. *Introductory Raman Spectroscopy*. (Elsevier, 2003).
19. Stanjek, H. & Häusler, W. Basics of X-ray Diffraction. *Hyperfine Interactions* 154, 107–119 (2004).
20. Chauhan, A. Powder XRD Technique and its Applications in Science and Technology. *J Anal Bioanal Tech* 5, (2014).
21. Ermrich, M. & Opper, D. XRD for the analyst: getting acquainted with the principles. (PANalytical B. V., 2013).
22. Schmidt, W. Calculation of XRD patterns of simulated FDU-15, CMK-5, and CMK-3 carbon structures. *Microporous and Mesoporous Materials* 117, 372–379 (2009).
23. Elementar. Vario EL cube. [www.elementar.com](https://www.elementar.com/en/products/organic-elemental-analysis/vario-el-cube.html)
<https://www.elementar.com/en/products/organic-elemental-analysis/vario-el-cube.html> (2020).
24. Andrade, J. D. *Surface and Interfacial Aspects of Biomedical Polymers: Volume 1 Surface Chemistry and Physics*. (Springer US, 1985).
25. Sanchez-Sanchez, A. et al. Excellent electrochemical performances of nanocast ordered mesoporous carbons based on tannin-related polyphenols as supercapacitor electrodes. *Journal of Power Sources* 344, 15–24 (2017).
26. Coates, J. Interpretation of infrared spectra, a practical approach. *Encyclopedia of analytical chemistry* (2000).
27. Ricci, A., Olejar, K. J., Parpinello, G. P., Kilmartin, P. A. & Versari, A. Application of Fourier Transform Infrared (FTIR) Spectroscopy in the Characterization of Tannins. *Applied Spectroscopy Reviews* 50, 407–442 (2015).
28. Peak, D. Fourier transform infrared spectroscopy. *Encyclopedia of Soils in the Environment* 80–85 (2005).

Chapter 3

Mechanosynthesis

3.1 Introduction

Section 1.4 generally described the different types of porous carbons that could be used as electrodes for SCs. Among them, mesoporous carbons (MCs), specifically ordered mesoporous carbons (OMCs), have been proven to present an improved SC performance due to favored diffusion of the electrolyte thanks to the hierarchical structure connecting the micro- and the mesoporosity.^{1,2} As aforementioned in Section 1.4.5, OMCs are usually produced by either hard or soft templating. In the former method, silica particles,³ zeolites^{3,4} or biosourced materials⁵⁻⁷ are coated with a carbon precursor and submitted to carbonization followed by template removal using HF or NaOH; the resultant OMC is a negative replica of the template. In the latter method, an amphiphilic surfactant, usually a triblock copolymer, is used in solution to form micelles that act as templates for the carbon precursor; a subsequent pyrolysis process then eliminates the surfactant, producing mesoporosity in the resultant carbon materials.⁸ Whether through hard or soft templating, OMC synthesis generally uses molecules of petrochemical origin (like resorcinol or phenol) as carbon precursor, takes several days and involves the use of hazardous substances such as formaldehyde, commonly used as a crosslinker, or HF or NaOH, used for leaching out the hard templates.

Pluronic® F127 (P) is often used in soft-templating methods, and different precursors and/or precursor to surfactant ratios can result in different orderings; among the latter, the 2D hexagonal array is one of the most commonly found. For example, by using phenol-formaldehyde resins with P, it is possible to obtain OMCs with cubic or hexagonal structure by changing the precursor to surfactant ratio.^{9,10} Moreover, OMCs with 2D hexagonal symmetry prepared by evaporation-induced self-assembly (EISA) were obtained using a resorcinol-formaldehyde resin and P.¹¹ Tannin as carbon precursor was used with P and without any crosslinker in an EISA process to obtain OMCs with a hexagonal structure.¹² OMCs having a hexagonal array were also produced by self-assembly of P and mimosa tannin in an aqueous medium¹³ (see Section 1.6).

Nowadays, solid-state synthesis methods are attracting increasing interest because: (i) they are either liquid-assisted (with low amounts of solvents) or even solvent-free¹⁴⁻¹⁷ (ii) the synthesis time is shorter compared to methods based on chemistry in solution;^{14,15} (iii) they are cheaper and more environment-friendly as they comprise fewer synthesis steps.^{17,18} In particular, mechanochemistry, by which mechanical energy is absorbed for synthesizing the material, has been used to produce ceramics,¹⁶ metal alloys,¹⁹ organic materials¹⁵ and more

recently OMCs.^{18,20,21} Mechanical energy can be provided by shearing, stretching or grinding.¹⁴ It has been reported that solvent-free hand-grinding of P in the presence of resorcinol and terephthalaldehyde produce OMCs having either cubic or hexagonal structures by changing the initial amount of P; replacing terephthalaldehyde by formaldehyde in liquid-assisted synthesis produces a material with hexagonal structure.¹⁸ Ball-milling of P, resorcinol, terephthalaldehyde, and melamine was also used to synthesize nitrogen-doped OMCs with a hexagonal structure.²⁰ In these studies, a curing or aging step of the material at low temperature (80 or 100 °C) was needed before carbonization. Furthermore, OMCs were obtained by ball-milling tannin, P and metal acetates used as crosslinkers; in this case, washing and drying steps before carbonization were again required.²¹ Nevertheless, ball-milling thus appears as a suitable method for synthesizing OMCs because it can provide higher energy and repeatability than hand-grinding,¹⁵ and it has a great industrial potential as it reduces the energy requirements related to solvent production, purification, and recycling.¹⁴

This chapter presents the methodology followed for the development of a green one-pot method for preparing OMCs with a 2D hexagonal structure using a planetary ball mill, schematized in Figure 3.1. Commercial mimosa tannin extract (T), kindly provided by the company SilvaChimica (St Michele Mondovi, Italy) and available on the market under the name Fintan OP, was used as carbon precursor. Such tannin extract is a light-brown powder that contains 80-82 % of phenolic (flavonoid) material. Pluronic® F127 (P) from Sigma-Aldrich was used as the pore-directing agent. P is a triblock copolymer based on a hydrophobic polypropylene oxide (PPO) chain and two hydrophilic polyethylene oxide (PEO) chains that can form micelles in the presence of water. No crosslinker was required, but only a small amount of water (W) was added and no curing or drying steps were needed either. The impact

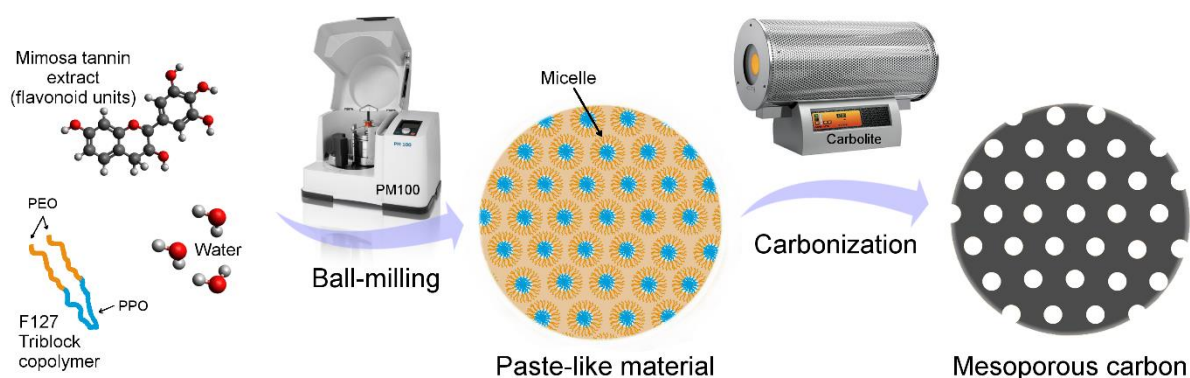


Figure 3.1. Schematic of the mechanochemistry method. [Adapted from Castro-Gutiérrez et al. (2018)²²]

of key process parameters such as milling time, pH, P:W weight ratio and carbonization temperature on the porous structure of the resultant carbons was carefully analyzed, aiming to produce the most ordered mesoporous carbon.

For the mechanochemistry, several groups of samples were prepared by changing independently one of the following parameters: milling time, pH of the added liquid, and P:W weight ratio. In all cases, the same amount of T (2 g) was systematically used as carbon precursor, added to the rest of components, and milled in a PM 100 planetary ball-milling machine from Retsch. The device was equipped with a 50 mL agate milling bowl and 10 agate balls of diameter 1 cm and was used at a constant rotation speed of 500 rpm. For pH studies, aqueous solutions of HCl with pH ranging from 0 to 4 were prepared from a commercial solution (1 M HCl).

Paste-like materials retrieved from the ball-mill were carbonized immediately after synthesis, without further drying or additional steps. The carbonization was performed under nitrogen flow (100 mL min^{-1}) in a tubular furnace from Carbolite, using a quartz boat in a quartz tube (inner diameter 3.4 cm) heated up to $900 \text{ }^\circ\text{C}$ at a rate of $1 \text{ }^\circ\text{C min}^{-1}$. The final temperature was held for 1 h, and then the samples were left to cool down naturally under nitrogen flow. Pyrolysis at higher temperatures (1100, 1300 and $1500 \text{ }^\circ\text{C}$) was carried out in another tubular furnace, using a ceramic boat in an alumina tube (inner diameter 7.5 cm) flushed with argon at the same flow rate as before. The temperature was again increased at $1 \text{ }^\circ\text{C min}^{-1}$, the set point was maintained for 1 h, and the samples were cooled down under argon at a rate of $3 \text{ }^\circ\text{C min}^{-1}$.

Characterization of all samples was carried out using the different techniques detailed in Chapter 2. Given that the production of OMCs is the main goal of this study, the emphasis was done on PSDs in the mesoporous range, which was calculated using the BJH-KJS method applied to the desorption branch of the N_2 adsorption-desorption isotherms.

3.2 Effect of components

To reveal the effect of each component of the mixture on the structure of the final carbons, the milling time was fixed at 60 min, and three reference samples were prepared by removing P, W, or both (T2P0W2_60, T2P2W0_60, and T2P0W0_60, respectively). After carbonizing them at $900 \text{ }^\circ\text{C}$, those samples were thus compared to CT2P2W2_60. Figure 3.2 shows their

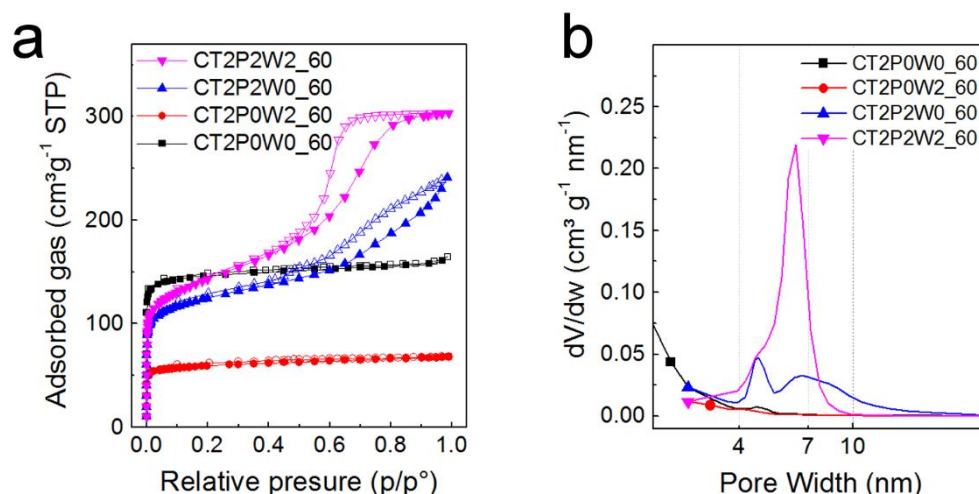


Figure 3.2. N₂ adsorption-desorption isotherms and corresponding PSDs for CT2P2W2_60 and of carbonized reference samples CT2P0W0_60, CT2P0W2_60, and CT2P2W0_60. [Adapted from Castro-Gutiérrez et al. (2018)²²]

adsorption-desorption isotherms and the corresponding PSDs. CT2P0W0_60 and CT2P0W2_60 presented type Ia isotherms that are typical of purely microporous solids. They show that, in the absence of P, adding W decreased the A_{BET} of the final carbon material from 578 to 231 m² g⁻¹, thus evidencing that carbonizing a dry powder instead of a paste-like agglomerated material produced a higher microporosity. This effect might be due to the easier release of volatiles from a powder. CT2P2W0_60 and CT2P2W2_60 presented isotherms resulting from the combination of type Ia and type IV. They show that, whether W was present or not, adding P was necessary for producing mesopores; however, the material prepared without water, CT2P2W0_60, had a broader PSD and a much lower V_{meso} than CT2P2W2_60, see Table A1.1 in Annex 1 for the pore texture parameters obtained from N₂ and CO₂ adsorption-desorption isotherms. Hence, it can be concluded that both P and W are simultaneously needed for achieving mesoporous materials with the narrowest mesopore-size distribution. No mesopores were indeed formed without P, whereas W was required to form micelles and to allow the best interaction between T and P.

Thermogravimetric analysis (TGA) led to the results shown in Figure 3.3a, where samples are compared after subtraction of the mass loss attributed to the evaporation of water and further normalization. The same behavior of mass loss is observed for T2P0W0_60 and T2P0W2_60 samples, revealing that the differences of the observed carbon yield, 41 and 26%, respectively, are only related to the initial amount of water in them. Figure 3.3a also shows that a peak of

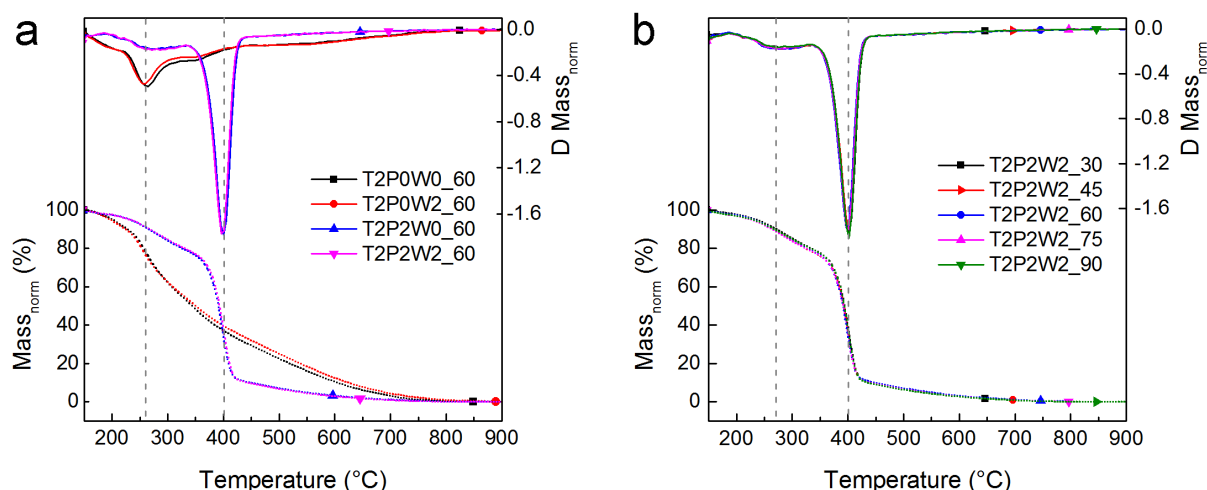


Figure 3.3. Absolute (left scale) and differential (right scale) normalized mass losses of (a) T2P2W2_60 and reference samples; and (b) samples T2P2W2_*t* prepared at various milling times, ranging from 30 to 90 min. The normalization was performed after removing the mass loss attributed to the evaporation of water. [Reproduced from Castro-Gutiérrez et al. (2018)²²]

mass loss at ~ 260 °C for T2P0W0_60 vanished when adding P to the formulation, implying that the interaction of P with T improves the thermal stability at this temperature. For T2P2W0_60 and T2P2W2_60, *i.e.*, for samples containing P, an intense peak of differential mass loss was observed when the temperature reached 400 °C, due to the degradation of the surfactant,¹³ after which the material remained fairly stable until 900 °C. Even more, T2P2W0_60 and T2P2W2_60 have identical mass loss curves when compared on dry basis, confirming that the major role of W during the synthesis is to form micelles and to improve the interaction between T and P, affecting in this way the resultant mesoporous structure but not the thermal stability of the material.

3.3 Effect of milling time

To study the effect of milling time, mechanochemistry of the materials was carried out by ball-milling the same quantities (2 g) of tannin (T), Pluronic® F127 (P) and water (W) during times ranging from 30 to 120 min. The resultant paste-like materials were labeled T2P2W2_*t*, where “*t*” accounts for the milling time in minutes, and the final carbon materials were identified by adding a “C” to the sample names. Figure 3.4 shows the changes of N₂ adsorption-desorption isotherms and the derived PSDs with milling time and Table A1.1 lists the corresponding pore texture parameters. The BET area (A_{BET}) ranged from 484 to 553 m² g⁻¹,

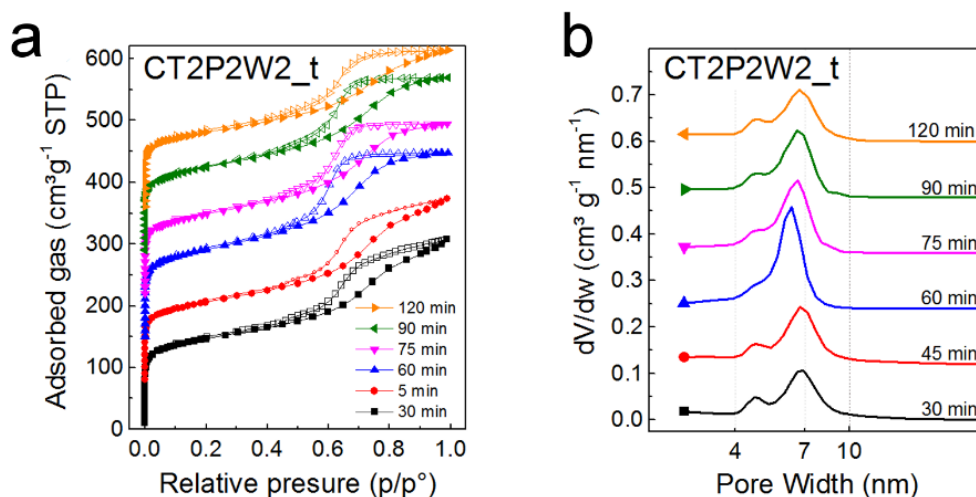


Figure 3.4. N_2 adsorption-desorption isotherms and corresponding PSDs for: (a, b) CT2P2W2_ t samples, $30 < t < 120$ min, for easier viewing isotherms and PSDs are offset by $70 \text{ cm}^3 \text{ g}^{-1} \text{ STP}$ and by $0.12 \text{ cm}^3 \text{ g}^{-1} \text{ nm}^{-1}$, respectively. [Adapted from Castro-Gutiérrez et al. (2018)²²]

and no clear trend could be observed. However, 60 min appeared as an optimum milling time for obtaining the highest mesopore fraction (Table A1.1). In addition, materials milled during 30 or 45 min presented PSDs with two distinct peaks: increasing the milling time up to 60 min decreased the first peak to just a shoulder, but longer milling resulted in broader PSDs and the reappearance of the first peak (Figure 3.4b). Therefore, it can be assumed that, up to 60 min, the milling process decreased the particle size of T and P powders and thus improved their intimate mixing. As a consequence, contact area and interaction between the components increased,¹⁴ thereby favoring the creation of hydrogen bonds between T and P. Indeed, FTIR spectra of the paste-like materials showed that for the samples obtained at different milling times, an increase of intensity of the polymeric stretching peak was observed, see Figure 3.5; since the ratio of components during the mechanochemistry was kept constant, this finding supports the hypothesis of hydrogen bond formation.^{21,23} Nonetheless, longer milling times ($t > 60$ min) may produce the destabilization of micelles and hence explain the two peaks observed on the PSDs.

In addition, TGA showed that changing the milling time did not seem to have any significant effect on the thermal stability of the materials since similar curves of mass loss were obtained for all samples with milling times ranging from 30 to 90 min (Figure 3.3b). This result is in agreement with the carbonization yields that remained constant for all tested milling times. Therefore, it can be stated again that the milling time only modifies the resultant mesoporous structure of the carbon materials.

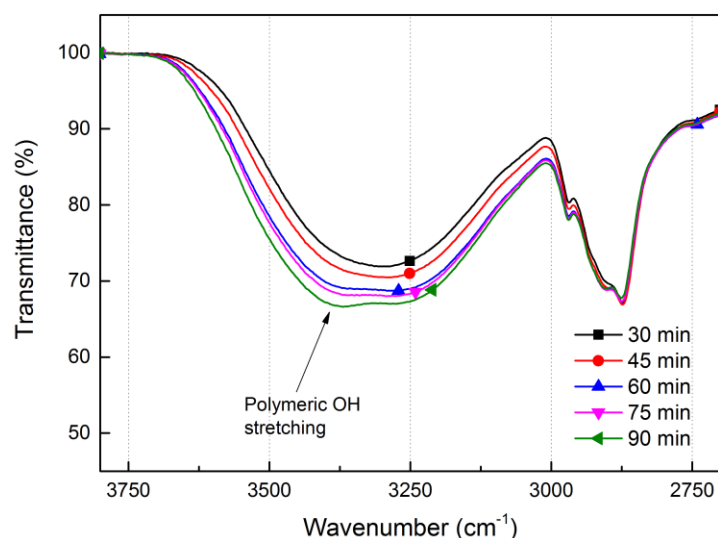


Figure 3.5. Detailed view of the FTIR spectra of samples T2P2W2_t synthesized during different milling times, ranging from 30 to 90 min. For comparison, the data were normalized with respect to a common peak (1452 cm⁻¹). [Reproduced from Castro-Gutiérrez et al. (2018)²²]

3.4 Effect of pH

Formerly published studies showed that a low pH favors the self-assembly of surfactants with carbon precursors,²⁴ thereby affecting the textural properties of the final carbon materials.²⁵ The effect of pH was investigated herein by, instead of adding 2 g of W, adding 2 g of aqueous HCl solutions with pH values ranging from 0 to 4. All samples were then milled for 60 min, carbonized at 900 °C, and labeled CT2P2pH_x_60, where “x” stands for the pH of the added solution; Figure 3.6 shows their N₂ adsorption-desorption isotherms and corresponding PSDs. The sample prepared at pH 0 presented a rather different mesopore-size distribution, with two overlapping peaks, the highest centered at 4.7 nm and a lower one centered at 5.4 nm. The highly acidic medium present during the synthesis of CT2P2pH0_60 may have produced significant T autocondensation, a well-known behavior of tannin at low pH, thus preventing it from having a good interaction with P, hence its different PSD.

Overall, when compared to CT2P2W2_60, *i.e.*, with the sample at unaltered pH, no significant change of porous texture was observed (Table A1.1). Besides, the modification of the pH of added liquid during synthesis did not improve the ordering of the resultant carbon materials. In particular, CT2P2pH1_60 resembles the most to CT2P2W2_60 sample in terms of PSD and TEM images as shown in Figure 3.7. Thus, for simplicity, the following studies described below were carried out using only pure distilled water.

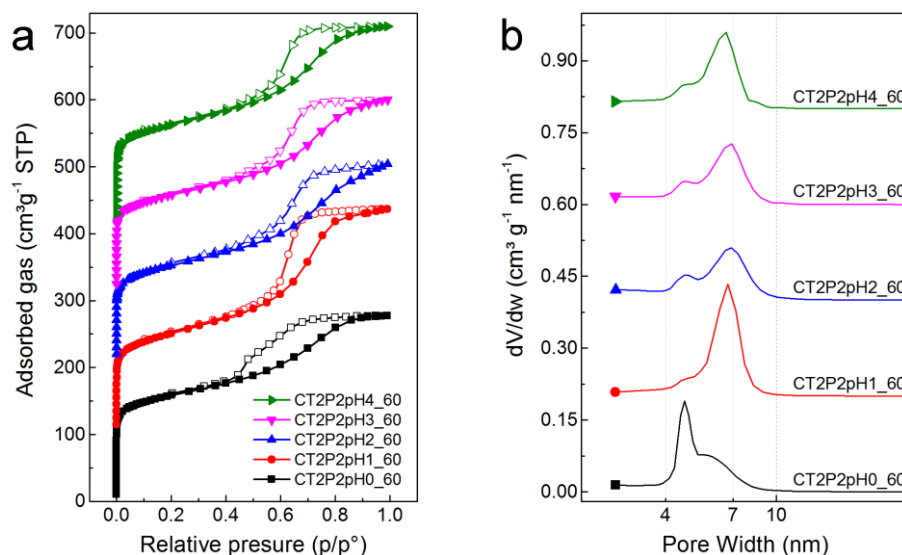


Figure 3.6. (a) N₂ adsorption-desorption isotherms and (b) corresponding PSDs of carbon materials CT2P2pH_x_60, synthesized by using aqueous solutions of HCl at pH ranging from 0 to 4 instead of water, and a milling time of 60 min. For easier viewing, isotherms and PSDs are offset by 105 cm³ g⁻¹ STP and by 0.2 cm³ g⁻¹ nm⁻¹, respectively. [Reproduced from Castro-Gutiérrez et al. (2018)²²]

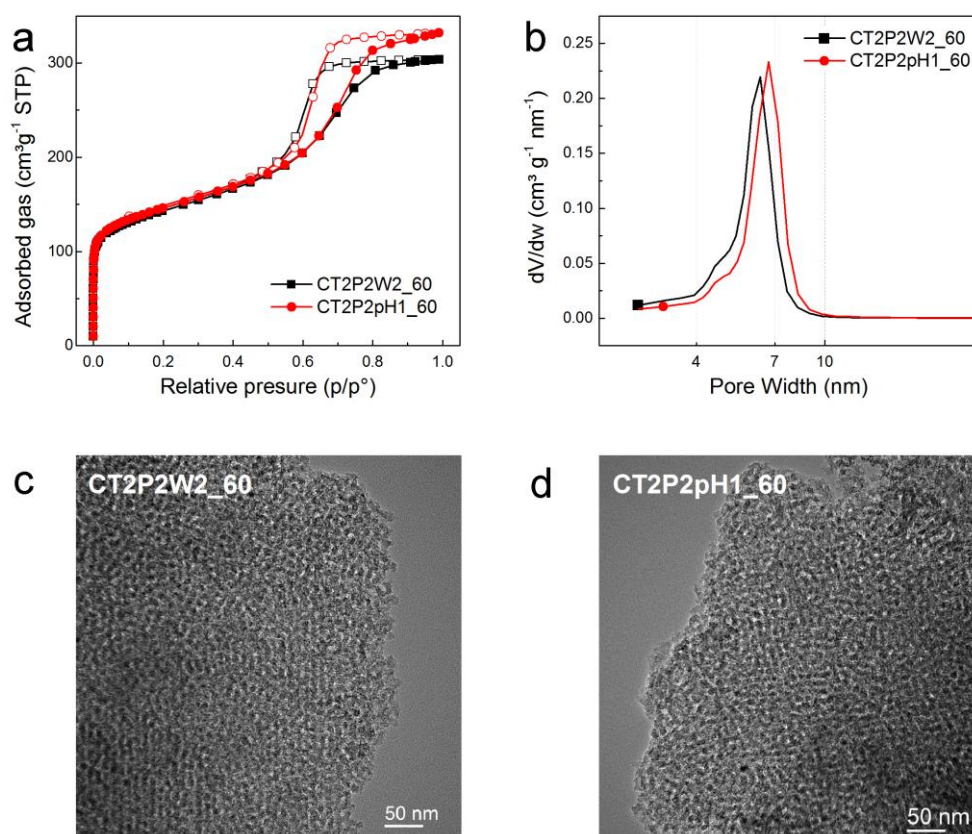


Figure 3.7. Comparison between CT2P2W2_60 and CT2P2pH1_60: (a) N₂ adsorption-desorption isotherms; (b) PSDs; and (c,d) TEM images. [Reproduced from Castro-Gutiérrez et al. (2018)²²]

3.5 Effect of P:W weight ratio

Since changes of surfactant concentration in aqueous solutions can give rise to micellar, cubic, rod-like or hexagonal phases,^{26–37} the effect of the P:W weight ratio on the resultant carbon materials was investigated at constant milling time of 60 min. The corresponding samples were named CT2P n W m _60, according to their $n:m$ (P:W) weight ratio, expressed in g/g. First, the amount of P was changed from 1 to 3 g while keeping W constant and equal to 2 g, Figure 3.8a and 3.8b shows the N₂ adsorption-desorption isotherms and the PSDs. Low amounts of P (0.5 g) did not allow the formation of mesopores since CT2P0.5W2_60 adsorption-desorption isotherm is a type Ia, typical of microporous materials. P amounts from 1 to 2 g produced type Ia-IV isotherms with H2 loops, while higher amounts (up to 3 g) produced H4 loops with broader and bimodal PSDs. Therefore, a minimum of P was necessary to form micelles but an optimum was found to exist for getting unimodal, well-defined PSDs. As was concluded with P, when changing the amount of W from 1 to 3 g while maintaining P constant and equal to 2 g, there seems to be an optimum of 2 g of W for getting type Ia-IV isotherms and narrow PSDs. Figure 3.8c and 3.8d shows the N₂ adsorption-desorption isotherms and PSDs obtained. Moreover, Figure 3.8e-h shows TEM images of CT2P2W1_60, CT2P2W2_60, and CT2P1W2_60. Transversal and longitudinal sections of CT2P1W2_60, CT2P2W1_60, CT2P2W2_60, and CT2P1W2_60.

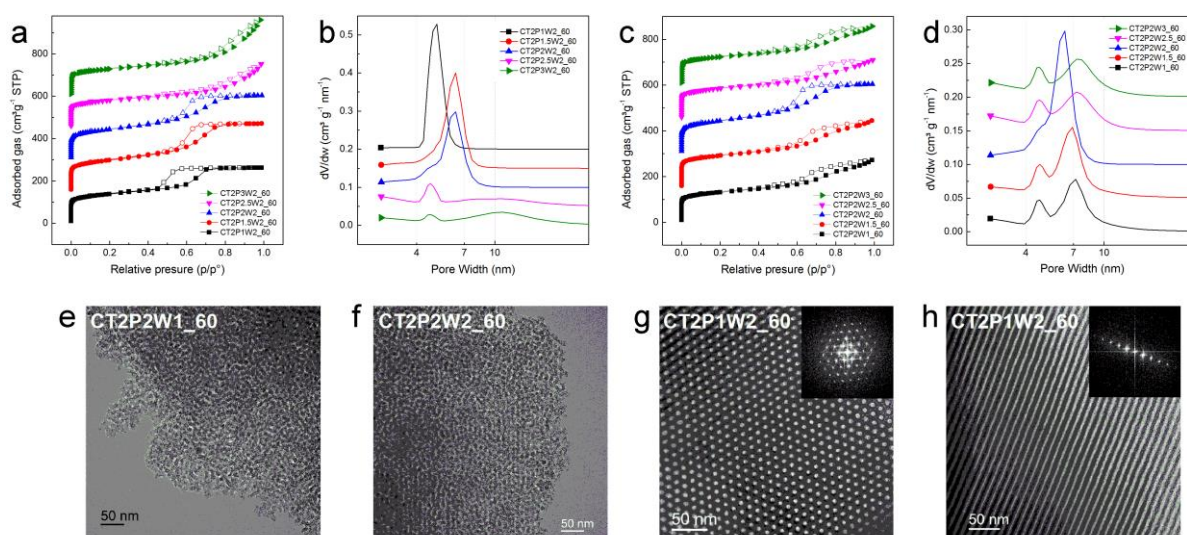


Figure 3.8. (a,c) N₂ adsorption-desorption isotherms and (b,d) corresponding PSDs of carbon materials synthesized using 60 min of milling and various P:W weight ratios. For easier viewing, isotherms and PSDs are offset by 150 cm³ g⁻¹ STP and by 0.05 cm³ g⁻¹ nm⁻¹, respectively. TEM images of (e) CT2P2W1_60, (f) CT2P2W2_60 and (g, h) transversal and longitudinal views of CT2P1W2_60. The insets in (g, h) represent the corresponding FFT of CT2P1W2_60. [Adapted from Castro-Gutiérrez et al. (2018)²²]

together with the corresponding Fast Fourier Transforms (FFT) (Figure 3.8g and 3.8h and respective insets), revealed that the sample possesses a 2D hexagonal mesoporous structure. On the contrary, CT2P2W1_60 and CT2P2W2_60 (Figure 3.8e and 3.8f) have bimodal PSDs and show a long-range disordered mesostructure.

To improve our understanding of these phenomena and to optimize the synthesis method, a second set of 16 carbon materials was synthesized. The PSDs curves of all 28 materials were deconvoluted and the maximum height (M), the full width at half-maximum (FWHM) and the peak position (PP) of the PSDs peaks were calculated. Examples of those deconvolutions are presented in Figure A1.1 and Table A1.2 reports the peak parameters thus obtained. Figure 3.9a shows a contour graph of the M / FWHM ratio, only considering the highest peak in the case of bimodal PSDs. This ratio indeed characterizes the shape of the PSD peaks, and the higher is its value, the higher and the narrower is the peak. The experimental P:W ratios tested are also represented using different symbols for separating purely microporous materials, *i.e.*, without peaks of PSD in the mesoporous range ($M = 0$), from those having unimodal or bimodal mesopore size distributions. A ring-like plot was observed, indicating that unimodal PSDs are found in limited ranges of values of P and W. Therefore, a single mesopore size, corresponding to PSDs with a unique and intense peak, can be obtained in the range of P and W amounts

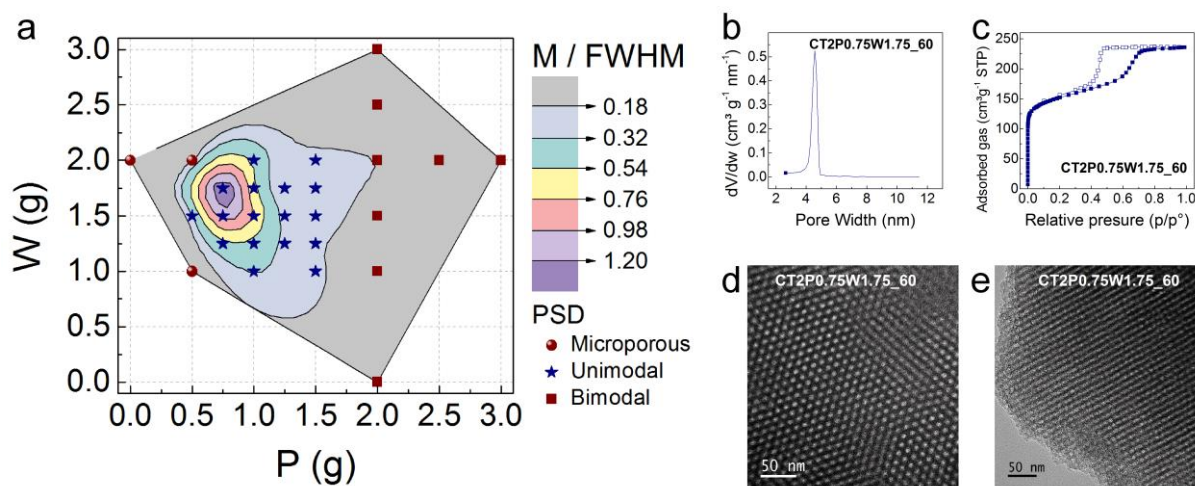


Figure 3.9. (a) Contour plot of the ratio M / FWHM of peaks obtained by deconvolution of the PSDs of samples synthesized using different P:W weight ratios and 60 min of ball-milling. The experimental P:W ratios tested are represented by points for purely microporous materials ($M=0$), and by stars and squares for unimodal and bimodal mesoporous distributions, respectively. (b) Highest and narrowest PSD and (c) corresponding N₂ adsorption-desorption isotherm found for sample CT2P0.75W1.75_60 (located in the central region of the ring-like contour graph of (a)). (d, e) TEM images confirming the 2D hexagonal structure of the same sample. [Adapted from Castro-Gutiérrez et al. (2018)²²]

located in the small area outlined by the central rings. The PSD having the highest intensity and the narrowest peak was found for the sample CT2P0.75W1.75_60, see Figure 3.9b. The corresponding N_2 adsorption-desorption isotherm is shown in Figure 3.9c, and the TEM images confirming the 2D hexagonal ordered structure of the material are displayed in Figure 3.9d and 3.9e.

In addition, the PP of unimodal PSDs was found to increase linearly with the amount of surfactant, and V_{meso} followed a similar trend. Figure 3.10 shows that the PP varied from 4.1 to 6.2 nm while the V_{meso} varied from 0.12 to 0.35 $cm^3 g^{-1}$. A similar behavior has been reported for 2D hexagonal mesoporous carbons self-assembled by P and using resorcinol-furfural or resorcinol-formaldehyde as carbon precursor, where a slight increase of pore volume and pore size with the P:carbon precursor ratio was observed.^{38–40} These phenomena can be related to the degree of swelling of the PEO chains in the triblock copolymer. Higher amounts of P reduces the amount of water available to swell the PEO chains, increasing the aggregation number and lowering the curvature of the hydrophilic/hydrophobic interface, and as a result the micelle size increases.^{38,41,42} The $V_{\mu,NLDFT}$ were mainly unaffected by the changes of P:W ratio and A_{BET} remained around 500 $m^2 g^{-1}$ for all samples (see Table A1.3). It thus appears that, through the variation of the P:W ratio, it is possible to tune the parameters of the ordered mesoporous structure, such as mesopore volume and size, without an impact on the microporosity.

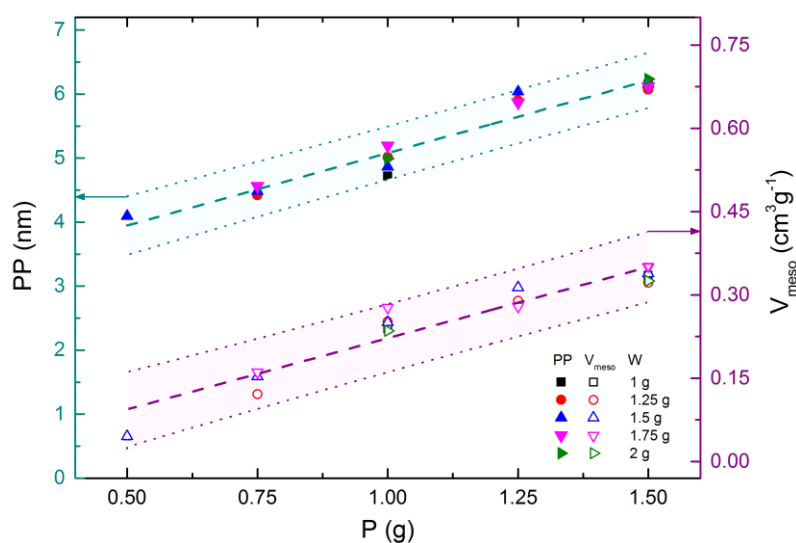


Figure 3.10. Peak position (PP, solid symbols) and mesopore volume (V_{meso} , hollow symbols) as a function of the initial mass of P and W; linear fits and corresponding 95 % prediction intervals (dashed and dotted lines, respectively) are presented for both quantities. [Adapted from Castro-Gutiérrez et al. (2018)²²]

3.6 Effect of carbonization temperature

T2P1W2_60 was subjected to higher carbonization temperatures, up to 1500 °C, to test the thermal stability of the mesostructure and to study some possible changes in pore texture. When heated up from 900 to 1500 °C, type Ia-IV isotherms were obtained in all cases as shown in Figure 3.11 along with their corresponding PSDs, and a 2D hexagonal structure was further corroborated by TEM images (Figure 3.12a). A slight widening of the mesopores with temperature, from 5 to 5.4 nm, can be observed from the PSDs (Figure 3.11b). Besides, Figure 3.12b shows the evolution with the temperature of $V_{\mu,NLDFT}$ and V_{meso} as well as the changes of A_{BET} . An increase of V_{meso} with temperature was observed, from 0.24 to 0.43 cm³ g⁻¹. From 900 to 1100 °C, a development of microporosity occurred, reflected by an increase of $V_{\mu,NLDFT}$ from 0.17 to 0.26 cm³ g⁻¹ and thus by an increase of A_{BET} . However, higher temperatures had no significant impact on these quantities, in the range from 1100 to 1500 °C their values remained at 0.25 ± 0.02 cm³ g⁻¹ for $V_{\mu,NLDFT}$ and at 797 ± 41 m² g⁻¹ for A_{BET} .

Aside from the pore texture characteristics, Raman spectra of CT2P1W2_60 samples treated at different temperatures and given in Figure 3.12c, show that these OMCs are poorly crystallized at the nanoscale. All samples indeed displayed the typical spectra of highly disordered carbon, where the D₁ band is more intense than the G band^{13,43-46} (see Figure A1.2 for detailed deconvolution of spectra). Due to the phenolic nature of tannin, all materials were non-graphitizable and were in the carbonization regime within the present experimental conditions, for which the intensity of the D₁ band (~1345 cm⁻¹) increases with temperature.

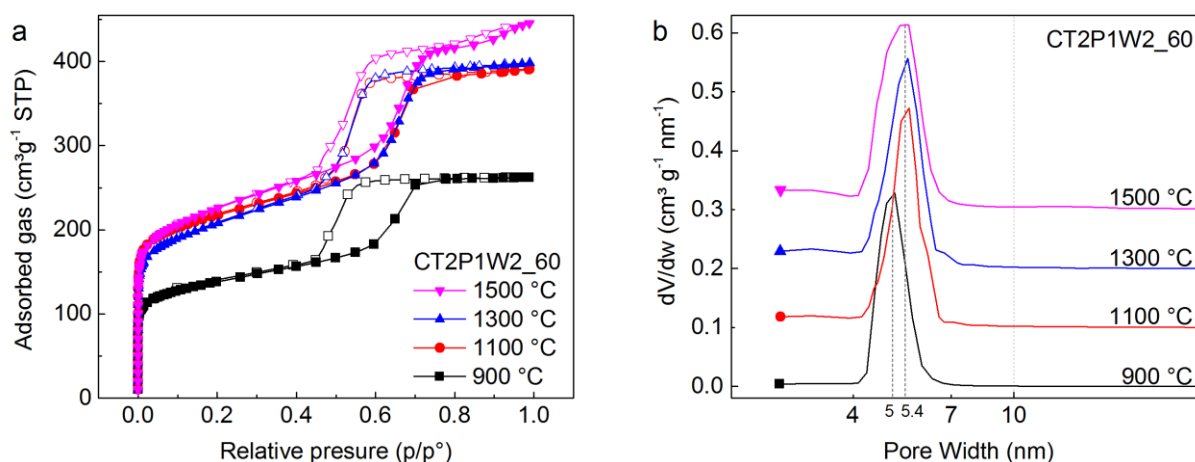


Figure 3.11. (a) N₂ adsorption-desorption isotherms and (b) corresponding PSDs for CT2P1W2_60 pyrolyzed at different temperatures. For easier viewing, the PSDs are offset by 0.1 cm³ g⁻¹ nm⁻¹. [Reproduced from Castro-Gutiérrez et al. (2018)²²]

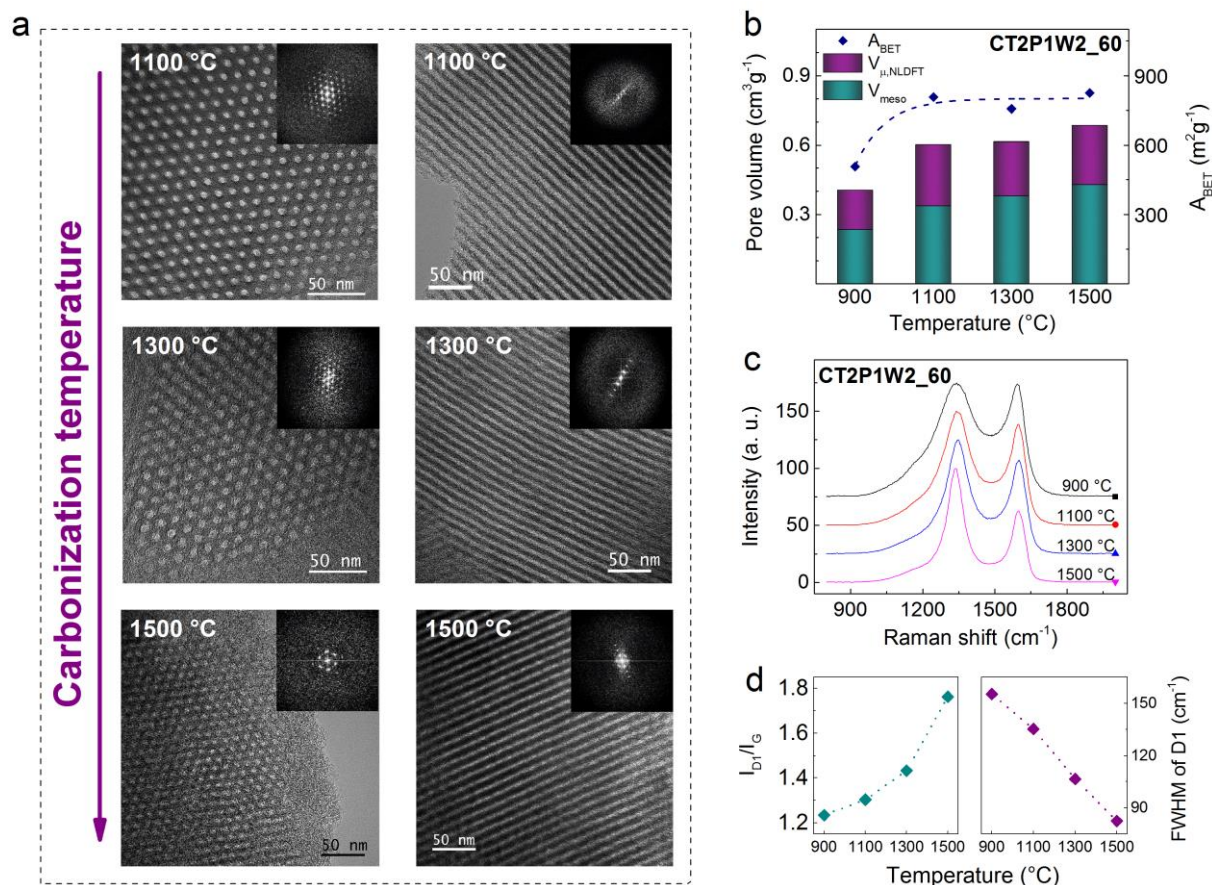


Figure 3.12. (a) TEM images of CT2P1W2_60 pyrolyzed at 1100, 1300 and 1500 °C; the corresponding FFT are shown in the insets. (b) BET area (A_{BET}) and micro and mesopore volume ($V_{\mu, NLDFT}$ and V_{meso} , respectively) of CT2P1W2_60 as a function of pyrolysis temperature; the dotted line provides only a guide for the eye. (c) Raman spectra of CT2P1W2_60 pyrolyzed at different temperatures, presented with an offset of 20 a. u. of intensity for easier viewing; (d) D₁/G intensity ratio and full width at half-maximum (FWHM) of the D₁ band as a function of temperature. [Reproduced from Castro-Gutiérrez et al. (2018)²²]

Thus, the increase of the D₁/G intensity ratio (I_{D1}/I_G in Figure 3.12d), associated with an obvious narrowing of the D₁ band (FWHM of D₁ in Figure 3.12d) at higher temperatures, indicates an increase of the crystallite size and hence an improvement of the long-range order in the carbon.⁴⁶

3.7 Applications

Besides the foreseen applications as electrodes for SCs, which are detailed in Chapters 5 to 7, other applications for the mechano-synthesized materials are proposed and briefly discussed below.

3.7.1 Oil spill remediation

Figure 3.13a shows measurements of the water contact angle (WCA) on CT2P1W2_60 as high as 157° and it only slightly decreased to 147° when pyrolysis temperature was increased up to 1500°C . The material exhibited low affinity to the water drop that remained attached to the needle when it was pulled up from the surface and the volume of the drop had to be double up to $4\ \mu\text{L}$ to get it on the surface and measure the WCA. These very high WCAs are in the range of materials used for efficient oil/water separation based on graphene oxide aerogels³ or polymers.⁴ Therefore, a simple proof of concept for organics removal from water was performed. For this purpose, $0.3\ \text{mL}$ of heptane were poured in $1.5\ \text{mL}$ of water, afterwards a piece of $100\ \text{mg}$ of agglomerated CT2P1W2_60 was introduced. Total heptane removal was obtained in less than $50\ \text{s}$, as showed in Figure 3.13b. The ability to selectively remove oil/organic solvents while repelling water is an interesting feature of these materials that merits further research since the use of sorbent materials is considered one of the most efficient and cost-effective methods among the environmental remediation strategies for oil spills.^{47,48}

3.7.2 CO₂ adsorption from humid gases

All the OMCs synthesized herein presented a high V_{meso} sometimes associated with an ordered mesostructure; both factors should facilitate gas diffusion to the ultra-microporosity. In a previous study, phenolic resin-based mesoporous carbons were tested as CO₂ adsorbents after activation, CO₂ uptakes (at $0.1\ \text{MPa}$ and 0°C) were comparable to the values achieved for MOFs.⁴⁹ Figure 3.13c shows the CO₂ adsorption of as-synthesized OMCs presented in this chapter and of some activated materials described in detail in the following chapters. CO₂ storage increased from 2.8 to $5.6\ \text{mmol g}^{-1}$ as a function of $V_{\mu, \text{NLDFT}}$, these CO₂ capacities were

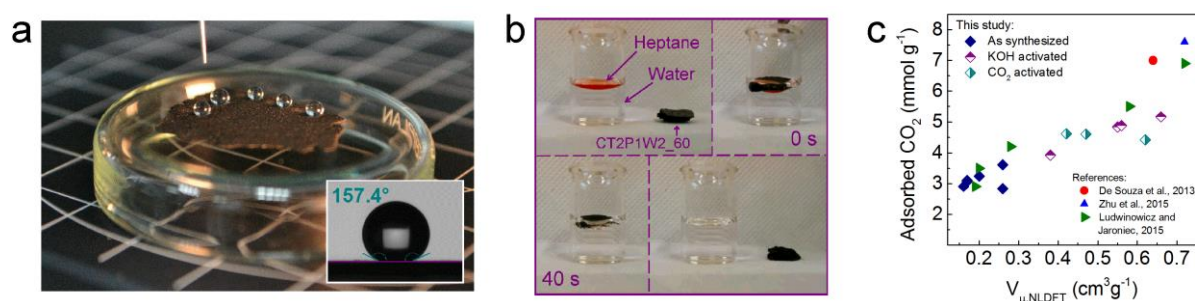


Figure 3.13. (a) Set of water drops on CT2P1W2_60, the insert shows a WCA = 157.4° . (b) Adsorption of heptane by CT2P1W2_60 in $40\ \text{s}$. (c) CO₂ adsorption capacities, at $0.1\ \text{MPa}$ and 0°C , as a function of micropore volume for materials from this study and materials reported in the open literature.^{49–51} [Adapted from Castro-Gutiérrez et al. (2018)²²]

in the range of the values reported in the open literature.^{49–51} In contrast to MOFs, the tannin-derived materials of this study would have the advantage of being cheaper and insensitive to humidity.

3.8 Conclusion

A novel surfactant-water-assisted mechanochemical mesostructuration (SWAMM) method for preparing OMCs was developed; this method is environment-friendly due to the use of mimosa tannin, a natural and renewable carbon precursor, and to the absence of toxic or hazardous substances during synthesis.

Different parameters, such as the milling time, the pH of the added liquid and the surfactant to water weight ratio (P:W) were optimized to develop an easy and fast, one-pot method. Indeed, the SWAMM method requires only 1 h of ball-milling to obtain a mesophase using only tannin, Pluronic ® F127 and small quantities of water (unaltered pH); no additional drying or curing steps were needed before carbonization. Furthermore, materials can be tailored between a disordered or an ordered 2D hexagonal mesostructure just by adjusting P:W.

The resultant OMCs, exhibit BET areas of $\sim 600 \text{ m}^2 \text{ g}^{-1}$ and proved to be thermally stable under inert atmosphere up to $1500 \text{ }^\circ\text{C}$, maintaining their 2D hexagonal geometry with minimum changes of peak mesopore width and increasing its BET area to $\sim 800 \text{ m}^2 \text{ g}^{-1}$. Upon activation, the micropore volume increased from ~ 0.1 to $\sim 0.3 \text{ cm}^3 \text{ g}^{-1}$ for the as-synthesized materials to ~ 0.4 to $\sim 0.7 \text{ cm}^3 \text{ g}^{-1}$ for the activated ones.

Besides the main intended application as electrodes for SCs, being the objective of this thesis, these materials could find relevant applications in environmental remediation strategies for oil spills or in selective CO_2 adsorption from humid gases or as electrodes of supercapacitors using aqueous or organic electrolytes, among others.

3.9 References

1. Frackowiak, E. Carbon materials for supercapacitor application. *Physical Chemistry Chemical Physics* 9, 1774 (2007).
2. Inagaki, M., Konno, H. & Tanaike, O. Carbon materials for electrochemical capacitors. *Journal of Power Sources* 195, 7880–7903 (2010).
3. Lee, J., Han, S. & Hyeon, T. Synthesis of new nanoporous carbon materials using nanostructured silica materials as templates. *Journal of Materials Chemistry* 14, 478–486 (2004).
4. Lee, J., Kim, J. & Hyeon, T. Recent Progress in the Synthesis of Porous Carbon Materials. *Advanced Materials* 18, 2073–2094 (2006).
5. Cai, X. et al. Diatom-Templated Synthesis of Ordered Meso/Macroporous Hierarchical Materials. *European Journal of Inorganic Chemistry* 2006, 3641–3645 (2006).
6. Xia, Y. et al. Biotemplated fabrication of hierarchically porous NiO/C composite from lotus pollen grains for lithium-ion batteries. *Journal of Materials Chemistry* 22, 9209–9215 (2012).
7. Liu, H.-J. et al. Highly ordered mesoporous carbon nanofiber arrays from a crab shell biological template and its application in supercapacitors and fuel cells. *Journal of Materials Chemistry* 20, 4223 (2010).
8. Libbrecht, W., Verberckmoes, A., Thybaut, J. W., Van Der Voort, P. & De Clercq, J. Soft templated mesoporous carbons: Tuning the porosity for the adsorption of large organic pollutants. *Carbon* 116, 528–546 (2017).
9. Meng, Y. et al. A Family of Highly Ordered Mesoporous Polymer Resin and Carbon Structures from Organic–Organic Self-Assembly. *Chemistry of Materials* 18, 4447–4464 (2006).
10. Huang, Y. et al. Highly Ordered Mesoporous Carbonaceous Frameworks from a Template of a Mixed Amphiphilic Triblock-Copolymer System of PEO–PPO–PEO and Reverse PPO–PEO–PPO. *Chemistry – An Asian Journal* 2, 1282–1289 (2007).
11. Wang, X., Liang, C. & Dai, S. Facile Synthesis of Ordered Mesoporous Carbons with High Thermal Stability by Self-Assembly of Resorcinol–Formaldehyde and Block Copolymers under Highly Acidic Conditions. *Langmuir* 24, 7500–7505 (2008).
12. Schlienger, S., Graff, A.-L., Celzard, A. & Parmentier, J. Direct synthesis of ordered mesoporous polymer and carbon materials by a biosourced precursor. *Green Chem.* 14, 313–316 (2012).
13. Braghiroli, F. L., Fierro, V., Parmentier, J., Pasc, A. & Celzard, A. Easy and eco-friendly synthesis of ordered mesoporous carbons by self-assembly of tannin with a block copolymer. *Green Chem.* 18, 3265–3271 (2016).
14. James, S. L. et al. Mechanochemistry: opportunities for new and cleaner synthesis. *Chem. Soc. Rev.* 41, 413–447 (2012).
15. Wang, G.-W. Mechanochemical organic synthesis. *Chemical Society Reviews* 42, 7668–7700 (2013).
16. Kaupp, G. Mechanochemistry: the varied applications of mechanical bond-breaking. *CrystEngComm* 11, 388–403 (2009).

17. Tanaka, K. & Toda, F. Solvent-Free Organic Synthesis. *Chemical Reviews* 100, 1025–1074 (2000).
18. Wang, Q. et al. A facile solvent-free route to synthesize ordered mesoporous carbons. *RSC Advances* 4, 32113–32116 (2014).
19. Kaupp, G. Reactive milling with metals for environmentally benign sustainable production. *CrystEngComm* 13, 3108 (2011).
20. Zhu, J. et al. Nitrogen-enriched, ordered mesoporous carbons for potential electrochemical energy storage. *J. Mater. Chem. A* 4, 2286–2292 (2016).
21. Zhang, P. et al. Solid-state synthesis of ordered mesoporous carbon catalysts via a mechanochemical assembly through coordination cross-linking. *Nature Communications* 8, 15020 (2017).
22. Castro-Gutiérrez, J. et al. Synthesis of perfectly ordered mesoporous carbons by water-assisted mechanochemical self-assembly of tannin. *Green Chemistry* 20, 5123–5132 (2018).
23. Liang, C., Hong, K., Guiochon, G. A., Mays, J. W. & Dai, S. Synthesis of a Large-Scale Highly Ordered Porous Carbon Film by Self-Assembly of Block Copolymers. *Angewandte Chemie International Edition* 43, 5785–5789 (2004).
24. Xu, F. et al. Acid Induced Self-Assembly Strategy to Synthesize Ordered Mesoporous Carbons from Biomass. *ACS Sustainable Chemistry & Engineering* 4, 4473–4479 (2016).
25. Braghiroli, F. L. et al. Hydrothermal carbons produced from tannin by modification of the reaction medium: Addition of H⁺ and Ag⁺. *Industrial Crops and Products* 77, 364–374 (2015).
26. Mortensen, K. Phase behaviour of poly (ethylene oxide)-poly (propylene oxide)-poly (ethylene oxide) triblock-copolymer dissolved in water. *EPL (Europhysics Letters)* 19, 599 (1992).
27. Mortensen, K. & Pedersen, J. S. Structural study on the micelle formation of poly (ethylene oxide)-poly (propylene oxide)-poly (ethylene oxide) triblock copolymer in aqueous solution. *Macromolecules* 26, 805–812 (1993).
28. Mortensen, K. & Brown, W. Poly (ethylene oxide)-poly (propylene oxide)-poly (ethylene oxide) triblock copolymers in aqueous solution. The influence of relative block size. *Macromolecules* 26, 4128–4135 (1993).
29. Wanka, G., Hoffmann, H. & Ulbricht, W. Phase diagrams and aggregation behavior of poly (oxyethylene)-poly (oxypropylene)-poly (oxyethylene) triblock copolymers in aqueous solutions. *Macromolecules* 27, 4145–4159 (1994).
30. Almgren, M., Brown, W. & Hvidt, S. Self-aggregation and phase behavior of poly (ethylene oxide)-poly (propylene oxide)-poly (ethylene oxide) block copolymers in aqueous solution. *Colloid & Polymer Science* 273, 2–15 (1995).
31. Mortensen, K. & Talmon, Y. Cryo-TEM and SANS microstructural study of pluronic polymer solutions. *Macromolecules* 28, 8829–8834 (1995).
32. Alexandridis, P. & Hatton, T. A. Poly(ethylene oxide)-poly(propylene oxide)-poly(ethylene oxide) block copolymer surfactants in aqueous solutions and at interfaces: thermodynamics, structure, dynamics, and modeling. *Colloids and Surfaces A: Physicochemical and Engineering Aspects* 96, 1–46 (1995).

33. Mortensen, K. Structural studies of aqueous solutions of PEO-PPO-PEO triblock copolymers, their micellar aggregates and mesophases; a small-angle neutron scattering study. *Journal of Physics: Condensed Matter* 8, A103–A124 (1996).
34. Mortensen, K. Structural properties of self-assembled polymeric aggregates in aqueous solutions. *Polymers for Advanced Technologies* 12, 2–22 (2001).
35. Riess, G. Micellization of block copolymers. *Progress in Polymer Science* 28, 1107–1170 (2003).
36. Liu, S. & Li, L. Multiple Phase Transition and Scaling Law for Poly(ethylene oxide)–Poly(propylene oxide)–Poly(ethylene oxide) Triblock Copolymer in Aqueous Solution. *ACS Applied Materials & Interfaces* 7, 2688–2697 (2015).
37. Liu, S. & Li, L. Molecular interactions between PEO–PPO–PEO and PPO–PEO–PEO triblock copolymers in aqueous solution. *Colloids and Surfaces A: Physicochemical and Engineering Aspects* 484, 485–497 (2015).
38. Long, D., Qiao, W., Zhan, L., Liang, X. & Ling, L. Effect of template and precursor chemistry on pore architectures of triblock copolymer-templated mesoporous carbons. *Microporous and Mesoporous Materials* 121, 58–66 (2009).
39. Jin, J., Nishiyama, N., Egashira, Y. & Ueyama, K. Pore structure and pore size controls of ordered mesoporous carbons prepared from resorcinol/formaldehyde/triblock polymers. *Microporous and Mesoporous Materials* 118, 218–223 (2009).
40. Xu, J., Wang, A. & Zhang, T. A two-step synthesis of ordered mesoporous resorcinol–formaldehyde polymer and carbon. *Carbon* 50, 1807–1816 (2012).
41. Yang, Z., Gu, X. & Liang, X. Classification and Optimization Model of Mesoporous Carbons Pore Structure and Adsorption Properties Based on Support Vector Machine. *Computer Modeling in Engineering & Sciences* 74, 161–181 (2011).
42. Smarsly, B., Gibaud, A., Ruland, W., Sturmayr, D. & Brinker, C. J. Quantitative SAXS Analysis of Oriented 2D Hexagonal Cylindrical Silica Mesostructures in Thin Films Obtained from Nonionic Surfactants. *Langmuir* 21, 3858–3866 (2005).
43. Nathan, M. I., Smith, J. E. & Tu, K. N. Raman spectra of glassy carbon. *Journal of Applied Physics* 45, 2370–2370 (1974).
44. Dillon, R. O., Woollam, J. A. & Katkanant, V. Use of Raman scattering to investigate disorder and crystallite formation in as-deposited and annealed carbon films. *Physical Review B* 29, 3482 (1984).
45. Ferrari, A. C. & Robertson, J. Interpretation of Raman spectra of disordered and amorphous carbon. *Physical review B* 61, 14095 (2000).
46. Szczurek, A. et al. Carbon periodic cellular architectures. *Carbon* 88, 70–85 (2015).
47. Khin, M. M., Nair, A. S., Babu, V. J., Murugan, R. & Ramakrishna, S. A review on nanomaterials for environmental remediation. *Energy & Environmental Science* 5, 8075 (2012).
48. Tran, D. N. H., Kabiri, S., Sim, T. R. & Losic, D. Selective adsorption of oil–water mixtures using polydimethylsiloxane (PDMS)–graphene sponges. *Environmental Science: Water Research & Technology* 1, 298–305 (2015).
49. de Souza, L. K. C. et al. Enhancement of CO₂ adsorption on phenolic resin-based mesoporous carbons by KOH activation. *Carbon* 65, 334–340 (2013).

50. Zhu, B., Qiu, K., Shang, C. & Guo, Z. Naturally derived porous carbon with selective metal- and/or nitrogen-doping for efficient CO₂ capture and oxygen reduction. *Journal of Materials Chemistry A* 3, 5212–5222 (2015).
51. Ludwinowicz, J. & Jaroniec, M. Effect of activating agents on the development of microporosity in polymeric-based carbon for CO₂ adsorption. *Carbon* 94, 673–679 (2015).

Chapter 4

Detailed study of the mesoporous structure

4.1 Introduction

In Chapter 3, it was demonstrated that the surfactant-water-assisted mechanochemical mesostructuration (SWAMM) method can be used to produce either disordered mesoporous carbons (DMCs) with a worm-like mesostructure or ordered mesoporous carbons (OMCs) with a 2D hexagonal mesostructure by just changing the amounts of surfactant and water. In this chapter, one of each type of such mesoporous carbons (MCs) was chosen for deeper characterization, aiming to obtain further information on the connectivity of their mesoporous structure and their possible effect on the performance of the materials as electrodes for SCs or in other potential applications.

A deeper analysis of the adsorption-desorption isotherms obtained using different probe molecules and their corresponding PSDs, combined with the scanning of the hysteresis loops can provide more information on the connectivity of the pore network by identifying the mechanisms that control the desorption. As shown in Figure 4.1, desorption in H1 loops occurs by liquid-vapor transitions at equilibrium (Figure 4.1a), while in H2 loops is controlled by either pore blocking/percolation or cavitation and, for ink-bottle pores, the occurring desorption mechanism depends on a critical value of neck width, w_c (Figure 4.1b-d). H5 loops can be associated to two types of desorption mechanisms due to the presence of open and blocked pores in the mesoporous structure (Figure 4.1e).¹ Thanks to the adsorption analysis carried out using different adsorbates, it is possible to identify the desorption mechanism occurring in a material. Indeed, when desorption occurs by percolation, the pressure at which the onset of desorption is observed depends only on the size of the necks of the ink-bottle pores and not on the chosen adsorbate. On the contrary, when desorption is controlled by cavitation, a shift of the pressure that marks the onset of desorption is observed when using different adsorbates. Even more, the comparison of the PSDs derived from the adsorption and desorption branches of the isotherms provides information on the pore bodies and necks sizes, respectively.^{2,3} On the other hand, the information gathered from the scanning of the hysteresis loops is based on the behavior of the scanned (secondary) desorption branches compared to that of the principal (boundary) desorption branch, as shown in (Figure 4.1f). Materials' structures with independent pores exhibit desorption branches retaining the same shapes even for partial filling of the network (Figure 4.1f (left)). In a connected pore system, desorption depends on the state of neighboring pores, so the scanning of the hysteresis loop gives rise to secondary desorption curves of different shapes (Figure 4.1f (right)).⁴⁻⁶

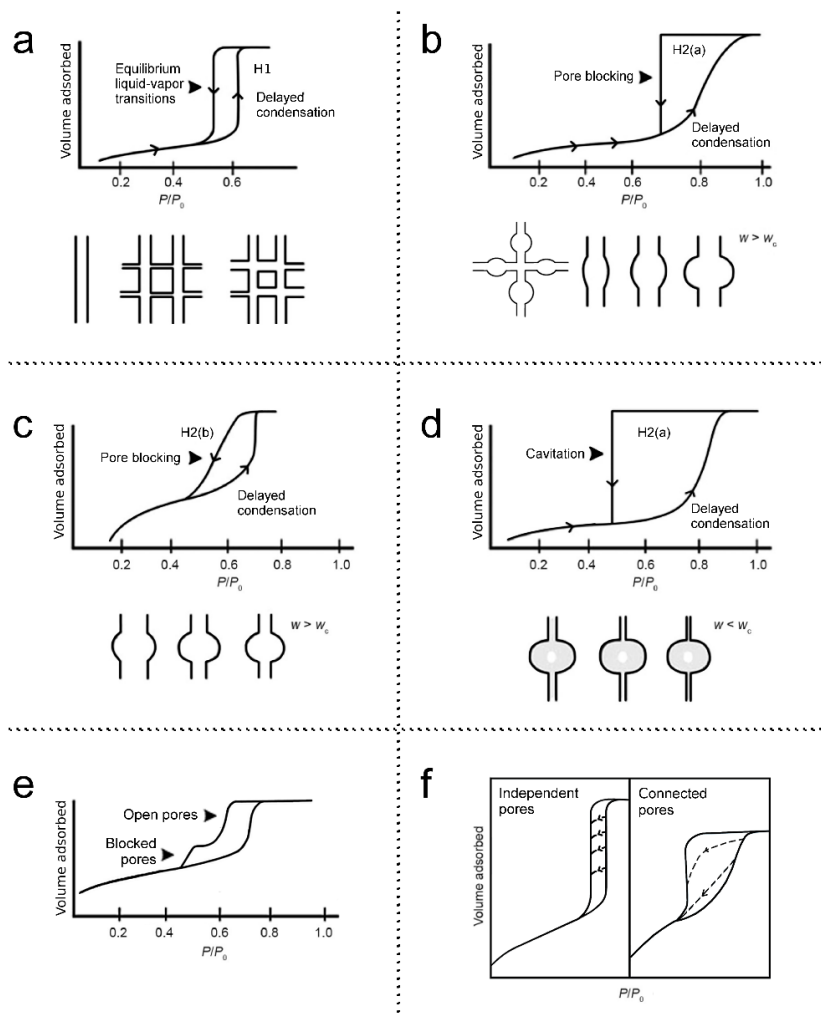


Figure 4.1. Hysteresis loops and their associated mesoporous structures and adsorption-desorption mechanisms: (a) H1 type, corresponding to uniform cylindrical or ordered 3D pore networks; (b – d) H2 type, corresponding to ink-bottle pore networks; if the width of the neck is below a critical value (w_c), desorption occurs by cavitation; (e) H5 type found in pore structures with open and blocked pores. (f) Examples of scanned hysteresis loops for materials having independent or connected mesopores. [Adapted from Thommes and Cychosz (2014)¹ and Thommes (2010)⁶].

Although the application of DFT models to the adsorption-desorption isotherms of gases is a powerful tool to obtain and analyze the PSD of materials, it normally assumes pores with slit, cylinder or sphere geometries. The idealization of the pore shapes and the dependence on the correct selection of fitting parameters of the DFT models lead to uncertainties in the PSD calculations.⁷ In this sense, immersion calorimetry tests provide an alternative model-independent method to obtain the PSD in the microporous range to complement physisorption-derived data, allowing also to estimate the accessible surface area to molecules of different sizes and to observe molecular sieve and connectivity effects.^{7,8} The immersion calorimetry method

assumes that the heat of immersion ($-\Delta H_{imm}$) is proportional to the available surface of the liquid, which can be calculated by using the areal enthalpy of immersion ($-\Delta h_{imm}$) of a reference materials as the proportionality constant (see Section 2.3).

Therefore, this chapter presents the deeper textural characterization of a DMC and an OMC performed by three techniques: adsorption of nitrogen and argon; immersion calorimetry in *n*-hexane (nHEX), 2-methylpentane (2MP) and 2,2-dimethylbutane (22DMB) in liquid phase; and, adsorption of the aforementioned C₆ alkanes in vapor phase.

Herein, the SWAMM method was used to synthesized a DMC and an OMC material. As described in Chapter 3, mimosa tannin (T), Pluronic® F127 (P) and water (W) were milled together in a planetary ball mill for 60 min and the recovered materials were carbonized at 900 °C. The T:P:W weight ratio used during the synthesis was 2:2:2 g for producing the DMC, and 2:0.75:1.75 g for the OMC. TEM images of each material were obtained to confirm their disordered or ordered mesoporous structure.

The characterization techniques were detailed described in Chapter 2, Section 2.2 and 2.3, and briefly described below. Physisorption measurements were carried out using argon (at -186 °C), nitrogen (at -196 °C) and carbon dioxide (at 0 °C) in an Autosorb iQMP device (Quantachrome) and a 3Flex manometric sorption analyzer (Micromeritics) Prior to the measurement, both samples were outgassed at 150 °C for 12 h under turbo pump vacuum. Adsorption experiments in vapor phase were performed in a manometric system designed and manufactured by the LMA group at the University of Alicante and currently commercialized by Quantachrome Instruments under the name Vstar. Finally, the evaluation of the heat of immersion of DMC and OMC samples in the three C₆ alkanes in liquid phase was performed in a Setaram C80D calorimeter working at 30 °C.

4.2 Morphology of the mesoporous carbons

Transmission electron microscopy (TEM) images of DMC and OMC materials are shown in Figure 4.2. In agreement with the results previously described for materials synthesized by the SWAMM method (Chapter 3),⁹ the DMC exhibits a highly disordered worm-like mesopore structure (Figure 4.2a) whereas the OMC presents a 2D hexagonal structure (*p6mm* space group) with cylindrical mesopore channels, clearly recognized in the longitudinal and

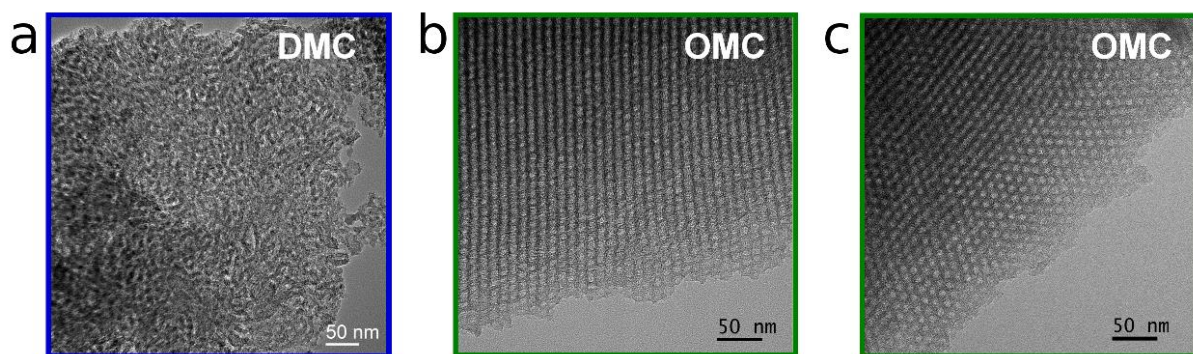


Figure 4.2. TEM images of (a) the disordered mesoporous carbon (DMC); and (b) longitudinal and (c) transversal views of the ordered mesoporous carbon (OMC).

transversal views of the material shown in Figure 4.2b and 4.2c, respectively. Also from the TEM images, the pore size in the OMC can be roughly estimated to be between 5 and 7 nm. Given the disordered nature of the mesoporous structure in the DMC, to obtain an estimation of pore size from TEM images of this material is rather complicated; however, a broader pore size distribution (PSD), compare to that of OMC, can be expected.

4.3 Adsorption of Ar, N₂ and CO₂

Figure 4.3a and 4.3b show the Ar and N₂ adsorption-desorption isotherms of DMC and OMC, respectively, which are combinations of type Ia, typical of ultramicroporous solids, and type IV(a) characteristic of mesoporous materials where monolayer-multilayer adsorption is followed by capillary condensation.¹⁰ Irrespective of the used adsorbate, all isotherms reveal “low-pressure hysteresis”, which has been reported for some carbon materials and was associated with slow desorption kinetics due to an extremely tortuous micropore network or a possible swelling effect.^{11–13} For the DMC and OMC samples, it can be seen that the observed low-pressure hysteresis is fully reproducible between consecutive sorption experiments on the same sample, *i.e.*, a potential deformation is also fully reversible for both materials, and the adsorption/desorption isotherms are fully repeatable (see Figure 4.4). Therefore, it is possible to carry out a comparative textural analysis, where the derived values are considered as qualitative tools for comparison between DMC and OMC materials, rather than as an absolute assessment of these properties.

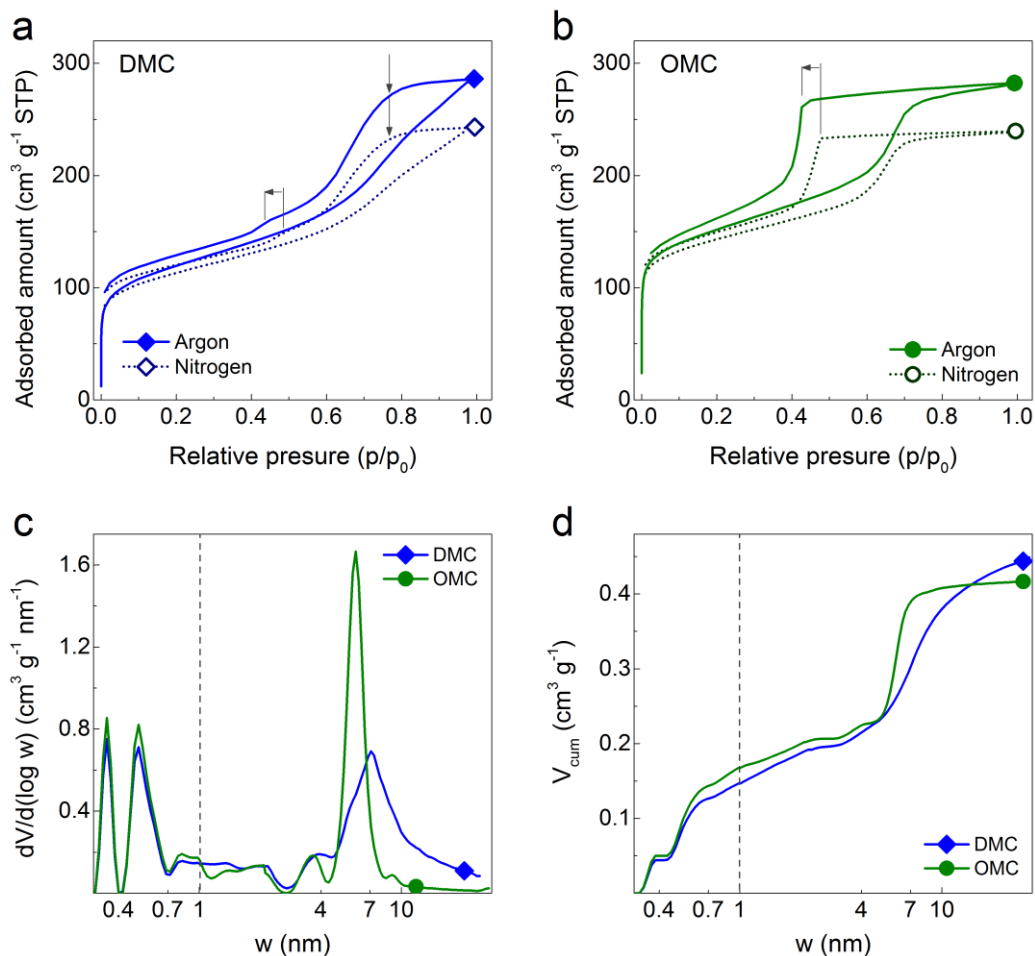


Figure 4.3. Argon (87 K) and nitrogen (77 K) adsorption-desorption isotherms for: (a) DMC and (b) OMC materials; the arrows mark the approximate onset of desorption in each case. Combined pore size distributions (PSDs) derived from the adsorption branches of argon and carbon dioxide isotherms (for $w > 1$ nm and $w < 1$ nm, respectively, separated by the dashed line), presented in (c) differential ($dV/d(\log w)$) and (d) cumulated (V_{cum}) forms.

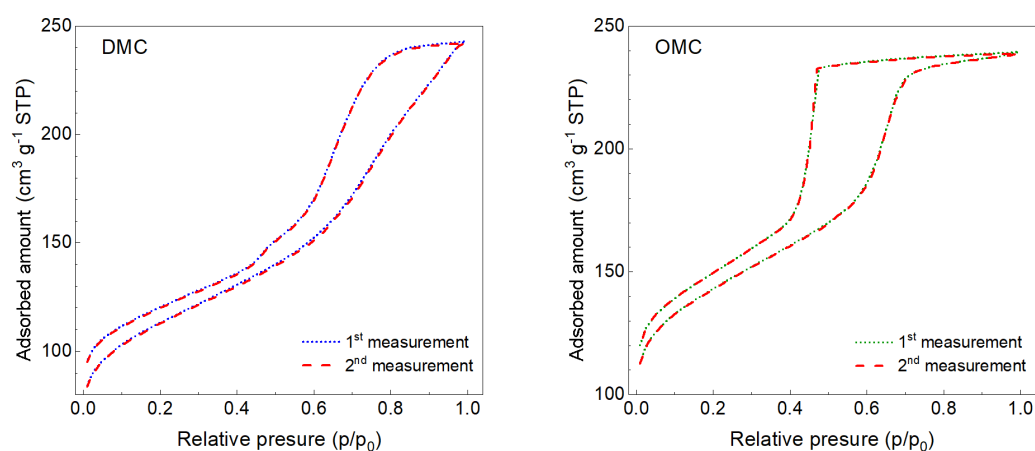


Figure 4.4. Nitrogen (N_2) isotherms at 77 K obtained by performing two consecutive measurements on the same sample of a disordered and an ordered mesoporous carbon (DMC and OMC, respectively).

The combined pore size distributions (PSDs) in Figure 4.3c and the cumulative pore volumes in Figure 4.3d were obtained by applying a dedicated Ar/carbon QSDFT kernel to the Ar adsorption branch and a dedicated CO₂/carbon NLDFT kernel to the CO₂ adsorption isotherm data for assessing ultramicropores in a reliable way.^{7,10} The Ar-QSDFT kernel accounts for surface heterogeneities and takes quantitatively into account the delay in the condensation due to the existence of metastable adsorption film and hindered nucleation of liquid bridges.¹⁴⁻¹⁶ The pore geometries of both samples were assumed as a slit/cylindrical hybrid pore model, *i.e.*, a slit pore model in the micropore range and a cylindrical pore model for pores larger than 2 nm. The CO₂-NLDFT kernel assumes, similarly to the Ar-QSDFT kernel, a slit pore geometry in the micropore range.

Figure 4.3c and 4.3d clearly demonstrate the similarity of the PSDs in the ultramicroporous regime (< 0.7 nm) for both materials, which implies that they have similar microporous textures, due to the use of the same carbon precursor, the MT extract, for their synthesis. As shown in Figure 4.3a and 4.3b, the differences are essentially in the mesopore range, which is reflected in the different adsorption/desorption behavior at higher relative pressures ($p/p_0 > 0.4$) and the corresponding PSDs (Figure 4.3c). The OMC exhibits a narrower PSD centered at ~6 nm while the DMC contains pores over a wider range of mesopores from 3 to 30 nm. From the Ar adsorption isotherms, the apparent BET areas (A_{BET} , calculated by applying the procedure described by Thommes et al.³⁹ and Rouquerol et al.⁴⁷) are 379 and 487 m² g⁻¹ for DMC and OMC, respectively. The micropore volume (V_{μ}) was found to be slightly higher for the OMC, but of similar magnitude to that of the DMC, *i.e.*, ~0.2 cm³ g⁻¹. This is consistent with previous studies that have shown that when pure MT extract is submitted to pyrolysis, the resultant carbon material is essentially microporous, with V_{μ} always around 0.2 ± 0.05 cm³ g⁻¹. In contrast, the DMC has a slightly higher mesopore volume (V_{meso}) than the OMC. The mesopores and their pore sizes can be developed by hydrothermal carbonization (HTC) treatments or by template methods, therefore V_{meso} can vary much more, depending on the synthesis method.^{32,48-52}

The textural analysis discussed so far already reveals that both samples are hierarchical micro-mesoporous materials. However, information on pore network connectivity can only be gained by a thorough comparison and analysis of their PSDs, obtained from both adsorption and desorption branches using different probe molecules such as Ar at 87 K and N₂ at 77 K. By

identifying the mechanisms that control gas desorption/evaporation from the mesopores, it is possible to distinguish between freely accessible and constricted mesopores.^{53,54}

Figure 4.5b and 4.5e demonstrate that both probe molecules (Ar and N₂) yield the same PSD from the adsorption branch for DMC and OMC, respectively. Figure 4.5a compares the PSDs obtained from the adsorption and desorption of Ar for the DMC, for which the Ar-QSDFT metastable adsorption branch kernel was applied to the adsorption branch and the equilibrium transition kernel was applied to the desorption data. Hence, in the absence of pore networking effects (*e.g.*, pore blocking/percolation, cavitation), the PSD curves from adsorption and desorption branches should overlap.^{44,45} Indeed, the PSDs derived from the Ar adsorption and desorption branches coincide over a wide range of pore sizes, but for the mesopore size range, deviations are observed. This indicates that a large portion of the mesoporous network in the DMC is freely accessible, while the other part of the mesopores can only be accessed through narrow necks. The type of constriction, *i.e.*, necks that lead to either pore blocking or to cavitation-induced desorption/evaporation, can be distinguished by comparing the effects of the pore network on the adsorption of two different fluids, here N₂ and Ar. Figure 4.5b demonstrates very good agreement between Ar and N₂ PSDs obtained from the corresponding adsorption

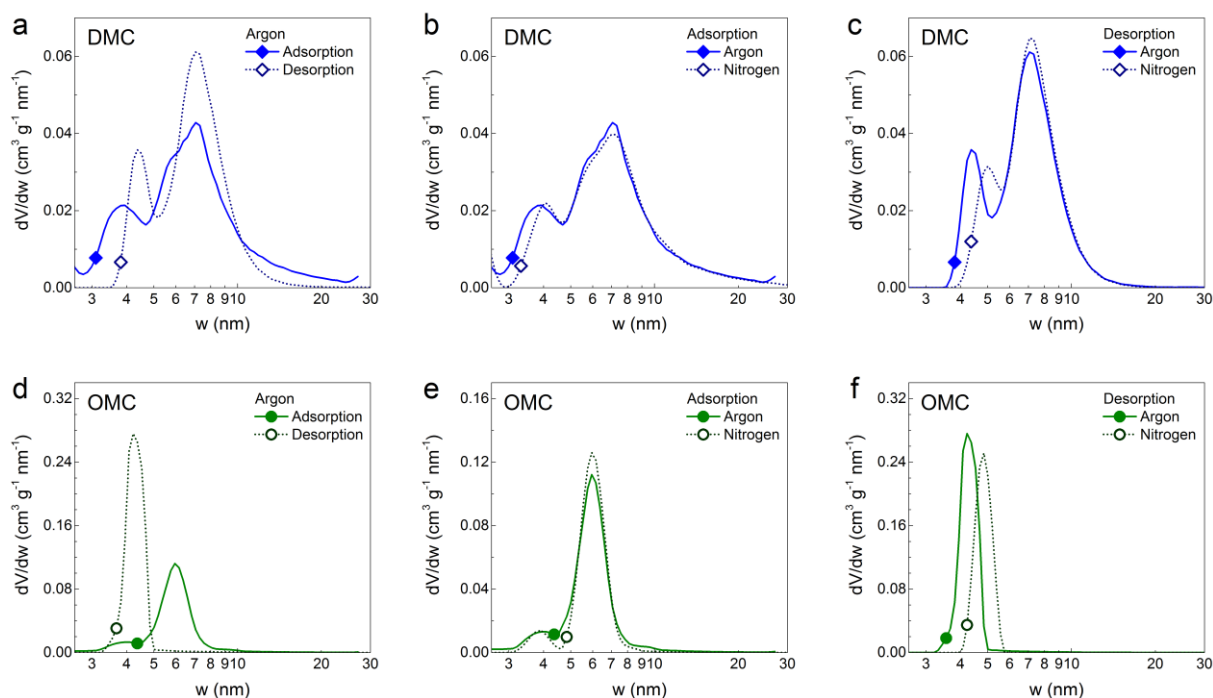


Figure 4.5. Pore size distributions (PSDs) in the mesopore range for (a, b, c) DMC and (d, e, f) OMC samples. (a, d) PSDs obtained from the adsorption and desorption branches of Ar isotherms. PSDs obtained from Ar and N₂ isotherms using their (b, e) adsorption branches and (c, f) desorption branches.

branches. The PSDs obtained from the desorption branches also show very good agreement over a wide range of pore sizes; however, differences are observed in the lower mesopore range, caused by cavitation-induced evaporation from a small fraction of the mesopores which can only be accessed through narrow pore necks. The size of these necks can be in ranges from micropores up to a critical width of *ca.* 5 – 7 nm.^{53–55} These results combined with data from the comparison of the Ar adsorption and desorption branches, reveal a complex pore network structure with differently accessible mesopores within the DMC material. Based on the performed analysis, the majority of mesopores are freely accessible, while a small part of the mesopore network is accessible through narrow necks.

In contrast, for the OMC material, almost the whole mesopore network is only accessible through narrow constrictions. The existence of pore network effects such as pore blocking or cavitation for the underlying pore evaporation mechanism is confirmed by the disagreement of the PSDs obtained from the Ar adsorption/desorption branches, see Figure 4.5d. Moreover, the strong disagreement of PSDs obtained from the Ar and N₂ desorption isotherms (Figure 4.5f) suggests that evaporation of condensed fluid from the complete mesoporosity of the OMC occurs mostly only by cavitation. As already discussed, in addition to its mesopore network, the OMC exhibits mainly ultramicropores with pore sizes of 0.35 and 0.5 nm and a small fraction of wider micropores (Figure 4.3c). Hence, these micropores must be the entrances of the mesopores, which then lead to cavitation upon depletion of the mesopores. As OMC and DMC have similar textural properties in the microporous range (see Figure 4.3c), the micropores should also be responsible for the fraction of the mesopores that is emptied by cavitation in the DMC material.

Furthermore, Figure 4.6 shows the scanning of the N₂ adsorption isotherm confirming the previous analysis. Figure 4.6a shows that for the DMC the behavior of the scanned desorption branches confirms the presence of the two porous systems. In the upper part of the hysteresis loop ($p/p_0 > 0.6$), desorption occurs by percolation effects for the secondary branches exhibiting the behavior shown in Figure 4.1f (right), which corresponds to a well-connected network with a broad distribution of neck sizes.^{22,23} In the lower-pressure part of the loop ($p/p_0 < 0.6$) secondary desorption branches of the same shape are found, confirming the presence of independent or restricted pores (Figure 4.1f (left)).^{4,24} On the other side, Figure 4.6b shows the scanning of the hysteresis loop performed for the OMC material; the secondary

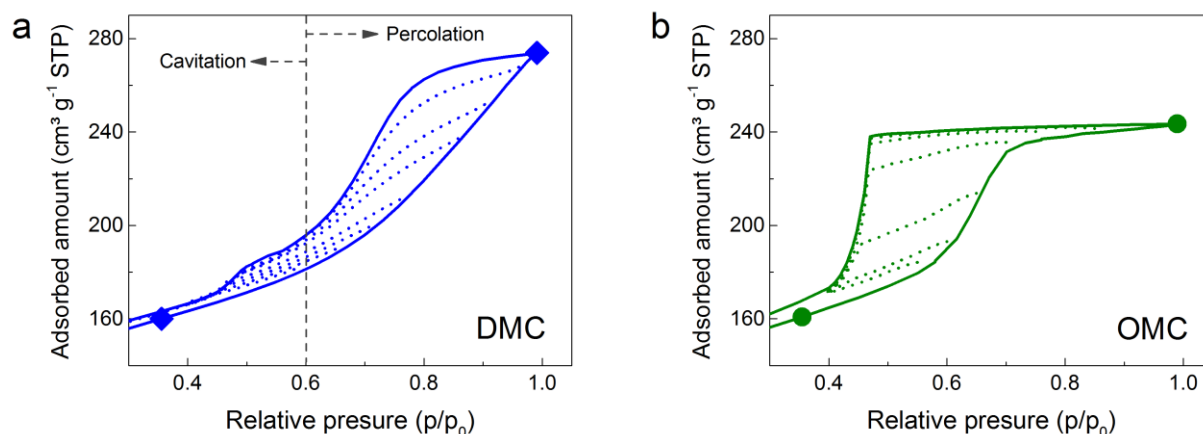


Figure 4.6. Scanned hysteresis loop of N_2 adsorption-desorption isotherms for (a) DMC and (b) OMC materials. Solid lines represent the principal or boundary curves while dotted lines represent the secondary desorption branches.

branches follow a straight line until $p/p_0 \approx 0.48$, where a sudden evaporation of N_2 occurs. This delayed desorption confirms that mesopores are indeed independent or only connected through narrow pores.

The illustration of the different pore networks is discussed later for both materials together with the adsorption of different hexane isomers and their accessibility into the mesopores.

4.4 Immersion calorimetry

To evaluate further the accessibility of the C_6 isomers to the inner pores of OMC and DMC, immersion calorimetry measurements were performed using the three iso-alkanes nHEX, 2MP and 22DMB in liquid phase. As can be appreciated in Table 4.1, the enthalpy of immersion, $-\Delta H_{imm}$, is the largest for the linear hydrocarbon, followed by the mono- and di-branched isomers. A slightly larger $-\Delta H_{imm}$ for nHEX was measured in the DMC. This can be ascribed to the better connectivity of the pore network that, compared to the OMC, allows better diffusion and provides a larger accessible area to the liquid. In addition, $-\Delta H_{imm}$ decreases as the kinetic diameter of the molecule increases for both DMC and OMC. However, a larger decrease in enthalpy is observed for 22DMB in the OMC. $-\Delta H_{imm}$ was used to calculate the surface area accessible to each C_6 isomer, S , by assuming that $-\Delta H_{imm} = S(-\Delta h_{imm})$, where $-\Delta h_{imm}$ is the areal enthalpy of immersion.³⁵ This method of calculation requires the use of a

Table 4.1. Kinetic diameters (\emptyset) of the hexane isomers used as probe molecules.^{26–29} Enthalpy of immersion ($-\Delta H_{imm}$) and accessible surface area (S) for the different C₆ isomers in samples DMC and OMC.

Sample	nHEX		2MP		22DMB	
	[$\emptyset=0.43$ nm]		[$\emptyset=0.5 - 0.54$ nm]		[$\emptyset=0.62$ nm]	
	$-\Delta H_{imm}$ (J g ⁻¹)	S (m ² g ⁻¹)	$-\Delta H_{imm}$ (J g ⁻¹)	S (m ² g ⁻¹)	$-\Delta H_{imm}$ (J g ⁻¹)	S (m ² g ⁻¹)
DMC	63.3	497	44.2	369	32.1	296
OMC	58.7	461	20.0	167	10.0	92

non-porous reference material, usually a carbon black, $-\Delta h_{imm}$ being characteristic of a specific solid-liquid system. Consequently, the accessible surface area for a given liquid in a target solid can be estimated provided that the sample and the reference share similar physicochemical characteristics.^{35,56,57} For this study, carbon black V3G was used as the reference, having a surface area of 62 m² g⁻¹ and $-\Delta h_{imm}$ values of 7.89 J g⁻¹, 7.42 J g⁻¹ and 6.73 J g⁻¹ in nHEX, 2MP and 22DMB, respectively; the calculated values of S are also listed in Table 4.1. S values decrease as the kinetic diameter of the probe molecule increase; however, for the OMC, S decreases at a faster rate than for the DMC. The poor accessibility of 22DMB in the OMC sample indicates that the constrictions connecting its mesoporous network are slightly wider than 0.5 nm, allowing partial access to 2MP and almost excluding 22DMB. On the contrary, the higher S values observed for the three C₆ isomers in the DMC corroborate that its pore network is connected by pores of more varied sizes, which improves the accessibility of the surface to even the largest probe molecule, *i.e.*, 22DMB. These results are in close agreement with the conclusions drawn from the textural characterization carried out by Ar, N₂ and CO₂ adsorption.

4.5 Vapor adsorption of hexane isomers

The adsorption performance of DMC and OMC samples was evaluated for the three C₆ hydrocarbon isomers, *i.e.*, nHEX, 2MP and 22DMB. Figure 4.7 shows the adsorption-desorption isotherms for the C₆ isomers at 25 °C and 45 °C for the two evaluated samples. In general, the adsorption profile of the three isomers is similar for a given sample, with a certain amount adsorbed at low relative pressures, due to the presence of micropores, and a hysteresis loop at medium to high relative pressures, associated with the presence of mesoporosity. The shape of the hysteresis loop resembles that observed with Ar or N₂ at cryogenic temperatures,

thus reflecting an analogous sensitivity of larger hydrocarbons to the size and shape of the mesopores during condensation. However, important differences between DMC and OMC samples were observed.

Figure 4.7a and 4.7c show that nHEX is able to access the inner porous structure of both DMC and OMC. For the two mesoporous carbons, low-pressure hysteresis is present and potentially associated to kinetic restrictions. To verify this hypothesis, vapor isotherms were performed at a slightly higher temperature of 45 °C (Figure 4.7b and 4.7d). Under these conditions, for both DMC and OMC materials, the general behavior does not change but the adsorption irreversibility is reduced, thus reflecting the mitigation of these kinetic restrictions at higher adsorption temperatures. Figure 4.7a and 4.7b show that in the DMC sample, nHEX has full access to the entire inner structure, whereas mono- and di-branched hydrocarbons have only partial access to the porosity. Indeed, increasing the molecule size reduces the accessible pore volume, while the hysteresis loop associated with condensation/evaporation in the mesoporous network has remained practically unchanged, *i.e.*, this indicates that the accessibility to the mesopore network characteristic of DMC is not completely limited, even

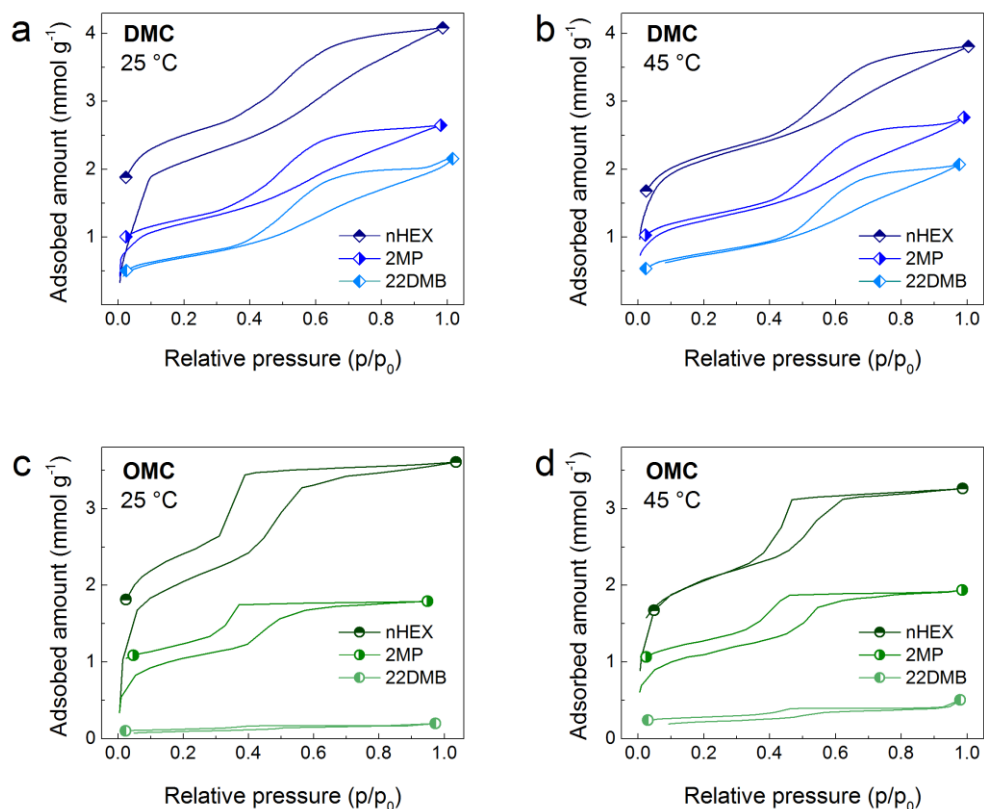


Figure 4.7. Vapor adsorption-desorption isotherms of nHEX, 2MP and 22DMB for (a, b) DMC and (c, d) OMC materials, at (a, c) 25 °C and (b, d) at 45 °C.

for the bulkier 22DMB. Concerning the OMC sample, the scenario changes completely, the study of the vapor adsorption isotherms indicates a highly selective performance with respect to DMC as shown in Figure 4.7c and 4.7d. In the OMC, nHEX is able to access the inner porous structure, while the mono-branched C₆, 2MP, has limited accessibility to the micro-mesopore network. The observed low-pressure hysteresis here may be due to slow kinetics due to existing pore constrictions; finally, 22DMB is almost completely excluded, regardless of the temperature.

All observations are in line with the results of the immersion calorimetry experiments discussed above (see Table 4.1) and the results of the advanced textural analysis. This is reflected in the scheme in Figure 4.8 that illustrates the connectivity of the porous structure of the DMC and OMC materials based on our advanced adsorption and calorimetric characterization results. Thus, the DMC material has pore bodies and necks of different sizes that would allow access to all the C₆ isomers, to a greater or lesser extent, to micropores and mesopores. In contrast to the well-connected structure of the DMC, the OMC exhibits a pore structure with reverse hierarchy⁵⁸ where the uniform mesopores are mainly connected through narrow micropores of sizes around or below ~0.5 nm.

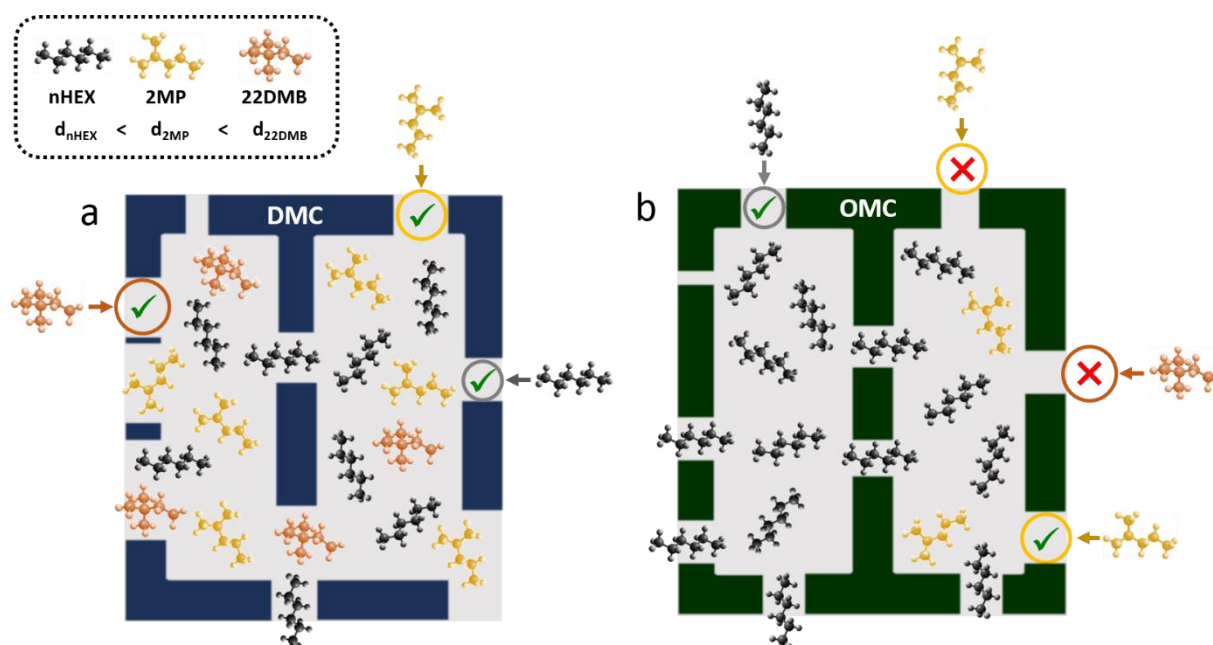


Figure 4.8. Scheme of the connectivity of the porous structure of (a) DMC and (b) OMC materials. The different kinetic diameters of the C₆ isomers ($d_{\text{nHEX}} < d_{\text{2MP}} < d_{\text{22DMB}}$) result in different accessibility of each molecule into the porous structure due to the presence of pore necks with similar or larger sizes.

4.6 Applications

4.6.1 Supercapacitors

Bearing in mind that the main goal is to use the mechanosynthesized materials as electrodes for SCs, the results from the deeper characterization presented in this chapter showed that, although an ordered mesoporous structure is expected to improve the diffusion of the electrolyte ions within the material, the restricted access to mesopores could result in an opposite, unwanted, effect. In particular, electrochemical performance in organic electrolytes could be reduced, as large-size ions, *e.g.* those in organic electrolytes (see Table 1.1), would not have full access to the surface. To circumvent this drawback, activation of the tannin-derived mesoporous carbons can be performed.

An activation process could produce two positive effects: the increase of surface area due to the creation of new pores would enhance the SC performance by increasing the amount of charge storage sites; and, the widening and unblocking of pre-existing porosity would improve the connectivity of the micro-mesoporous structure, hence the diffusion of ions. The physical and chemical activation of the tannin-derived mesoporous carbons and their electrochemical performance as electrodes for SCs are detailed in Chapters 5 to 7.

4.6.2 Molecular sieves

Moreover, the textural analysis revealed a well-defined, unimodal, microporosity, a property that is essential for the gas separation of linear and di-branched mixtures of hydrocarbons to obtain higher quality gasoline;³¹ thus, the DMC and OMC materials could be used as molecular sieves for such application. In particular, for the OMC, the narrow constrictions found at the mesopores entrance that limit the adsorption of the mono-branched isomer, whereas the di-branched isomer is almost excluded from the inner porous structure, would increase considerably its separation selectivity. In addition, the total uptakes at 25 °C, 4.1 and 3.6 mmol g⁻¹ for the DMC and OMC, respectively, are comparable to those reported recently for nHEX adsorption in MOFs, commonly used as molecular sieves,²⁹ with the advantage of being produced by an easy, low-cost and green synthesis method.

4.7 Conclusion

Herein, the textural properties of two types of mesoporous carbons derived from mimosa tannin, a disordered mesoporous carbon (DMC) and an ordered mesoporous carbon (OMC), were deeply characterized showing that the combination of vapor adsorption of different adsorbates and immersion calorimetry allows obtaining detailed information about their PSDs and the connectivity of their porous networks.

The DMC was found to have a well-connected porous network with a wide PSD in the mesopore range, while the OMC displayed a narrower PSD in the mesopore range with highly restricted access through narrow meso- and micropores. This in-depth characterization provides valuable information that will aid in the understanding of the effect of the mesoporous structure on the development of porosity during physical or chemical activation processes and, as a consequence, in the electrochemical performance of the materials as electrodes for SCs.

4.8 References

1. Thommes, M. & Cychosz, K. A. Physical adsorption characterization of nanoporous materials: progress and challenges. *Adsorption* 20, 233–250 (2014).
2. Cychosz, K. A., Guillet-Nicolas, R., García-Martínez, J. & Thommes, M. Recent advances in the textural characterization of hierarchically structured nanoporous materials. *Chemical Society Reviews* 46, 389–414 (2017).
3. Thommes, M., Smarsly, B., Groenewolt, M., Ravikovitch, P. I. & Neimark, A. V. Adsorption Hysteresis of Nitrogen and Argon in Pore Networks and Characterization of Novel Micro- and Mesoporous Silicas. *Langmuir* 22, 756–764 (2006).
4. Cychosz, K. A., Guillet-Nicolas, R., García-Martínez, J. & Thommes, M. Recent advances in the textural characterization of hierarchically structured nanoporous materials. *Chemical Society Reviews* 46, 389–414 (2017).
5. Cimino, R., Cychosz, K. A., Thommes, M. & Neimark, A. V. Experimental and theoretical studies of scanning adsorption–desorption isotherms. *Colloids and Surfaces A: Physicochemical and Engineering Aspects* 437, 76–89 (2013).
6. Thommes, M. Physical Adsorption Characterization of Nanoporous Materials. *Chemie Ingenieur Technik* 82, 1059–1073 (2010).
7. Madani, S. H. et al. Pore size distributions derived from adsorption isotherms, immersion calorimetry, and isosteric heats: A comparative study. *Carbon* 96, 1106–1113 (2016).
8. Madani, S. H., Silvestre-Albero, A., Biggs, M. J., Rodríguez-Reinoso, F. & Pendleton, P. Immersion Calorimetry: Molecular Packing Effects in Micropores. *ChemPhysChem* 16, 3984–3991 (2015).
9. Castro-Gutiérrez, J. et al. Synthesis of perfectly ordered mesoporous carbons by water-assisted mechanochemical self-assembly of tannin. *Green Chemistry* 20, 5123–5132 (2018).
10. Thommes, M. et al. Physisorption of gases, with special reference to the evaluation of surface area and pore size distribution (IUPAC Technical Report). *Pure and Applied Chemistry* 87, (2015).
11. Linares-Solano, A., Rodríguez-Reinoso, F., Martín-Martínez, J. M. & López-González, J. de D. Adsorption of Hydrocarbons on Air-Reacted Activated Carbons. II. High and Low Pressure Hysteresis. *Adsorption Science & Technology* 1, 317–327 (1984).
12. Rodríguez-Reinoso, F., Martín-Martínez, J. M., Linares-Solano, A. & Torregrosa, R. Further Comments on Low Pressure Hysteresis in Activated Carbons: Effect of Preparation Method. in *Studies in Surface Science and Catalysis* (eds. Rodríguez-Reinoso, F., Rouquerol, J., Sing, K. S. W. & Unger, K. K.) vol. 62 419–427 (Elsevier, 1991).
13. Volosin, A. M., Chen, S. & Seo, D.-K. High-surface area mesoporous carbons from gel templating and inorganic-organic hybrid gel formation. *Journal of Solid State Chemistry* 281, 121040 (2020).
14. Gor, G. Yu., Thommes, M., Cychosz, K. A. & Neimark, A. V. Quenched solid density functional theory method for characterization of mesoporous carbons by nitrogen adsorption. *Carbon* 50, 1583–1590 (2012).

15. Dantas, S., Struckhoff, K. C., Thommes, M. & Neimark, A. V. Phase Behavior and Capillary Condensation Hysteresis of Carbon Dioxide in Mesopores. *Langmuir* 35, 11291–11298 (2019).
16. Neimark, A. V., Lin, Y., Ravikovitch, P. I. & Thommes, M. Quenched solid density functional theory and pore size analysis of micro-mesoporous carbons. *Carbon* 47, 1617–1628 (2009).
17. Schlienger, S., Graff, A.-L., Celzard, A. & Parmentier, J. Direct synthesis of ordered mesoporous polymer and carbon materials by a biosourced precursor. *Green Chem.* 14, 313–316 (2012).
18. Braghiroli, F. L. et al. Hydrothermally treated aminated tannin as precursor of N-doped carbon gels for supercapacitors. *Carbon* 90, 63–74 (2015).
19. Braghiroli, F. L., Fierro, V., Parmentier, J., Pasc, A. & Celzard, A. Easy and eco-friendly synthesis of ordered mesoporous carbons by self-assembly of tannin with a block copolymer. *Green Chem.* 18, 3265–3271 (2016).
20. Sanchez-Sanchez, A. et al. Excellent electrochemical performances of nanocast ordered mesoporous carbons based on tannin-related polyphenols as supercapacitor electrodes. *Journal of Power Sources* 344, 15–24 (2017).
21. Selmi, T. et al. Tetracycline removal with activated carbons produced by hydrothermal carbonisation of *Agave americana* fibres and mimosa tannin. *Industrial Crops and Products* 115, 146–157 (2018).
22. Thommes, M. et al. Physisorption of gases, with special reference to the evaluation of surface area and pore size distribution (IUPAC Technical Report). *Pure and Applied Chemistry* 87, (2015).
23. Cychosz, K. A. & Thommes, M. Progress in the Physisorption Characterization of Nanoporous Gas Storage Materials. *Engineering* 4, 559–566 (2018).
24. Garcia-Martinez, J. et al. Evidence of Intracrystalline Mesostructured Porosity in Zeolites by Advanced Gas Sorption, Electron Tomography and Rotation Electron Diffraction. *ChemCatChem* 6, 3110–3115 (2014).
25. Silvestre-Albero, J. Characterization of microporous solids by immersion calorimetry. *Colloids and Surfaces A: Physicochemical and Engineering Aspects* 187–188, 151–165 (2001).
26. Ferreira, A. F. P. et al. Sieving di-branched from mono-branched and linear alkanes using ZIF-8: experimental proof and theoretical explanation. *Phys. Chem. Chem. Phys.* 15, 8795–8804 (2013).
27. Gobin, O. C., Reitmeier, S. J., Jentys, A. & Lercher, J. A. Role of the Surface Modification on the Transport of Hexane Isomers in ZSM-5. *J. Phys. Chem. C* 115, 1171–1179 (2011).
28. Funke, H. H., Argo, A. M., Falconer, J. L. & Noble, R. D. Separations of Cyclic, Branched, and Linear Hydrocarbon Mixtures through Silicalite Membranes. *Ind. Eng. Chem. Res.* 36, 137–143 (1997).
29. Cuadrado-Collados, C. et al. Reverse Hierarchy of Alkane Adsorption in Metal–Organic Frameworks (MOFs) Revealed by Immersion Calorimetry. *J. Phys. Chem. C* 123, 11699–11706 (2019).
30. Silvestre-Albero, A. et al. Well-defined mesoporosity on lignocellulosic-derived activated carbons. *Carbon* 50, 66–72 (2012).

31. Laredo, G., Trejo-Zarraga, F., Jimenez-Cruz, F. & Garcia-Gutierrez, J. Separation of Linear and Branched Paraffins by Adsorption Processes for Gasoline Octane Number Improvement. CHENG 5, 153–173 (2013).

Chapter 5

CO₂ activation of tannin-derived OMCs

5.1 Introduction

As summarized in Chapter 1, Section 1.4, attempts to increase the specific energy of SCs are centered on the development of high surface area porous materials and the control of pore size. Although surface chemistry modification, *i.e.*, the introduction of heteroatoms into the carbon structure, is also a frequent path to enhance the performances through pseudocapacitance contributions in SCs and hybrid capacitors.^{1,2}

Mesoporosity in carbon materials could improve ion diffusion towards micropores, hence OMCs were considered for use in electrochemical applications.³⁻⁵ However, as-synthesized OMCs usually have low to moderate surface areas, like those presented in Chapter 3, and an additional activation process is generally needed to enhance their textural characteristics and thus their electrochemical performances. Activated OMCs (AOMCs) are valuable materials in energy storage devices due to their high surface area and hierarchical pore structure that facilitates the diffusion of electroactive species.^{3,6,7} Therefore, in this chapter, the effect of CO₂ activation of mechanosynthesized OMCs on their porosity, surface chemistry and electrochemical performances is studied.

The successive preparation steps to obtain the AOMCs are schematized in Figure 5.1. The SWAMM method (see Chapter 3) was followed to synthesize the mesophase and carbonized it to produce the OMCs using a Tannin:Surfactant:Water weight ratio of 2:0.75:1.75 g. Before CO₂ activation, the carbonized materials were manually ground to get a homogenous particle size. The temperature was raised to 900 °C at a rate of 5 °C min⁻¹ under N₂ flow (100 mL min⁻¹) in the same device as that used for carbonization. Afterwards, N₂ was switched to CO₂ (50 mL min⁻¹) and held for a time ranging from 15 to 120 min. Then, CO₂ was switched back to N₂ and the materials were left to cool down until room temperature. Samples were labeled *A_t*-CTPW, where “*t*” stands for the activation time in minutes.

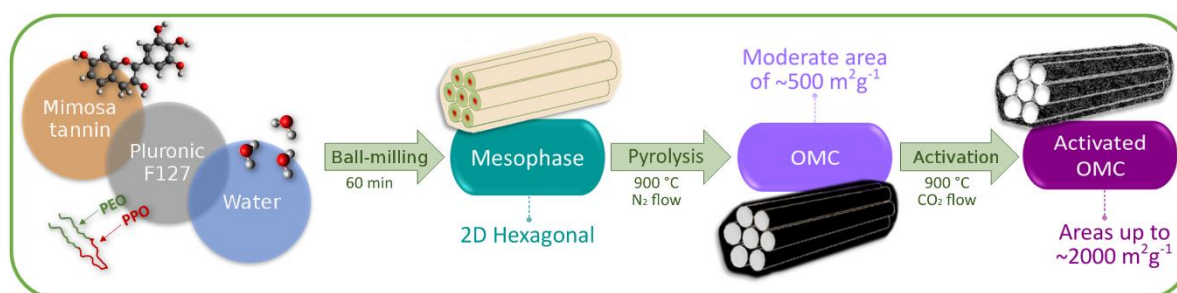


Figure 5.1. Scheme of the followed procedure to synthesized and activate OMCs derived from mimosa tannin. [Reproduced from Castro-Gutiérrez et al. (2019)⁸]

Characterization of the materials was performed through physisorption of N₂ and CO₂ using the ASAP devices from Micromeritics, TEM imaging, small-angle XRD, elemental analysis and XPS, all of which are detailed in the corresponding sections of Chapter 2. The electrochemical performances were evaluated in two-electrode cells using 1 M H₂SO₄, 1 M Na₂SO₄ and 1 M TEABF₄/ACN electrolytes; the preparation of the electrodes and the cell is described in Section 2.10, while the equations used for the calculation of capacitance, energy and power of the assembled SCs are detailed in Section 1.2.3.

5.2 Textural properties

Figure 5.2a shows the N₂ adsorption-desorption isotherms of the as-synthesized OMC, label CTPW, and the AOMCs label At-CTPW, “*t*” ranging from 15 to 120 min of activation. The corresponding textural properties are listed in Table A2.1 in Annex 2. All the materials exhibit isotherms corresponding to micro-mesoporous materials, for which the adsorbed volume keep increasing in the range of relative pressures p/p_0 from 0.1 to 0.4, and the slope increases with the activation time, indicating a progressive pore widening. The “knee” of the isotherm at low p/p_0 indeed becomes gradually broader and more open when the activation time increases due to pore filling in wide micropores.⁹ Such pore filling induces an overestimation of the surface area by the BET method, which assumes monolayer adsorption of the probe molecule.^{10–12} On the contrary, the BET method underestimates the surface area when very narrow pores exist, because only a single pore wall is taken into account.¹³ The 2D-NLDFT HS method¹⁴ applied to both N₂ and CO₂ adsorption isotherms provides a better estimation of the surface area and hence of its contribution to the electrochemical performances of SCs.^{11,15,16} Therefore, herein, the analysis using the textural properties calculated from the 2D-NLDFT HS method is prioritized. In Figure 5.2b, the BET and the NLDFT surface areas, A_{BET} and S_{NLDFT} , respectively, are plotted as a function of burn-off (BO). It can be noticed that A_{BET} and S_{NLDFT} values cross at BO around 0.4. For BO < 0.4, the pristine OMC and poorly activated samples still present narrow pores so that the area is underestimated by the BET method: $A_{BET} < S_{NLDFT}$. In contrast, for more activated samples such as A75-CTPW and A90-CTPW, A_{BET} is higher than S_{NLDFT} due to multilayer adsorption in the wider pores. Both A_{BET} and S_{NLDFT} increase with the BO, reaching a maximum at BO ~0.8 and then decrease drastically due to pore broadening and merging. Indeed, as shown in Table A2.1, the pores widen with

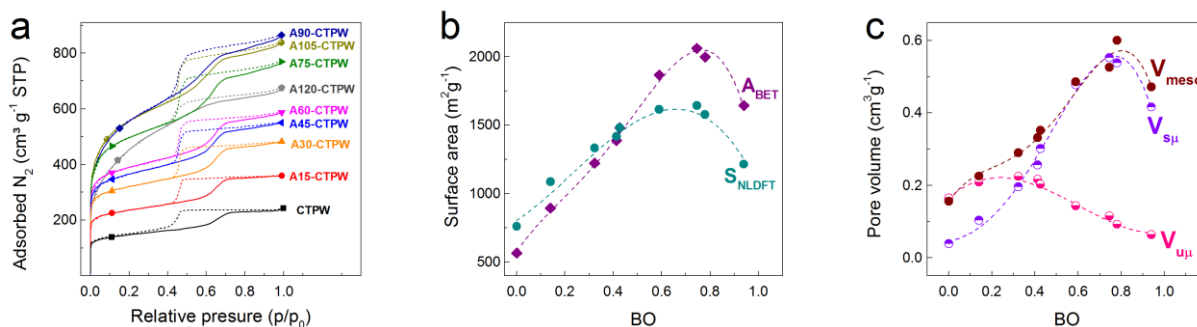


Figure 5.2. (a) N₂ adsorption-desorption isotherms for the activated carbons and the as-synthesized material. (b) BET area and NLDFT surface area of the AOMCs as a function of burn-off, BO. (c) Changes of pore volume with BO. [Adapted from Castro-Gutiérrez et al. (2019)⁸]

activation time, given that the average pore size (w_{av}) increases with the BO, from 0.9 to 1.6 nm for CTPW and A120-CTPW, respectively. Figure 5.2c presents the changes of pore volume with BO, in the different ranges of pore width (w): ultramicropore ($w < 0.7$ nm), supermicropore ($0.7 < w < 2$ nm) and mesopore ($2 < w < 50$ nm) volumes, $V_{u\mu}$, $V_{s\mu}$ and V_{meso} , respectively. All materials exhibit a decrease in $V_{u\mu}$ and an increase of $V_{s\mu}$ and V_{meso} , up to a BO of ~ 0.8 , due to pore widening by CO₂ activation. Further activation results in a drastic decrease of pore volume caused by pore merging, producing the vanishing of the porosity of the AOMC at 120 min (BO = 0.94).

Figure 5.3a and 5.3c display the PSD in the mesopore range calculated by the BJH-KJS model, as well as the PSD calculated by the 2D-NLDFT HS method in the whole pore diameter interval, respectively. In the mesopore range, progressive development of pores narrower than 4 nm and the widening of the peak centered at 4.6 nm are observed with activation time until the nearly complete loss of the original mesoporous structure for A120-CTPW. Non- or poorly activated OMCs present two clear and separated pore systems corresponding to micro- and mesoporosity, whereas a continuous PSD is observed for BO > 0.59 ($t > 75$ min), as shown in Figure 5.3c. Such non-discrete PSD might favor ion diffusion and hence improve the electrochemical performances of SCs.⁴ In addition, Figure 5.3b displays TEM images of the 2D hexagonal ordered mesoporous structure that withstands the activation process up to a BO of 78 %; this was confirmed by the small-angle XRD measurements shown in Figure 5.4, where the peak associated to the ordered structure in the d(100) direction is still present for the AOMCs. The decreased intensity and broadening of the XRD peak is to be expected as the gasification of the carbon produce imperfections on the original 2D hexagonal structure.

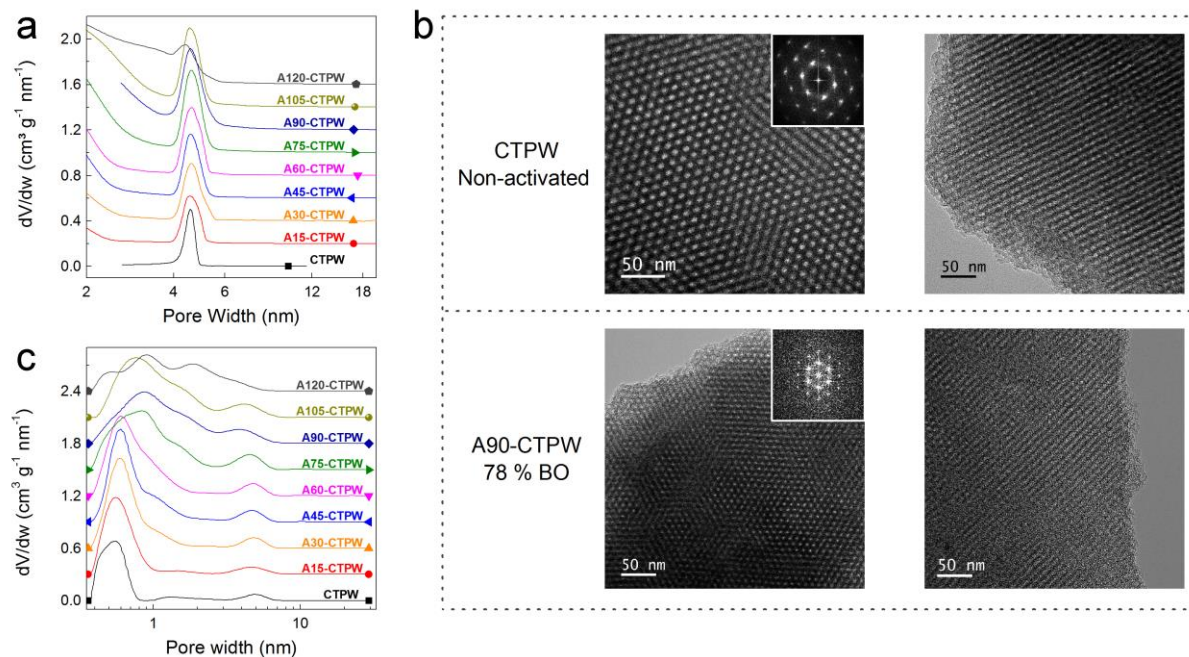


Figure 5.3. PSDs (a) in the mesopore range and (c) in the whole pore width interval. (b) TEM images, the inset shows the corresponding diffraction patterns, confirming the 2D hexagonal ordered mesopore structure of CTPW (non-activated) and A90-CTPW (78 % BO). [Adapted from Castro-Gutiérrez et al. (2019)⁸]

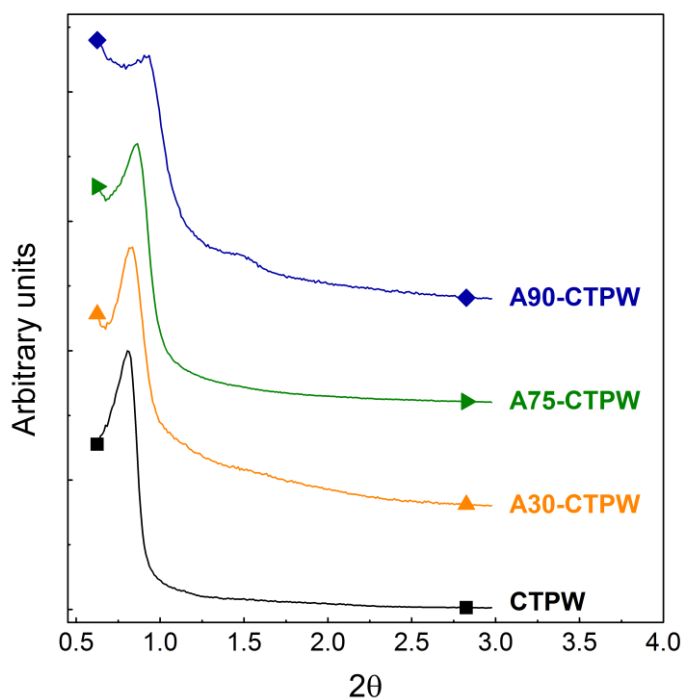


Figure 5.4. Small-angle XRD measurements for the as-synthesized material and AOMCs activated during 30, 75 and 90 min. [Reproduced from Castro-Gutiérrez et al. (2019)⁸]

5.3 Surface and bulk composition

Figure 5.5a shows the oxygen content of the materials, measured in the bulk by elemental analysis (EA) and at the surface by XPS. CTPW present oxygen functionalities on the surface that are eliminated at low activation times ($t = 15$ min), as suggested by the drastic drop of O content measured by XPS. Then, the O content increases with the activation time ($t > 15$ min), and its concentration is always higher at the surface than in the bulk of the materials. It has been reported that a high oxygen content can improve the electrochemical performances of materials used as electrodes of SCs.¹⁷ However, not all the functional groups are useful and some of them may even have a negative impact on their performances.¹⁸

Recalling Section 1.4.6, quinone and carbonyl type functionalities (OI) are known to be electrochemically active in aqueous electrolytes and can lead to redox reactions yielding pseudocapacitance contributions that allow increasing the amount of energy stored in the device. On the contrary, high-polarity O functionalities present in carboxylic groups (OIII) could produce resistance to ion diffusion in aqueous electrolytes, reducing the performances at high current densities.¹ Figure 5.5b shows the relative contribution of each kind of O moiety to the O1s peak determined by XPS for the AOMCs; the complete assignment of the XPS peaks and the relative contributions of functionalities to the surface composition are listed in Table A2.2. The most common oxygen surface functionalities are hydroxyl groups in phenols (OII), in good agreement with the phenolic nature of the tannin used as carbon precursor. The second most important contribution comes from the OI group, and finally the OIII contributions

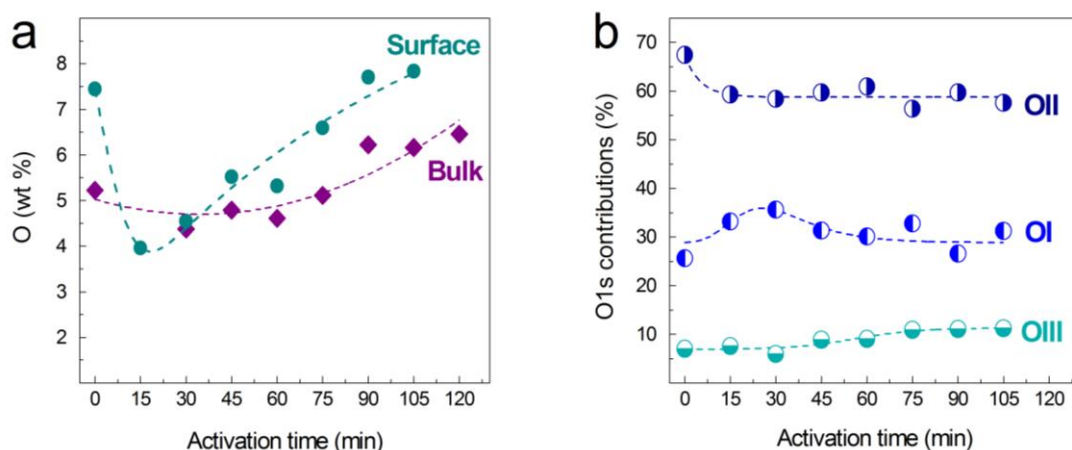


Figure 5.5. (a) Oxygen content measured in the bulk, by elemental analysis, and at the surface, measured by XPS. (b) Relative contributions to the oxygen surface functionalities. The dotted lines are only guides for the eye. [Reproduced from Castro-Gutiérrez et al. (2019)⁸]

are the least common. After activation, the relative amount of OII functionalities first decreases and then remains nearly constant with activation time, whereas OIII slightly increases and OI slightly decreases. Although the amount of oxygen surface functionalities globally increases with activation time, the majority of OII functionalities that are not as electrochemically active in acid electrolyte along with the combined increase of OIII and decrease of OI could make negligible the pseudocapacitance contribution of the oxygen functionalities. On the other hand, the presence of heteroatoms in a carbon material is usually associated with a reduced lifetime;⁶ however, as it will be shown below, the activated materials tested as electrodes for SCs exhibited high long-term stability despite the presence of the aforementioned oxygen functionalities.

5.4 Electrochemical characterization

The electrochemical performances of A30- to A90-CTPW materials as electrodes for SCs were first studied by cyclic voltammetry (CV) in 1 M H₂SO₄ electrolyte. Figure 5.6a displays the quasi-rectangular CV curves at 5 mV s⁻¹ found for all the tested materials, representing a supercapacitive behavior. The values of specific cell capacitance (C_{cell}), calculated from the CV curves, are shown in Figure 5.6b, this plot shows that A75- CTPW reaches a maximum C_{cell} of 40 F g⁻¹ at 5 mV s⁻¹. In order to relate the capacitance to the pore texture, the normalized electrode capacitance ($C_{eN,BET}$) is plotted against w_{av} in Figure 5.6c; for comparative purposes with the literature,^{12,19,20} the capacitance is normalized using A_{BET} instead of S_{NLDFT} . An increase of $C_{eN,BET}$ is observed with the decrease of w_{av} , which is in agreement with previously reported results;^{19,21} this capacitance increase is attributed to a distortion of the solvated ions, which reduces the distance to the carbon surface.¹⁹ The values of the present study are slightly higher than those previously reported, which can be due to:

- i. Different measurement conditions for the electrochemical tests, *e.g.* scan rate.
- ii. Different electrode preparation processes, *e.g.* carbon load or amount and type of binder.
- iii. The calculation method of w_{av} , either from the NLDFT model or from Dubinin's theory.
- iv. The limitations of the model that assumed unimodal PSDs.

Most likely, the factor (iv) has the highest impact on the deviations from the model given the micro-mesoporous nature of the AOMCs. Therefore, the bimodal nature of the PSDs might induce a shift towards higher w_{av} and hence produce a significant shift from the theoretical line (see again Figure 5.6c).

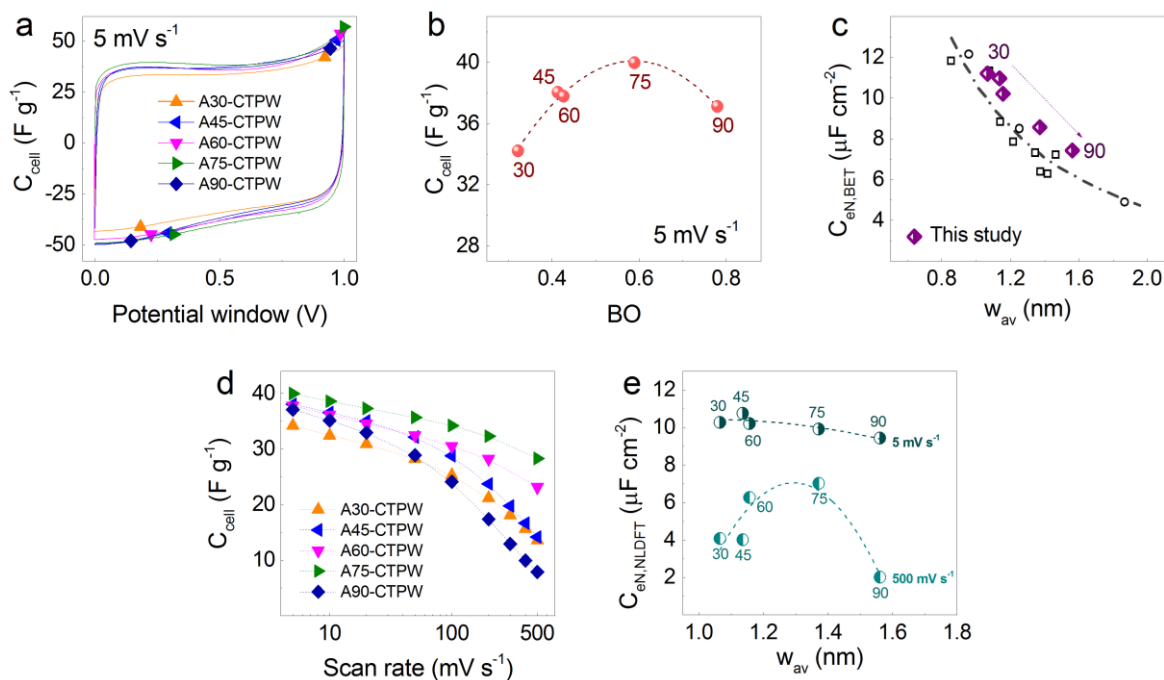


Figure 5.6. Electrochemical performances of A30- to A90-CTPW samples in 1 M H₂SO₄. (a) CV curves at 5 mV s⁻¹. (b) Specific cell capacitance, C_{cell} , as a function of BO. (c) Normalized electrode capacitance with respect to the BET area, $C_{eN,BET}$, as a function of average pore size, w_{av} , compared to experimental (squares) and theoretical (dashed-dotted line) data from previous studies.^{12,19,20} (d) C_{cell} as a function of scan rate; (e) normalized capacitance with respect to NLDFT surface area, $C_{eN,NLDFT}$, as a function of w_{av} . Labels in (b, c, e) represent the activation time in minutes; the lines in (b, e) are given just as guide for the eye. [Reproduced from Castro-Gutiérrez et al. (2019)⁸]

Further on, Figure 5.6d shows that only A60- and A75-CTPW samples retain more than 60 % of their initial C_{cell} when the scan rate increases from 5 to 500 mV s⁻¹. Figure 5.6e shows the normalized electrode capacitance, with respect to S_{NLDFT} ($C_{eN,NLDFT}$), at 5 and 500 mV s⁻¹ as a function of w_{av} ; the continuous decrease of $C_{eN,NLDFT}$ with w_{av} that is observed at 5 mV s⁻¹ does not hold anymore at high scan rates, for which a maximum is found for A75-CTPW. In addition, A60-CTPW presents a higher $C_{eN,NLDFT}$ than A45-CTPW at 500 mV s⁻¹ despite their rather similar textural properties (see again Table A2.1). The main difference between these two samples is their PSD (Figure 5.3c): both present a large peak centered on 0.6 nm but whose width is lower for A45-CTPW, 0.30 nm, than for A60-CTPW, 0.86 nm. On the other hand, A30- and A45-CTPW reach similar values of $C_{cell} \sim 14$ F g⁻¹ at 500 mV s⁻¹, despite the higher S_{NLDFT} of the latter, but their PSDs reveal isolated peaks for micro- and mesopore sizes in both samples. A90-CTPW is a particular case: the activation process has widened its pores with the concomitant decrease of $V_{\mu\mu}$ and increase of $V_{S\mu}$; wider pores would not allow solvated ion deformation, thus lessening the SC performance, as seen in Figure 5.6.

Because of their superior performance in CV experiments, A60- and A75-CTPW materials were further characterized electrochemically; Figure 5.7 summarizes the results from CV and GCD measurements. As shown in Figure 5.7c and 5.7d, GCD tests result in triangular-shaped curves for A60- and A75-CPTW; good supercapacitor behavior is revealed by the symmetry of the curves and the small IR drops at current densities up to 50 A g⁻¹. A75-CTPW presents a slightly higher C_{cell} of 37 F g⁻¹ compared to A60-CTPW with C_{cell} of 35 F g⁻¹, both determined at 0.2 A g⁻¹. Figure 5.7e shows that A75-CTPW exhibits a capacitance retention (C_{ret}) of 70 % at the highest value of applied current, 80 A g⁻¹, while A60-CTPW reaches only a C_{ret} of 51 %. The higher values of C_{ret} of A75-CTPW are probably due to a lower ESR,

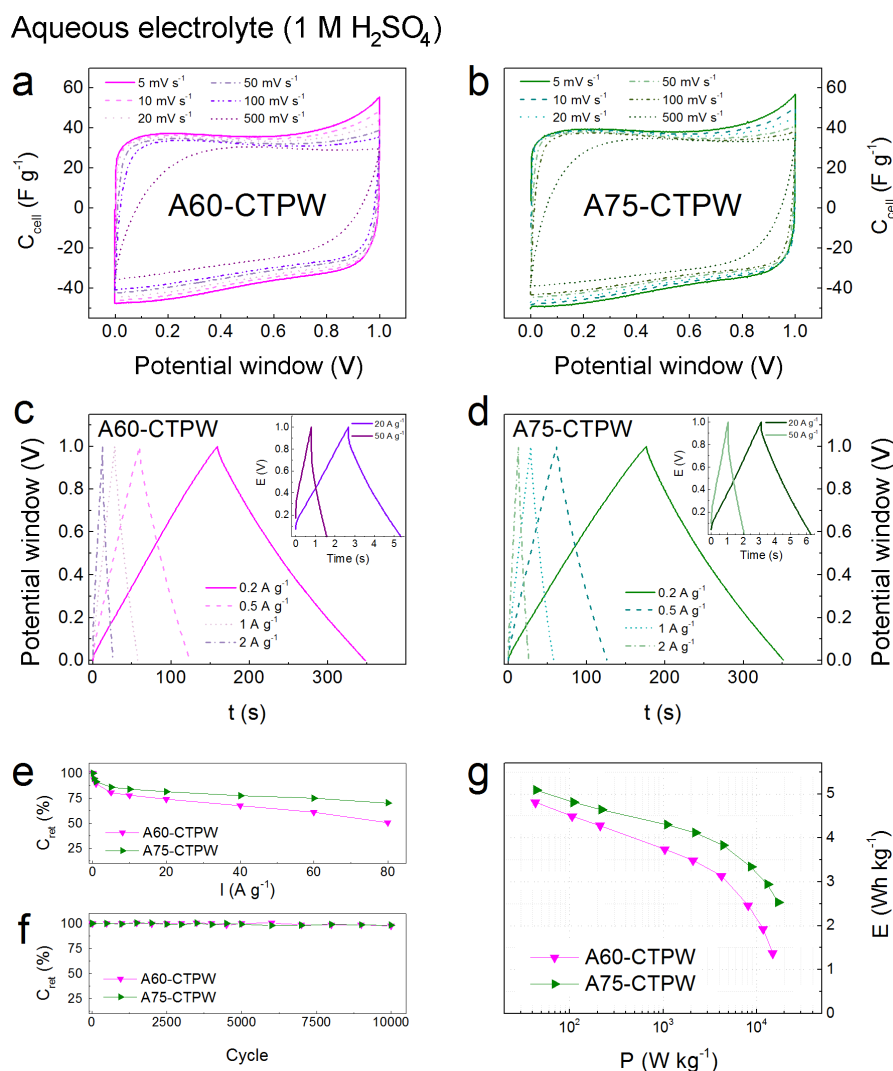


Figure 5.7. Electrochemical performances in aqueous electrolyte (1 M H₂SO₄) of A60-CTPW and A75-CTPW: (a, b) CV curves at different scan rates; (c, d) GCD curves at different applied currents; capacitance retention, C_{ret} , as a function of (e) applied current and (f) after continuous cycling at 5 A g⁻¹; (g) Ragone-like plot obtained from GCD tests. [Adapted from Castro-Gutiérrez et al. (2019)⁸]

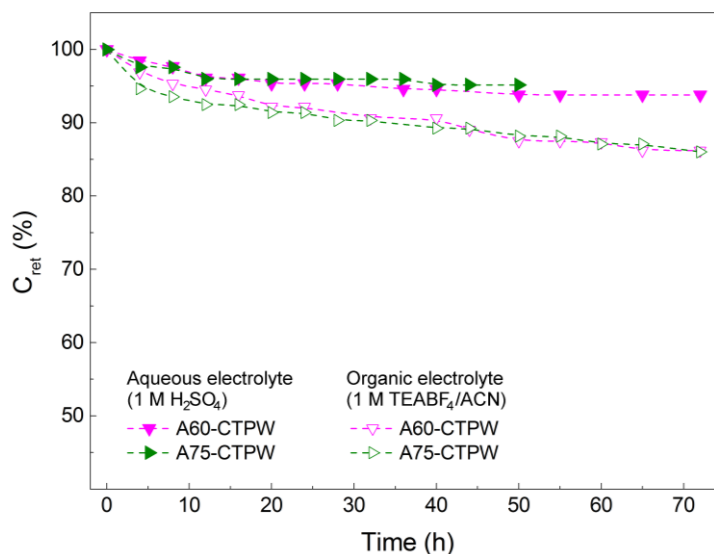


Figure 5.8. Capacitance retention over time by potentiostatic hold at maximum cell voltage in 1 M H₂SO₄ (aqueous electrolyte, 1 V, solid symbols) and TEABF₄/ACN (organic electrolyte, 2.7 V, open symbols) electrolytes. [Adapted from Castro-Gutiérrez et al. (2019)⁸]

suggested by the lower potential drops observed than in A60-CTPW's case.^{22,23} As a consequence, the values of specific energy and power are higher for A75-CTPW, as can be seen on the Ragone-like plot in Figure 5.7g, where the stored energy (E) reaches a maximum of 5 Wh kg⁻¹ with a power output (P) of 44 W kg⁻¹ at 0.2 A g⁻¹. Besides, a long-term stability was evidenced by continuous GCD tests at 5 A g⁻¹; Figure 5.7f shows that both selected samples present $C_{ret} \sim 98\%$ after 10 000 cycles and, by potentiostatic hold at 1 V it remains above 94% after 50 h as shown in Figure 5.8, thereby proving the robustness of the assembled SCs.

Most commercial SCs use organic electrolytes due to their wider potential window, hence the possibility of storing more energy than their aqueous counterparts.²⁴ The electrochemical performance of the selected AOMCs was thus tested in an organic electrolyte (1 M TEABF₄ in acetonitrile (ACN)) and it is summarized in Figure 5.9. Figure 5.9a and 5.9b show the rectangular CV curves obtained for A60- and A75-CTPW samples at 5 mV s⁻¹. From GCD, a more important drop of C_{ret} , than that of the corresponding tests in aqueous electrolyte (1 M H₂SO₄), is observed in Figure 5.9c (top); indeed, the decrease is $\sim 40\%$ when the current increases up to 40 A g⁻¹. This is due to the combination of the bigger size of the organic electrolyte ions and its lower ionic conductivity, which increases both the EDR and ESR, as can be seen in the Nyquist plots in Figure 5.10, and ultimately the total cell resistance. Slightly better performance is observed for A75-CTPW at low current densities; however, as the current increased both tested materials presented the same performance. The PSD that favors ion

diffusion in A75-CTPW at high current densities in aqueous electrolyte could no longer be enough to compensate for the low mobility of ions in the organic electrolyte. In addition, even if the ions reach the microporosity their bigger size difficult the access to it, thus reducing the available sites for the storage of charge and explaining also the lower values of specific capacitance when compared to the aqueous counterparts. Nonetheless, the materials maintain high long-term stability with C_{ret} above 90 % after 8 000 cycles at 5 A g⁻¹ (Figure 5.9c (bottom)) and 86 % by potentiostatic hold at 2.7 V after 72 h (Figure 5.8). As expected, the values of specific energy and power (E and P , respectively) are higher than those attained in aqueous electrolyte. A maximum E of ca. 28 Wh kg⁻¹ with a P output of 138 W kg⁻¹ is reached by A75-CTPW, and similar values are reached by A60-CTPW, as revealed by the Ragone-like plot in Figure 5.9d. Importantly, at a high power of 12 kW kg⁻¹, both SCs are still able to provide ~13 Wh kg⁻¹.

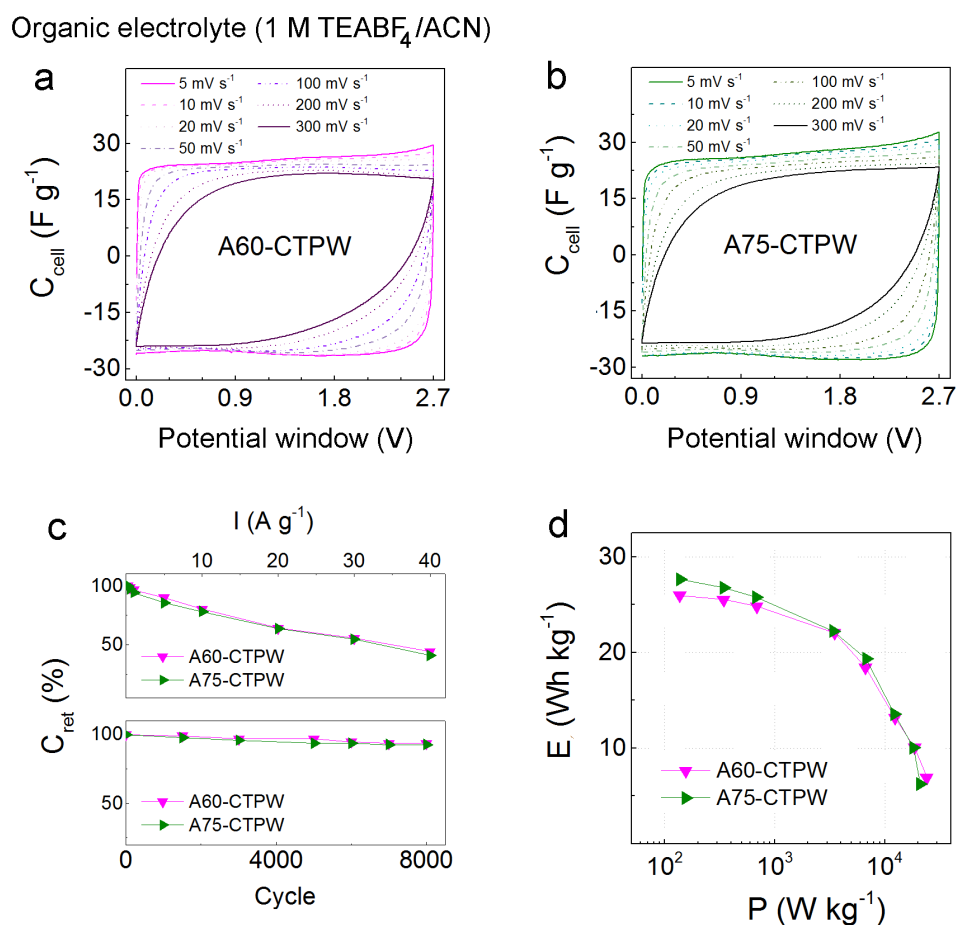


Figure 5.9. Electrochemical performances in the organic electrolyte (1 M TEABF₄/ACN) of A60-CTPW and A75-CTPW: (a, b) CV curves at different scan rates; (c) capacitance retention, C_{ret} , as a function of applied current (top) and after continuous cycling at 5 A g⁻¹ (bottom); (d) Ragone-like plot obtained from GCD tests. [Adapted from Castro-Gutiérrez et al. (2019)⁸]

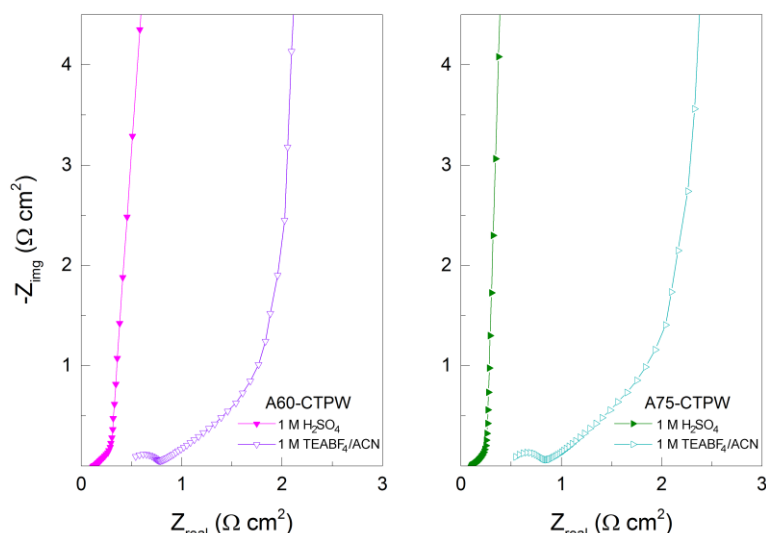


Figure 5.10. Nyquist plots for A60- and A75-CTPW in both aqueous and organic electrolytes. [Adapted from Castro-Gutiérrez et al. (2019)⁸]

The capacitance values achieved by the materials synthesized herein are comparable with other un-doped mesoporous carbons of similar properties reported in the literature, see Table A2.3,^{22,25–35} but the AOMCs of this study present higher rate capability compared to the values usually reported for this type of materials (see Figure 5.11). In aqueous electrolyte (1 M H₂SO₄, Figure 5.11a), the values of C_{ret} of A60- and A75-CTPW are higher than the values reported both for disordered mesoporous carbons synthesized either from activated bio-sourced materials^{25,27} or from precursors of petrochemical origin,^{28,29} and for hard-templated OMCs derived from tannin, phenols, furfuryl alcohol or lignin.^{26,30,31} Even more, AOMCs produced through pH-controlled self-assembly of tannin and further CO₂ activation led to lower retentions than those presented herein.²² On the other hand, in the organic electrolyte (Figure 5.11b), C_{ret} is in general comparable to the values from the literature. However, the synthesis of the formerly reported materials involved the use of dangerous or toxic substances for etching out hard templates^{29,30,33} or for activating the carbon material with NaOH³⁴ or ZnCl₂.³⁵ In contrast, the synthesis of the AOMCs presented herein does not require the use of hazardous chemicals.

Additionally, some of the compared studies of Figure 5.11 reported the electrochemical performance using electrodes with lower carbon loads (CLs)^{25,31,33–35} than those of the present study. Now, it is known that a very low CL may lead to an overestimation of the capacitance of a material and certainly does improve the rate capability. For this reason, CLs close to that of commercial devices, *i.e.*, ~10 mg cm⁻², are used here as such value is usually recommended for

realistic studies.^{24,36} For the sake of comparison, additional GCD tests were then performed with A60-CTPW using a CL of $5.7 \pm 0.5 \text{ mg cm}^{-2}$; Figure 5.12 shows C_{cell} and C_{ret} of supercapacitor cells with CLs of ~ 10 and $\sim 6 \text{ mg cm}^{-2}$. As expected, higher values of C_{cell} with increasing rate are found when using lower CLs, demonstrating the difficulty of doing pertinent comparisons with literature data.

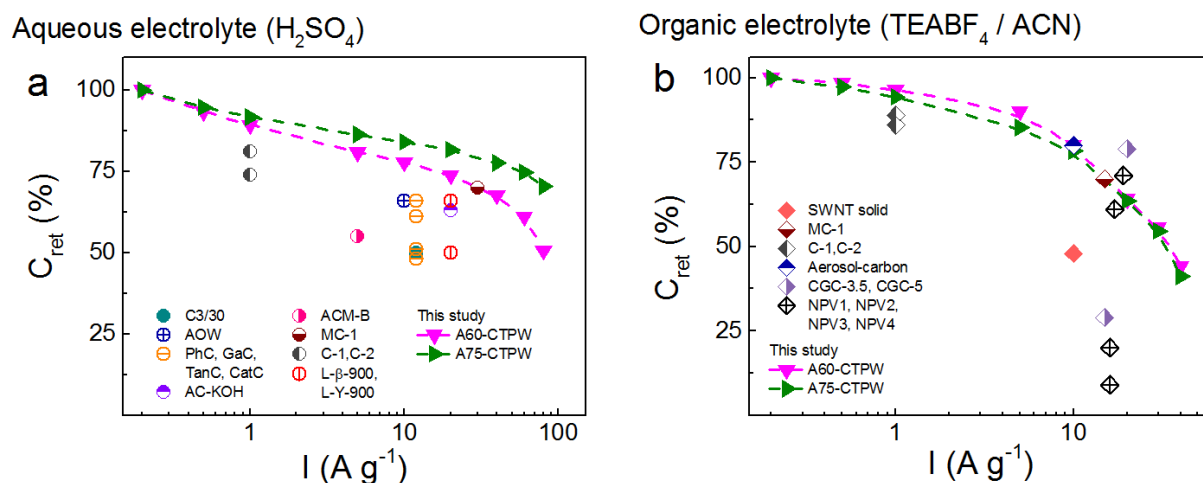


Figure 5.11. Capacitance retention in (a) aqueous and (b) organic electrolytes for the AOMCs of this study in comparison with similar materials reported in the literature.^{22,25–35} The sample names correspond to those of their respective bibliographic references. [Adapted from Castro-Gutiérrez et al. (2019)⁸]

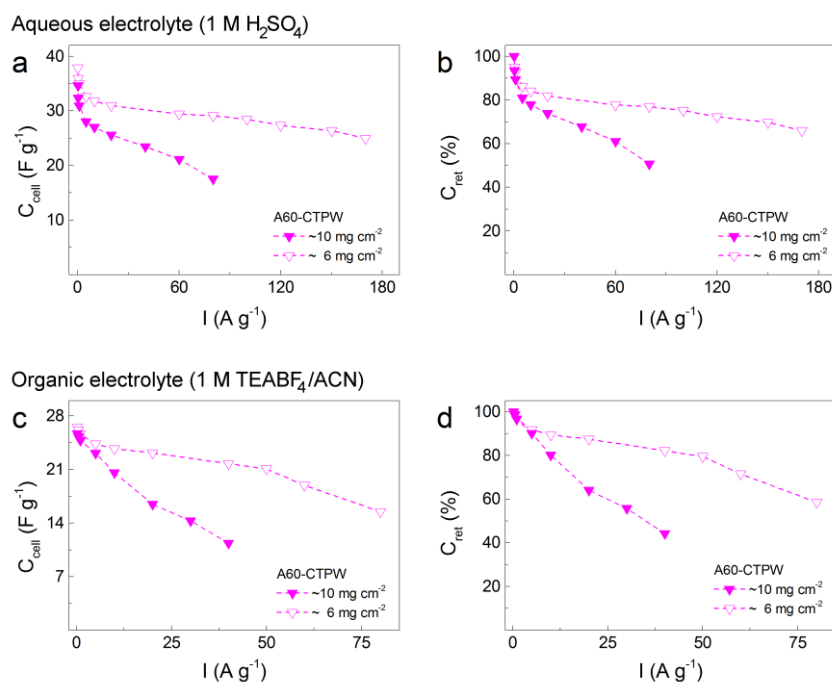


Figure 5.12. Specific cell capacitance, C_{cell} , and capacitance retention, C_{ret} , of A60-CTPW in (a,b) aqueous and (c,d) organic electrolytes, calculated from GCD tests at different current densities using electrodes with carbon loads of ~ 10 and $\sim 6 \text{ mg cm}^{-2}$. [Adapted from Castro-Gutiérrez et al. (2019)⁸]

Although H₂SO₄ and TEABF₄/ACN are widely used at the laboratory and commercial scales, respectively, they still have the disadvantage of being hazardous substances. Thus, attention has been drawn to neutral aqueous electrolytes, as they are safer and can reach larger potential windows than the acidic ones.³⁷ Considering this, the electrochemical performances of A60-CTPW and A75-CTPW in 1 M Na₂SO₄ were tested and the main results are reported in Figure 5.13. The materials again exhibited supercapacitor behavior because rectangular curves were obtained from CV tests at 5 mV s⁻¹ within a potential window of 1.6 V (Figure 5.13a). From the GCD, it was observed that the values of C_{cell} were ~30 % lower than those reached in H₂SO₄ and in the range of values previously reported for similar materials.^{38–40} Figure 5.13b also shows that the values of C_{ret} at 20 A g⁻¹ were 69 and 67 % for A60-CTPW and A75-CTPW, respectively, lower to the corresponding C_{ret} of 74 and 82 % at the same applied current in acidic medium (Figure 5.7e). This decrease in rate capability may be due to the larger size and lower mobility of the Na⁺ ions relative to the H⁺ ions,⁴¹ resulting in hindered diffusion at high rates. As expected, the values of specific energy achieved by the AOMCs in Na₂SO₄ were higher than those reached in acidic medium (Figure 5.13c and Figure 5.7g), because of the

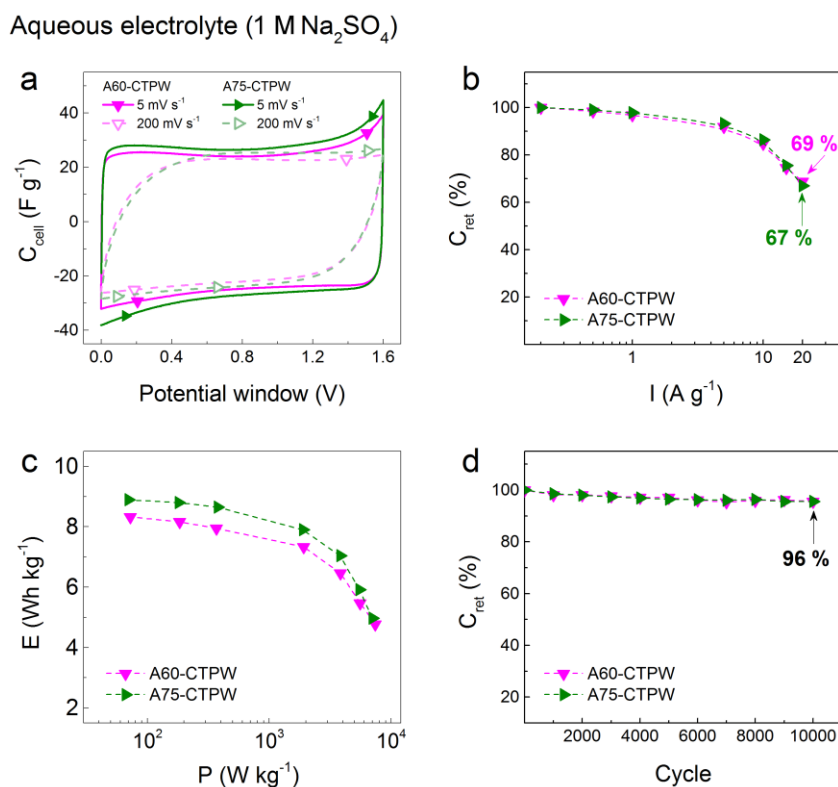


Figure 5.13. Electrochemical performance of A60-CTPW and A75-CTPW in NaSO₄ as aqueous electrolyte: (a) CV curves at 5 and 200 mV s⁻¹; (b) capacitance retention with applied current; (c) Ragone-like plot for the achieved energy and power of the assembled SCs; (d) capacitance retention after continuous cycling at 5 A g⁻¹. The potential window was 1.6 V in all cases. [Adapted from Castro-Gutiérrez et al. (2019)⁸]

larger potential window used in the neutral medium. The lower values of C_{cell} in Na₂SO₄ are counterbalanced by the broader potential window, resulting in a difference of $\sim 3 - 4 \text{ Wh kg}^{-1}$ between the maximum values of achieved stored energy compared to C_{cell} in H₂SO₄, which represents an increase of more than 60%. Besides, the assembled SCs exhibited high long-term stability after continuous cycling at 5 A g^{-1} , with C_{ret} remaining at 96 % after 10 000 cycles, see Figure 5.13d.

Finally, for comparison, Figure 5.14 shows the values of gravimetric and volumetric electrode capacitance (C_e), as well as the energy and power densities for the AOMCs in the three electrolytes used in this study (H₂SO₄, Na₂SO₄ and TEABF₄/ACN). The volumetric values

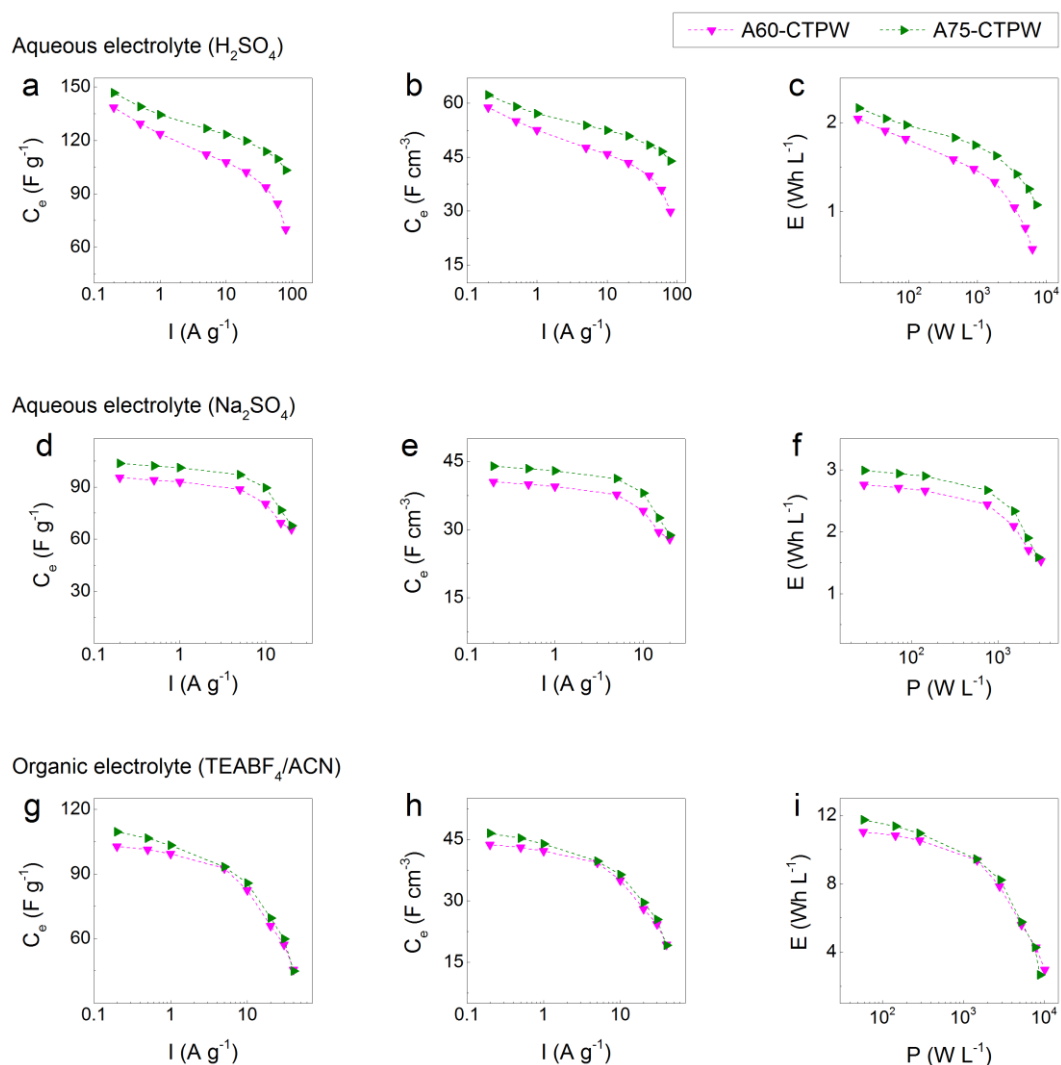


Figure 5.14. (a, d, g) Gravimetric and (b, e, h) volumetric single electrode capacitance as a function of the applied current and (c, f, i) Ragone-like plot presenting the achieved energy and power densities. Values presented for both tested materials, A60-CTPW and A75-CTPW, in the three electrolytes: (a, b, c) 1 M H₂SO₄, (d, e, f) 1 M Na₂SO₄ and (g, h, i) 1 M TEABF₄/ACN. [Reproduced from Castro-Gutiérrez et al. (2019)⁸]

were obtained by using the packing density of the electrodes, 0.50 g cm⁻³ (determined by measuring the thickness of the electrodes with a non-contact profilometer), and taking into account the amount of active material they contain, 85 %.⁴² Although the performance evaluated by the volumetric parameters is lower than that obtained with the gravimetric ones, the electrodes used in this study were not pressed, so the volumetric performance might be further improved by rolling - flattening. Nonetheless, note that the maximum achievable packing density is 0.74 g cm⁻³ for A60-CTPW and 0.62 g cm⁻³ for A75-CTPW, which are their respective particle densities.

5.5 Conclusion

High surface area-carbon materials were obtained by the physical activation of tannin-derived OMCs. It was found that the 2D hexagonal ordered mesoporous structure is preserved after CO₂ activation up to a BO of ~80 % and it increases both the connectivity between micro- and mesopores and the oxygen content at the material surface.

Activation for 60 or 75 min produces materials with an adequate balance between high surface area and suitable pore size distribution that results in high performance in both aqueous and organic electrolytes. The tested materials display square-shaped CV curves and exhibit high values of capacitance and high specific energy and power.

The improved connectivity of the porous structure in the AOMCs is especially important at high charge/discharge rates, resulting in high rate capability with capacitance retentions up to 70 % at 80 A g⁻¹. In addition, the AOMCs present very good long-term stability over time and after continuous cycling under realistic testing conditions.

In conclusion, the easy synthesis, the use of an environment-friendly precursor and the good electrochemical performances of these tannin-derived AOMCs make them suitable candidates to be used as electrodes in supercapacitors.

5.6 References

1. Sevilla, M. & Mokaya, R. Energy storage applications of activated carbons: supercapacitors and hydrogen storage. *Energy Environ. Sci.* 7, 1250–1280 (2014).
2. Yang, B. et al. 3D nitrogen-doped framework carbon for high-performance potassium ion hybrid capacitor. *Energy Storage Materials* (2019) doi:10.1016/j.ensm.2019.04.008.
3. Wang, Y., Song, Y. & Xia, Y. Electrochemical capacitors: mechanism, materials, systems, characterization and applications. *Chemical Society Reviews* 45, 5925–5950 (2016).
4. Lim, E., Jo, C. & Lee, J. A mini review of designed mesoporous materials for energy-storage applications: from electric double-layer capacitors to hybrid supercapacitors. *Nanoscale* 8, 7827–7833 (2016).
5. Gao, Z., Zhang, Y., Song, N. & Li, X. Biomass-derived renewable carbon materials for electrochemical energy storage. *Materials Research Letters* 5, 69–88 (2017).
6. González, A., Goikolea, E., Barrena, J. A. & Mysyk, R. Review on supercapacitors: Technologies and materials. *Renewable and Sustainable Energy Reviews* 58, 1189–1206 (2016).
7. Sánchez-Sánchez, Á., Centeno, T. A., Suárez-García, F., Martínez-Alonso, A. & Tascón, J. M. D. The importance of electrode characterization to assess the supercapacitor performance of ordered mesoporous carbons. *Microporous and Mesoporous Materials* 235, 1–8 (2016).
8. Castro-Gutiérrez, J. et al. High-Rate Capability of Supercapacitors Based on Tannin-Derived Ordered Mesoporous Carbons. *ACS Sustainable Chem. Eng.* 7, 17627–17635 (2019).
9. Thommes, M. et al. Physisorption of gases, with special reference to the evaluation of surface area and pore size distribution (IUPAC Technical Report). *Pure and Applied Chemistry* 87, (2015).
10. Brunauer, S., Emmett, P. H. & Teller, E. Adsorption of gases in multimolecular layers. *Journal of the American chemical society* 60, 309–319 (1938).
11. Shi, H. Activated carbons and double layer capacitance. *Electrochimica Acta* 41, 1633–1639 (1996).
12. Lota, G., Centeno, T. A., Frackowiak, E. & Stoeckli, F. Improvement of the structural and chemical properties of a commercial activated carbon for its application in electrochemical capacitors. *Electrochimica Acta* 53, 2210–2216 (2008).
13. Centeno, T. A. & Stoeckli, F. The assessment of surface areas in porous carbons by two model-independent techniques, the DR equation and DFT. *Carbon* 48, 2478–2486 (2010).
14. Jagiello, J., Ania, C., Parra, J. B. & Cook, C. Dual gas analysis of microporous carbons using 2D-NLDFT heterogeneous surface model and combined adsorption data of N₂ and CO₂. *Carbon* 91, 330–337 (2015).
15. Zuliani, J. E., Caguiat, J. N., Kirk, D. W. & Jia, C. Q. Considerations for consistent characterization of electrochemical double-layer capacitor performance. *Journal of Power Sources* 290, 136–143 (2015).
16. Sanchez-Sanchez, A. et al. Sugarcane molasses as a pseudocapacitive material for supercapacitors. *RSC Advances* 6, 88826–88836 (2016).

17. Braghiroli, F. L. et al. Electrochemical performances of hydrothermal tannin-based carbons doped with nitrogen. *Industrial Crops and Products* 70, 332–340 (2015).
18. Qu, D. Studies of the activated carbons used in double-layer supercapacitors. *Journal of Power Sources* 109, 403–411 (2002).
19. Huang, J., Sumpter, B. G. & Meunier, V. A Universal Model for Nanoporous Carbon Supercapacitors Applicable to Diverse Pore Regimes, *Carbon Materials, and Electrolytes. Chemistry - A European Journal* 14, 6614–6626 (2008).
20. Chmiola, J., Yushin, G., Dash, R. & Gogotsi, Y. Effect of pore size and surface area of carbide derived carbons on specific capacitance. *Journal of Power Sources* 158, 765–772 (2006).
21. Chmiola, J. et al. Anomalous Increase in Carbon Capacitance at Pore Sizes Less Than 1 Nanometer. *Science* 313, 1760–1763 (2006).
22. Sanchez-Sanchez, A. et al. Ordered mesoporous carbons obtained by soft-templating of tannin in mild conditions. *Microporous and Mesoporous Materials* 270, 127–139 (2018).
23. Hsieh, C.-T. & Teng, H. Influence of oxygen treatment on electric double-layer capacitance of activated carbon fabrics. *Carbon* 40, 667–674 (2002).
24. Stoller, M. D. & Ruoff, R. S. Best practice methods for determining an electrode material's performance for ultracapacitors. *Energy & Environmental Science* 3, 1294 (2010).
25. Elmouwahidi, A. et al. Activated carbons from agricultural waste solvothermally doped with sulphur as electrodes for supercapacitors. *Chemical Engineering Journal* 334, 1835–1841 (2018).
26. Sanchez-Sanchez, A. et al. Excellent electrochemical performances of nanocast ordered mesoporous carbons based on tannin-related polyphenols as supercapacitor electrodes. *Journal of Power Sources* 344, 15–24 (2017).
27. Li, Z. et al. Carbonized Chicken Eggshell Membranes with 3D Architectures as High-Performance Electrode Materials for Supercapacitors. *Advanced Energy Materials* 2, 431–437 (2012).
28. Ruiz, V. et al. An activated carbon monolith as an electrode material for supercapacitors. *Carbon* 47, 195–200 (2009).
29. Li, Q. et al. Synthesis of mesoporous carbon spheres with a hierarchical pore structure for the electrochemical double-layer capacitor. *Carbon* 49, 1248–1257 (2011).
30. Fuertes, A. B., Lota, G., Centeno, T. A. & Frackowiak, E. Templated mesoporous carbons for supercapacitor application. *Electrochimica Acta* 50, 2799–2805 (2005).
31. Ruiz-Rosas, R. et al. Electrochemical Performance of Hierarchical Porous Carbon Materials Obtained from the Infiltration of Lignin into Zeolite Templates. *ChemSusChem* 7, 1458–1467 (2014).
32. Futaba, D. N. et al. Shape-engineerable and highly densely packed single-walled carbon nanotubes and their application as super-capacitor electrodes. *Nature Materials* 5, 987–994 (2006).
33. Chen, Z. et al. High-Performance Supercapacitors Based on Hierarchically Porous Graphite Particles. *Advanced Energy Materials* 1, 551–556 (2011).
34. Xu, B. et al. Activated carbon prepared from PVDC by NaOH activation as electrode materials for high performance EDLCs with non-aqueous electrolyte. *International Journal of Hydrogen Energy* 35, 632–637 (2010).

35. Rufford, T. E., Hulicova-Jurcakova, D., Fiset, E., Zhu, Z. & Lu, G. Q. Double-layer capacitance of waste coffee ground activated carbons in an organic electrolyte. *Electrochemistry Communications* 11, 974–977 (2009).
36. Gogotsi, Y. & Simon, P. True Performance Metrics in Electrochemical Energy Storage. *Science* 334, 917–918 (2011).
37. Zhong, C. et al. A review of electrolyte materials and compositions for electrochemical supercapacitors. *Chemical Society Reviews* 44, 7484–7539 (2015).
38. Bichat, M. P., Raymundo-Piñero, E. & Béguin, F. High voltage supercapacitor built with seaweed carbons in neutral aqueous electrolyte. *Carbon* 48, 4351–4361 (2010).
39. Demarconnay, L., Raymundo-Piñero, E. & Béguin, F. A symmetric carbon/carbon supercapacitor operating at 1.6V by using a neutral aqueous solution. *Electrochemistry Communications* 12, 1275–1278 (2010).
40. Jiménez-Cordero, D., Heras, F., Gilarranz, M. A. & Raymundo-Piñero, E. Grape seed carbons for studying the influence of texture on supercapacitor behaviour in aqueous electrolytes. *Carbon* 71, 127–138 (2014).
41. Lu, S. et al. Effect of aqueous electrolytes on the electrochemical behaviors of ordered mesoporous carbon composites after KOH activation as supercapacitors electrodes. *Journal of Electroanalytical Chemistry* 818, 58–67 (2018).
42. Fuertes, A. B., Ferrero, G. A. & Sevilla, M. Commentary: Methods of calculating the volumetric performance of a supercapacitor. *Energy Storage Materials* 4, 154–155 (2016).

Chapter 6

Effect of mesopore order on SC performance

6.1 Introduction

As detailed in Chapter 1 (Section 1.2), SCs store energy by accumulation of charges at the electrolyte-electrode interface, thus high surface area materials are required for their fabrication. In addition, this surface needs to be available for the electrolyte ions; hence, the importance of adapting the size of the pores to that of the ions of the selected electrolyte to increase accessibility and fully occupy the charge storage sites.

Studies have reported that a hierarchical structure connecting the micro-, meso- and macroporosity (pore size < 2 nm, between 2 and 50 nm, and > 50 nm, respectively) improves the diffusion in the material, thus enhancing the SCs performance, in particular at high charging rates.¹⁻⁴ Indeed, it is generally accepted that, in a porous material, micropores provide charge storage sites while mesopores act as channels for ion transport and diffusion, and the macropores serve as an electrolyte reservoir.⁴ It has also been hypothesized that ion transfer and diffusion could be more efficient in an ordered mesopore structure than in a disordered one.^{5,6} Therefore, many studies have focused on designing and engineering mesoporous carbons (MCs) with adjusted size and morphology of mesopores^{1,7} (Section 1.4).

In most cases, studies focus on the electrochemical performance of materials with different surface areas and porosity properties (pore volume, size and distribution) having either a disordered structure as in ACs, or an ordered one as in AOMCs, but the effect of the mesopore order is generally disregarded. A study from Li et al. (2019)⁸ reported differences between the electrochemical performances in an organic electrolyte (TEABF₄/ACN) of two KOH-activated mesoporous carbons with cylinder and gyroid geometries. It was found that the gyroid material reached higher values of capacitance, but this could be ascribed to its more developed microporosity and not necessarily to the morphology differences. In addition, electrochemical tests were performed up to moderate charging rates (5 A g⁻¹) where diffusion differences due to the presence of mesopores are less noticeable. A detailed discussion of the effect of order and its connectivity on the SC performances is still needed. Furthermore, direct comparison between published studies to gain more knowledge about the effect of the order remains difficult, since the order cannot be easily isolated from other factors that also influence the SCs performance such as surface area, pore volume and size, surface chemistry, or even testing conditions.

Thus, the study presented in this chapter aims to deepen on the understanding of the effect of the order on the electrochemical performances of activated mesoporous carbons (AMCs) for

which disordered MCs (DMCs), as those characterized in Chapter 4, were synthesized by the SWAMM method ⁹ (Chapter 3) and further activated with CO₂. After activation, the physicochemical properties of the activated DMCs (ADMCS) were compared to those of the tannin-derived AOMCs from Chapter 5.¹⁰ Finally, the electrochemical performances of two model materials, only differing by the mesopore order, were compared when used as electrodes for SCs in aqueous and organic electrolytes.

CO₂ activation of the DMC material was carried out using the same procedure followed for obtaining the AOMCs of Chapter 5. Briefly, the temperature was raised to 900 °C under N₂ atmosphere, then the gas was switched to CO₂, hold for times ranging from 15 to 60 min and finally left to cool down by switching back the gas to N₂. The materials were labeled *A_t*-DMC, where “*t*” stands for the activation time in minutes. For comparison, the AOMCs of Chapter 5 are referred herein as *A_t*-OMC, with “*t*” again representing the activation time in minutes.

Pore texture analysis was carried out using the ASAP devices from Micromeritics to acquire N₂ and CO₂ isotherms at -196 and 0 °C, respectively, and applying the BET and 2D-NLDFT HS to calculate the surface area, total pore volume and the pore volume in different ranges of pore width, using the software Microactive® and SAIEUS® from Micromeritics. The nanostructure was analyzed through Raman spectroscopy. Chemical characterization was performed by EA and XPS. Electrochemical measurements were carried out in aqueous and organic electrolytes, 1 M H₂SO₄ and 1 M TEABF₄/CAN, respectively. See details in the corresponding sections of Chapter 2.

6.2 CO₂ activation process

Figure 6.1a shows the burn-off (BO) of the DMC and the OMC with the activation time; note that the activation process seems to be more efficient on the DMC because a higher BO was observed for any given activation time. This finding can be attributed to a higher effective residence time of CO₂ within the particles of the DMC. Due to the disordered structure, CO₂ molecules entering a porous DMC particle should indeed follow a longer path to exit than that in an OMC, as shown schematically in Figure 6.1b. This longer residence time would result in faster and easier development of the porosity, thus requiring shorter activation times than

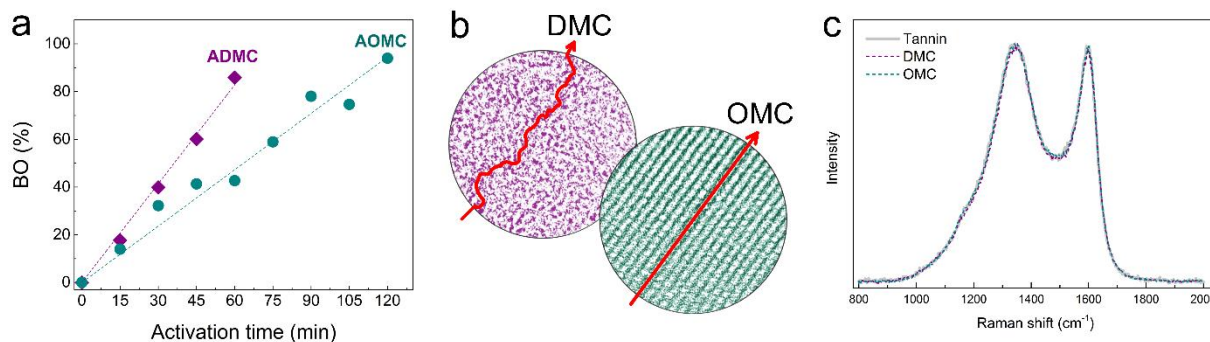


Figure 6.1. (a) Burn-off (BO) as a function of activation time for the activated ordered and disordered carbons (AOMC and ADMC, respectively). (b) Scheme of different diffusion paths within a particle of disordered and ordered mesoporous carbon (DMC and OMC, respectively). (c) 1st order Raman spectra of as-synthesized DMC, OMC and mimosa tannin carbonized at the same temperature of 900 °C.

those of the OMCs, as detailed below. This hypothesis is valid as long as the nanostructure of the non-activated carbons is comparable, which has been confirmed by Raman spectroscopy. Figure 6.1c shows the Raman spectra of the DMC, the OMC, and the tannin carbonized (without mesostructuration) at the same temperature. These spectra are strictly identical, verifying that there is no difference regarding the nanostructure, which corresponds to that of very poorly crystallized (*i.e.*, highly defective) carbon. Thus, DMC and OMC should have the same reactivity with CO₂, confirming that the higher texture development of DMC at a given activation time is due to the differences in the mesopore connectivity and therefore in the residence time.

6.3 Textural properties

Figure 6.2a shows the N₂ adsorption-desorption isotherms for the ADMC series. According to the IUPAC classification,¹¹ the adsorption branches could be identified as a combination of types I and IV, and the desorption branches presented H5 hysteresis loops, resulting from the combination of two H2 loops. The increasing N₂ uptake for $p/p_0 < 0.2$ after activation is due to the development of microporosity while the shape obtained for $p/p_0 > 0.2$ is related to the presence of large mesopores. Indeed, the PSD of the as-synthesized material presented a broad peak centered at ~ 6 nm that extends to pores wider than 10 nm. As expected, the activation resulted in a widening of the mesoporosity (see Figure 6.2b). In contrast, OMC and AOMCs showed PSDs with a narrower peak centered at slightly lower pore diameters of

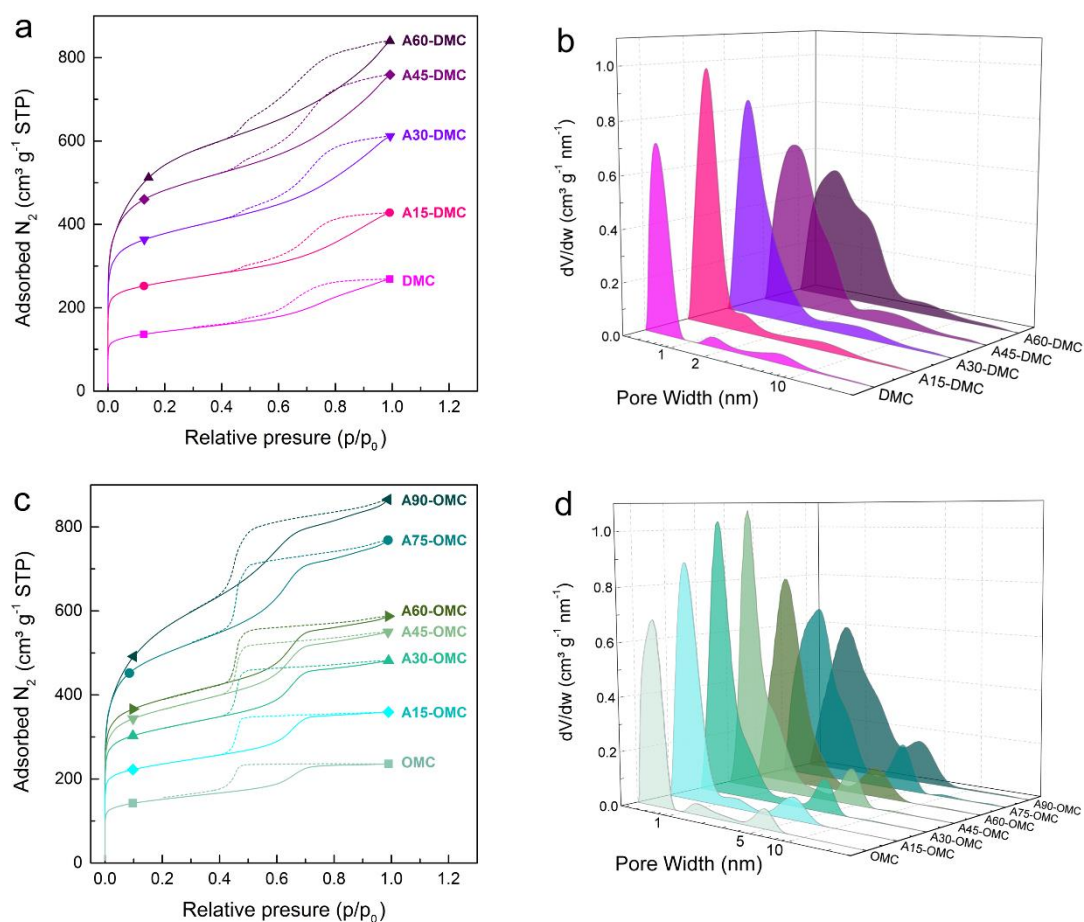


Figure 6.2. (a, c) N_2 adsorption-desorption isotherms of raw and activated DMCs and OMCs; (b, d) corresponding PSDs of the same materials.

~ 5 nm. This peak increased in height and width, along with the development of the mainly narrow mesoporosity¹⁰ (see Figure 6.2c and 6.2d). Besides, both DMC and OMC materials presented a narrow peak centered at ~ 0.5 nm, *i.e.*, ultramicropores that progressively broadened with activation time until they extended across the full micropore range.

Figure 6.3 shows that when comparing the evolution of surface area (S_{NLDFT} and A_{BET}) and pore volume as a function of BO (all calculated values for the ADMCs are listed in Table A3.1 in Annex 3), the two series of AMC materials followed the same trends with the BO. The values of S_{NLDFT} and A_{BET} of the ADMCs crossed at $BO \approx 40\%$ due to under- and over-estimations linked to the assumptions made by the BET method when pores less than 0.7 or wider than 1.2 nm, respectively, are involved.^{12,13} In any case, the textural properties increased with activation up to a maximum value at $BO \approx 80\%$ (Figure 6.3), and the same behavior as that observed for

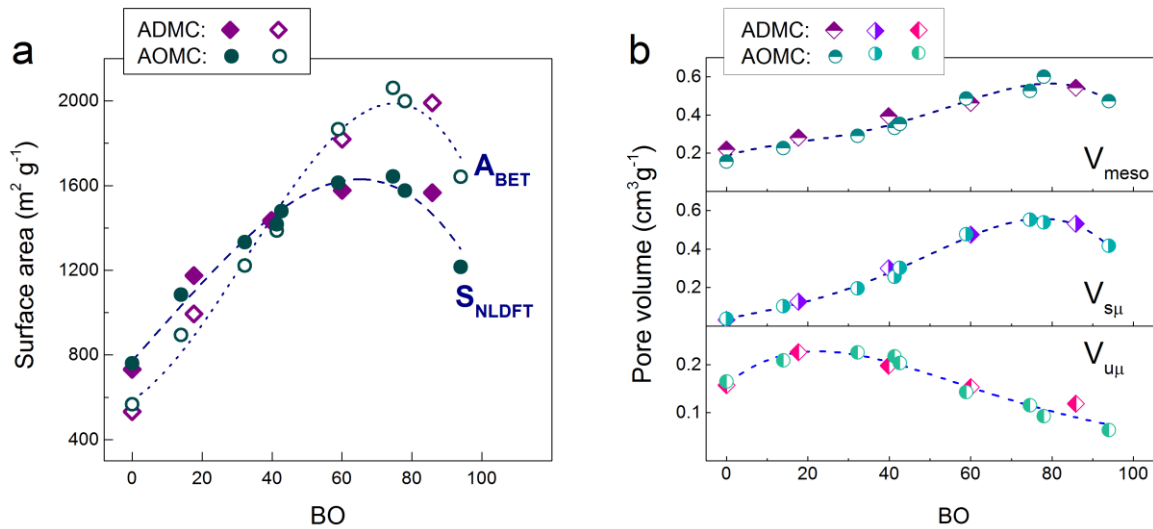


Figure 6.3. Evolution of (a) 2D-NLDFT HS surface area (S_{NLDFT}) and BET area (A_{BET}), and (b) meso-, supermicro- and ultramicropore volumes (V_{meso} , $V_{S\mu}$ and $V_{u\mu}$, respectively) as a function of burn-off (BO) for the two series of activated DMCs and OMCs.

the surface area was followed by the volumes of supermicropores ($0.7 < \text{pore size} < 2 \text{ nm}$) and mesopores ($2 < \text{pore size} < 50 \text{ nm}$), $V_{S\mu}$ and V_{meso} , respectively (Figure 6.3b). On the contrary, the ultramicropore (pore size $< 0.7 \text{ nm}$) volume, $V_{u\mu}$, reached a maximum at $\text{BO} \approx 20 \%$, after which it started to decrease due to the widening and merging of pores. Pore widening and merging also caused the observed drop of $V_{S\mu}$ and V_{meso} for $\text{BO} > 80 \%$. This similar textural evolution can be explained by the fact that DMC and OMC are derived from the same carbon precursor, *i.e.*, mimoso tannin, which after carbonization gives the same microporous highly defective carbon.

The scanning of the hysteresis loops of the adsorption-desorption isotherms is a useful tool for obtaining more information on the pore network and its connectivity.^{14,15} As shown in Chapter 4, in a connected pore system desorption depends on the state of neighboring pores, thus partial filling of the pore network gives rise to desorption curves of different shapes. On the contrary, when independent pores are present in the material, the onset of desorption is not affected by the state of adjacent pores and the desorption branches obtained from the scanning of the hysteresis loop retain the same shapes. In addition, desorption in H2 loops, associated to the presence of ink-bottle pores, can occur by pore blocking/percolation effects or by cavitation if the neck width, w , is above or below a critical value w_c , respectively.^{11,16} Figure 6.4 shows the scanning of the hysteresis loops of N_2 isotherms that was carried out on as-synthesized and

activated materials of the two series studied herein, and similar analysis to that detailed in Section 4.3 can be carried out.

Figure 6.4a, 6.4c and 6.4e show the scanning of hysteresis loops of DMC, A15-DMC and A30-DMC isotherms. The H5 loops observed for the ADMCs are related to the presence of open and blocked pores,¹¹ which can be identified from the behavior of the scanned (or secondary) desorption branches, similar to what had been observed previously for mesostructured zeolites.¹⁷ For the first part of the hysteresis loop (*ca.* $p/p_0 > 0.6$), the different shape of the secondary desorption branches with respect to the boundary relates to a network connected through a broad distribution of neck sizes, *i.e.*, desorption occurs due to percolation

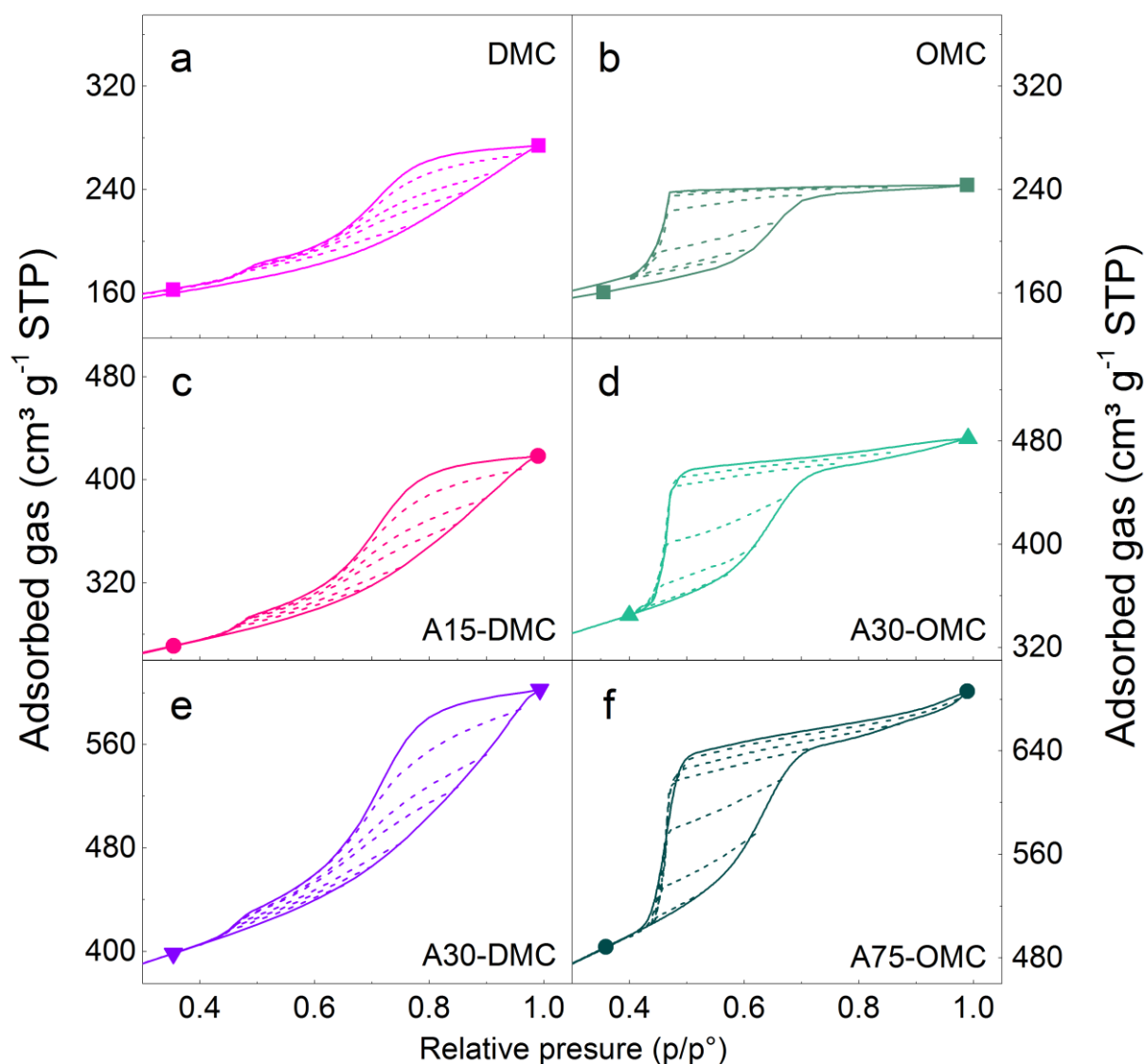


Figure 6.4. Scanned hysteresis loops of as-synthesized and activated (a, c, e) disordered and (b, d, f) ordered MCs. Solid lines represent the boundary adsorption and desorption curves while dotted lines represent the scanned or secondary desorption branches.

effects.^{11,16} Conversely, on the loop section found for lower relative pressures (*ca.* $p/p_0 < 0.6$), the desorption branches retain the same shapes, a behavior observed in materials with independent or restricted pores. This indicates that desorption is controlled by cavitation, thus suggesting that even after activation some of the mesopores are still connected by micropores or narrow mesopores, such that $w < w_c$ with w_c being 5 nm.^{14,18}

To deepen on the analysis of the scanned hysteresis, the slope of the tangent line at the starting point (p_{des}) of the scanned desorption branches was calculated and plotted as a function of p_{des} , see Figure 6.5a. From the changes of these slopes, it is also possible to identify two pore systems in the ADMCs. For the desorption branches starting at $p_{des} > 0.8$, the slopes increased when p_{des} decreased, faster at higher activation time (*i.e.*, at higher BO), indicating that percolation effects are more important and suggesting improved pore connectivity after activation. For $p_{des} < 0.8$, only the narrow mesopores are partially or completely filled, and the fact that the slopes change at the same rate regardless of the activation time and that they decrease as does p_{des} is an indication of desorption hindered due to restricted access to pores. These analyses allow classifying the mesopores based on their width as open or restricted (blocked), *i.e.*, such that $w > 5$ nm or $2 < w < 5$ nm, respectively. Figure 6.5b shows the volume of open and restricted pores ($V_{>5\text{ nm}}$ and $V_{2-5\text{ nm}}$, respectively), and Figure 6.5c displays their average width along with the average pore width of the whole mesoporous system ($w_{av,>5\text{ nm}}$, $w_{av,2-5\text{ nm}}$ and $w_{av, meso}$, respectively) for the ADMCs. It was found that, in all cases, the amount of open pores is greater than that of the restricted pores, that $w_{av,>5\text{ nm}}$ increased from 8 to 9 nm due to pore widening, and that $w_{av,2-5\text{ nm}}$ decreased slightly from 3.5 to 2.8 nm due to the development of narrow mesopores. Finally, it is reasonable to establish that mesopores in ADMCs constitute a well-connected open network since $w_{av,meso}$ remains above the critical pore width ($w_c = 5$ nm), below which access to pores is restricted.

The scanning of the hysteresis loop of the OMC, shown in Figure 6.4b, revealed straight secondary desorption branches with a steep decrease at approximately the same relative pressure. Likewise, A30-OMC and A75-OMC materials exhibited straight scanned desorption branches (Figure 6.4d and 6.4f). Even so, these lines progressively change their slope, Figure 6.5d displays these changes as a function of p_{des} for the AOMCs, where again it is possible to distinguish two trends. For the desorption branches originating from $p/p_0 > 0.7$, the slope is almost constant. Such delayed desorption indicates that wider pores, which are filled last, are isolated or connected only through micropores and/or narrow mesopores ($w < w_c = 5$ nm).

For $p/p_0 < 0.7$, a decrease in the slope with a decrease in p_{des} was observed for the OMC. Interestingly, as the BO increased due to activation, the behavior was reversed, *i.e.*, the slopes increased as p_{des} decreased. These variations in the desorption rate of partially filled pores suggest the occurrence of percolation, at some extent, in the narrow-mesopore network, which is more important for the A75-OMC. Using the same criteria as for the ADMCs, the mesopores in the AOMCs can be classified as open and restricted. Figure 6.5e and 6.5f show $V_{>5\text{ nm}}$, $V_{2-5\text{ nm}}$, $w_{av,>5\text{ nm}}$, $w_{av,2-5\text{ nm}}$ and $w_{av,meso}$ for the ordered materials. In the case of the AOMCs, the major contribution to the mesoporous volume comes from the narrow pores, $V_{2-5\text{ nm}}$, which is always higher than $V_{>5\text{ nm}}$. Therefore, even though activation widens the channels of the AOMCs (see $w_{av,>5\text{ nm}}$ in Figure 6.5f), thereby improving their connectivity, they are still connected through narrow pores and the mesoporous network remains mainly restricted because $w_{av,meso}$ is consistently lower than 5 nm.

The differences in connectivity between the ADMCs and the AOMCs will be shown to have an effect on the electrochemical performance of the materials, in particular, in the organic electrolyte, as explained below.

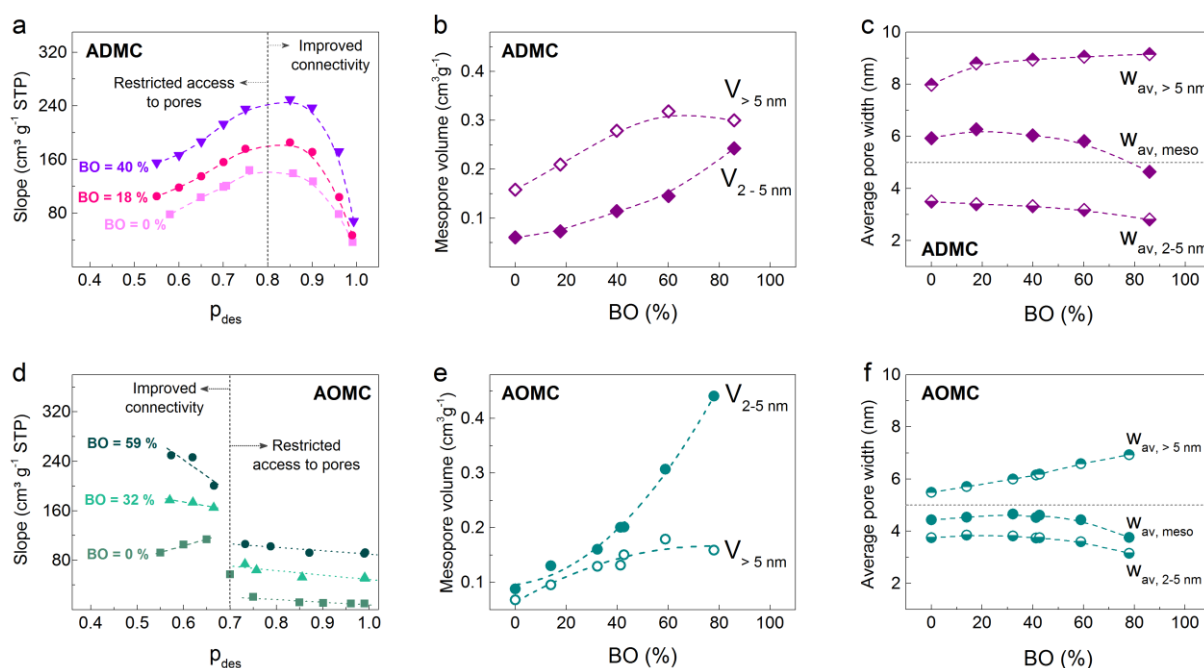


Figure 6.5. Slope of (a) the tangent line at the starting point (p_{des}) of scanned desorption branches as a function of p_{des} , for DMC, A15-DMC and A30-DMC samples; and (d) of desorption branches as a function of p_{des} for OMC, A30-OMC and A75-OMC samples. Contribution to the mesoporous volume of pores having widths below and above 5 nm ($V_{2-5\text{ nm}}$ and $V_{>5\text{ nm}}$, respectively) for (b) ADMCs and (e) AOMCs materials. Average pore width of mesopores, as well of mesopores in the 2 – 5 nm and 5 – 50 nm ranges ($w_{av,meso}$, $w_{av,2-5\text{ nm}}$ and $w_{av,>5\text{ nm}}$, respectively) for (c) ADMCs and (f) AOMCs materials.

6.4 Surface and bulk composition

Figure 6.6a and 6.6b show the oxygen (O) content of the materials determined by elemental analysis (EA) and by X-ray photoelectron spectroscopy (XPS). In general, a sharp decrease in the O content was produced when materials were slightly activated (BO < 20 %). Additional activation resulted in an augmentation in the O content for ADMCs and AOMCs. In addition, the EA revealed that the amount of O in the bulk is consistently higher for ADMCs than for AOMCs, see Figure 6.6a; yet, there is a parallel evolution of the O content for the two series of materials, as this difference remains ~4 % for a given value of BO. Besides, as shown in Figure 6.6b, the O content at the surface remained roughly the same for the two series of materials, following the same trend as the BO increases. This similar behavior of the surface O content suggests that both materials, DMC and OMC, have a similar reactivity towards CO₂ regardless of the differences found in the bulk, again implying that the faster development of porosity properties observed in the ADMC series is due to longer diffusion paths within its particles.

Nonetheless, some differences were found on the relative contributions of surface functional groups for each series when compared as a function of activation time, see

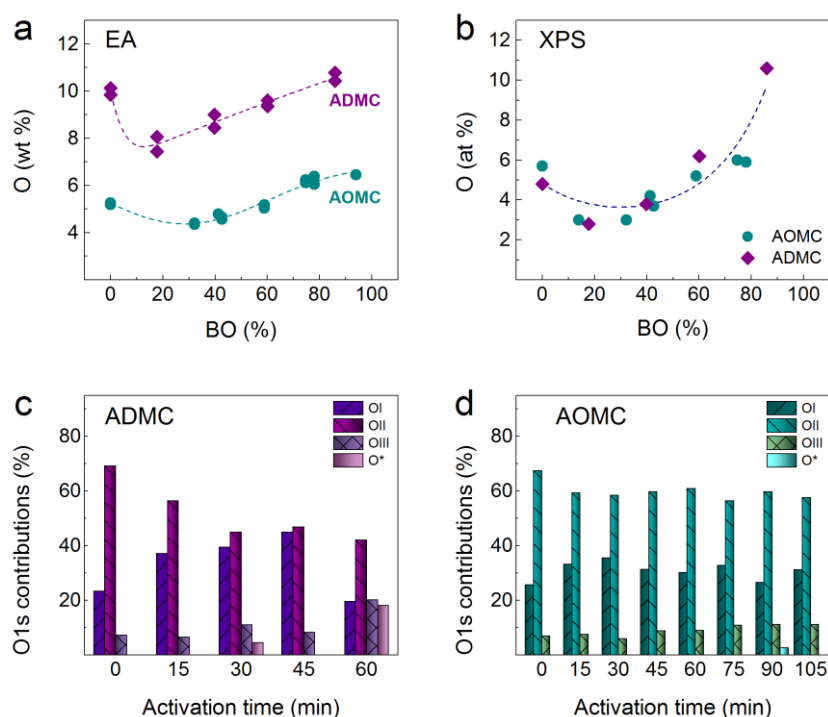


Figure 6.6. Oxygen content of the two series of activated materials, ADMCs and AOMCs measured (a) by elemental analysis (EA) and (b) by X-ray photoelectron spectroscopy (XPS). O1s contributions to the different functional groups for (c) ADMC and (d) AOMC series.

Figure 6.6c and 6.6d. The complete assignment of peaks and the relative contributions of the functional groups are listed in Table A3.2. In the ADMCs, quinone- and carbonyl-type functionalities (OI) increased up to 45 % for A45-DMC and decreased drastically to ~20 % after 60 min of activation. Meanwhile, for the AOMCs, the highest OI contribution was found for A30-OMC (36 %), but for $t > 30$ min, this contribution remained close to 30 %. For the ADMCs, the contribution of carboxylic groups (OIII) increased considerably with activation time, from 7 to 20 %, whereas it increased moderately for AOMCs, going from 7 to 11%. Finally, the greatest contribution to O functionalities in both the ADMCs and the AOMCs comes from phenolic groups (OII) due to the polyphenolic nature of the precursor. The presence of certain groups on the surface of carbon materials can contribute to the performances of supercapacitors when using aqueous electrolytes (Section 1.4.6). Especially, OI contributions are reported to be among the most electrochemically active groups that can lead to pseudocapacitance contributions, whereas the high polarity of OIII groups might hinder the diffusion of ions.¹⁹

6.5 Electrochemical characterization

Based on the characterization carried out on the ADMCs and the AOMCs, a sample from each series was chosen to study the effect of mesopore order on the electrochemical performance. Figure 6.7 compares the textural properties of the selected samples, A45-DMC

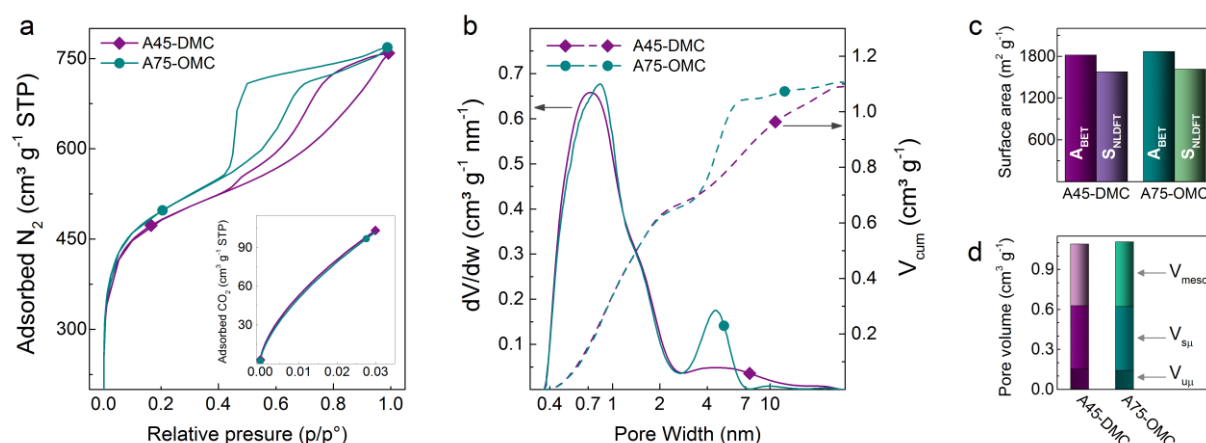


Figure 6.7. Comparison of textural properties of A45-DMC and A75-OMC: (a) N₂ and (inset) CO₂ isotherms; (b) pore size distributions, differential (dV/dw , solid lines) and cumulative pore volumes (V_{cum} , dashed lines); (c) BET area (A_{BET}) and 2D-NLDFT HS surface area (S_{NLDFT}); and (d) ultramicro-, supermicro- and mesopore volumes (*i.e.*, V_{ul} , V_{sm} and V_{meso} , respectively).

and A75-OMC. It shows their N₂ and CO₂ adsorption isotherms, PSDs, surface areas and pore volumes. Indeed, the two samples have practically the same textural properties with the exception of the mesopore order and a wider PSD in the mesopore range for the disordered sample. Electrodes for SCs were prepared using A45-DMC and CV, GCD and EIS tests were carried out in aqueous (1 M H₂SO₄) and organic (1 M TEABF₄/ACN) electrolytes. Then, the performance of A45-DMC was compared to that of A75-OMC, which has been found to have the best performance among the materials of the AOMC series¹⁰ (Chapter 5).

In aqueous electrolyte, Figure 6.8b shows that A45-DMC, like A75-OMC, presents quasi-rectangular CV curves at a low scan rate (5 mV s⁻¹), proof of the ideal supercapacitor behavior of the materials. As the scan rate increases, A75-OMC performs slightly better than A45-DMC, see Figure 6.8c. For the GCD tests, it is observed that as the charge rate increases, the difference of specific cell capacitance, C_{cell} , increases, A75-OMC reaching higher values, see Figure 6.8d. Note that for low-rate GCD tests, where possible redox reactions have a greater impact on the performance of SCs, the C_{cell} of the two materials is practically the same, suggesting that the differences in their surface chemistry have a negligible contribution to the capacitance. C_{cell} values obtained from GCD curves were used to calculate the specific energy and power (E and P , respectively) of the assembled SCs, and the resultant Ragone-like plot is shown in Figure 6.8e. A maximum E of 5 Wh kg⁻¹ with a P output of 44 W kg⁻¹ is found for both materials.

EIS tests show that A45-DMC has a larger Warburg region in the Nyquist plot, displayed in Figure 6.9a, resulting in a higher equivalent distributed resistance (EDR) associated with slower ion diffusion in the micropores. The higher EDR of A45-DMC could be due to the presence of OIII groups that hinder ion diffusion. However, there is only a ~1 % difference of O content on the surface of the materials (higher for A45-DMC, see Figure 6.6 for a BO of ~60 %), from which there is a ~3 % difference between the contribution of OIII groups (higher for A75-OMC, see Table A3.2). Hence, the two selected carbons have approximately the same percentage of OIII groups on their surface, thus the larger EDR observed for A45-DMC cannot be completely explained by the surface chemistry. Then, the difference of EDR between A45-DMC and A75-OMC is attributed to the disordered mesostructure in A45-DMC, which leads to longer diffusion paths for the ions (Figure 6.1b), slightly reducing its performance, especially at high charging rates.

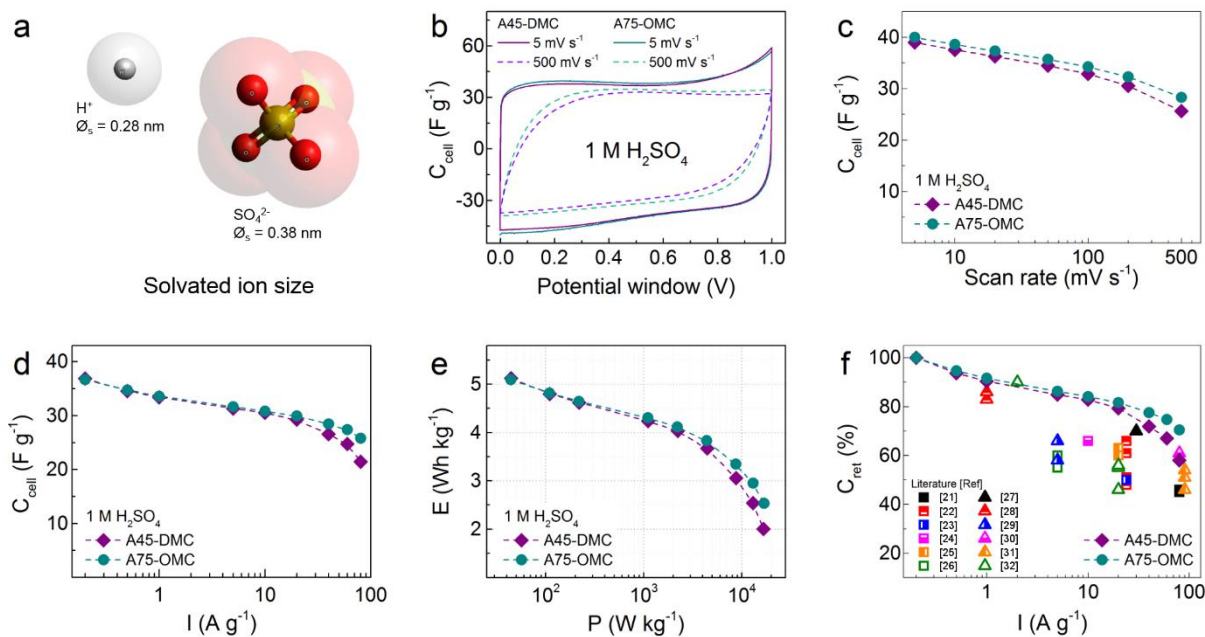


Figure 6.8. (a) Solvated ion size of H₂SO₄ in water.²⁰ Electrochemical performance of A45-DMC and A75-OMC in aqueous electrolyte (1 M H₂SO₄): (b) CV curves at 5 mV s⁻¹; C_{cell} as a function of (c) scan rate and (d) applied current; (e) Ragone-like plot showing the specific energy and power (*E* and *P*, respectively); and (f) C_{ret} vs applied current compared to similar materials reported in the literature.^{21–32}

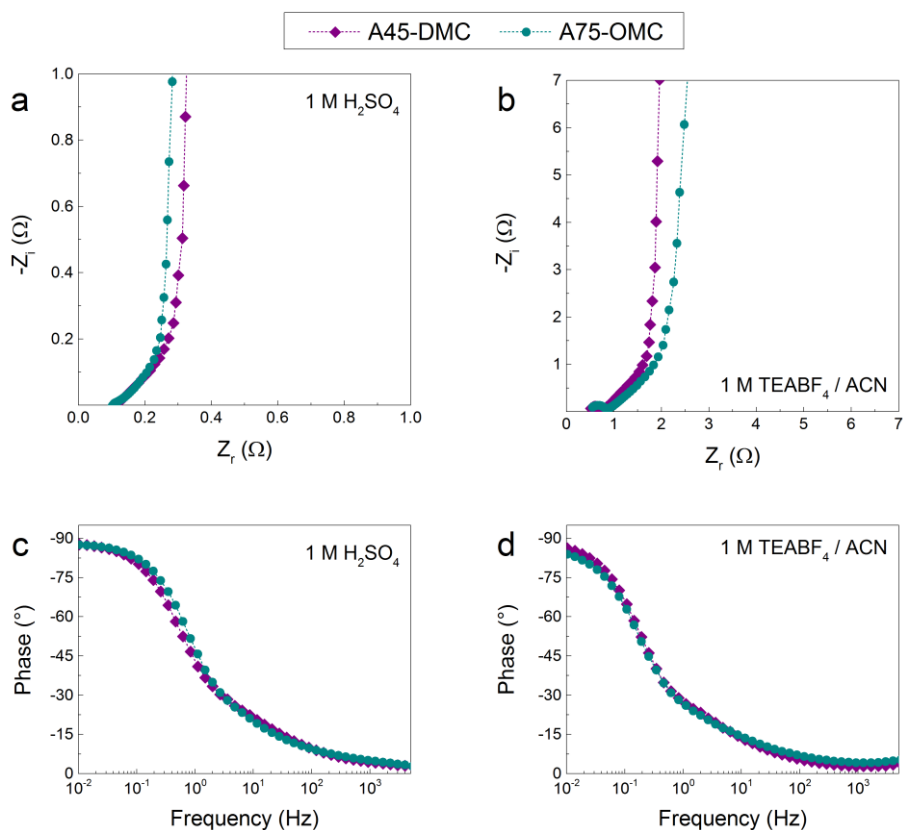


Figure 6.9. (a, b) Nyquist and (c, d) Bode plots for A45-DMC and A75-OMC in (a) aqueous and (b) organic electrolytes.

Figure 6.10 summarizes the performance of A45-DMC and A75-OMC in the organic electrolyte. Figure 6.10a shows that the two materials present rectangular CV curves at 5 mV s^{-1} ; but as the scan rate increases, the C_{cell} values of A75-OMC decrease more rapidly than those of A45-DMC, see Figure 6.10b. The GCD results are consistent with the aforementioned behavior, in Figure 6.10c it is possible to see the change of C_{cell} with the applied current density where, again, A45-DMC outperforms A75-OMC. As expected, in the Ragone-like plot of Figure 6.10e, similar values of P are found, but A45-DMC reaches higher values of E than A75-OMC, due to the higher C_{cell} of the former material; a maximum E of 29 Wh kg^{-1} with a P of 139 W kg^{-1} was attained by A45-DMC. The better performance of A45-DMC in the organic electrolyte might be due to the different solvated ion sizes, shown in Figure 6.8a and Figure 6.10a. Indeed, the ions in TEABF₄/ACN are of larger size than those in H₂SO₄,^{20,33} and the scanning of the hysteresis loops showed that most of the mesopores in A75-OMC are only accessible through narrow mesopores or even micropores, which would reduce the mobility and diffusion of large-sized ions. Despite the larger diffusion path that the disordered structure of A45-DMC represents, its wider PSD in the mesopore range compared to that of A75-OMC (Figure 6.7) and the well-connected network made up of unrestricted mesopores (Figure 6.5) make this material more accessible to TEABF₄/ACN ions. From the Nyquist plot obtained from EIS measurements in the organic electrolyte (Figure 6.9b), is possible to see that the Warburg zone is larger for A75-OMC than for A45-DMC. This linear region appearing at mid-frequencies is associated with ion diffusion and indicates that full access to the surface of the material is more difficult for the ordered material due to the narrow connections between mesopores. Consequently, a higher EDR is observed for A75-OMC in comparison with A45-DMC, explaining the better behavior of the latter material due to a favored diffusion of ions at any given charging rate.

Figure 6.11 shows the capacitance retention, C_{ret} , of A45-DMC and A75-OMC after continuous cycling at 5 A g^{-1} and after potentiostatic hold at the maximum voltage (1 V and 2.7 V in aqueous and organic electrolytes, respectively). For both materials, C_{ret} remained above 95 % after 10 000 cycles in the aqueous electrolyte and at 93 % after 8 000 cycles in the organic electrolyte. Moreover, while maintaining the potential at its maximum, C_{ret} again remained above 95 % after 72 h in the aqueous electrolyte and reached 86 % after 72 h in the organic electrolyte. The similarity of the results for both types of materials in each type of electrolyte evidenced that the mesoporous structure has no impact on the long-term stability of the assembled SCs as it does on its rate capability.

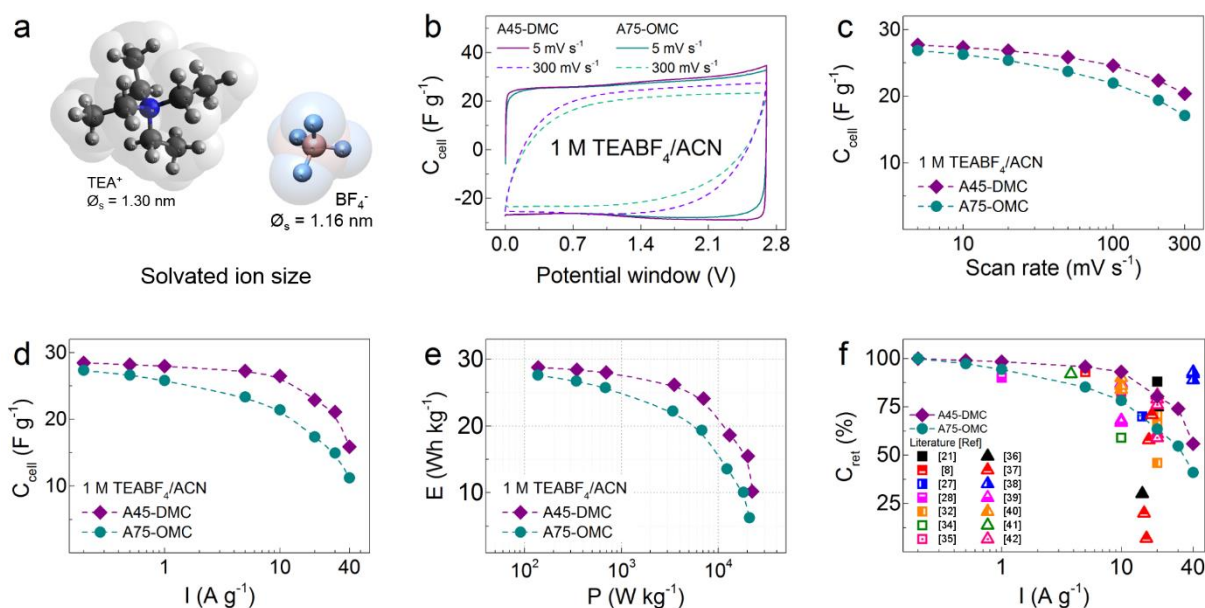


Figure 6.10. (a) Solvated ion size of TEABF₄ in acetonitrile.³³ Electrochemical performance of A45-DMC and A75-OMC in the organic electrolyte (1 M TEABF₄/ACN): (b) CV curves at 5 mV s⁻¹; C_{cell} as a function of (c) scan rate and (d) applied current; (e) Ragone-like plot showing the specific energy and power (*E* and *P*, respectively); and (f) C_{ret} vs applied current compared to similar materials reported in the literature.^{8,21,27,28,32,34–42}

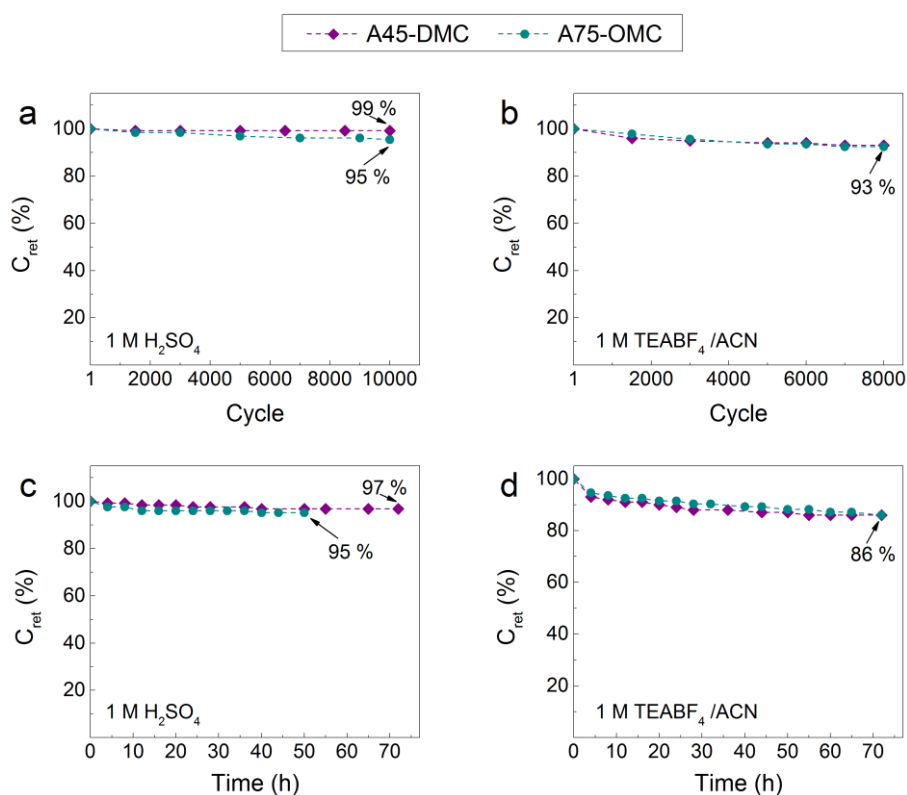


Figure 6.11. Long-term stability of A45-DMC and A75-OMC in aqueous (1 M H₂SO₄) and organic (1 M TEABF₄/ACN) electrolytes after (a, b) continuous cycling at 5 A g⁻¹ and (c, d) potentiostatic hold at the maximum potential (1 V and 2.7 V for aqueous and organic electrolytes, respectively).

The electrochemical tests also corroborated the importance of the correct choice of the material-electrolyte pair. Indeed, the improved diffusion of the small-size ions of the aqueous electrolyte A75-OMC resulted in a 12 % higher capacitance retention at 80 A g⁻¹ compared to that of A45-DMC at the same conditions (Figure 6.8f). On the other hand, the more interconnected porosity of A45-DMC allows better diffusion of large-size ions, thus improving the electrochemical performance in the organic electrolyte by 15 % at 40 A g⁻¹ when compared to that attained by the A75-OMC (Figure 6.10f).

As carried out for the AOMCs in Chapter 5, the comparison with other materials previously reported in the literature (Figure 6.8f, Figure 6.10f, Table A3.3 and Table A3.4) revealed that the materials studied herein show better rate capabilities in aqueous electrolyte and comparable values in organic electrolyte than other activated MCs synthesized by soft-templating techniques;^{8,23} silica- and zeolite-templated carbons;^{22,27–30,35} carbon nanotubes obtained by chemical vapor deposition of ethylene;³⁴ carbonized MOFs;³⁹ graphene oxide-derived materials;^{39–41} or ACs, from different precursors, activated using NaOH, ZnCl₂, KOH, KHCO₃ or K₂CO₃.^{21,24–26,31,32,36,37,39,42} In particular, from this materials, Figure 6.12 shows a comparison of the values of C_{ret} as a function of A_{BET} at 20 and 10 A g⁻¹ in aqueous and organic electrolytes, respectively. It is possible to observe that A45-DMC and A75-OMC exhibit superior C_{ret} in aqueous electrolyte (Figure 6.12a) and that A45-DMC is among the materials with the highest retention in the organic electrolyte (Figure 6.12b); this high rate capability of the tannin-derived mesoporous carbons is an advantage given that supercapacitors are generally needed to supply energy at high power outputs.

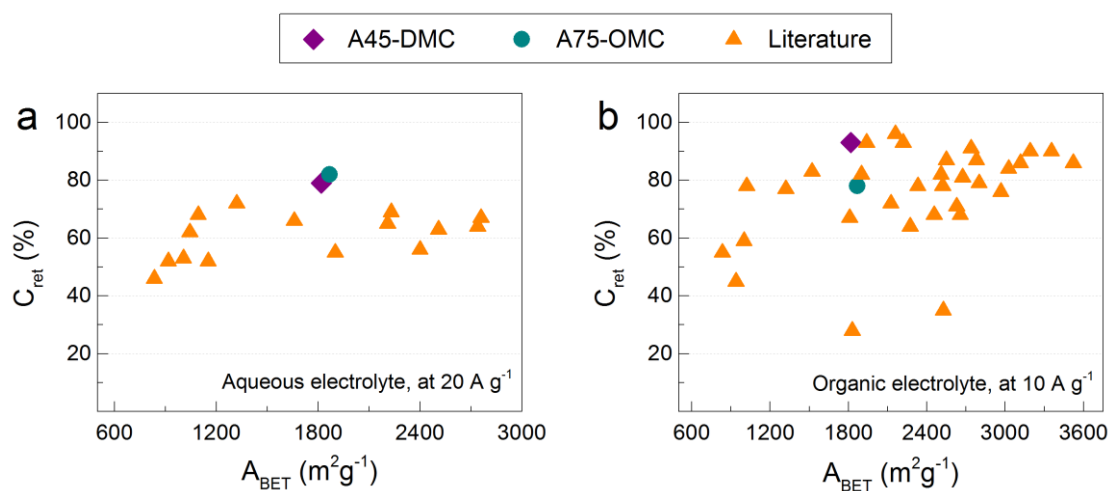


Figure 6.12. Comparison of the capacitance retention (C_{ret}) as a function of the BET area (A_{BET}) for the materials of this study and others reported in the literature: (a,b) in aqueous electrolyte (H₂SO₄) at 20 A g⁻¹ and (c,d) in organic electrolyte (TEABF₄) at 10 A g⁻¹.^{8,21–23,27,28,30–32,34–40,42}

Besides, the methods to produce most of the materials above mentioned, involve multiple steps for the synthesis and etching of templates, pre-treatment of the precursor by freeze-drying, pyrolysis at low temperatures or hydrothermal carbonization, and/or washing of impurities, all of which is time-consuming and usually entails the use of hazardous substances like HF, NaOH or HCl. The synthesis method presented herein requires *ca.* 1.5 days for the production of the AMCs, including the time needed for obtaining the mesophase and performing the carbonization and activation processes. This fast and easy synthesis is a considerable advantage over other complex methods that require not only synthesis times of several days or even weeks, but also drying, aging and/or washing steps. On the other side, note also in Figure 6.10f that the direct pyrolysis of potassium citrate resulted in ACs with higher rate capabilities than those of the AMCs presented herein.³⁸ The main advantages of the tannin-derived AMCs over the potassium citrate-derived ACs are the absence of washing steps (with HCl and water) as part of the production process and the considerably lower price of the precursor. Indeed, mimosa tannin is currently available for ~ 2 US\$ kg⁻¹, which is less than 5 % of the price of potassium citrate.^{43,44} Thus, compared to other synthesis processes, the method proposed herein for the production of tannin-derived AMCs could result in lower costs and easier processability in an eventual transition towards large-scale production.⁴⁵

6.6 Conclusion

It was shown that the mechanosynthesis of tannin-based MCs and its further CO₂ activation provides the possibility of preparing model materials with minor differences of physicochemical properties such as surface area, pore volume, PSD and surface chemistry. This allowed studying the effect that the order of the mesoporous structure has not only on the activation process but also on the electrochemical performances of the materials.

It was found that the development of textural properties was faster for the DMC. Furthermore, the selected activated materials, A45-DMC and A75-OMC, when tested as electrodes for SCs, exhibited good supercapacitor behavior, high-rate capabilities and long-term stabilities over time and after continuous cycling. By scanning the hysteresis loop of adsorption-desorption isotherms, it was possible to better understand the connectivity of the mesopore network and relate it to the electrochemical performance of the materials, an approach that was not yet being used to correlate such properties. Even if the channels of A75-OMC slightly improve the diffusion in the aqueous electrolyte, their constrictions hinder the

movement of the larger ions in the organic electrolyte, thus reducing the performance. In contrast, the open structure of A45-DMC facilitated the mobility of larger ions, thus outperforming A75-OMC in organic electrolyte tests.

This study of AMCs evidenced that the presence of mesoporosity improves the diffusion of ions and with it the rate capability of the materials. Moreover, the study corroborated that, although an ordered structure is somehow beneficial, the connectivity of the mesopore network and the correct correspondence of the size of pores and ions are important factors that have an even greater impact on the electrochemical performance of SCs.

6.7 References

1. Zhang, M., He, L., Shi, T. & Zha, R. Nanocasting and Direct Synthesis Strategies for Mesoporous Carbons as Supercapacitor Electrodes. *Chem. Mater.* 30, 7391–7412 (2018).
2. González, A., Goikolea, E., Barrena, J. A. & Mysyk, R. Review on supercapacitors: Technologies and materials. *Renewable and Sustainable Energy Reviews* 58, 1189–1206 (2016).
3. Wang, Y., Song, Y. & Xia, Y. Electrochemical capacitors: mechanism, materials, systems, characterization and applications. *Chemical Society Reviews* 45, 5925–5950 (2016).
4. *Supercapacitors: Materials, Systems, and Applications.* (John Wiley & Sons, Ltd, 2013).
5. Liu, H.-J., Wang, J., Wang, C.-X. & Xia, Y.-Y. Ordered Hierarchical Mesoporous/Microporous Carbon Derived from Mesoporous Titanium-Carbide/Carbon Composites and its Electrochemical Performance in Supercapacitor. *Advanced Energy Materials* 1, 1101–1108 (2011).
6. Karthik, M. et al. Effect of Mesopore Ordering in Otherwise Similar Micro/Mesoporous Carbons on the High-Rate Performance of Electric Double-Layer Capacitors. *J. Phys. Chem. C* 118, 27715–27720 (2014).
7. Inagaki, M., Toyoda, M., Soneda, Y., Tsujimura, S. & Morishita, T. Templated mesoporous carbons: Synthesis and applications. *Carbon* 107, 448–473 (2016).
8. Li, J.-G., Ho, Y.-F., Ahmed, M. M. M., Liang, H.-C. & Kuo, S.-W. Mesoporous Carbons Templated by PEO-PCL Block Copolymers as Electrode Materials for Supercapacitors. *Chemistry - A European Journal* 25, 10456–10463 (2019).
9. Castro-Gutiérrez, J. et al. Synthesis of perfectly ordered mesoporous carbons by water-assisted mechanochemical self-assembly of tannin. *Green Chemistry* (2018) doi:10.1039/C8GC02295J.
10. Castro-Gutiérrez, J. et al. High-Rate Capability of Supercapacitors Based on Tannin-Derived Ordered Mesoporous Carbons. *ACS Sustainable Chem. Eng.* 7, 17627–17635 (2019).
11. Thommes, M. et al. Physisorption of gases, with special reference to the evaluation of surface area and pore size distribution (IUPAC Technical Report). *Pure and Applied Chemistry* 87, (2015).
12. Brunauer, S., Emmett, P. H. & Teller, E. Adsorption of Gases in Multimolecular Layers. *Journal of the American Chemical Society* 60, 309–319 (1938).
13. Centeno, T. A. & Stoeckli, F. The assessment of surface areas in porous carbons by two model-independent techniques, the DR equation and DFT. *Carbon* 48, 2478–2486 (2010).
14. Cychosz, K. A., Guillet-Nicolas, R., García-Martínez, J. & Thommes, M. Recent advances in the textural characterization of hierarchically structured nanoporous materials. *Chemical Society Reviews* 46, 389–414 (2017).
15. Cimino, R., Cychosz, K. A., Thommes, M. & Neimark, A. V. Experimental and theoretical studies of scanning adsorption–desorption isotherms. *Colloids and Surfaces A: Physicochemical and Engineering Aspects* 437, 76–89 (2013).
16. Cychosz, K. A. & Thommes, M. Progress in the Physisorption Characterization of Nanoporous Gas Storage Materials. *Engineering* 4, 559–566 (2018).

17. Garcia-Martinez, J. et al. Evidence of Intracrystalline Mesostuctured Porosity in Zeolites by Advanced Gas Sorption, Electron Tomography and Rotation Electron Diffraction. *ChemCatChem* 6, 3110–3115 (2014).
18. Thommes, M. & Cychosz, K. A. Physical adsorption characterization of nanoporous materials: progress and challenges. *Adsorption* 20, 233–250 (2014).
19. Sevilla, M. & Mokaya, R. Energy storage applications of activated carbons: supercapacitors and hydrogen storage. *Energy Environ. Sci.* 7, 1250–1280 (2014).
20. Zhong, C. et al. A review of electrolyte materials and compositions for electrochemical supercapacitors. *Chemical Society Reviews* 44, 7484–7539 (2015).
21. Díez, N., Ferrero, G. A., Sevilla, M. & Fuertes, A. B. A sustainable approach to hierarchically porous carbons from tannic acid and their utilization in supercapacitive energy storage systems. *J. Mater. Chem. A* 7, 14280–14290 (2019).
22. Sanchez-Sanchez, A. et al. Excellent electrochemical performances of nanocast ordered mesoporous carbons based on tannin-related polyphenols as supercapacitor electrodes. *Journal of Power Sources* 344, 15–24 (2017).
23. Sanchez-Sanchez, A. et al. Ordered mesoporous carbons obtained by soft-templating of tannin in mild conditions. *Microporous and Mesoporous Materials* 270, 127–139 (2018).
24. Elmouwahidi, A. et al. Activated carbons from agricultural waste solvothermally doped with sulphur as electrodes for supercapacitors. *Chemical Engineering Journal* 334, 1835–1841 (2018).
25. Li, Z. et al. Carbonized Chicken Eggshell Membranes with 3D Architectures as High-Performance Electrode Materials for Supercapacitors. *Advanced Energy Materials* 2, 431–437 (2012).
26. Ruiz, V. et al. An activated carbon monolith as an electrode material for supercapacitors. *Carbon* 47, 195–200 (2009).
27. Li, Q. et al. Synthesis of mesoporous carbon spheres with a hierarchical pore structure for the electrochemical double-layer capacitor. *Carbon* 49, 1248–1257 (2011).
28. Fuertes, A. B., Lota, G., Centeno, T. A. & Frackowiak, E. Templated mesoporous carbons for supercapacitor application. *Electrochimica Acta* 50, 2799–2805 (2005).
29. Ruiz-Rosas, R. et al. Electrochemical Performance of Hierarchical Porous Carbon Materials Obtained from the Infiltration of Lignin into Zeolite Templates. *ChemSusChem* 7, 1458–1467 (2014).
30. Ferrero, G. A., Fuertes, A. B. & Sevilla, M. N-doped porous carbon capsules with tunable porosity for high-performance supercapacitors. *Journal of Materials Chemistry A* 3, 2914–2923 (2015).
31. Sevilla, M. & Fuertes, A. B. A Green Approach to High-Performance Supercapacitor Electrodes: The Chemical Activation of Hydrochar with Potassium Bicarbonate. *ChemSusChem* 9, 1880–1888 (2016).
32. Lota, G., Centeno, T. A., Frackowiak, E. & Stoeckli, F. Improvement of the structural and chemical properties of a commercial activated carbon for its application in electrochemical capacitors. *Electrochimica Acta* 53, 2210–2216 (2008).
33. Yang, C.-M. et al. Nanowindow-Regulated Specific Capacitance of Supercapacitor Electrodes of Single-Wall Carbon Nanohorns. *Journal of the American Chemical Society* 129, 20–21 (2007).

34. Futaba, D. N. et al. Shape-engineerable and highly densely packed single-walled carbon nanotubes and their application as super-capacitor electrodes. *Nature Materials* 5, 987–994 (2006).
35. Chen, Z. et al. High-Performance Supercapacitors Based on Hierarchically Porous Graphite Particles. *Advanced Energy Materials* 1, 551–556 (2011).
36. Rufford, T. E., Hulicova-Jurcakova, D., Fiset, E., Zhu, Z. & Lu, G. Q. Double-layer capacitance of waste coffee ground activated carbons in an organic electrolyte. *Electrochemistry Communications* 11, 974–977 (2009).
37. Xu, B. et al. Activated carbon prepared from PVDC by NaOH activation as electrode materials for high performance EDLCs with non-aqueous electrolyte. *International Journal of Hydrogen Energy* 35, 632–637 (2010).
38. Sevilla, M. & Fuertes, A. B. Direct Synthesis of Highly Porous Interconnected Carbon Nanosheets and Their Application as High-Performance Supercapacitors. *ACS Nano* 8, 5069–5078 (2014).
39. Gadipelli, S. et al. Superior Multifunctional Activity of Nanoporous Carbons with Widely Tunable Porosity: Enhanced Storage Capacities for Carbon-Dioxide, Hydrogen, Water, and Electric Charge. *Adv. Energy Mater.* 10, 1903649 (2020).
40. Zhang, L. et al. Porous 3D graphene-based bulk materials with exceptional high surface area and excellent conductivity for supercapacitors. *Sci Rep* 3, 1408 (2013).
41. Zhu, Y. et al. Carbon-Based Supercapacitors Produced by Activation of Graphene. *Science* 332, 1537–1541 (2011).
42. Wei, L., Sevilla, M., Fuertes, A. B., Mokaya, R. & Yushin, G. Hydrothermal Carbonization of Abundant Renewable Natural Organic Chemicals for High-Performance Supercapacitor Electrodes. *Advanced Energy Materials* 1, 356–361 (2011).
43. Fierro, V., Sánchez-Sánchez, A. & Celzard, A. Tannins as Precursors of Supercapacitor Electrodes. in *Sustainable Energy Technologies* (eds. Rincón-Mejía, E. & de las Heras, A.) 201–228 (CRC Press, 2018).
44. Sigma-Aldrich, Inc. Potassium citrate tribasic monohydrate. Milipore Sigma https://www.sigmaaldrich.com/catalog/product/sial/25107?lang=en®ion=US&cm_sp=Insite-_-caContent_prodMerch_raiOtherymlCtr-_-prodMerch10-2.
45. Schütter, C., Pohlmann, S. & Balducci, A. Industrial Requirements of Materials for Electrical Double Layer Capacitors: Impact on Current and Future Applications. *Adv. Energy Mater.* 9, 1900334 (2019).

Chapter 7

KOH activation of tannin-derived OMCs

7.1 Introduction

Chapters 5 and 6 focused on the physical activation of tannin-derived mesoporous carbons (MCs) produced by the SWAMM method (Chapter 3). The BET area of the CO₂ activated mesoporous carbons (CO₂-AMCs) reached maximum values of ~2000 m² g⁻¹ and the electrochemical tests evidenced the beneficial role of the mesopores and their connectivity to achieve high rate capabilities when used as electrodes for SCs. On the other side, as aforementioned in Section 1.4.1, KOH activation is known to produce materials with BET areas above 2000 m² g⁻¹.¹ Therefore, this chapter presents a study on the textural properties and the electrochemical performance of KOH activated OMCs (KOH-AOMCs) in aqueous electrolyte. It is expected that, as a result of KOH activation, the textural properties of the materials will be more developed compared to those of the CO₂-AOMCs of the previous chapters and probably their SC performance will be then increased.

For this study, OMC materials synthesized by the SWAMM method using a Tannin:Pluronic:Water weight ratio (T:P:W) of 2:0.75:1.75 were activated by two routes: (i) impregnation with 6 M KOH aqueous solution, followed by a drying step at 70 °C under vacuum until a slurry was obtained; (ii) physical mixing with KOH pellets in an agate mortar. For both routes (i and ii), the OMC was mixed with KOH using different KOH/carbon weight ratios and submitted to heat treatment in a stainless steel tubular oven, inner diameter 15 cm. The treatment was performed under 150 mL min⁻¹ N₂ flow, with a heating rate of 5 °C min⁻¹ until reaching 800 °C and holding this temperature for 1 h. The recovered materials were washed to eliminate residues of the activation process with 1 M HCl aqueous solution and water and, dried at 105 °C. Finally, the KOH-AOMCs were labeled OMC-*a-r*, where “*a*” stands for the activation route, either *imp* or *pm* for (i) or (ii) routes, respectively, and “*r*” stands for the KOH/carbon weight ratio ranging from 3 to 8.

Characterization of the materials was carried out using the techniques detailed in Chapter 2. Specifically, N₂ and CO₂ adsorption isotherms were acquired in ASAP devices (Micromeritics) and analyzed using Microactive[®] and SAIEUS[®] software from Micromeritics. TEM images and small-angle XRD were obtained to study the morphology and order of the mesopores. Chemical composition was obtained by EA and XPS. As the CO₂-OMCs exhibited the best performance in aqueous electrolyte (Chapter 6), the electrochemical characterization was performed also in 1 M H₂SO₄ for comparison.

7.2 Morphology and textural properties

Figure 7.1 shows TEM images of as-synthesized and activated materials, where it is possible to observe the 2D hexagonal geometry of the OMC (Figure 7.1a and 7.1d). After activation, TEM images showed that the AOMCs maintain their ordered structure regardless of the activation route and even when high KOH/carbon weight ratios are used (Figure 7.1b and 7.1f for the *imp* route and Figure 7.1c and 7.1g for *pm* route). Small-angle XRD measurements, shown in Figure 7.2, confirmed the presence of the ordered structure and evidenced that the mesostructure is better preserved after KOH activation than after CO₂ activation. The

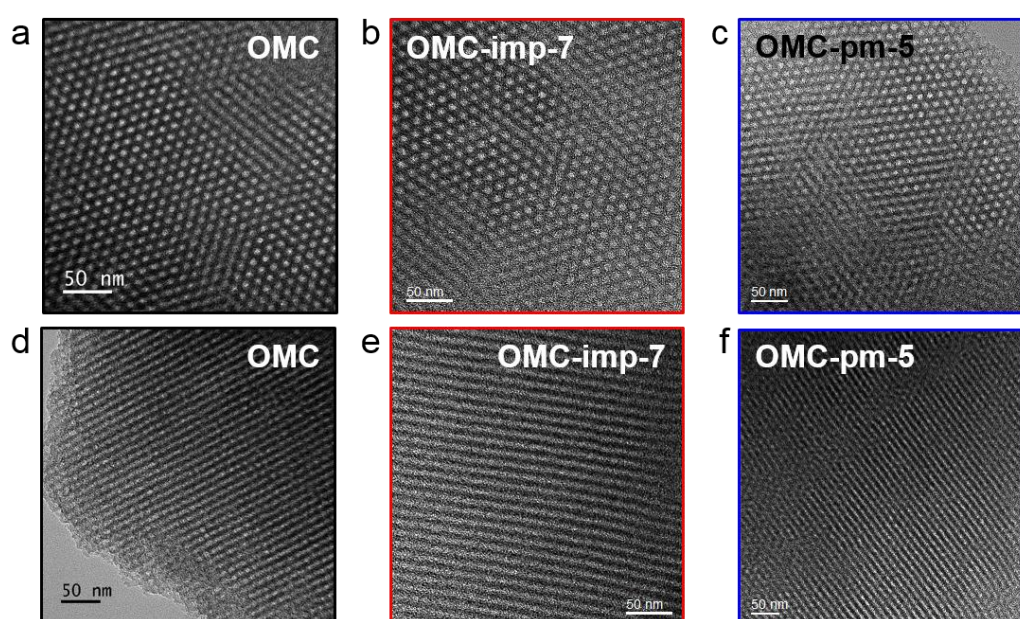


Figure 7.1. TEM images of OMC (a, d) before and after activation by (b, e) impregnation and (c, f) physical mixing routes.

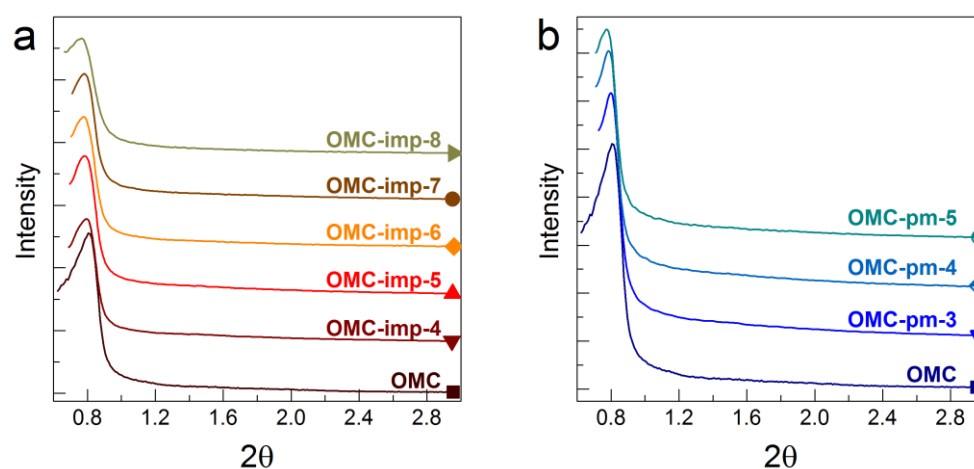


Figure 7.2. Small-angle XRD measurements for (a) OMC-imp and (b) OMC-pm series of activated materials.

latter is suggested by the lower deformation of the $d(100)$ peaks observed in Figure 7.2 with increasing r in comparison of that observed in Figure 5.4 for the CO_2 -AOMCs with increasing t (activation time).

Figure 7.3a and 7.3b show the N_2 adsorption-desorption isotherms for the two series of activated materials of this study. In all cases, the isotherms are a combination of type I and IV,² which are commonly observed for micro-mesoporous materials. Indeed, the increasing uptake of gas at low relative pressures ($p/p_0 < 0.2$) indicated a development of microporosity with increasing r , which is also observed on the PSDs of Figure 7.3c and 7.3d, obtained by applying the 2D-NLDFT HS to N_2 and CO_2 isotherms. At higher relative pressures ($p/p_0 > 0.2$) the characteristic hysteresis loops of the OMC materials were also observed, *i.e.*, H2a hysteresis loops.² Note also, that when compared to the N_2 isotherms of the CO_2 -AOMCs (Figure 5.2), the shape of the hysteresis loops remains mostly unchanged, indicating that the mesoporous structure is better preserved, in agreement with the small-angle XRD results. Indeed, in the mesopore range, the PSDs revealed that the OMC's narrow peak widens slightly and only shifts its center from 5 nm to 5.1 nm after activation.

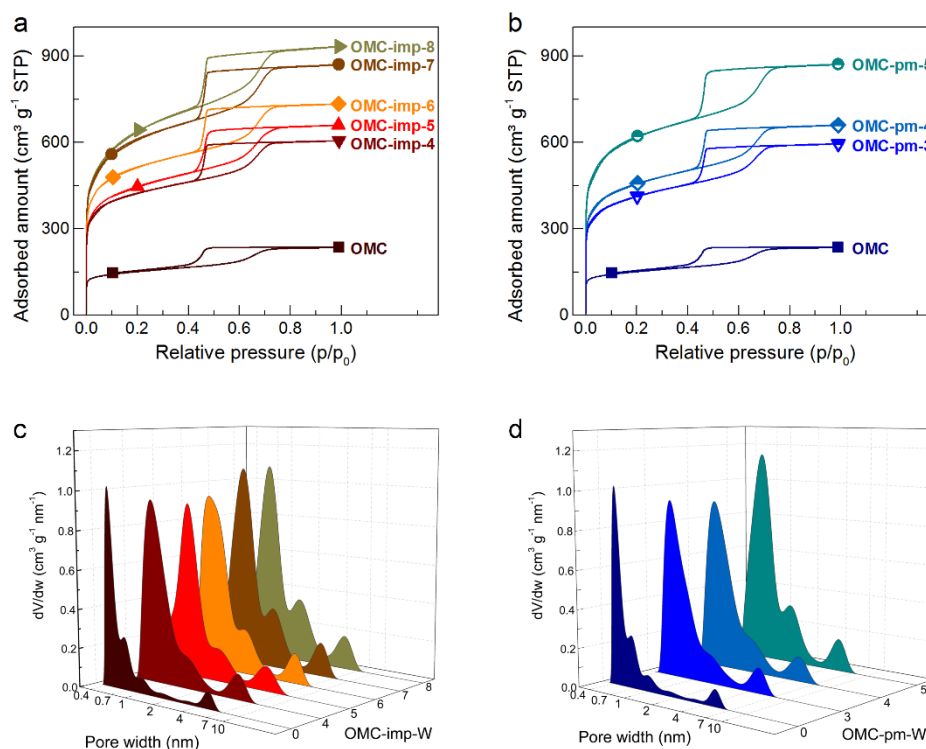


Figure 7.3. (a-c) Nitrogen adsorption-desorption isotherms and (d-f) pore size distributions for the different series of activated materials: (a, d) OMC-*imp-r*, (b, e) OMC-*pm-r* and (c, f) DMC-*pm-r*.

The calculated textural parameters of the activated materials, such as the surface area (S_{NLDFT}), the total pore volume (V_{tot}) and the pore volume at different ranges of pore width are reported in Table A4.1 of Annex 4. For comparison, the area obtained by applying the BET method to N_2 isotherms (A_{BET}) is also reported in Table A4.1; however, due to the known uncertainties of the BET method when there is a high presence of micropores,² a more in-depth analysis of textural properties and their relationship to surface chemistry and electrochemical behavior is performed using the values of S_{NLDFT} . Figure 7.4a shows that S_{NLDFT} increases with r for both series of activated carbons and, as expected, higher surface areas are reached than with physical activation*. Also note that the *pm* route of KOH addition seems to be more efficient since it requires lower amounts of activation agent to reach similar values of S_{NLDFT} than the *imp* route. This difference of activation efficiency between the two KOH incorporation routes could be due to a low water affinity of the OMC material. Indeed, in Chapter 3, it is reported that similar tannin-derived OMCs exhibit water contact angles (WCAs) above 90° , a sign of high hydrophobicity.³ The OMC used herein was also found to be hydrophobic, given that it exhibits a WCA of $140 \pm 2^\circ$. Thus, this high hydrophobicity together with the low connectivity between micropores and mesopores in the OMC, identified through the

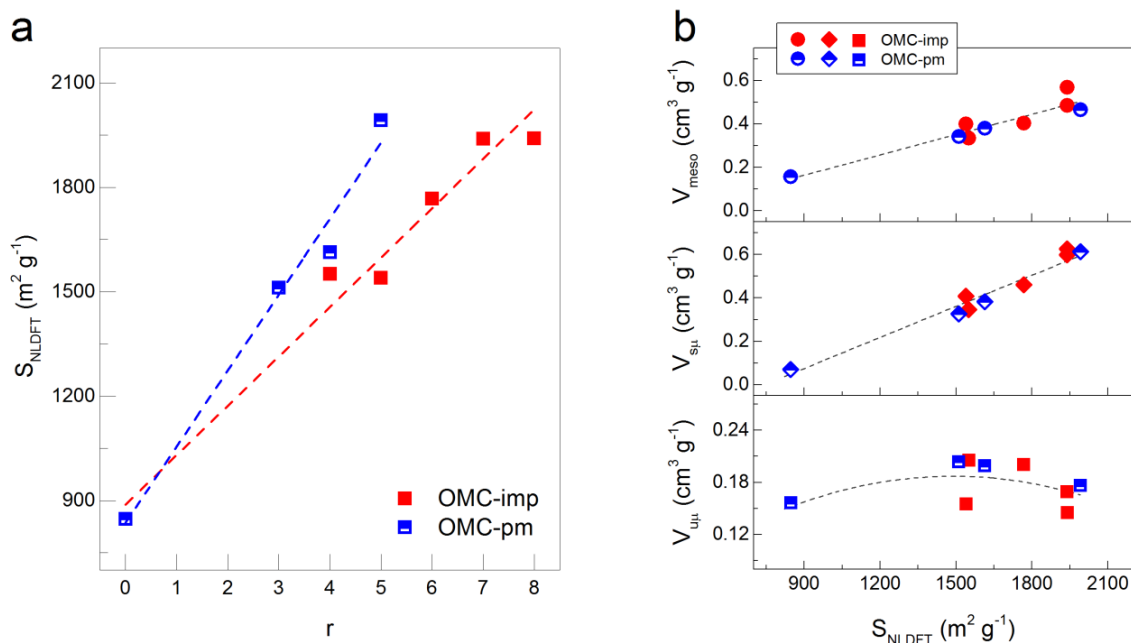


Figure 7.4. (a) Surface area calculated using the 2D-NLDFT HS (S_{NLDFT}) as a function of the KOH/carbon weight ratio (r). (b) Pore volume as a function of S_{NLDFT} for different ranges of pore width: mesopores (V_{meso}), supermicropores (V_{sm}) and ultramicropores (V_{um}).

* See Table A4.1 for BET areas, that indeed could reach values above the $2000 m^2 g^{-1}$.

characterization presented in Chapter 4, might be impairing the access of the KOH aqueous solution to the inner porosity of the carbon particles delaying the activation process and probably developing the porosity mainly on the outer particle surface. Previous studies on the KOH activation of coals with a high presence of micropores have reported an inhibition of activation due to the presence of water.^{4,5} Indeed, it has been hypothesized that as the temperature increases during the drying step the KOH is drawn outside the material by the water, causing the reactions to occur mainly on the exterior of the carbon particle, hence the underdevelopment of porosity.⁵ Despite the differences in activation efficiency, Figure 7.4b shows that the ultramicro-, supermicro- and mesopore volume ($V_{u\mu}$, $V_{S\mu}$ and V_{meso} , respectively) of the materials each follow the same tendency when plotted as a function of S_{NLDFT} , regardless of the activation route. Specifically, $V_{u\mu}$ increases slightly from $\sim 0.15 \text{ cm}^3 \text{ g}^{-1}$ to a maximum of $\sim 0.2 \text{ cm}^3 \text{ g}^{-1}$ at $\sim 1500 \text{ m}^2 \text{ g}^{-1}$, then it slightly decreases due to pore widening and merging; whereas $V_{S\mu}$ increases linearly with S_{NLDFT} from ~ 0.1 to $0.6 \text{ cm}^3 \text{ g}^{-1}$. This higher development of $V_{S\mu}$ is consistent with previous studies that reported that KOH activation enlarge the existing microporosity at activation temperatures above $700 \text{ }^\circ\text{C}$.¹ The mesopore volume (V_{meso}) also increases linearly with S_{NLDFT} for the AOMCs from ~ 0.2 to $0.6 \text{ cm}^3 \text{ g}^{-1}$.

7.3 Surface and bulk composition

The EA results are reported in Table A4.2 showing that oxygen is the main heteroatom present in the carbon structure whose O content in the bulk decreases with activation, as shown in Figure 7.5a. On the other side, Figure 7.5b and 7.5c show the O content and the O surface concentration, measured by XPS, values are also reported in Table A4.2. In general, O content

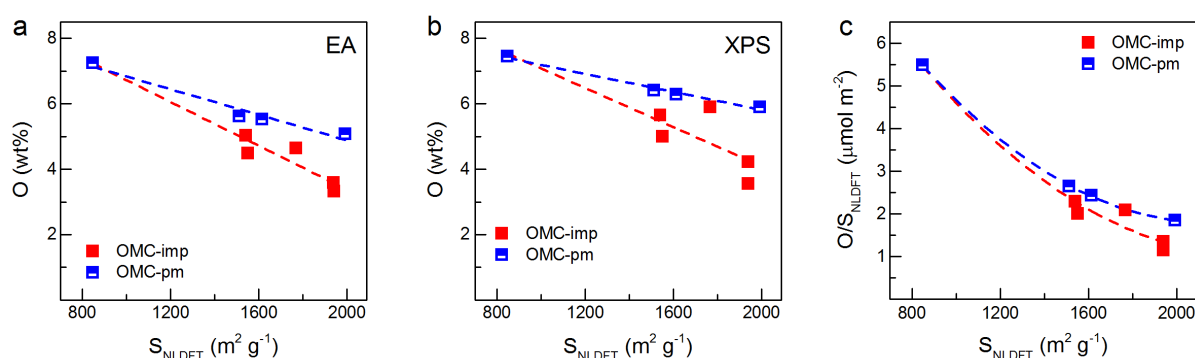


Figure 7.5. (a) Bulk and (b) surface oxygen content, measured by elemental analysis (EA) and X-ray photoelectron spectroscopy (XPS), respectively, and (c) oxygen surface concentration, calculated from XPS measurements, as a function of the surface area of the as-synthesized and activated materials.

on the surface is slightly higher than in the bulk. The contribution of the different functional groups to the O content of the surface is listed in Table A4.3 for all the materials. In all cases, due to the nature of the precursor, the main contribution to the oxygen surface moieties, ~75 – 85 %, comes from phenolic groups (OII), followed by quinone- and carbonyl-type (OI) with contributions in the range of 10 – 20 %, the rest coming from carboxylic groups (OIII) and, in some cases, chemisorbed oxygen or water (OIV). Even though the surface O content is moderate, it is shown below that it has an impact on the electrochemical performance of these materials, especially at low charging rates.

7.4 Electrochemical characterization

7.4.1 Effect of activation method

Electrochemical tests were carried out in 1 M H₂SO₄ aqueous solution using four activated carbons, namely OMC-imp-6, OMC-imp-7, OMC-pm-4 and OMC-pm-5 as electrode material. Cyclic voltammetry (CV) tests were performed using scan rates from 5 to 500 mV s⁻¹ and Figure 7.6a and 7.6b show examples of the obtained CV curves. In all cases, quasi-rectangular curves were observed indicating SC behavior; also, at low scan rates (up to 10 mV s⁻¹), the curves exhibited small humps suggesting the occurrence of faradaic reactions. The redox humps were less pronounced for the OMC-imp-7, which is the material with the lowest amount of O surface content among the tested samples.

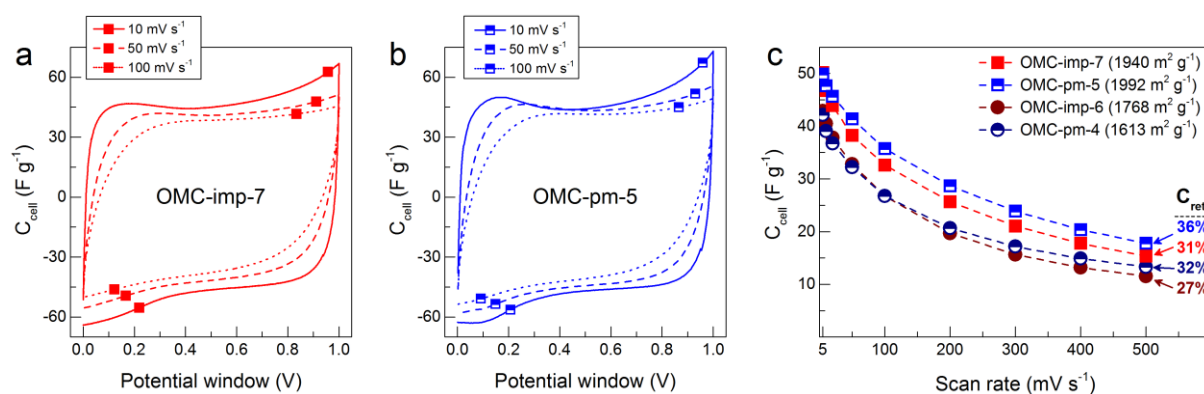


Figure 7.6. Electrochemical performance of KOH-AOMCs obtained by impregnation (OMC-imp-6, OMC-imp-7) and physical mixing (OMC-pm-4, OMC-pm-5) routes obtained from CV tests. Curves at different scan rates for (a) OMC-imp-7 and (b) OMC-pm-5. (c) Specific cell capacitance (C_{cell}) as a function of the scan rate; the capacitance retention (C_{ret}) at 500 mV s⁻¹ and the values of S_{NLDFT} for each material are also shown.

Figure 7.6c shows that at a low scan rate of 5 mV s^{-1} , OMC-pm-5 and OMC-imp-7 reached a specific cell capacitance (C_{cell}) of 50 F g^{-1} , the higher value among the tested samples, which is expected due to their superior surface area. OMC-imp-6 and OMC-pm-4 have similar values of C_{cell} 43 and 42 F g^{-1} , respectively, despite the higher surface area of OMC-imp-6 (see Table A4.1). This could be explained considering that OMC-pm-4 has a slightly higher O surface concentration (Figure 7.5c) and a larger contribution of the electrochemically active OI groups than OMC-imp-6, all of which can result in pseudocapacitance contributions increasing the performance at such low scan rate (5 mV s^{-1}). As the scan rate increases, faradaic reactions are gradually reduced and the redox humps on CV eventually fade (see Figure 7.6a and 7.6b); also, C_{cell} decreases drastically for the four materials tested as shown in Figure 7.6c. However, from Figure 7.6c is also possible to observe that capacitance retention (C_{ret}) is $\sim 5\%$ higher for the materials prepared by the *pm* route in comparison with those prepared by the *imp* route having similar textural properties, *i.e.*, the pairs OMC-imp-7 and OMC-pm-5; and, OMC-imp-6 and OMC-pm-4. As hypothesized in Section 7.2, during the *imp* activation process the development of porosity might be occurring mainly on the outer surface of the carbon particles leading to the formation of pores unconnected to the inner, unaffected, porosity resulting in hindered ion diffusion when compared to the materials obtained from the *pm* route.

Further on, galvanostatic charge-discharge (GCD) tests were carried out varying the applied current from 0.5 A g^{-1} to 20 A g^{-1} . Figure 7.7a shows examples of the obtained curves at 1 A g^{-1} ; all curves are triangular in shape, again indicating SC behavior. C_{cell} was calculated from the discharge curve and is shown in Figure 7.7b as a function of the applied current. Note that for OMC-pm-4, C_{cell} reaches a high value of 49 F g^{-1} at 0.5 A g^{-1} , the same as that attained by the OMC-pm-5 with a higher surface area. Close inspection of the GCD curves at 0.5 and 1 A g^{-1} revealed a Coulombic efficiency ($CE = t_{discharge}/t_{charge}$) above 1 for the OMC-pm-4, an indication of electrolyte decomposition, which could be indeed promoted by the high presence of O surface functionalities especially at low charging rates. The electrolyte decomposition produces an excess of charge that delays the discharge of the SC resulting in an apparent increase of capacitance; similar to the behavior observed in Li batteries due to the accumulation of Li in the overhand region.⁶ For $I > 1 \text{ A g}^{-1}$, the OMC-pm-4 exhibits CE below 1 and the behavior is consistent with the CV results (Figure 7.7b). Besides the particular case above described, the behavior of the rest of the samples is also consistent with CV results, at 0.5 A g^{-1} , the OMC-pm-5 reached the maximum value of capacitance, 49 F g^{-1} , then decreasing

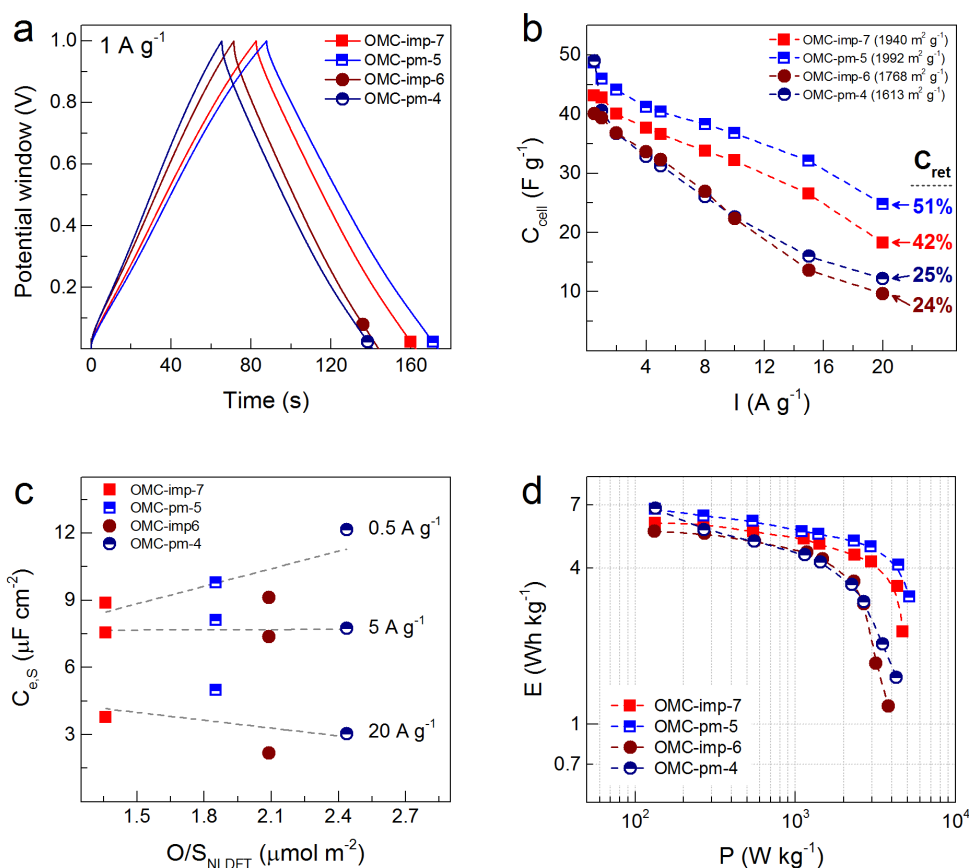


Figure 7.7. Electrochemical performance of KOH-AOMCs obtained by impregnation (OMC-imp-6, OMC-imp-7) and physical mixing (OMC-pm-4, OMC-pm-5) routes obtained from GCD tests. (a) Curves at 1 A g^{-1} . (b) Specific cell capacitance (C_{cell}) with increasing applied current (I); the capacitance retention (C_{ret}) at 20 A g^{-1} and the values of S_{NLDFT} for each material are also shown. (c) Interfacial electrode capacitance ($C_{e,s}$) as a function of oxygen surface concentration (O/S_{NLDFT}); the lines are given only as a guide. (d) Ragone-like plot.

down to 40 F g^{-1} for OMC-imp-6 (Figure 7.7b). OMC-pm-5 and OMC-imp-7 exhibit capacitance retentions of 51 and 42 %, respectively (see again Figure 7.7b); these values of C_{ret} are higher than those obtained from CV experiments, thus indicating that these materials have less resistance to electron mobility than to ion mobility, which are the respective charging mechanisms of GCD and CV tests.⁷ Moreover, Figure 7.7c shows the interfacial electrode capacitance ($C_{e,s}$) as a function of the O surface concentration (O/S_{NLDFT}) at different applied currents; $C_{e,s}$ is obtained after normalization of C_{cell} using the corresponding values of S_{NLDFT} and Equation 1.7 (see Chapter 1, Section 1.2.3.1). In agreement with the previous analysis, at 0.5 A g^{-1} , OMC-pm-4 exhibits the highest $C_{e,s}$ due to its higher surface O concentration, which results in pseudocapacitance contributions through redox reactions, but also due to the decomposition of the electrolyte as above explained. At 5 A g^{-1} , all materials have similar values

of $C_{e,s}$ regardless of the O surface concentration, thus suggesting that at this point energy is mainly stored through the formation of the EDL. For an even higher charging rate of 20 A g⁻¹, $C_{e,s}$ for OMC-imp-6 and OMC-pm-4 decreases considerably compared to the other samples, suggesting again hindered diffusion that does not allow for the rapid formation of the EDL. It is important to note once again that *pm*-activated materials have a superior performance than the *imp*-activated counterparts, as $C_{e,s}$ is always, to a greater or lesser extent, higher for the former than for the latter. Besides, Figure 7.7d shows the Ragone-like plot with the values of specific energy and power (E and P , respectively) of the SC cells calculated from GCD curves. OMC-pm-5 has the maximum storage capacity of 6.7 Wh kg⁻¹ with a power output of 133.3 W kg⁻¹, while the lowest value of 5.5 Wh kg⁻¹ at a power output of 132 W kg⁻¹ was observed for OMC-imp-6; intermediate values were found for OMC-imp-7 and OMC-pm-4. These values of E and P are within the range reported for similar materials and testing conditions in H₂SO₄, see Table A4.4.⁸⁻¹⁶

The resistive behavior of the materials was studied by electrochemical impedance spectroscopy (EIS) tests. Figure 7.8a shows the Nyquist plot obtained from EIS tests, the equivalent distributed resistance (EDR) increased in the order OMC-pm-5 < OMC-imp-7 < OMC-pm-4 < OMC-imp-6 (Figure 7.8a). The inset in Figure 7.8a of the Nyquist plot shows that the intersection of all curves with the Z_r axis at high frequencies (HF) is between 0.3 and 0.5 Ω, which is consistent with the small IR drops found during GCD measurements. EIS tests, thus revealed that the most important contribution to the EDR of the materials comes from the limited ion diffusion, which manifests at middle frequencies (MF, between ~10⁻¹ to ~10¹ Hz) as a straight line in the Nyquist plot.¹⁷ The “knee” frequency, f_{knee} , that determines the point at which the electrolyte reached full access to the electrode surface can be identified by analyzing the frequency response of the real part of the complex capacitance:

$$C_r(f) = \frac{-Z_i}{2\pi f |Z|^2} \quad (7.1)$$

where $|Z|$ is the modulus of the complex impedance; f_{knee} is defined as the frequency at which C_r is half of the maximum capacitance reached at low frequencies (LF). The lower the value of f_{knee} , the longer it takes for ions to diffuse within the material.¹⁷ Figure 7.8b shows the values of C_r as function of the frequency for the tested materials, for comparison C_r was normalized by the capacitance at $f = 0.01$ Hz, $C_{0.01}$. OMC-imp-7 and OMC-pm-5 exhibited comparable values of f_{knee} , 0.15 and 0.16 Hz, respectively, but diffusion is found to be slightly faster in the

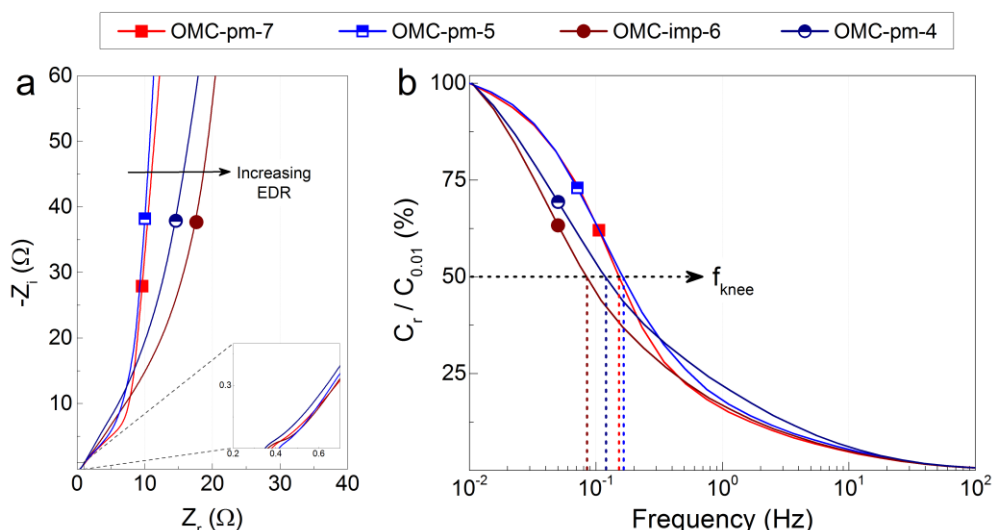


Figure 7.8. (a) Nyquist plot and (b) frequency response of the real part of the complex capacitance (C_r) normalized by the value of capacitance at 0.01 Hz ($C_{0.01}$) for the KOH-AOMCs obtained by impregnation (OMC-imp-6, OMC-imp-7) and physical mixing (OMC-pm-4, OMC-pm-5) routes.

OMC-pm-5. Figure 7.8b shows that ion diffusion is even more limited in OMC-imp-6 and OMC-pm-4, as indicated by the lower values of f_{knee} of 0.084 and 0.118 Hz for OMC-imp-6 and OMC-pm-4, respectively. These results support the conclusions drawn from CV and GCD tests, which suggest that diffusion in *pm*-activated materials is better in comparison with that in *imp*-activated ones, thus resulting in higher rate capabilities for the former than for the later.

7.4.2 Comparison with CO₂ activated materials

KOH activation was used in this study aiming to produce materials with higher surface areas and a more developed porosity than with the CO₂ activation process, presented in Chapters 5 and 6. The objective was to further improve the electrochemical performances of the tannin-derived materials. Indeed, at low charging rates, the attained values of C_{cell} and E of, for example, OMC-pm-5 are higher than those obtained under the same conditions with the CO₂-AOMCs, see Figure 7.6c, Figure 7.7b and Figure 6.8c and 6.8d, due to its larger surface area. However, when CO₂-AOMCs are compared to the KOH-AOMCs of similar surface area a more complex behavior is observed.

To provide a clearer comparison between the materials, Figure 7.9a shows the $C_{e,s}$ as a function of applied current for OMC-pm-4 and A75-OMC samples, with S_{NLDFT} of 1613 and 1614 m² g⁻¹ respectively. From this data, it is possible to observe that pseudocapacitance

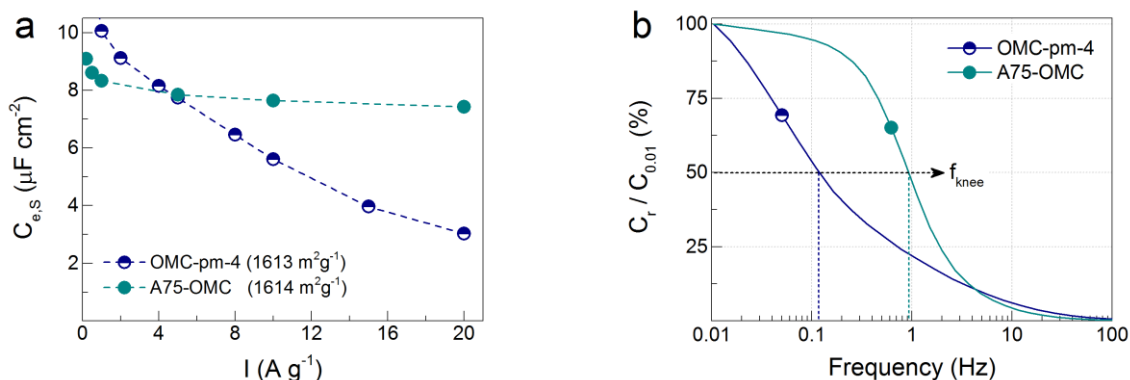


Figure 7.9. (a) Interfacial electrode capacitance ($C_{e,s}$) as a function of applied current and (b) frequency response of the real part of the complex capacitance (C_r) normalized by the value of capacitance at 0.01 Hz ($C_{0.01}$) for OMC-pm-4 compared to the corresponding values for the CO₂-activated A75-OMC presented in Chapters 5 and 6.

contributions in A75-OMC are only occurring at low charging rates ($I < 1 \text{ A g}^{-1}$), afterwards energy is stored by the EDL mechanism given that $C_{e,s}$ remains nearly constant up to a current of 20 A g^{-1} . For OMC-pm-4, $C_{e,s}$ is higher than that of the CO₂-activated counterpart for $I < 4 \text{ A g}^{-1}$, but drastically drops with the increasing current, suggesting that the surface is not easily accessible. Even more, Figure 7.9b shows the values of $C_r/C_{0.01}$ as a function of frequency, from which it is observed that f_{knee} for A75-OMC is about an order of magnitude higher than that of OMC-pm-4, evidence of significantly better ion diffusion. This fast response of A75-OMC would explain why, despite having higher O surface content (Figure 6.6b) than the KOH-activated material, redox reactions are less likely to occur. In contrast, the slow diffusion of ions in the OMC-pm-4 material would provide enough time for the ions to react with the surface functionalities resulting in the presence of pseudocapacitance contributions even at a relative high current of 4 A g^{-1} .

The difference of diffusion within the materials could be due key differences of their textural properties beyond the values of their surface area. Figure 7.10a and 7.10b show the volume and surface based PSDs of the compared materials and Figure 7.10c shows the contribution to the pore volume from pores of different sizes. Although both materials exhibit the same surface area, OMC-pm-4 has a narrower micropore distribution, mostly located in the ultramicropore range ($w < 0.7 \text{ nm}$), while the A75-OMC exhibits a broader PSD distribution that expands through all the micropore range ($w < 2 \text{ nm}$) resulting in a higher value of supermicropore volume ($V_{s\mu}$). In addition, A75-OMC has a higher contribution to the mesopore

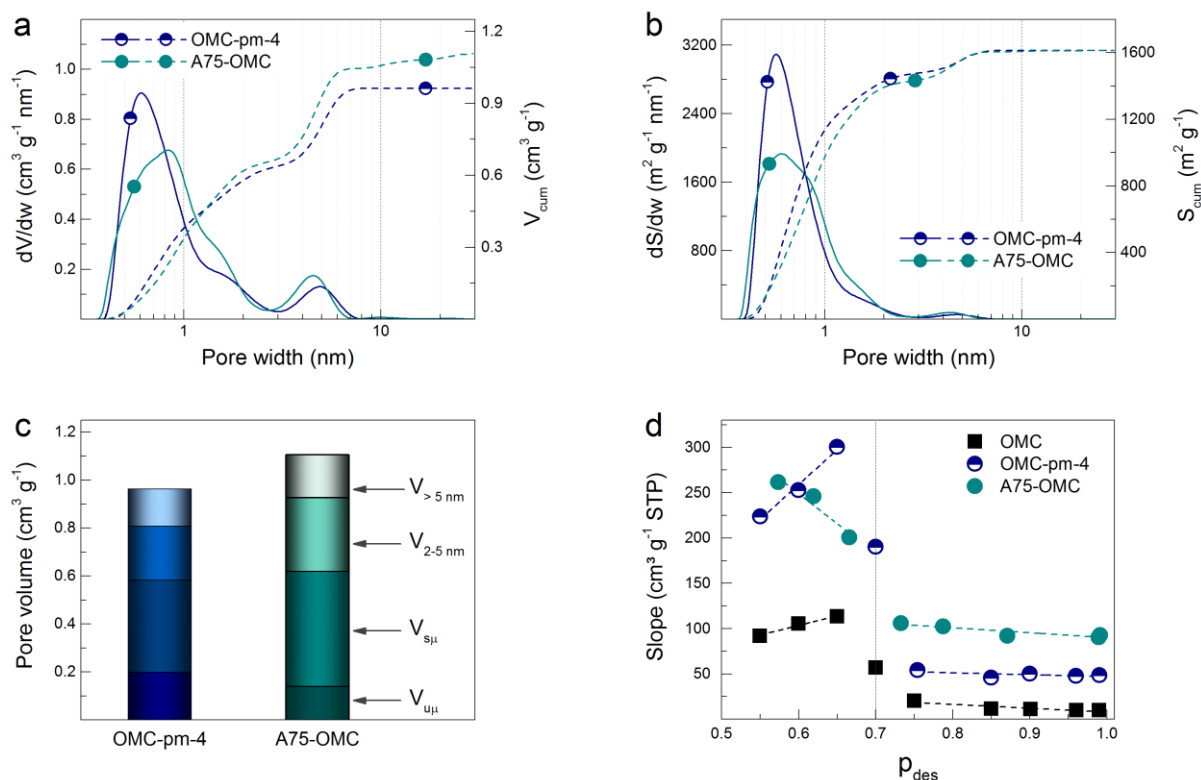


Figure 7.10. Differential and cumulative (a) volume and (b) surface PSDs of OMC-pm-4 and A75-OMC; (c) contribution to the pore volume from pores of different sizes. (d) Slope of the desorption branches as a function of the relative pressure at their starting point (p_{des}) for OMC-pm-4, A75-OMC and OMC materials.

volume from pores with widths between 2 and 5 nm than the OMC-pm-4. As established in Chapter 4, the channels of the OMC are mainly connected through narrow micropores that are generally enlarged by the activation process by either CO_2 or KOH; however, Figure 7.10c, shows that CO_2 activation resulted in a material with wider pores, which improved the connectivity between micro- and mesopores. The latter was further studied by scanning the hysteresis loop of OMC-pm-4 (see Figure A4.1 for the isotherms) and carrying an analysis of the slopes of the secondary branches as described in Chapter 6. Figure 7.10d presents the values of the aforementioned slopes, those of the non-activated OMC are also shown for comparison purposes. In the narrow-mesopore network ($p/p_0 < 0.7$), the desorption rate is more important for the A75-OMC where the slopes continue to increase as the relative pressure decreases. On the other hand, OMC-pm-4 showed a behavior similar to that of the non-activated material, which has a restricted access to the larger mesopores ($w > 5 \text{ nm}$). Thus, the pores connecting the micropores to the large mesopores are not sufficiently developed leading to the hindered diffusion observed in OMC-pm-4 with respect to A75-OMC. Based on the results of the scanning hysteresis and the electrochemical characterization, it can be assumed that the pore

structure in the A75-OMC material is better connected than that of OMC-pm-4. However, in order to corroborate this hypothesis, complementary characterizations are required as, for example, immersion calorimetry experiments using probe molecules with small kinetic diameters like dichloromethane (0.33 nm), benzene (0.37 nm), methanol (0.43 nm), among others,¹⁸ that could provide information regarding the connectivity of the micropores.

7.5 Conclusion

In this chapter, two routes of KOH addition to the OMC material before chemical activation were implemented: impregnation (*imp*) and physical mixing (*pm*). In both cases, the surface area increased as the amount of activating agent increased. However, the *pm* route has been shown to be more effective since it requires smaller amounts of KOH to reach similar values of surface area and pore volume than the *imp* route. Thus, the porous structure has an impact on the effectivity of the KOH activation process as observed for the physical activation presented in Chapters 5 and 6. Indeed, it is assumed that the difficult access to the mesopores in the OMC leads to a development of microporosity mainly on the outer surface of the carbon particles and in high preservation of the mesoporous structure.

The electrochemical performance of the KOH-AOMCs in aqueous electrolyte revealed the SC behavior of the materials and high values of capacitance at low charging rates. As the charge rate increases, either during CV or GCD tests, the capacitance of the assembled SC decreases considerably. Indeed, all the KOH-AOMCs presented clear signs of hindered diffusion that increased their EDR, thus reducing the electrochemical performance of the materials. After a comparison against the performance of the materials presented in Chapters 5 and 6, the CO₂-AOMCs exhibit, in general, higher values of $C_{e,S}$ coupled with faster frequency responses. All these elements indicate a rapid diffusion of the ions and good accessibility to the inner porosity.

This study has shown that materials with similar textural properties (S_{NLDFT} , V_{μ} , V_{meso}) and surface chemistry can result in considerably different electrochemical performances, which is the case of the pairs OMC-*imp*-7 and OMC-*pm*-5 or OMC-*pm*-4 and A75-OMC. It is therefore obvious that pore texture analysis should be completed in order to observe other characteristics of the materials that affect the electrochemical performance. For example, the accessible area may not be properly assessed; an in-depth characterization of the textural

properties could be carried out by acquiring hydrogen adsorption isotherms, in addition to CO₂ adsorption isotherms, along with immersion calorimetry experiments to further study the microporosity. Immersion calorimetry carried out using liquids with smaller kinetic diameters than those already used in Chapter 4, would allow for an improved evaluation of the accessibility and the connectivity of the micro-mesopore network that cannot be analyzed only through gas adsorption measurements. The information acquired could help to better understand the mechanisms of pore formation in these tannin-derived materials during the different activation processes as well as their performance when used as electrodes for SCs.

7.6 References

1. Sevilla, M. & Mokaya, R. Energy storage applications of activated carbons: supercapacitors and hydrogen storage. *Energy Environ. Sci.* 7, 1250–1280 (2014).
2. Thommes, M. et al. Physisorption of gases, with special reference to the evaluation of surface area and pore size distribution (IUPAC Technical Report). *Pure and Applied Chemistry* 87, (2015).
3. Castro-Gutiérrez, J. et al. Synthesis of perfectly ordered mesoporous carbons by water-assisted mechanochemical self-assembly of tannin. *Green Chemistry* 20, 5123–5132 (2018).
4. Illán-Gómez, M. J. & García-García, A. Activated Carbons from Spanish Coals. 2. Chemical Activation. 7 (1996).
5. Jibril, B. Y., Al-Maamari, R. S., Hegde, G., Al-Mandhary, N. & Houache, O. Effects of feedstock pre-drying on carbonization of KOH-mixed bituminous coal in preparation of activated carbon. *Journal of Analytical and Applied Pyrolysis* 80, 277–282 (2007).
6. Gyenes, B., Stevens, D. A., Chevrier, V. L. & Dahn, J. R. Understanding Anomalous Behavior in Coulombic Efficiency Measurements on Li-Ion Batteries. *J. Electrochem. Soc.* 162, A278–A283 (2015).
7. Zuliani, J. E., Caguiat, J. N., Kirk, D. W. & Jia, C. Q. Considerations for consistent characterization of electrochemical double-layer capacitor performance. *Journal of Power Sources* 290, 136–143 (2015).
8. Díez, N., Ferrero, G. A., Sevilla, M. & Fuertes, A. B. A sustainable approach to hierarchically porous carbons from tannic acid and their utilization in supercapacitive energy storage systems. *J. Mater. Chem. A* 7, 14280–14290 (2019).
9. Sanchez-Sanchez, A. et al. Ordered mesoporous carbons obtained by soft-templating of tannin in mild conditions. *Microporous and Mesoporous Materials* 270, 127–139 (2018).
10. Chen, P. et al. Ordered Mesoporous Carbons Loading on Graphene after Different Molten Salt Activations for Supercapacitor Applications. *Energy Technol.* 6, 2273–2281 (2018).
11. Lu, S. et al. Effect of aqueous electrolytes on the electrochemical behaviors of ordered mesoporous carbon composites after KOH activation as supercapacitors electrodes. *Journal of Electroanalytical Chemistry* 818, 58–67 (2018).
12. Jain, A. et al. Mesoporous activated carbons with enhanced porosity by optimal hydrothermal pre-treatment of biomass for supercapacitor applications. *Microporous and Mesoporous Materials* 218, 55–61 (2015).
13. Sevilla, M. & Fuertes, A. B. A Green Approach to High-Performance Supercapacitor Electrodes: The Chemical Activation of Hydrochar with Potassium Bicarbonate. *ChemSusChem* 9, 1880–1888 (2016).
14. Ferrero, G. A., Fuertes, A. B. & Sevilla, M. N-doped porous carbon capsules with tunable porosity for high-performance supercapacitors. *Journal of Materials Chemistry A* 3, 2914–2923 (2015).
15. Olivares-Marín, M. et al. Cherry stones as precursor of activated carbons for supercapacitors. *Materials Chemistry and Physics* 114, 323–327 (2009).
16. Mostazo-López, M. J. et al. Ultraporous nitrogen-doped zeolite-templated carbon for high power density aqueous-based supercapacitors. *Carbon* 129, 510–519 (2018).

17. Supercapacitors: Materials, Systems, and Applications. (John Wiley & Sons, Ltd, 2013).
18. Madani, S. H., Silvestre-Albero, A., Biggs, M. J., Rodríguez-Reinoso, F. & Pendleton, P. Immersion Calorimetry: Molecular Packing Effects in Micropores. *ChemPhysChem* 16, 3984–3991 (2015).

Conclusions et perspectives

Dans cette thèse, l'objectif principal était de produire des matériaux biosourcés pour des électrodes de supercondensateurs (SC) et, en parallèle, de réduire l'impact environnemental lié à sa synthèse. En effet, les travaux menés ont donné des résultats intéressants et originaux concernant la synthèse «verte», la caractérisation et l'application des carbones mésoporeux (CM) dérivés du tanin comme électrodes pour des SC.

Une nouvelle méthode de synthèse a été mise au point pour la préparation des CM; cette méthode de mésostructuration mécano-chimique assistée par l'interaction de l'eau et d'un tensioactif en une seule étape a été appelée SWAMM. Elle est respectueuse de l'environnement, grâce à l'utilisation du tanin de mimosa comme précurseur de carbone naturel et renouvelable et à l'absence de substances toxiques ou dangereuses lors de la synthèse. Divers paramètres, ont été optimisés pour que la méthode reste aussi simple et rapide que possible. En effet, la méthode SWAMM ne nécessite qu'une heure de broyage à billes pour obtenir une mésophase en utilisant uniquement du tanin, du Pluronic® F127 et des petites quantités d'eau (à pH inchangé); aucune étape de séchage ou de durcissement supplémentaire n'a été nécessaire avant la carbonisation. En outre, il est possible de passer d'une mésostructure désordonnée à une mésostructure ordonnée simplement en ajustant le rapport massique du tensioactif à l'eau. Les CMO produits ont des aires BET de $\sim 600 \text{ m}^2 \text{ g}^{-1}$ et se sont révélés stables thermiquement sous atmosphère inerte jusqu'à $1500 \text{ }^\circ\text{C}$, en conservant leur géométrie ordonnée avec des changements minimes de la taille des mésopores et en augmentant leur aire BET jusqu'à $\sim 800 \text{ m}^2 \text{ g}^{-1}$.

Les propriétés texturales de deux carbones mésoporeux dérivés du tanin de mimosa synthétisés par la méthode SWAMM: un carbone mésoporeux désordonné (CMD) et un carbone mésoporeux ordonné (CMO), ont été minutieusement étudiées. La combinaison des techniques d'adsorption de gaz, adsorption de vapeur et de la calorimétrie d'immersion a permis d'obtenir des informations détaillées sur leurs distributions de taille des pores (DTP) et la connectivité de leurs réseaux poreux. La caractérisation a révélé que le CMD a un réseau de pores bien connecté, tandis que le CMO a montré une DTP étroite dans la gamme des mésopores avec un accès très restreint à travers des mésopores et micropores étroits. Cette caractérisation détaillée a fourni des informations qui ont aidé à comprendre l'effet de la structure mésoporeuse sur le développement de la porosité pendant les processus d'activation physique ou chimique et, par conséquent, sur les performances électrochimiques des matériaux en tant qu'électrodes pour les SC.

Après activation physique par CO₂, des CMO ont augmenté leur aire BET jusqu'à ~2000 m² g⁻¹, préservant leur structure ordonnée, jusqu'à un taux d'usure de ~80 %, et améliorant la connectivité de leur structure micro-mésoporeuse. L'activation pendant 60 ou 75 min permet de produire des matériaux présentant un équilibre adéquat entre une surface spécifique élevée et une DTP appropriée, ce qui se traduit par des performances élevées dans les électrolytes aqueux et organiques. Les matériaux testés présentent des courbes de voltampérométrie cyclique (VC) carrées et affichent des valeurs élevées de capacité et d'énergie à des puissances de sortie élevées. L'amélioration de la connectivité de la structure poreuse dans les CMO activés (CMOA) est particulièrement importante à des taux de charge élevés, ce qui se traduit par des rétentions de capacité élevées pouvant atteindre 70% à 80 A g⁻¹. De plus, les CMOA présentent de bonne stabilité à long terme dans le temps et après un cyclage continu dans des conditions d'essai réalistes.

De plus, il a été montré que l'activation physique des CMO et des CMD offre la possibilité de préparer des matériaux modèles avec des différences mineures dans leurs propriétés physicochimiques telles que la surface, le volume des pores, la DTP et la chimie de surface. Cela a permis d'étudier l'effet que l'ordre et la connectivité de la structure mésoporeuse ont sur le processus d'activation et sur les performances électrochimiques des matériaux. Il a été constaté que le développement des propriétés texturales était plus rapide pour le CMD. En outre, les matériaux activés sélectionnés pour la comparaison de leurs performances en tant qu'électrodes des SC, ont montré une rétention de capacité importante à des courants élevés et une bonne stabilité à long terme dans le temps et après un cyclage continu. Grâce aux résultats de balayage des boucles d'hystérésis des isothermes d'adsorption-désorption d'azote, il a été possible de mieux comprendre la connectivité du réseau mésoporeux et de la mettre en relation avec les performances électrochimiques des matériaux. Il a été constaté que, même si les canaux dans le CMOA améliorent légèrement la diffusion dans l'électrolyte aqueux, leurs constriction obstruent le mouvement des ions plus gros dans l'électrolyte organique, ce qui réduit les performances. En revanche, la structure ouverte et bien connecté du CMD activé (CMDA) facilite la mobilité des ions plus gros, montrant ainsi une performance supérieure à celle du CMOA dans l'électrolyte organique. Cette étude comparative des CM activés (CMA) a montré que la présence de mésoporosité améliore la diffusion des ions et, par conséquent, la performance à des hauts taux de charge. En outre, l'étude a confirmé que, bien qu'une structure ordonnée soit en quelque sorte bénéfique, la connectivité du réseau mésoporeux et une correcte

correspondance entre la taille des pores et des ions sont des facteurs importants qui ont un impact encore plus grand sur les performances électrochimiques des SC.

L'activation chimique des CMO a été réalisée en incorporant du KOH par imprégnation (*imp*) ou par mélange physique (*mp*). Comme prévu, la surface a augmenté avec la quantité d'agent d'activation et des CMOA avec des aires BET maximales de $\sim 2300 \text{ m}^2 \text{ g}^{-1}$ ont été obtenues. Néanmoins, comme on l'a observé pour l'activation physique, les propriétés de la structure poreuse ont un impact sur l'efficacité du processus d'activation au KOH. En effet, on suppose que l'accès limité aux mésopores dans le CMO entraîne un développement de la porosité principalement à la surface des particules de carbone et en une préservation élevée de la structure mésoporeuse. Les performances électrochimiques des CMOA dans l'électrolyte aqueux ont révélé un comportement supercapacitif et des valeurs élevées de capacité à faible taux de charge. À mesure que le taux de charge augmente, la capacité des SC assemblés diminue considérablement. Tous les CMOA activés avec du KOH ont montré des signes évidents de diffusion limitée qui augmentaient leur EDR, réduisant ainsi leur performance électrochimique. Par rapport aux performances des matériaux activés au CO_2 , ces dernières ont généralement montré des réponses en fréquence plus rapides. Tout cela indique une diffusion rapide des ions et une bonne accessibilité à la porosité interne.

Même après la caractérisation approfondie effectuée dans ce travail de thèse et à partir des résultats rapportés, la question demeure de savoir pourquoi des matériaux ayant des propriétés texturales et une chimie de surface similaires peuvent conduire à des performances électrochimiques aussi différentes, en particulier celles obtenues à partir de différents processus d'activation. On peut supposer que certaines caractéristiques des matériaux qui affectent leurs performances électrochimiques ne sont pas détectables avec les techniques habituellement utilisées. Par exemple, la surface accessible peut ne pas être correctement évaluée; en fait, la microporosité a été étudiée en utilisant des isothermes d'adsorption de CO_2 (diamètre cinétique de 0.33 nm), mais les ions H^+ dans le milieu aqueux ont une taille plus petite (diamètre cinétique des ions solvatés de 0.28 nm). Ainsi, une caractérisation plus poussée des propriétés texturales pourrait être réalisée en acquérant des isothermes d'adsorption d'hydrogène et complétée par des expériences de calorimétrie d'immersion. La calorimétrie d'immersion réalisée avec des liquides de diamètre cinétique plus petit que ceux déjà utilisés dans cette thèse, permettrait d'étudier la surface accessible des micropores qui ne peut pas être analysé par des mesures d'adsorption de gaz. Les informations acquises pourraient aider à mieux comprendre les mécanismes de formation des pores dans ces matériaux dérivés des tanins au cours des

différents processus d'activation et leur relation avec les performances électrochimiques lorsqu'ils sont utilisés comme électrodes pour les SC.

D'autre part, il convient de rappeler qu'en général, les principaux inconvénients de la production des matériaux de carbone poreux avancés sont leurs procédures de synthèse complexes et à plusieurs étapes. Dans ce travail de thèse, les meilleures performances des SC ont été obtenues avec des CM activés au CO₂; même si l'activation ajoute une étape supplémentaire à la production des matériaux, le temps total nécessaire pour la production de ces CMA est d'environ 1.5 jours, y compris le temps nécessaire pour obtenir la mésophase, effectuer la carbonisation et l'activation. Cette synthèse rapide et facile est un avantage considérable par rapport aux autres méthodes, qui nécessitent non seulement des temps de synthèse de plusieurs jours ou semaines, mais aussi des étapes de séchage, de vieillissement et / ou de lavage, telle que l'activation au KOH également étudiée dans cette thèse. Par conséquent, on estime que les efforts de recherche sur les matériaux pour des applications de SC devraient continuer à se concentrer sur le développement et l'optimisation de procédures simples et respectueuses de l'environnement comme les méthodes de synthèse en une seule étape qui permettent le dopage *in situ* et / ou l'activation de la biomasse ou des précurseurs biosourcés. La simplification et la réduction du nombre d'étapes permettraient de réduire les coûts et d'accroître les possibilités de mise en œuvre de procédés à l'échelle industrielle, ce qui se traduirait par l'utilisation de carbones biosourcés avancés dans les SC commerciaux.

Finalement, il faut signaler que la caractérisation des CM dérivées du tanin, synthétisés par la méthode SWAMM, développée dans ce travail de thèse, a révélé que ces matériaux ont des propriétés que les rend appropriés pour des autres applications que celles du stockage d'énergie dans les SC. En effet, la faible affinité pour l'eau des matériaux permettrait leur utilisation pour le nettoyage des marées noires ou pour l'adsorption sélective de CO₂ à partir de gaz humides. En outre, la microporosité bien définie et unimodale du CMO est une propriété essentielle pour la séparation des hydrocarbures linéaires et ramifiés pour la production d'essence à indice d'octane élevé, application qui est en train d'être exploré en collaboration avec l'*Universidad de Alicante* à Alicante, Espagne et la *Friedrich-Alexander-Universität* à Erlangen-Nürnberg, Allemagne.

Annex 1

Complementary data for Chapter 3

Complementary data for Chapter 3

Table A1.1. Pore texture parameters, calculated from N₂ and CO₂ adsorption isotherms, of carbon materials: (i) prepared with various amounts of Pluronic® F127 and water, and used as references; (ii) obtained after various milling times; and (iii) synthesized with 2 g of aqueous HCl solutions with different pH values. [Adapted from Castro-Gutiérrez et al. (2018)¹]

Samples	Milling time (min)	S_{NLDFT} (m ² g ⁻¹)	A_{BET} (m ² g ⁻¹)	$V_{0.97,N_2}$ (cm ³ g ⁻¹)	$V_{\mu,NLDFT}$ (cm ³ g ⁻¹)	V_{meso} (cm ³ g ⁻¹)	F_{meso} (%)
(i) References							
CT2P0W0_60	60	829	578	0.25	0.23	0.02	8
CT2P0W2_60	60	503	231	0.10	0.11	--	--
CT2P2W0_60	60	672	466	0.36	0.17	0.19	53
(ii) Milling time							
CT2P2W2_30	30	735	543	0.46	0.18	0.28	60
CT2P2W2_45	45	683	497	0.46	0.16	0.30	64
CT2P2W2_60	60	695	522	0.47	0.16	0.30	65
CT2P2W2_75	75	703	521	0.44	0.17	0.27	61
CT2P2W2_90	90	709	538	0.46	0.18	0.28	61
CT2P2W2_120	120	663	484	0.40	0.16	0.24	60
(iii) pH							
CT2P2pH0_60	60	775	591	0.43	0.20	0.23	53
CT2P2pH1_60	60	713	533	0.51	0.17	0.34	67
CT2P2pH2_60	60	696	522	0.45	0.17	0.28	61
CT2P2pH3_60	60	713	528	0.44	0.18	0.26	60
CT2P2pH4_60	60	698	524	0.45	0.17	0.28	62

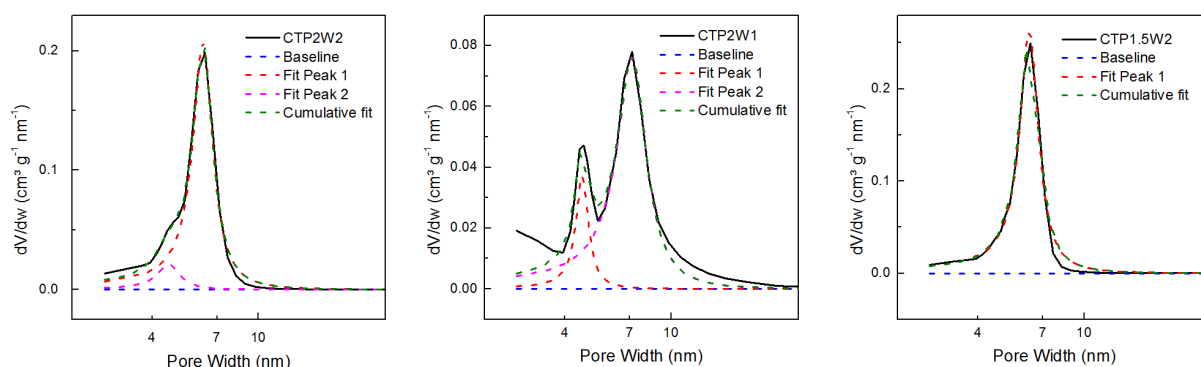


Figure A1.1. Examples of deconvolution into Lorentzian contributions performed on the PSDs of CT2P2W2_60, CT2P2W1_60 and CT2P1.5W2_60 samples. [Adapted from Castro-Gutiérrez et al. (2018)]

Table A1.2. Characteristics of the main peaks in the PSDs of carbon materials synthesized using 60 min of milling and various P:W weight ratios. [Adapted from Castro-Gutiérrez et al. (2018)]

Sample	Maximum height (M) ($\text{cm}^3 \text{g}^{-1} \text{nm}^{-1}$)	FWHM (nm)	M / FWHM	Peak position (nm)
CT2P0W2_60	0.0	--	0.0	--
CT20.5W2_60	0.0	--	0.0	--
CT2P1W2_60	0.37	0.73	0.50	5.0
CT2P1.5W2_60	0.26	1.24	0.21	6.2
CT2P2W2_60	0.02	1.13	0.02	4.7
	0.23	1.20	0.19	6.2
CT2P2.5W2_60	0.05	0.51	0.10	4.7
	0.02	17.22	0.001	10.3
CT2P3W2_60	0.02	0.48	0.03	4.7
	0.03	10.65	0.003	11.3
CT2P2W0_60	0.03	0.44	0.06	4.7
	0.03	7.40	0.004	7.0
CT2P2W1_60	0.04	0.61	0.06	4.7
	0.08	2.21	0.03	7.1
CT2P2W1.5_60	0.04	0.59	0.06	4.7
	0.11	1.84	0.06	6.8
CT2P2W2.5_60	0.03	0.63	0.05	4.7
	0.06	3.42	0.02	7.4
CT2P2W3_60	0.03	0.58	0.06	4.6
	0.06	3.37	0.02	7.6
CT2P0.5W1_60	0.0	--	0.0	--
CT2P0.5W1.5_60	0.09	0.71	0.12	4.1
CT2P0.75W1.25_60	0.25	0.54	0.46	4.4
CT2P0.75W1.5_60	0.44	0.37	1.20	4.5
CT2P0.75W1.75_60	0.56	0.32	1.77	4.6
CT2P1W1_60	0.31	0.87	0.35	4.7
CT2P1W1.25_60	0.34	0.82	0.42	5.0
CT2P1W1.5_60	0.47	0.60	0.78	4.9
CT2P1W1.75_60	0.31	0.94	0.33	5.2
CT2P1.25W1.25_60	0.29	0.99	0.29	5.9
CT2P1.25W1.5_60	0.25	1.21	0.21	6.0
CT2P1.25W1.75_60	0.23	1.26	0.18	5.9
CT2P1.5W1_60	0.27	1.21	0.22	6.2
CT2P1.5W1.25_60	0.25	1.35	0.18	6.1
CT2P1.5W1.5_60	0.31	1.04	0.30	6.2
CT2P1.5W1.75_60	0.30	1.11	0.27	6.1

Table A1.3. Pore texture parameters of samples synthesized with different P:W initial ratios and obtained after 60 min of ball-milling, calculated from N₂ and CO₂ isotherms. [Adapted from Castro-Gutiérrez et al. (2018)]

Samples	S_{NLDFT} (m ² g ⁻¹)	A_{BET} (m ² g ⁻¹)	$V_{0.97,N_2}$ (cm ³ g ⁻¹)	$V_{\mu,NLDFT}$ (cm ³ g ⁻¹)	V_{meso} (cm ³ g ⁻¹)	F_{meso} (%)
CT2P0.5W1_60	566	304	0.12	0.13	--	--
CT2P0.5W1.5_60	732	529	0.25	0.20	0.05	18
CT2P0.5W2_60	657	457	0.19	0.18	0.01	3
CT2P0.75W1.25_60	659	477	0.30	0.17	0.12	41
CT2P0.75W1.5_60	731	537	0.35	0.19	0.15	44
CT2P0.75W1.75_60	761	567	0.36	0.20	0.16	44
CT2P1W1_60	733	546	0.42	0.18	0.24	57
CT2P1W1.25_60	755	568	0.44	0.19	0.25	57
CT2P1W1.5_60	750	556	0.44	0.19	0.25	58
CT2P1W1.75_60	784	587	0.47	0.19	0.28	59
CT2P1W2_60	712	508	0.41	0.17	0.24	58
CT2P1.25W1.25_60	713	532	0.46	0.17	0.29	63
CT2P1.25W1.5_60	732	547	0.49	0.17	0.31	64
CT2P1.25W1.75_60	696	527	0.45	0.17	0.28	62
CT2P1.5W1_60	742	565	0.51	0.18	0.34	66
CT2P1.5W1.25_60	715	539	0.49	0.17	0.32	66
CT2P1.5W1.5_60	767	588	0.52	0.18	0.34	65
CT2P1.5W1.75_60	750	577	0.53	0.18	0.35	66
CT2P1.5W2_60	726	541	0.50	0.17	0.33	66
CT2P2W1_60	689	486	0.40	0.17	0.23	58
CT2P2W1.5_60	721	524	0.44	0.18	0.26	60
CT2P2W2_60	695	522	0.47	0.16	0.30	65
CT2P2W2.5_60	696	503	0.39	0.18	0.21	54
CT2P2W3_60	641	454	0.38	0.16	0.22	59
CT2P2.5W2_60	686	486	0.43	0.17	0.26	60
CT2P3W2_60	638	476	0.53	0.16	0.37	70

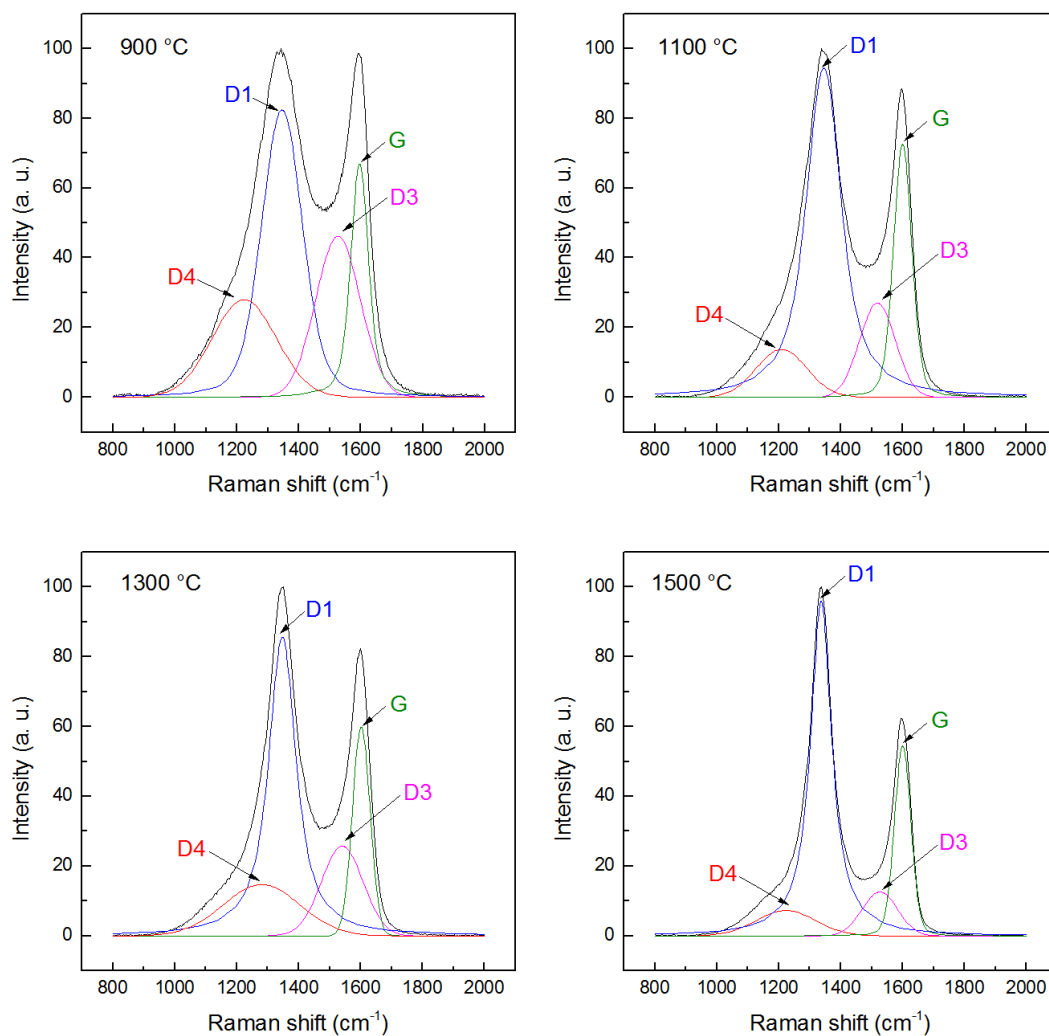


Figure A1.2. Raman spectra of CT2P1W2_60 pyrolyzed at different temperatures, and corresponding D₁, D₃, D₄ and G bands. [Reproduced from Castro-Gutiérrez et al. (2018)]

Reference

1. Castro-Gutiérrez, J. et al. Synthesis of perfectly ordered mesoporous carbons by water-assisted mechanochemical self-assembly of tannin. *Green Chemistry* 20, 5123–5132 (2018).

Annex 2

Complementary data for Chapter 5

Complementary data for Chapter 5

Table A2.1. Pore texture parameters, calculated from N₂ and CO₂ adsorption isotherms, for the as-synthesized material and the AOMCs. [Reproduced from Castro-Gutiérrez et al. (2019)]

Sample	Act. time (min)	BO (%)	S_{NLDFT} (m ² g ⁻¹)	A_{BET} (m ² g ⁻¹)	V_{tot} (cm ³ g ⁻¹)	V_{μ} (cm ³ g ⁻¹)	V_{μ} (cm ³ g ⁻¹)	V_{meso} (cm ³ g ⁻¹)	w_{av} (nm)
CTPW	0	0	761	567	0.36	0.16	0.04	0.16	0.9
A15-CTPW	15	14	1085	894	0.54	0.21	0.10	0.23	1.0
A30-CTPW	30	32	1333	1222	0.71	0.22	0.20	0.29	1.1
A45-CTPW	45	41	1416	1387	0.80	0.22	0.26	0.33	1.1
A60-CTPW	60	43	1480	1479	0.86	0.20	0.30	0.35	1.2
A75-CTPW	75	59	1614	1867	1.11	0.14	0.48	0.49	1.4
A90-CTPW	90	78	1576	1999	1.23	0.09	0.54	0.60	1.6
A105-CTPW	105	75	1644	2061	1.19	0.12	0.55	0.53	1.5
A120-CTPW	120	94	1215	1642	0.95	0.06	0.42	0.47	1.6

BO: burn-off due to the activation process. S_{NLDFT} and A_{BET} : specific surface areas calculated by applying 2D-NLDFT HS and BET models, respectively. Parameters calculated from the 2D-NLDFT HS pore size distribution: V_{tot} , total pore volume; V_{μ} , ultramicropore volume ($w < 0.7$ nm); V_{μ} , supermicropore volume ($0.7 < w < 2$ nm); $V_{meso} = V_{tot} - V_{\mu} - V_{\mu}$, mesopore volume; w_{av} , average pore size calculated using Equation (2.1) (see Chapter 2).

Table A2.2. Peak assignment and relative contributions of surface functionalities obtained by XPS analysis. [Reproduced from Castro-Gutiérrez et al. (2019)]

Sample	C1s contributions					O1s contributions			
	CI	CII	CIII	CIV	CV	OI	OII	OIII	O*
	A (BE) [% (eV)]								
CTPW	68.3 (284.4)	26.9 (285.5)	3.6 (287.6)	1.2 (289.2)	--	25.6 (531.3)	67.4 (532.7)	7.0 (534.5)	
A30-CTPW	76.3 (284.5)	21.8 (285.5)	1.9 (287.6)	--	--	35.6 (531.1)	58.4 (532.8)	5.9 (534.5)	
A45-CTPW	75.1 (284.5)	22.9 (285.5)	2.0 (287.6)	--	--	31.3 (531.1)	59.7 (532.7)	8.9 (534.5)	
A60-CTPW	75.7 (284.5)	22.2 (285.5)	2.1 (287.6)	--	--	30.1 (531.1)	60.9 (532.7)	9.0 (534.5)	
A75-CTPW	74.6 (284.5)	23.5 (285.5)	1.9 (287.6)	--	--	32.8 (531.1)	56.4 (532.7)	10.9 (534.5)	
A90-CTPW	73.9 (284.5)	24.7 (285.5)	1.4 (287.6)	--	--	26.6 (531.2)	59.7 (532.6)	11.1 (534.5)	2.6 (536.2)
A105-CTPW	71.5 (284.5)	25.1 (285.5)	2.1 (287.6)	1.4 (289.2)	--	31.2 (531.4)	57.6 (532.8)	11.2 (534.9)	

Table A2.3. Single electrode specific capacitance ($C_e = 4 C_{cell}$) at 5 A g^{-1} of A60-CTPW and A75-CTPW and other un-doped materials with similar properties reported in the literature. The samples names correspond to their respective bibliographic references.¹⁻¹³ [Adapted from Castro-Gutiérrez et al. (2019)]

Sample	Cell type	Electrolyte concentration	Potential window	C_e
Aqueous electrolyte (H_2SO_4)				
A60-CTPW	2-e	1 M	1 V	112 F g^{-1}
A75-CTPW				128 F g^{-1}
C3/30	2-e	2 M	0.8 V	140 F g^{-1}
AOW	2-e	1 M	1 V	120 F g^{-1}
MC-1	3-e	2 M	0.7 V	172 F g^{-1}
C-1*	2-e	1 M	1 V	144 F g^{-1}
C-2*				132 F g^{-1}
PhC	2-e	1 M	0.8 V	148 F g^{-1}
GaC				128 F g^{-1}
CatC				128 F g^{-1}
TanC				116 F g^{-1}
L-b-700				76 F g^{-1}
L-b-900	3-e	1 M	0.8 V	80 F g^{-1}
L-Y-700				52 F g^{-1}
L-Y-900				124 F g^{-1}
AC-KOH	3-e	1 M	1 V	132 F g^{-1}
Organic electrolyte (TEABF_4)				
A60-CTPW	2-e	1 M / ACN	2.7 V	92 F g^{-1}
A75-CTPW				92 F g^{-1}
SWNT solid	2-e	1 M / PC	2.5 V	44 F g^{-1}
Aerosol-carbon	3-e	1 M / PC	2.7 V	96 F g^{-1}
MC-1	3-e	1 M / PC	3 V	80 F g^{-1}
C-1*	2-e	1 M / ACN	2 V	88 F g^{-1}
C-2*				80 F g^{-1}
CGC-3.5	2-e	1 M / ACN	2.7 V	80 F g^{-1}
CGC-5				120 F g^{-1}
NPV1	2-e	1 M / PC	2.5 V	52 F g^{-1}
NPV2				80 F g^{-1}

Cell type: 2-e, two-electrode configuration; 3-e, three-electrode configuration.

* Measured at 1 A g^{-1} , the maximum reported in the corresponding study. ACN and PC stand for acetonitrile and propylene carbonate, respectively.

References

1. Castro-Gutiérrez, J. et al. High-Rate Capability of Supercapacitors Based on Tannin-Derived Ordered Mesoporous Carbons. *ACS Sustainable Chem. Eng.* 7, 17627–17635 (2019).
2. Sanchez-Sanchez, A. et al. Ordered mesoporous carbons obtained by soft-templating of tannin in mild conditions. *Microporous and Mesoporous Materials* 270, 127–139 (2018).
3. Elmouwahidi, A. et al. Activated carbons from agricultural waste solvothermally doped with sulphur as electrodes for supercapacitors. *Chemical Engineering Journal* 334, 1835–1841 (2018).
4. Sanchez-Sanchez, A. et al. Excellent electrochemical performances of nanocast ordered mesoporous carbons based on tannin-related polyphenols as supercapacitor electrodes. *Journal of Power Sources* 344, 15–24 (2017).
5. Li, Z. et al. Carbonized Chicken Eggshell Membranes with 3D Architectures as High-Performance Electrode Materials for Supercapacitors. *Advanced Energy Materials* 2, 431–437 (2012).
6. Ruiz, V. et al. An activated carbon monolith as an electrode material for supercapacitors. *Carbon* 47, 195–200 (2009).
7. Li, Q. et al. Synthesis of mesoporous carbon spheres with a hierarchical pore structure for the electrochemical double-layer capacitor. *Carbon* 49, 1248–1257 (2011).
8. Fuertes, A. B., Lota, G., Centeno, T. A. & Frackowiak, E. Templated mesoporous carbons for supercapacitor application. *Electrochimica Acta* 50, 2799–2805 (2005).
9. Ruiz-Rosas, R. et al. Electrochemical Performance of Hierarchical Porous Carbon Materials Obtained from the Infiltration of Lignin into Zeolite Templates. *ChemSusChem* 7, 1458–1467 (2014).
10. Futaba, D. N. et al. Shape-engineerable and highly densely packed single-walled carbon nanotubes and their application as super-capacitor electrodes. *Nature Materials* 5, 987–994 (2006).
11. Chen, Z. et al. High-Performance Supercapacitors Based on Hierarchically Porous Graphite Particles. *Advanced Energy Materials* 1, 551–556 (2011).
12. Xu, B. et al. Activated carbon prepared from PVDC by NaOH activation as electrode materials for high performance EDLCs with non-aqueous electrolyte. *International Journal of Hydrogen Energy* 35, 632–637 (2010).
13. Rufford, T. E., Hulicova-Jurcakova, D., Fiset, E., Zhu, Z. & Lu, G. Q. Double-layer capacitance of waste coffee ground activated carbons in an organic electrolyte. *Electrochemistry Communications* 11, 974–977 (2009).

Annex 3

Complementary data for Chapter 6

Complementary data for Chapter 6

Table A3.1. Pore texture parameters of the as-synthesized and activated disordered mesoporous carbons.

Sample	Act. Time (min)	BO (%)	S_{NLDFT} ($m^2 g^{-1}$)	A_{BET} ($m^2 g^{-1}$)	V_{tot} ($cm^3 g^{-1}$)	$V_{u\mu}$ ($cm^3 g^{-1}$)	$V_{s\mu}$ ($cm^3 g^{-1}$)	V_{meso} ($cm^3 g^{-1}$)
DMC	0	0	732	533	0.41	0.16	0.03	0.22
A15-DMC	15	18	1175	995	0.64	0.23	0.13	0.28
A30-DMC	30	40	1430	1436	0.89	0.20	0.30	0.39
A45-DMC	45	60	1578	1819	1.09	0.15	0.47	0.46
A60-DMC	60	86	1566	1991	1.19	0.12	0.53	0.54

S_{NLDFT} and A_{BET} , specific surface areas calculated by applying 2D-NLDFT HS and BET models, respectively. Parameters calculated from the 2D-NLDFT HS PSD: V_{tot} , total pore volume; $V_{u\mu}$, ultramicropore volume ($w < 0.7$ nm); $V_{s\mu}$, supermicropore volume ($0.7 < w < 2$ nm); $V_{meso} = V_{tot} - V_{s\mu} - V_{u\mu}$, mesopore volume ($2 \text{ nm} < w$).

Table A3.2. Peak assignment and relative contributions of surface functionalities obtained by XPS of the as-synthesized and activated disordered mesoporous carbons.

Sample	C1s contributions					O1s contributions			
	CI	CII	CIII	CIV	CV	OI	OII	OIII	O*
	A (BE) [% (eV)]								
DMC	68.4 (284.5)	24.8 (285.5)	5.3 (287.6)	0.3 (289.1)	1.2 (290.1)	23.4 (531.1)	69.2 (532.6)	7.3 (534.5)	--
A15-DMC	69.7 (284.4)	24.2 (285.5)	3.9 (287.6)	1.1 (289.2)	1.0 (290.4)	37.1 (531.1)	56.4 (532.3)	6.5 (534.5)	--
A30-DMC	69.0 (284.5)	24.6 (285.5)	4.5 (287.6)	0.3 (289.2)	1.6 (290.1)	39.5 (531.1)	45.0 (532.6)	11.0 (534.5)	4.5 (536.4)
A45-DMC	68.4 (284.5)	25.1 (285.5)	4.8 (287.6)	0.4 (289.2)	1.3 (290.2)	45.0 (531.1)	46.8 (532.6)	8.2 (534.5)	--
A60-DMC	68.4 (284.4)	26.3 (285.5)	3.7 (287.6)	0.3 (289.2)	1.3 (290.0)	19.6 (531.2)	42.1 (532.5)	20.1 (534.5)	18.2 (536.6)

Table A3.3. BET area and electrochemical performance in aqueous electrolyte (H₂SO₄) of the materials of this study and others reported in the literature. Names of the samples correspond to those of their reference source.¹⁻¹³

Sample	Commentary	A_{BET} ($m^2 g^{-1}$)	Cell type	Aqueous electrolyte (H ₂ SO ₄)	
				C_e	C_{ret}
A45-DMC	Soft-templated by mechano-synthesis, CO ₂ -activated mesoporous carbons from mimosa tannin	1819	2-e	148 Fg^{-1} at 0.2 Ag^{-1}	58 % at 80 Ag^{-1}
A75-OMC		1867		148 Fg^{-1} at 0.2 Ag^{-1}	70 % at 80 Ag^{-1}
CK-800	Salt templated-assisted K ₂ CO ₃ - activated tannic acid	2510	2-e	260 Fg^{-1} at 0.2 Ag^{-1}	45 % at 80 Ag^{-1}
CK-900		2740		210 Fg^{-1} at 0.2 Ag^{-1}	46 % at 80 Ag^{-1}
PhC	Hard templated (SBA-15) OMCs from phloroglucinol, gallic acid, catechin and mimosa tannin	1094	2-e	196 ± 12 Fg^{-1} at 0.2 Ag^{-1}	66 % at 24 Ag^{-1}
GaC		1045			61 % at 24 Ag^{-1}
CatC		917			48 % at 24 Ag^{-1}
TanC		1006			51 % at 24 Ag^{-1}
Gyroid Cylinder	Soft-templated by EISA, KOH- activated mesoporous carbons	93	2-e		
C3/30	Soft templated by phase separation, CO ₂ -activated OMC from mimosa tannin	1152	2-e	244 Fg^{-1} at 0.2 Ag^{-1}	50 % at 24 Ag^{-1}
AOW	KOH-activated olive mill wastewater	1952	2-e	107 Fg^{-1} at 0.125 Ag^{-1}	66 % at 10 Ag^{-1}
AC-KOH	KOH-activated carbonized chicken eggshell	1575	3-e	200 Fg^{-1} at 0.2 Ag^{-1}	63 % at 10 Ag^{-1}
CESM-300		221		284 Fg^{-1} at 0.2 Ag^{-1}	60 % at 10 Ag^{-1}
ACM-A	KOH-activated carbon from ethylene- tar	2652	2-e	334 Fg^{-1} at 0.05 Ag^{-1}	60 % at 5 Ag^{-1}
ACM-B		1107		183 Fg^{-1} at 0.05 Ag^{-1}	55 % at 5 Ag^{-1}
MC-1	Hard templated (foam-like structure) mesoporous carbon spheres from phenol	1321	3-e	208 Fg^{-1} at 0.5 Ag^{-1}	70 % at 30 Ag^{-1}
C-1	Hard templated (SBA-16) OMCs from furfuryl alcohol	1880	2-e	172 Fg^{-1} at 0.2 Ag^{-1}	83 % at 1 Ag^{-1}
C-2		1510		154 Fg^{-1} at 0.2 Ag^{-1}	86 % at 1 Ag^{-1}
L-β-900	Hard templated (zeolites) OMCs from lignin	785	3-e	149 Fg^{-1} at 0.05 Ag^{-1}	66 % at 5 Ag^{-1}
L-Y-900		650		189 Fg^{-1} at 0.05 Ag^{-1}	58 % at 5 Ag^{-1}
CC	Hard templated (solid core, mesoporous shell) carbon spheres	1660	2-e	200 Fg^{-1} at 0.1 Ag^{-1}	61 % at 80 Ag^{-1}
HG180-KB6	KHCO ₃ - and KOH-activated hydrochars from α-D-glucose	2210	2-e	239 Fg^{-1} at 0.1 Ag^{-1}	46 % at 90 Ag^{-1}
HG240-KB6		2230		246 Fg^{-1} at 0.1 Ag^{-1}	54 % at 90 Ag^{-1}
HG180-KOH		2760		270 Fg^{-1} at 0.1 Ag^{-1}	51 % at 90 Ag^{-1}
N0	KOH-activated commercial activated carbon Norit® SX2 POCH-Poland	835	2-e	106 Fg^{-1} at 0.05 Ag^{-1}	46 % at 20 Ag^{-1}
N1		1901		172 Fg^{-1} at 0.05 Ag^{-1}	55 % at 20 Ag^{-1}
N2		2400		182 Fg^{-1} at 0.05 Ag^{-1}	56 % at 20 Ag^{-1}
N3		2522		153 Fg^{-1} at 0.05 Ag^{-1}	90 % at 2 Ag^{-1}
N4		2800		196 Fg^{-1} at 0.05 Ag^{-1}	---

Cell type: 2-e, two-electrode configuration; 3-e, three-electrode configuration.

Table A3.4. BET area and electrochemical performance in organic electrolytes (TEABF₄) of the materials of this study and others reported in the literature. Names of the samples correspond to those of their reference source.^{2,8,9,13–23}

Sample	Commentary	A_{BET} ($m^2 g^{-1}$)	Cell type	Organic electrolyte (TEABF ₄)	
				C_e	C_{ret}
A45-DMC	Soft-templated by SWAMM, CO ₂ -activated mesoporous carbons from mimosa tannin	1819	2-e	114 Fg^{-1} at 0.2 Ag^{-1}	114 Fg^{-1} at 0.2 Ag^{-1}
A75-OMC		1867		108 Fg^{-1} at 0.2 Ag^{-1}	108 Fg^{-1} at 0.2 Ag^{-1}
CK-800	Salt templated-assisted K ₂ CO ₃ -activated tannic acid	2510	2-e	140 Fg^{-1} at 0.2 Ag^{-1}	140 Fg^{-1} at 0.2 Ag^{-1}
CK-900		2740		160 Fg^{-1} at 0.2 Ag^{-1}	160 Fg^{-1} at 0.2 Ag^{-1}
Gyroid Cylinder	Soft-templated by EISA, KOH-activated mesoporous carbons	93	2-e	155 Fg^{-1} at 0.05 Ag^{-1}	155 Fg^{-1} at 0.05 Ag^{-1}
MC-1	Hard templated (foam-like structure) mesoporous carbon spheres from phenol	1321	3-e	97 Fg^{-1} at 0.5 Ag^{-1}	97 Fg^{-1} at 0.5 Ag^{-1}
C-1	Hard templated (SBA-16) OMCs from furfuryl alcohol	1880	2-e	96 Fg^{-1} at 0.2 Ag^{-1}	96 Fg^{-1} at 0.2 Ag^{-1}
C-2		1510		89 Fg^{-1} at 0.2 Ag^{-1}	89 Fg^{-1} at 0.2 Ag^{-1}
N0	KOH-activated commercial activated carbon Norit® SX2 POCH-Poland	835	2-e	46 Fg^{-1} at 0.05 Ag^{-1}	46 Fg^{-1} at 0.05 Ag^{-1}
N1		1901		125 Fg^{-1} at 0.05 Ag^{-1}	125 Fg^{-1} at 0.05 Ag^{-1}
N2		2400		140 Fg^{-1} at 0.05 Ag^{-1}	140 Fg^{-1} at 0.05 Ag^{-1}
N3		2522		120 Fg^{-1} at 0.05 Ag^{-1}	120 Fg^{-1} at 0.05 Ag^{-1}
N4		2800		145 Fg^{-1} at 0.05 Ag^{-1}	145 Fg^{-1} at 0.05 Ag^{-1}
SWNT solid		Single-walled carbon nanotubes produced by CVD of C ₂ H ₄		1000	2-e
Aerosol carbon	Hard templated (silicate) mesoporous particles produced by an aerosol process	1522	2-e	115 Fg^{-1} at 0.1 Ag^{-1}	83 % at 10 Ag^{-1}
CGC-3.5	ZnCl ₂ -activated coffee grounds	940	2-e	134 Fg^{-1} at 0.05 Ag^{-1}	30 % at 15 Ag^{-1}
CGC-5		1021		75 % at 20 Ag^{-1}	
NPV1	NaOH-activated carbons from PVDC	1829	2-e	108 Fg^{-1} at 0.05 Ag^{-1}	7 % at 16.2 Ag^{-1}
NPV2		2527		142 Fg^{-1} at 0.05 Ag^{-1}	20 % at 15.5 Ag^{-1}
NPV3		2630		147 Fg^{-1} at 0.05 Ag^{-1}	58 % at 17 Ag^{-1}
NPV4		2675		155 Fg^{-1} at 0.05 Ag^{-1}	71 % at 18 Ag^{-1}
CK-800		1940		135 Fg^{-1} at 0.05 Ag^{-1}	93 % at 40 Ag^{-1}
CK-850	Carbonized potassium citrate	2220	2-e	140 Fg^{-1} at 0.05 Ag^{-1}	89 % at 40 Ag^{-1}
CK-900		2160		125 Fg^{-1} at 0.05 Ag^{-1}	92 % at 40 Ag^{-1}
CMC650	KOH-activated carbons from pine cones, coffee grounds and graphene oxide. Also, carbonized MOFs.	2656	2-e	230 Fg^{-1} at 0.5 Ag^{-1}	68 % at 10 Ag^{-1}
PMC450		1810		200 Fg^{-1} at 0.5 Ag^{-1}	67 % at 10 Ag^{-1}
MC-2		2550		167 Fg^{-1} at 1 Ag^{-1}	87 % at 10 Ag^{-1}
GC-2		2780		141 Fg^{-1} at 1 Ag^{-1}	87 % at 10 Ag^{-1}
PF16G-HA	KOH-activated carbons from hydrothermal treatment of graphene oxide mixed with either phenol-formaldehyde, polyvinyl alcohol, lignin, sucrose or cellulose	3523	2-e	202 Fg^{-1} at 1 Ag^{-1}	86 % at 10 Ag^{-1}
PVA20G-HA		3192		174 Fg^{-1} at 1 Ag^{-1}	90 % at 10 Ag^{-1}
LI24G-HA		3026		190 Fg^{-1} at 1 Ag^{-1}	84 % at 10 Ag^{-1}
SU24G-HA		3355		191 Fg^{-1} at 1 Ag^{-1}	90 % at 10 Ag^{-1}
CE24G-HA		3117		185 Fg^{-1} at 1 Ag^{-1}	86 % at 10 Ag^{-1}
a-MEGO		KOH-activated microwave-exfoliated graphene oxide		3100	2-e
AC-C700	KOH-activated hydrochars from cellulose, potato starch and eucalyptus wood sawdust	2457	2-e	185 Fg^{-1} at 0.2 Ag^{-1}	61 % at 20 Ag^{-1}
AC-C800		2125		145 Fg^{-1} at 0.2 Ag^{-1}	79 % at 20 Ag^{-1}
AC-S700		2273		180 Fg^{-1} at 0.2 Ag^{-1}	59 % at 20 Ag^{-1}
AC-W700		2331		190 Fg^{-1} at 0.2 Ag^{-1}	76 % at 20 Ag^{-1}
AC-W800		2967		230 Fg^{-1} at 0.2 Ag^{-1}	81 % at 20 Ag^{-1}

Cell type: 2-e, two-electrode configuration; 3-e, three-electrode configuration.

References

1. Castro-Gutiérrez, J. et al. High-Rate Capability of Supercapacitors Based on Tannin-Derived Ordered Mesoporous Carbons. *ACS Sustainable Chem. Eng.* 7, 17627–17635 (2019).
2. Díez, N., Ferrero, G. A., Sevilla, M. & Fuertes, A. B. A sustainable approach to hierarchically porous carbons from tannic acid and their utilization in supercapacitive energy storage systems. *J. Mater. Chem. A* 7, 14280–14290 (2019).
3. Sanchez-Sanchez, A. et al. Excellent electrochemical performances of nanocast ordered mesoporous carbons based on tannin-related polyphenols as supercapacitor electrodes. *Journal of Power Sources* 344, 15–24 (2017).
4. Sanchez-Sanchez, A. et al. Ordered mesoporous carbons obtained by soft-templating of tannin in mild conditions. *Microporous and Mesoporous Materials* 270, 127–139 (2018).
5. Elmouwahidi, A. et al. Activated carbons from agricultural waste solvothermally doped with sulphur as electrodes for supercapacitors. *Chemical Engineering Journal* 334, 1835–1841 (2018).
6. Li, Z. et al. Carbonized Chicken Eggshell Membranes with 3D Architectures as High-Performance Electrode Materials for Supercapacitors. *Advanced Energy Materials* 2, 431–437 (2012).
7. Ruiz, V. et al. An activated carbon monolith as an electrode material for supercapacitors. *Carbon* 47, 195–200 (2009).
8. Li, Q. et al. Synthesis of mesoporous carbon spheres with a hierarchical pore structure for the electrochemical double-layer capacitor. *Carbon* 49, 1248–1257 (2011).
9. Fuertes, A. B., Lota, G., Centeno, T. A. & Frackowiak, E. Templated mesoporous carbons for supercapacitor application. *Electrochimica Acta* 50, 2799–2805 (2005).
10. Ruiz-Rosas, R. et al. Electrochemical Performance of Hierarchical Porous Carbon Materials Obtained from the Infiltration of Lignin into Zeolite Templates. *ChemSusChem* 7, 1458–1467 (2014).
11. Ferrero, G. A., Fuertes, A. B. & Sevilla, M. N-doped porous carbon capsules with tunable porosity for high-performance supercapacitors. *Journal of Materials Chemistry A* 3, 2914–2923 (2015).
12. Sevilla, M. & Fuertes, A. B. A Green Approach to High-Performance Supercapacitor Electrodes: The Chemical Activation of Hydrochar with Potassium Bicarbonate. *ChemSusChem* 9, 1880–1888 (2016).
13. Lota, G., Centeno, T. A., Frackowiak, E. & Stoeckli, F. Improvement of the structural and chemical properties of a commercial activated carbon for its application in electrochemical capacitors. *Electrochimica Acta* 53, 2210–2216 (2008).
14. Li, J.-G., Ho, Y.-F., Ahmed, M. M. M., Liang, H.-C. & Kuo, S.-W. Mesoporous Carbons Templated by PEO-PCL Block Copolymers as Electrode Materials for Supercapacitors. *Chemistry - A European Journal* 25, 10456–10463 (2019).
15. Futaba, D. N. et al. Shape-engineerable and highly densely packed single-walled carbon nanotubes and their application as super-capacitor electrodes. *Nature Materials* 5, 987–994 (2006).

16. Chen, Z. et al. High-Performance Supercapacitors Based on Hierarchically Porous Graphite Particles. *Advanced Energy Materials* 1, 551–556 (2011).
17. Rufford, T. E., Hulicova-Jurcakova, D., Fiset, E., Zhu, Z. & Lu, G. Q. Double-layer capacitance of waste coffee ground activated carbons in an organic electrolyte. *Electrochemistry Communications* 11, 974–977 (2009).
18. Xu, B. et al. Activated carbon prepared from PVDC by NaOH activation as electrode materials for high performance EDLCs with non-aqueous electrolyte. *International Journal of Hydrogen Energy* 35, 632–637 (2010).
19. Sevilla, M. & Fuertes, A. B. Direct Synthesis of Highly Porous Interconnected Carbon Nanosheets and Their Application as High-Performance Supercapacitors. *ACS Nano* 8, 5069–5078 (2014).
20. Gadipelli, S. et al. Superior Multifunctional Activity of Nanoporous Carbons with Widely Tunable Porosity: Enhanced Storage Capacities for Carbon-Dioxide, Hydrogen, Water, and Electric Charge. *Adv. Energy Mater.* 10, 1903649 (2020).
21. Zhang, L. et al. Porous 3D graphene-based bulk materials with exceptional high surface area and excellent conductivity for supercapacitors. *Sci Rep* 3, 1408 (2013).
22. Zhu, Y. et al. Carbon-Based Supercapacitors Produced by Activation of Graphene. *Science* 332, 1537–1541 (2011).
23. Wei, L., Sevilla, M., Fuertes, A. B., Mokaya, R. & Yushin, G. Hydrothermal Carbonization of Abundant Renewable Natural Organic Chemicals for High-Performance Supercapacitor Electrodes. *Advanced Energy Materials* 1, 356–361 (2011).

Annex 4

Complementary data for Chapter 7

Complementary data for Chapter 7

Table A4.1. Activation parameters and porosity properties of the two series of KOH activated OMCs of this study.

Sample	Activation route	KOH/Carbon weight ratio	A_{BET} ($m^2 g^{-1}$)	S_{NLDFT} ($m^2 g^{-1}$)	V_{tot} ($cm^3 g^{-1}$)	$V_{u\mu}$ ($cm^3 g^{-1}$)	$V_{s\mu}$ ($cm^3 g^{-1}$)	V_{meso} ($cm^3 g^{-1}$)
OMC	---	---	567	847	0.38	0.16	0.07	0.16
OMC-imp-4	Impregnation	4	1596	1551	0.89	0.21	0.35	0.33
OMC-imp-5	Impregnation	5	1657	1540	0.96	0.15	0.41	0.40
OMC-imp-6	Impregnation	6	1921	1768	1.07	0.20	0.46	0.40
OMC-imp-7	Impregnation	7	2265	1940	1.25	0.17	0.60	0.49
OMC-imp-8	Impregnation	8	2341	1940	1.34	0.14	0.62	0.57
OMC-pm-3	Physical mixing	3	1537	1511	0.87	0.16	0.07	0.16
OMC-pm-4	Physical mixing	4	1701	1613	0.96	0.20	0.33	0.34
OMC-pm-5	Physical mixing	5	2311	1992	1.26	0.20	0.38	0.38

Table A4.2. Chemical composition of as-synthesized and activated OMCs, measured by elemental analysis (EA) and X-ray photoelectron spectroscopy (XPS).

Sample	EA					XPS		
	N (wt%)	C (wt%)	H (wt%)	S (wt%)	O* (wt%)	C (wt%)	O (wt%)	O/ S_{NLDFT} ($\mu mol m^{-2}$)
OMC	0.5	91.5	0.7	0.0	7.2	92.5	7.5	5.5
OMC-imp-4	0.1	95.1	0.3	0.0	4.5	95	5	2.0
OMC-imp-5	0.2	94.5	0.3	0.0	5.0	94.4	5.7	2.3
OMC-imp-6	0.2	95.0	0.2	0.0	4.6	94.1	5.9	2.1
OMC-imp-7	0.2	96.0	0.1	0.0	3.6	95.8	4.2	1.4
OMC-imp-8	0.2	96.4	0.1	0.0	3.3	96.4	3.6	1.1
OMC-pm-3	0.2	93.7	0.5	0.0	5.6	93.6	6.4	2.6
OMC-pm-4	0.2	93.9	0.4	0.0	5.5	93.7	6.3	2.4
OMC-pm-5	0.1	94.6	0.2	0.0	5.1	94.1	5.9	1.8

* By difference

Table A4.3. Peak assignment and relative contributions of surface functionalities for the as-synthesized and activated materials, calculated by deconvolution of the C1s and O1s contributions obtained from XPS analysis.

Sample	C1s contributions					O1s contributions			
	CI	CII	CIII	CIV	CV	OI	OII	OIII	OIV
	A (BE) [% (eV)]								
OMC	68.3 (284.4)	26.9 (285.5)	3.6 (287.6)	1.2 (289.2)	---	25.6 (531.3)	67.4 (532.7)	7.0 (534.5)	---
OMC-imp-4	67.4 (284.5)	26.2 (285.5)	5.1 (287.6)	0.3 (289.1)	0.9 (290.0)	19.2 (531.7)	78.7 (533.0)	2.1 (534.5)	---
OMC-imp-5	65.9 (284.5)	26.0 (285.5)	4.1 (287.6)	0.2 (289.2)	0.3 (290.0)	5.6 (531.3)	92.8 (532.8)	1.6 (534.5)	---
OMC-imp-6	66.8 (284.5)	27.5 (285.5)	4.7 (287.6)	0.3 (289.2)	0.7 (290.0)	14.0 (531.7)	80.6 (532.9)	5.4 (534.5)	---
OMC-imp-7	64.1 (284.5)	28.2 (285.5)	5.8 (287.6)	0.4 (289.2)	1.4 (290.0)	9.7 (531.5)	84.7 (532.9)	5.6 (534.5)	---
OMC-imp-8	68.8 (284.5)	25.7 (285.5)	4.6 (287.6)	0.2 (289.2)	0.7 (290.0)	17.8 (531.4)	73.9 (532.9)	8.3 (534.5)	---
OMC-pm-3	62.4 (284.5)	28.1 (285.6)	6.8 (287.6)	0.7 (289.2)	2.0 (290.2)	11.2 (531.1)	81.1 (532.9)	7.7 (535.1)	---
OMC-pm-4	63.2 (284.5)	27.6 (285.5)	5.5 (287.6)	2.1 (289.2)	1.5 (290.4)	17.6 (531.2)	74.8 (532.9)	4.2 (534.5)	3.4 (536.8)
OMC-pm-5	61.5 (284.4)	27.4 (285.5)	6.1 (287.6)	2.1 (289.2)	2.9 (290.3)	22.2 (531.3)	66.7 (532.9)	6.6 (534.5)	4.4 (536.8)

Table A4.4. BET area and electrochemical performance in aqueous electrolyte (H₂SO₄) of the materials of this study and others reported in the literature. Names of the samples correspond to those of their reference source.¹⁻⁹

Sample	Commentary	A_{BET} ($m^2 g^{-1}$)	H ₂ SO ₄ concentration	Pot. window / current ($V / A g^{-1}$)	C_e ($F g^{-1}$)	E / P ($Wh kg^{-1} /$ $W kg^{-1}$)
OMC-imp-6	Soft-templated by mechanosynthesis, KOH- activated mesoporous carbons from mimosa tannin	1921	1 M	1 / 0.5	160	6 / 132
OMC-imp-7		2265			172	6 / 133
OMC-pm-4		1701			195	7 / 134
OMC-pm-5		2311			195	7 / 133
CK-800		2510			260	9 / 50
CK-900	Salt templated-assisted K ₂ CO ₃ -activated tannic acid	2740	1 M	1 / 0.2	210	7.5 / 47
C30/30	Soft templated by phase separation, CO ₂ - activated OMC from mimosa tannin	1152	2 M	0.8 / 0.2	244	5 / 48
OMC/G-KNO ₃	OMC/graphene oxide composites activated with molten salts	806	1 M	1 / 1	160	6 / 260
OMC/G-KClO ₃		881			185	7 / 250
OMC/G-K ₂ SO ₄		842			176	7 / 250
OMC/G-K ₂ CO ₃		1309			257	10 / 250
OMC-K	OMC/graphene oxide composites activated with KOH	1475	0.5 M	0.9 / 0.5	210	NR
OMC/G-K		2109			290	9 / 210
C1	HTC of coconut shell in the presence of H ₂ O ₂ and/or ZnCl ₂ followed by CO ₂ activation	1750	0.5 M	1 / 0.25	182	6 / 200
C2		1820			168	6 / 200
C3		2440			246	9 / 200
HG180-KB6	KHCO ₃ - and KOH- activated hydrochars from a-D-glucose	2210	1 M	1 / 0.1	239	7 / 120
HG240-KB6		2230			246	7 / 120
HG180-KOH		2760			270	8 / 120
CC	Hard templated (solid core, mesoporous shell) carbon spheres	1660	1 M	1.1 / 0.1	200	8 / 28
K3-800	Cherry stones, activated with ZnCl ₂ or KOH	1167	2 M	0.8 / 0.5	225	5 / 115
K3-900		1624			174	4 / 110
K1-800		1171			232	5 / 150
Z4-800		1267			163	4 / 120
ZTC	Zeolite templated carbon	3600	1 M	1.2 / 1	244	6 / 230

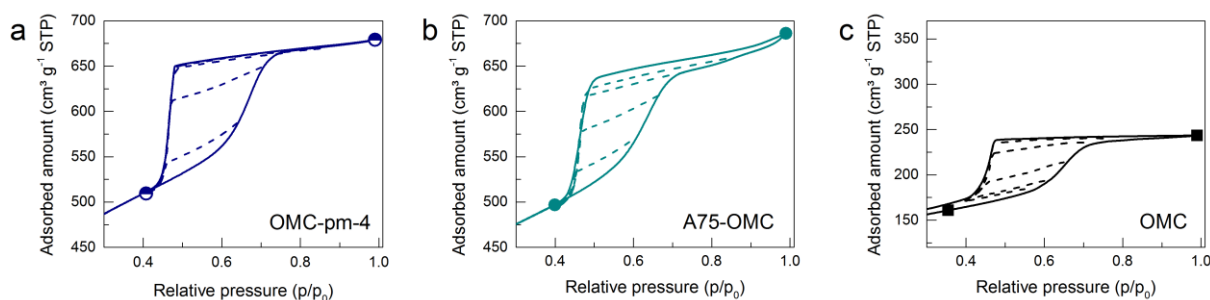


Figure A4.1. Scanned hysteresis of (a) OMC-pm-4, (b) A75-OMC and (c) OMC materials. Solid lines represent the boundary isotherms and dashed lines the scanned or secondary branches.

References

1. Díez, N., Ferrero, G. A., Sevilla, M. & Fuertes, A. B. A sustainable approach to hierarchically porous carbons from tannic acid and their utilization in supercapacitive energy storage systems. *J. Mater. Chem. A* 7, 14280–14290 (2019).
2. Sanchez-Sanchez, A. et al. Ordered mesoporous carbons obtained by soft-templating of tannin in mild conditions. *Microporous and Mesoporous Materials* 270, 127–139 (2018).
3. Chen, P. et al. Ordered Mesoporous Carbons Loading on Graphene after Different Molten Salt Activations for Supercapacitor Applications. *Energy Technol.* 6, 2273–2281 (2018).
4. Lu, S. et al. Effect of aqueous electrolytes on the electrochemical behaviors of ordered mesoporous carbon composites after KOH activation as supercapacitors electrodes. *Journal of Electroanalytical Chemistry* 818, 58–67 (2018).
5. Jain, A. et al. Mesoporous activated carbons with enhanced porosity by optimal hydrothermal pre-treatment of biomass for supercapacitor applications. *Microporous and Mesoporous Materials* 218, 55–61 (2015).
6. Sevilla, M. & Fuertes, A. B. A Green Approach to High-Performance Supercapacitor Electrodes: The Chemical Activation of Hydrochar with Potassium Bicarbonate. *ChemSusChem* 9, 1880–1888 (2016).
7. Ferrero, G. A., Fuertes, A. B. & Sevilla, M. N-doped porous carbon capsules with tunable porosity for high-performance supercapacitors. *Journal of Materials Chemistry A* 3, 2914–2923 (2015).
8. Olivares-Marín, M. et al. Cherry stones as precursor of activated carbons for supercapacitors. *Materials Chemistry and Physics* 114, 323–327 (2009).
9. Mostazo-López, M. J. et al. Ultraporous nitrogen-doped zeolite-templated carbon for high power density aqueous-based supercapacitors. *Carbon* 129, 510–519 (2018).

Annex 5

Lists of Figures and Tables

List of Figures

Résumé de la thèse

Figure 1. (a) Mécanisme de formation de la double couche électrostatique (DCE) dans un SC... (b) Graphique Ragone montrant les valeurs typiques d'énergie et de puissance de différents dispositifs de stockage d'énergie. -----	10
Figure 2. Principales unités flavonoïdes des tanins condensés, ainsi que la plante couramment utilisée pour leur extraction. -----	11
Figure 3. Schéma de la méthode de mécanosynthèse. -----	12
Figure 4. Graphique de contour corrélant le rapport P: W avec les caractéristiques du DTP des matériaux synthétisés et leur structure mésoporeuse. -----	13
Figure 5. Schéma de la connectivité de la structure poreuse des matériaux (a) DMC et (b) OMC... --	14
Figure 6. Performances électrochimiques des CMO activés dérivées du tanin... Les essais ont été effectués dans (a-c) l'électrolyte aqueux acide, (d-f) l'électrolyte organique et (g-i) l'électrolyte aqueux neutre. -----	16
Figure 7. (a) Taux d'usure en fonction du temps d'activation des carbones mésoporeux ordonnés et désordonnés activés (CMOA et CMDA, respectivement). (b) Schéma des différents chemins de diffusion dans les mésopores au sein d'une particule du CMD et du CMO. -----	17
Figure 8. (a) Balayage des boucles d'hystérèse des CMD (colonne à gauche) et des CMO (colonne à droite) avant et après l'activation. Capacité spécifique des SC (C_{cell}) assemblés et testés dans l'électrolyte (b) aqueuse (1 M H_2SO_4) et (c) organique (1 M $TEABF_4/ACN$). -----	18
Figure 9. (a) Surface spécifique (S_{NLDFT}) en fonction du rapport massique KOH/Carbone (r). (b) Volume des pores en fonction de S_{NLDFT} à des échelles des mésopores (V_{meso}), supermicropores ($V_{s\mu}$) et ultramicropores ($V_{u\mu}$). -----	19
Figure 10. (a, b) Courbes de VC à des différents taux de charge... (c) Capacité spécifique des SC (C_{cell}) en fonction de la taux de charges pendant des VC tests. (d) Curves de charge-décharge à 1 A g^{-1} . (e) C_{cell} en fonction de la courant appliqué pendant CDG tests. (f) Énergie spécifique en fonction de la puissance spécifique (graphiques de type Ragone) calculés à partir des courbes CDG. -----	20

Chapter 1

Figure 1.1. Energy storage technologies used at different scales in the power system. [Reproduced from Castro-Gutiérrez et al. (2020) ⁸]-----	26
Figure 1.2. (a) Mechanism of formation of the electrostatic double-layer (EDL) in a SC and its associated simplified electric circuit. (b) Ragone plot showing the typical values of energy and power of different energy storage devices. [Adapted from Castro-Gutiérrez et al. (2020) ⁸]-----	27
Figure 1.3. Different configurations for the electrochemical characterization of SCs: (a) three-electrode cell, (b) two-electrode cell, and (c) T-type cell. [Reproduced from Castro-Gutiérrez et al. (2020) ⁸]---	30
Figure 1.4. Expected behavior of a supercapacitor (SC) and a pseudocapacitor (PSC) compared to that of an ideal SC during different electrochemical tests... Simplified equivalent circuits for: (e) ideal SC, (f) SC and (g) PSC. [Reproduced from Castro-Gutiérrez et al. (2020) ⁸] -----	32
Figure 1.5. Schematic of the production process of activated carbons, from biomass and char, by physical or chemical activation. [Reproduced from Castro-Gutiérrez et al. (2020) ⁸]-----	36
Figure 1.6. (a) Activated CNFs... (b) Aligned CNTs... (c) Schematic of the conductive paths of electrons and ions in a SC electrode based on aligned CNTs and AC particles. (d) Different types of CNSs structures... Images of different types of CNSs (SEM and TEM in the insets)... [Adapted from Ra et al. (2009) ⁵⁵ , Kim et al. (2003) ⁵⁷ , Inagaki et al. (2010) ³⁰ , Liu et al. (2015) ⁶¹ , Braghioroli et al. (2012) ⁶² , Chen et al. (2013) ⁶³ , Fang et al. (2010) ⁶⁴ , and Liu et al. (2013) ⁶⁵]. -----	39

Figure 1.7. (a) Schematic synthesis of OMCs by hard and soft template methods. (b, c) Hard-templated OMCs using SBA-15 as template... and (d) KIT-6 template... (e-g) Soft-templated OMCs using Pluronic® F127 as surfactant... [Adapted from Castro-Gutiérrez et al. (2020) ⁸ , Sánchez-Sánchez et al. (2016) ⁷⁰ , Lang et al. (2011) ⁷¹ , Meng et al. (2005) ⁷² , and Li and Xue (2012) ⁷³]	40
Figure 1.8. (a) Oxygen and nitrogen surface functional groups commonly associated with the enhanced performance of carbon-based SCs. Proposed reactions of such (b – f) oxygen and (g – k) nitrogen surface functionalities. ^{70,84,85} [Reproduced from Castro-Gutiérrez et al. (2020) ⁸]	42
Figure 1.9. Main flavonoid units of condensed tannins, along with the plant commonly used for their extraction. [Reproduced from Castro-Gutiérrez et al. (2020) ⁸]	45
Figure 1.10. SEM images of materials obtained after HTC at 210 °C and subsequent pyrolysis at 900 °C of tannin in (a) water, or (b) ammonia solution, and (c) evaporated aminated tannin in water. (d) Examples of cyclic voltammetry curves... Normalized capacitance as a function of (e) nitrogen and (f) oxygen content of carbonized HTC materials... and of EAT-derived CGs... [Adapted from Braghiroli et al (2015) ⁶⁷ and Braghiroli et al (2015) ⁹⁴]	48
Figure 1.11. Synthesis of OMCs from mimosa tannin by (a) hard-templating, also carried out using other biomass-derived phenolic molecules; and soft-templating through (b) phase separation [Adapted from Sánchez-Sánchez et al. (2017) ¹⁰⁰ and Braghiroli et al. (2016) ⁷⁸].	54

Chapter 2

Figure 2.1. Schematic of a transmission electron microscope. [Adapted from Reimer and Kohl (2008) ¹]	69
Figure 2.2. IUPAC classification of (a) isotherms and (b) hysteresis loops found in physisorption analysis. [Adapted from Thommes et al. (2015) ²]	71
Figure 2.3. Automatic adsorption devices: (a) 3Flex, (b) ASAP 2020, and (c) ASAP 2420 from Micromeritics; and (d) Autosorb iQ from Quantachrome.	72
Figure 2.4. (a) Setaram C80 calorimeter. (b) Experimental set-up used for immersion calorimetry tests [Reprinted from Silvestre-Albero et al. (2001) ¹⁵].	75
Figure 2.5. (a) Raman and Rayleigh scattering produced after the interaction of a material with a monochromatic source of light. (b) Horiba Scientific XploRa Raman spectrometer used to analyze the carbon materials of this study.	76
Figure 2.6. (a) Geometric derivation of Bragg's law. (b) XRD pattern of pyrolytic graphite. (c) Examples of lattice planes in a crystal structure. (d) Simulated XRD patterns for OMCs with a 2D hexagonal geometrical structure. (e) Bruker D8 Advance X-ray powder diffractometer. [Adapted from Stanjek and Häusler (2004) ¹⁹ , Ermrich and Opper (2013) ²¹ and Schmidt (2009) ²²]	77
Figure 2.7. Typical curves obtained from the thermogravimetric analysis of samples carried out in the STA 449F3 Jupiter microbalance from Netzsch (inset).	78
Figure 2.8. (a) Vario EL Cube and (b) working principle of the device. [Adapted from Elementar ²³]	78
Figure 2.9. (a) Schematized operating principle of the XPS characterization technique. Examples of (a) carbon and (b) oxygen high-resolution XPS spectra of tannin-derived carbon materials. [Adapted from Andrade (1985) ²⁴ and Sánchez-Sánchez et al. (2017) ²⁵]	80
Figure 2.10. Typical FTIR spectra of mimosa tannin; the inset shows the Frontier 400 spectrometer from PerkinElmer used for the acquisition.	80
Figure 2.11. (a) MM 400 vibrational milling machine from Retsch. (b) VSP300 electrochemical working station from Bio-Logic and (c) Swagelok electrode cells used for the electrochemical characterization.	81
Figure 2.12. (a) DSA100 liquid-solid contact angle analyzer from Krüss and (b) example of measurement taken from the image capture by the device.	82
Figure 2.13. Photos of MATERLOR platform of Biosourced Materials Research team at <i>Institut Jean Lamour</i> at Epinal, France.	83

Chapter 3

- Figure 3.1.** Schematic of the mechanosynthesis method. [Adapted from Castro-Gutiérrez et al. (2018)²²] -----90
- Figure 3.2.** N₂ adsorption-desorption isotherms and corresponding PSDs for CT2P2W2_60 and of carbonized reference samples CT2P0W0_60, CT2P0W2_60, and CT2P2W0_60. [Adapted from Castro-Gutiérrez et al. (2018)²²]-----92
- Figure 3.3.** Absolute (left scale) and differential (right scale) normalized mass losses of (a) T2P2W2_60 and reference samples; and (b) samples T2P2W2_*t* prepared at various milling times... [Reproduced from Castro-Gutiérrez et al. (2018)²²] -----93
- Figure 3.4.** N₂ adsorption-desorption isotherms and corresponding PSDs for: (a, b) CT2P2W2_*t* samples, 30 < *t* < 120 min... [Adapted from Castro-Gutiérrez et al. (2018)²²] -----94
- Figure 3.5.** Detailed view of the FTIR spectra of samples T2P2W2_*t* synthesized during different milling times, ranging from 30 to 90 min... [Reproduced from Castro-Gutiérrez et al. (2018)²²]-----95
- Figure 3.6.** (a) N₂ adsorption-desorption isotherms and (b) corresponding PSDs of carbon materials CT2P2pH_x_60, synthesized by using aqueous solutions of HCl at pH ranging from 0 to 4 instead of water, and a milling time of 60 min... [Reproduced from Castro-Gutiérrez et al. (2018)²²] -----96
- Figure 3.7.** Comparison between CT2P2W2_60 and CT2P2pH1_60: (a) N₂ adsorption-desorption isotherms; (b) PSDs; and (c,d) TEM images. [Reproduced from Castro-Gutiérrez et al. (2018)²²] ----96
- Figure 3.8.** (a,c) N₂ adsorption-desorption isotherms and (b,d) corresponding PSDs of carbon materials synthesized using 60 min of milling and various P:W weight ratios... TEM images of (e) CT2P2W1_60, (f) CT2P2W2_60 and (g, h) transversal and longitudinal views of CT2P1W2_60... [Adapted from Castro-Gutiérrez et al. (2018)²²]-----97
- Figure 3.9.** (a) Contour plot of the ratio M / FWHM of peaks obtained by deconvolution of the PSDs of samples synthesized using different P:W weight ratios and 60 min of ball-milling. The experimental P:W ratios tested are represented by points... stars and squares... (b) Highest and narrowest PSD and (c) corresponding N₂ adsorption-desorption isotherm found for sample CT2P0.75W1.75_60... (d, e) TEM images confirming the 2D hexagonal structure of the same sample. [Adapted from Castro-Gutiérrez et al. (2018)²²]-----98
- Figure 3.10.** Peak position (PP, solid symbols) and mesopore volume (V_{meso} , hollow symbols) as a function of the initial mass of P and W... [Adapted from Castro-Gutiérrez et al. (2018)²²]-----99
- Figure 3.11.** (a) N₂ adsorption-desorption isotherms and (b) corresponding PSDs for CT2P1W2_60 pyrolyzed at different temperatures... [Reproduced from Castro-Gutiérrez et al. (2018)²²]----- 100
- Figure 3.12.** (a) TEM images of CT2P1W2_60 pyrolyzed at 1100, 1300 and 1500 °C... (b) BET area (A_{BET}) and micro and mesopore volume ($V_{\mu,NLDFT}$ and V_{meso} , respectively) of CT2P1W2_60 as a function of pyrolysis temperature... (c) Raman spectra of CT2P1W2_60 pyrolyzed at different temperatures... (d) D₁/G intensity ratio and full width at half-maximum (FWHM) of the D₁ band as a function of temperature. [Reproduced from Castro-Gutiérrez et al. (2018)²²]----- 101
- Figure 3.13.** (a) Set of water drops on CT2P1W2_60, the insert shows a WCA = 157.4°. (b) Adsorption of heptane by CT2P1W2_60 in 40 s. (c) CO₂ adsorption capacities, at 0.1 MPa and 0 °C, as a function of micropore volume for materials from this study and materials reported in the open literature.⁴⁹⁻⁵¹ [Adapted from Castro-Gutiérrez et al. (2018)²²] ----- 102

Chapter 4

- Figure 4.1.** Hysteresis loops and their associated mesoporous structures and adsorption-desorption mechanisms... (f) Examples of scanned hysteresis loops for materials having independent or connected mesopores. [Adapted from Thommes and Cychosz (2014)¹ and Thommes (2010)⁶]. ----- 112
- Figure 4.2.** TEM images of (a) the disordered mesoporous carbon (DMC); and (b) longitudinal and (c) transversal views of the ordered mesoporous carbon (OMC). ----- 114

Figure 4.3. Argon (87 K) and nitrogen (77 K) adsorption-desorption isotherms for: (a) DMC and (b) OMC materials... Combined pore size distributions (PSDs) derived from the adsorption branches of argon and carbon dioxide isotherms... -----	115
Figure 4.4. Nitrogen (N ₂) isotherms at 77 K obtained by performing two consecutive measurements on the same sample of a disordered and an ordered mesoporous carbon (DMC and OMC, respectively). -----	115
Figure 4.5. Pore size distributions (PSDs) in the mesopore range for (a, b, c) DMC and (d, e, f) OMC samples. (a, d) PSDs obtained from the adsorption and desorption branches of Ar isotherms. PSDs obtained from Ar and N ₂ isotherms using their (b, e) adsorption branches and (c, f) desorption branches. -----	117
Figure 4.6. Scanned hysteresis loop of N ₂ adsorption-desorption isotherms for (a) DMC and (b) OMC materials... -----	119
Figure 4.7. Vapor adsorption-desorption isotherms of nHEX, 2MP and 22DMB for (a, b) DMC and (c, d) OMC materials, at (a, c) 25 °C and (b, d) at 45 °C. -----	121
Figure 4.8. Scheme of the connectivity of the porous structure of (a) DMC and (b) OMC materials... -----	122

Chapter 5

Figure 5.1. Scheme of the followed procedure to synthesized and activate OMCs derived from mimosa tannin. [Reproduced from Castro-Gutiérrez et al. (2019) ⁸]-----	131
Figure 5.2. (a) N ₂ adsorption-desorption isotherms for the activated carbons and the as-synthesized material. (b) BET area and NLDFT surface area of the AOMCs as a function of burn-off, BO. (c) Changes of pore volume with BO. [Adapted from Castro-Gutiérrez et al. (2019) ⁸] -----	133
Figure 5.3. PSDs (a) in the mesopore range and (c) in the whole pore width interval. (b) TEM images... confirming the 2D hexagonal ordered mesopore structure of CTPW (non-activated) and A90-CTPW (78 % BO). [Adapted from Castro-Gutiérrez et al. (2019) ⁸] -----	134
Figure 5.4. Small-angle XRD measurements for the as-synthesized material and AOMCs activated during 30, 75 and 90 min. [Reproduced from Castro-Gutiérrez et al. (2019) ⁸]-----	134
Figure 5.5. (a) Oxygen content measured in the bulk, by elemental analysis, and at the surface, measured by XPS. (b) Relative contributions to the oxygen surface functionalities... [Reproduced from Castro-Gutiérrez et al. (2019) ⁸] -----	135
Figure 5.6. Electrochemical performances of A30- to A90-CTPW samples in 1 M H ₂ SO ₄ . (a) CV curves at 5 mV s ⁻¹ . (b) Specific cell capacitance, C_{cell} , as a function of BO. (c) Normalized electrode capacitance with respect to the BET area, $C_{e,NBET}$, as a function of average pore size, w_{av} ... (d) C_{cell} as a function of scan rate; (e) normalized capacitance with respect to NLDFT surface area, $C_{e,NLDFT}$, as a function of w_{av} ... [Reproduced from Castro-Gutiérrez et al. (2019) ⁸] -----	137
Figure 5.7. Electrochemical performances in aqueous electrolyte (1 M H ₂ SO ₄) of A60-CTPW and A75-CTPW: (a, b) CV curves at different scan rates; (c, d) GCD curves at different applied currents; capacitance retention, C_{ret} , as a function of (e) applied current and (f) after continuous cycling at 5 A g ⁻¹ ; (g) Ragone-like plot obtained from GCD tests. [Adapted from Castro-Gutiérrez et al. (2019) ⁸]---	138
Figure 5.8. Capacitance retention over time by potentiostatic hold at maximum cell voltage in 1 M H ₂ SO ₄ ... and TEABF ₄ /ACN... [Adapted from Castro-Gutiérrez et al. (2019) ⁸]-----	139
Figure 5.9. Electrochemical performances in the organic electrolyte (1 M TEABF ₄ /ACN) of A60-CTPW and A75-CTPW: (a, b) CV curves at different scan rates; (c) capacitance retention, C_{ret} , as a function of applied current (top) and after continuous cycling at 5 A g ⁻¹ (bottom); (d) Ragone-like plot obtained from GCD tests. [Adapted from Castro-Gutiérrez et al. (2019) ⁸] -----	140
Figure 5.10. Nyquist plots for A60- and A75-CTPW in both aqueous and organic electrolytes. [Adapted from Castro-Gutiérrez et al. (2019) ⁸]-----	141

Figure 5.11. Capacitance retention in (a) aqueous and (b) organic electrolytes for the AOMCs of this study in comparison with similar materials reported in the literature. ^{22,25–35} ... [Adapted from Castro-Gutiérrez et al. (2019) ⁸] -----	142
Figure 5.12. Specific cell capacitance, C_{cell} , and capacitance retention, C_{ret} , of A60-CTPW in (a,b) aqueous and (c,d) organic electrolytes, calculated from GCD tests... using electrodes with carbon loads of ~ 10 and ~ 6 mg cm ⁻² . [Adapted from Castro-Gutiérrez et al. (2019) ⁸] -----	142
Figure 5.13. Electrochemical performance of A60-CTPW and A75-CTPW in NaSO ₄ as aqueous electrolyte: (a) CV curves at 5 and 200 mV s ⁻¹ ; (b) capacitance retention with applied current; (c) Ragone-like plot for the achieved energy and power of the assembled SCs; (d) capacitance retention after continuous cycling at 5 A g ⁻¹ ... [Adapted from Castro-Gutiérrez et al. (2019) ⁸] -----	143
Figure 5.14. (a, d, g) Gravimetric and (b, e, h) volumetric single electrode capacitance as a function of the applied current and (c, f, i) Ragone-like plot presenting the achieved energy and power densities... in the three electrolytes: (a, b, c) 1 M H ₂ SO ₄ , (d, e, f) 1 M Na ₂ SO ₄ and (g, h, i) 1 M TEABF ₄ /ACN. [Reproduced from Castro-Gutiérrez et al. (2019) ⁸]-----	144

Chapter 6

Figure 6.1. (a) Burn-off (BO) as a function of activation time for the activated ordered and disordered carbons (AOMC and ADMC, respectively). (b) Scheme of different diffusion paths within a particle of disordered and ordered mesoporous carbon (DMC and OMC, respectively). (c) 1 st order Raman spectra of as-synthesized DMC, OMC and mimosa tannin carbonized at the same temperature of 900 °C. -	153
Figure 6.2. (a, c) N ₂ adsorption-desorption isotherms of raw and activated DMCs and OMCs; (b, d) corresponding PSDs of the same materials. -----	154
Figure 6.3. Evolution of (a) 2D-NLDFT HS surface area (S_{NLDFT}) and BET area (A_{BET}), and (b) meso-, supermicro- and ultramicropore volumes (V_{meso} , $V_{5\mu}$ and $V_{1\mu}$, respectively) as a function of burn-off (BO) for the two series of activated DMCs and OMCs. -----	155
Figure 6.4. Scanned hysteresis loops of as-synthesized and activated (a, c, e) disordered and (b, d, f) ordered MCs... -----	156
Figure 6.5. Slope of (a) the tangent line at the starting point (p_{des}) of scanned desorption branches as a function of p_{des} , for DMC, A15-DMC and A30-DMC samples; and (d) of desorption branches as a function of p_{des} for OMC, A30-OMC and A75-OMC samples. Contribution to the mesoporous volume of pores having widths below and above 5 nm... for (b) ADMCs and (e) AOMCs materials. Average pore width of mesopores, as well of mesopores in the 2 – 5 nm and 5 – 50 nm ranges... for (c) ADMCs and (f) AOMCs materials.-----	158
Figure 6.6. Oxygen content of the two series of activated materials, ADMCs and AOMCs measured (a) by elemental analysis (EA) and (b) by X-ray photoelectron spectroscopy (XPS). O1s contributions to the different functional groups for (c) ADMC and (d) AOMC series. -----	159
Figure 6.7. Comparison of textural properties of A45-DMC and A75-OMC... -----	160
Figure 6.8. (a) Solvated ion size of H ₂ SO ₄ in water. ²⁰ Electrochemical performance of A45-DMC and A75-OMC in aqueous electrolyte (1 M H ₂ SO ₄)... -----	162
Figure 6.9. (a, b) Nyquist and (c, d) Bode plots for A45-DMC and A75-OMC in (a) aqueous and (b) organic electrolytes.-----	162
Figure 6.10. (a) Solvated ion size of TEABF ₄ in acetonitrile. ³³ Electrochemical performance of A45-DMC and A75-OMC in the organic electrolyte (1 M TEABF ₄ /ACN)... -----	164
Figure 6.11. Long-term stability of A45-DMC and A75-OMC in aqueous (1 M H ₂ SO ₄) and organic (1 M TEABF ₄ /ACN) electrolytes after (a, b) continuous cycling at 5 A g ⁻¹ and (c, d) potentiostatic hold at the maximum potential (1 V and 2.7 V for aqueous and organic electrolytes, respectively). -----	164
Figure 6.12. Comparison of the capacitance retention (C_{ret}) as a function of the BET area (A_{BET}) for the materials of this study and others reported in the literature: (a,b) in aqueous electrolyte (H ₂ SO ₄) at 20 A g ⁻¹ and (c,d) in organic electrolyte (TEABF ₄) at 10 A g ⁻¹ . ^{8,21–23,27,28,30–32,34–40,42} -----	165

Chapter 7

- Figure 7.1.** TEM images of OMC (a, d) before and after activation by (b, e) impregnation and (c, f) physical mixing routes. ----- 174
- Figure 7.2.** Small-angle XRD measurements for (a) OMC-imp and (b) OMC-pm series of activated materials. ----- 174
- Figure 7.3.** (a-c) Nitrogen adsorption-desorption isotherms and (d-f) pore size distributions for the different series of activated materials: (a, d) OMC-imp-*r*, (b, e) OMC-pm-*r* and (c, f) DMC-pm-*r*. - 175
- Figure 7.4.** (a) Surface area calculated using the 2D-NLDFT HS (S_{NLDFT}) as a function of the KOH/carbon weight ratio (*r*). (b) Pore volume as a function of S_{NLDFT} for different ranges of pore width: mesopores (V_{meso}), supermicropores ($V_{S\mu}$) and ultramicropores ($V_{u\mu}$). ----- 176
- Figure 7.5.** (a) Bulk and (b) surface oxygen content, measured by elemental analysis (EA) and X-ray photoelectron spectroscopy (XPS), respectively, and (c) oxygen surface concentration, calculated from XPS measurements, as a function of the surface area of the as-synthesized and activated materials. 177
- Figure 7.6.** Electrochemical performance of KOH-AOMCs obtained by impregnation (OMC-imp-6, OMC-imp-7) and physical mixing (OMC-pm-4, OMC-pm-5) routes obtained from CV tests...----- 178
- Figure 7.7.** Electrochemical performance of KOH-AOMCs obtained by impregnation (OMC-imp-6, OMC-imp-7) and physical mixing (OMC-pm-4, OMC-pm-5) routes obtained from GCD tests... -- 180
- Figure 7.8.** (a) Nyquist plot and (b) frequency response of the real part of the complex capacitance (C_r) normalized by the value of capacitance at 0.01 Hz ($C_{0.01}$) for the KOH-AOMCs obtained by impregnation (OMC-imp-6, OMC-imp-7) and physical mixing (OMC-pm-4, OMC-pm-5) routes. - 182
- Figure 7.9.** (a) Interfacial electrode capacitance ($C_{e,s}$) as a function of applied current and (b) frequency response of the real part of the complex capacitance (C_r) normalized by the value of capacitance at 0.01 Hz ($C_{0.01}$) for OMC-pm-4 compared to the corresponding values for the CO₂-activated A75-OMC presented in Chapters 5 and 6. ----- 183
- Figure 7.10.** Differential and cumulative (a) volume and (b) surface PSDs of OMC-pm-4 and A75-OMC; (c) contribution to the pore volume from pores of different sizes. (c) Slope of the desorption branches as a function of the relative pressure at their starting point (*pdes*) for OMC-pm-4, A75-OMC and OMC materials.----- 184

Annex 1

- Figure A1.1.** Examples of deconvolution into Lorentzian contributions performed on the PSDs of CT2P2W2_60, CT2P2W1_60 and CT2P1.5W2_60 samples. [Adapted from Castro-Gutiérrez et al. (2018)]..... 197
- Figure A1.2.** Raman spectra of CT2P1W2_60 pyrolyzed at different temperatures, and corresponding D₁, D₃, D₄ and G bands. [Reproduced from Castro-Gutiérrez et al. (2018)]..... 200

Annex 4

- Figure A4.1.** Scanned hysteresis of (a) OMC-pm-4, (b) A75-OMC and (c) OMC materials. Solid lines represent the boundary isotherms and dashed lines the scanned or secondary branches. 220

List of Tables

Chapter 1

- Table 1.1.** Properties of aqueous and organic electrolytes often used in SCs.^{12,23,26,27} [Adapted from Castro-Gutiérrez et al. (2020)⁸] 34

Table 1.2. Hazard statements for phenol, resorcinol, formaldehyde and tannin with data from the National Center for Biotechnology Information ¹¹⁴ and the National Institute for Occupational Safety and Health. ¹¹⁵ [Adapted from Castro-Gutiérrez et al. (2020) ⁸]	46
Table 1.3. Summary of synthesis methods, properties and electrochemical performance of tannin-derived carbon materials.	56

Chapter 2

Table 2.1. Materials associated with the different types of adsorption-desorption isotherms and hysteresis loops, according to the IUPAC classification. ²	71
--	----

Chapter 4

Table 4.1. Kinetic diameters (\emptyset) of the hexane isomers used as probe molecules. ²⁶⁻²⁹ Enthalpy of immersion ($-\Delta H_{imm}$) and accessible surface area (S) for the different C ₆ isomers in samples DMC and OMC.....	120
--	-----

Annex 1

Table A1.1. Pore texture parameters, calculated from N ₂ and CO ₂ adsorption isotherms, of carbon materials: (i) prepared with various amounts of Pluronic® F127 and water, and used as references; (ii) obtained after various milling times; and (iii) synthesized with 2 g of aqueous HCl solutions with different pH values. [Adapted from Castro-Gutiérrez et al. (2018) ¹].....	197
Table A1.2. Characteristics of the main peaks in the PSDs of carbon materials synthesized using 60 min of milling and various P:W weight ratios. [Adapted from Castro-Gutiérrez et al. (2018)].....	198
Table A1.3. Pore texture parameters of samples synthesized with different P:W initial ratios and obtained after 60 min of ball-milling, calculated from N ₂ and CO ₂ isotherms. [Adapted from Castro-Gutiérrez et al. (2018)]	199

Annex 2

Table A2.1. Pore texture parameters, calculated from N ₂ and CO ₂ adsorption isotherms, for the as-synthesized material and the AOMCs. [Reproduced from Castro-Gutiérrez et al. (2019)]	203
Table A2.2. Peak assignment and relative contributions of surface functionalities obtained by XPS analysis. [Reproduced from Castro-Gutiérrez et al. (2019)]	203
Table A2.3. Single electrode specific capacitance ($C_e = 4 C_{cell}$) at 5 A g ⁻¹ of A60-CTPW and A75-CTPW and other un-doped materials with similar properties reported in the literature... [Adapted from Castro-Gutiérrez et al. (2019)]	204

Annex 3

Table A3.1. Pore texture parameters of the as-synthesized and activated disordered mesoporous carbons.	209
Table A3.2. Peak assignment and relative contributions of surface functionalities obtained by XPS of the as-synthesized and activated disordered mesoporous carbons.	209
Table A3.3. BET area and electrochemical performance in aqueous electrolyte (H ₂ SO ₄) of the materials of this study and others reported in the literature. Names of the samples correspond to those of their reference source. ¹⁻¹³	210

Table A3.4. BET area and electrochemical performance in organic electrolytes (TEABF₄) of the materials of this study and others reported in the literature. Names of the samples correspond to those of their reference source.^{2,8,9,13-23} 211

Annex 4

Table A4.1. Activation parameters and porosity properties of the two series of KOH activated OMCs of this study. 217

Table A4.2. Chemical composition of as-synthesized and activated OMCs, measured by elemental analysis (EA) and X-ray photoelectron spectroscopy (XPS). 217

Table A4.3. Peak assignment and relative contributions of surface functionalities for the as-synthesized and activated materials, calculated by deconvolution of the C1s and O1s contributions obtained from XPS analysis. 218

Table A4.4. BET area and electrochemical performance in aqueous electrolyte (H₂SO₄) of the materials of this study and others reported in the literature. Names of the samples correspond to those of their reference source.¹⁻⁹ 219

Annex 6

List of scientific works derived from
this thesis study

List of scientific works derived from this thesis study

Publications in scientific journals

Published:

- Castro-Gutiérrez, J.; Sanchez-Sanchez, A.; Ghanbaja, J.; Díez, N.; Sevilla, M.; Celzard, A.; Fierro, V. Synthesis of Perfectly Ordered Mesoporous Carbons by Water-Assisted Mechanochemical Self-Assembly of Tannin. *Green Chemistry* (2018). DOI: 10.1039/c8gc02295j
- Castro-Gutiérrez, J.; Díez, N.; Sevilla, M.; Izquierdo, M. T.; Ghanbaja, J.; Celzard, A.; Fierro, V. High-rate capability of supercapacitors based on tannin-derived ordered mesoporous carbons. *ACS Sustainable Chemistry and Engineering* (2019). DOI: 10.1021/acssuschemeng.9b03407
- Castro-Gutiérrez, J.; Celzard, A.; Fierro, V. Energy storage in supercapacitors: Focus on tannin-derived carbon electrodes. *Frontiers in Materials* (2020). DOI: 10.3389/fmats.2020.00217

Submitted:

- Castro-Gutiérrez, J.; Díez, N.; Sevilla, M.; Izquierdo, M. T.; Celzard, A.; Fierro, V. Understanding the effect of mesopore order on the supercapacitor performances of carbon materials.
- Castro-Gutiérrez, J.; Jardim, E. O.; Canevesi, R. L. S.; Silvestre-Albero, J.; Kriesten, M.; Thommes, M.; Celzard, A.; Fierro, V. Molecular sieving of linear and branched C₆ alkanes by tannin-derived carbons.

Oral communications

- Castro-Gutiérrez, J.; Sanchez-Sanchez, A.; Izquierdo, M. T.; Celzard, A.; Fierro, V. High surface area, tannin-derived, ordered mesoporous carbons as electrodes of supercapacitors. *World Conference on Carbon*, Madrid, Spain. July 1st – 6th, 2018.
- Fierro, V.; Castro-Gutiérrez, J.; Sanchez-Sanchez, A.; Celzard, A. Surfactant-water-assisted mechanochemical mesostructuring of tannins to synthesize OMCs. *World Conference on Carbon*, Madrid, Spain. July 1st – 6th, 2018. [Presented by Fierro, V.]
- Fierro, V.; Castro-Gutiérrez, J.; Sanchez-Sanchez, A.; Ghanbaja, J.; Celzard, A. Les tannins, de nouveaux précurseurs de carbones mésoporeux parfaitement ordonnés. *Matériaux*, Strasbourg, France. November 22nd, 2018. [Presented by Fierro, V.]

- Castro-Gutiérrez, J.; Sanchez-Sanchez, A.; Ghanbaja, J.; Díez, N.; Sevilla, M.; Celzard, A.; Fierro, V. Mechanochemical synthesis of mesoporous carbons derived from tannin. *Colloque Annuel de la Société Francophone d'Etude des Carbones*, Samatan, France. April 23th – 27th, 2019. [Awarded with the Micromeritics price for the best oral presentation from a PhD student]
- Castro-Gutiérrez, J.; Díez, N.; Sevilla, M.; Izquierdo, M. T.; Ghanbaja, J.; Celzard, A.; Fierro, V. Activated mesoporous carbons derived from tannin as electrodes for supercapacitors. *World Conference on Carbon*, Lexington, Kentucky, USA. July 14th – 19th, 2019.
- Castro-Gutiérrez, J.; Celzard, A.; Fierro, V. Carbones mésoporeux dérivés du tannin: Des matériaux modèles pour des applications énergétiques et environnementales. *Journée Thèses des Bois à l'Université Laval*, Québec, Canada. September 30th, 2019.
- Fierro, V.; Castro-Gutiérrez, J.; Díez, N.; Sevilla, M.; Izquierdo, M.T.; Ghanbaja, J.; Celzard, A. Tannins as new, green, precursors of mesoporous carbons. Woodchem, Nancy, France. November 22nd, 2019. [Presented by Fierro, V.]

Poster communications

- Castro-Gutiérrez, J.; Sanchez-Sanchez, A.; Izquierdo, M. T.; Celzard, A.; Fierro, V. Electrochemical performances of KOH-activated, tannin-based, ordered mesoporous carbons. *World Conference on Carbon*, Madrid, Spain. July 1st – 6th, 2018.
- Monsivais-Rocha, J. E.; Castro-Gutiérrez, J.; Sanchez-Sanchez, A.; Celzard, A.; Fierro, V. Hydrolysable tannins as alternative precursors to synthesize ordered mesoporous carbons. *World Conference on Carbon*, Madrid, Spain. July 1st – 6th, 2018.
- Monsivais-Rocha, J. E.; Castro-Gutiérrez, J.; Fierro, V.; Celzard, A. Nouveaux carbones mésoporeux ordonnés dérivés de tannins hydrolysables. *Matériaux*, Strasbourg, France. November 19th – 23th, 2018.
- Castro-Gutiérrez, J.; Ramírez-Vidal, P.; Izquierdo, M. T.; Ghanbaja, J.; Celzard, A.; Fierro, V. KOH activation of tannin-derived ordered mesoporous carbons for supercapacitor devices. *World Conference on Carbon*, Lexington, Kentucky, USA. July 14th – 19th, 2019.
- Castro-Gutiérrez, J.; Izquierdo, M. T.; Ghanbaja, J.; Celzard, A.; Fierro, V. Electrochemical performances of nitrogen-doped mesoporous carbons derived from tannin. *World Conference on Carbon*, Lexington, Kentucky, USA. July 14th – 19th, 2019.
- Castro-Gutiérrez, J.; Izquierdo, M. T.; Ghanbaja, J.; Celzard, A.; Fierro, V. Le tanin comme précurseur de carbones mésoporeux dopés à l'azote pour le stockage d'énergie. 8^{èmes} journées du GDR 3544 « Sciences du bois », Epinal, France, November 18th – 21st, 2019.

Abstract

In this thesis, the physicochemical properties of tannin-derived mesoporous carbons were studied and their electrochemical performance as electrodes for supercapacitors (SCs) was evaluated in aqueous and organic electrolytes. The main objective of this study was to develop a fast and easy, and environmentally friendly method for the synthesis of mesoporous carbons. A novel surfactant-water-assisted mechanochemical mesostructuration (SWAMM) one-pot method was developed and optimized to produce ordered and disordered mesoporous carbons (OMCs and DMCs, respectively), only by adjusting the surfactant to water weight ratio. Further physical or chemical activation of both OMCs and DMCs improved the textural properties of the materials that resulted in good SC performance, even at high charging rates, in aqueous and organic electrolytes. The in-depth characterization performed for these new materials has also led to a better understanding of the effect of order and connectivity of the micro-mesoporous structure on the development of textural properties by the different activation processes and, consequently, on the electrochemical performance of the assembled SC.

Résumé

Dans cette thèse, les propriétés physico-chimiques des carbones mésoporeux dérivés du tanin ont été étudiées et leurs performances électrochimiques en tant qu'électrodes pour des supercondensateurs (SC) ont été évaluées dans des électrolytes aqueux et organiques. L'objectif principal de cette étude était de développer une méthode de synthèse des carbones mésoporeux rapide, facile et respectueuse de l'environnement. Une nouvelle méthode de mésostructuration mécano-chimique, assistée par l'interaction de l'eau avec un tensioactif, en une seule étape (SWAMM) a été développée et optimisée. Elle a permis de produire des carbones mésoporeux ordonnés et désordonnés (CMO et CMD, respectivement), uniquement en ajustant le rapport pondéral entre le tensioactif et l'eau. L'activation physique ou chimique des CMO et des CMD a permis d'améliorer les propriétés texturales des matériaux, ce qui a entraîné de bonnes performances des SC, même à des taux de charge élevés, dans des électrolytes aqueux et organiques. La caractérisation approfondie de ces nouveaux matériaux a également permis de mieux comprendre l'effet de l'ordre et de la connectivité de la structure micro-mésoporeuse sur le développement des propriétés texturales par les différents processus d'activation et, par conséquent, sur les performances électrochimiques des SC assemblés.